Swansea University
Prifysgol Abertawe


# A Computational Framework for A First-Order System of Conservation Laws in Thermoelasticity

by

Ataollah Ghavamian

Submitted to the College of Engineering
in partial fulfilment of the requirements for the degree of

Doctor of Philosophy

at

Swansea University

April 2020

# Declaration

This work has not previously been accepted in substance for any degree and is not being concurrently submitted in candidature for any degree.

Signed ..... [redacted] ..... (candidate)

Date ..... 16/04/2020 .....

**STATEMENT 1**

This thesis is the result of my own investigations, except where otherwise stated. When correction services have been used, the extent and nature of the correction is clearly marked in a footnote(s). Other sources are acknowledged by footnotes giving explicit references. A bibliography is appended.

Signed ..... [redacted] ..... (candidate)

Date ..... 16/04/2020 .....

**STATEMENT 2**

I hereby give consent for my thesis, if accepted, to be available for photocopying and for inter-library loan, and for the title and summary to be made available to outside organisations.

Signed ..... [redacted] ..... (candidate)

Date ..... 16/04/2020 .....

به راه بادیه رفتن به از نشستن باطل

که گر مراد نیابم به قدر وسع بکوشم

*Wandering off to the Wonderland is better than sitting vainly*

*I will always try my best to find my wishes*

*Saadi (Persian poet)*

*To my wonderful wife and my supportive parents*

# Acknowledgements

I firstly would like to express my deep gratitude to my supervisors at Swansea University (SWA). Prof. Antonio J. Gil whose motivation, enthusiasm and expertise assisted me to professionally enrich my academic and personal attitudes. I am pleased to experience his foremost skill as translating complex scientific concepts into a simplified form with a mesmerising amusing approach. Dr. Chun Hean Lee, a humble but knowledgeable person whose patience, dedication and availability have dramatically facilitated my journey throughout the course of this work. Without his contribution and determination in the development of the presented mixed-based numerical methodologies, this thesis would not have been piled up, perhaps. I am also thankful to Dr. Rogelio Ortigosa whose guidance and productive discussions boost my progress during the second year of this work.

I am grateful to the supervisory team at Ecole Centrale de Nantes (ECN), Prof. Laurent Stainier and Dr. Thomas Heuzé to whom I got benefits from their guidance and support during the last year of this work in France. Moreover, I really appreciate the opportunity given by Prof. Stainier to work at ECN as a Research Engineer during the write up of this thesis. A special thanks to Prof. Javier Bonet from Greenwich University for his fundamental ideas and valuable influence on this work. I am very much proud to have the opportunity and privilege of working under the direction of these remarkable academics.

I really appreciate the financial support provided by the European Commission EACEA Agency under the Framework Partnership Agreement 2013-0043 Erasmus Mundus Action 1b as part of the EM Joint Doctorate Simulation in Engineering and Entrepreneurship Development (SEED). This provided me a great opportunity in order to fully focus on conducting high-quality research in two globally recognised institutions/centres in the field of computational mechanics, as SWA (ZCCE centre) and ECN (GeM group). I thank all my friends and also my colleagues in Swansea University and Ecole Centrale de Nantes who I knew already or came across during the last four years of my life as in particular, Arash, Mohammad, Ata, Javad, Emilio, Jibran, Vasudevan and Tauno for their support whenever it was needed.

Above all, I would like to dedicate this work to my beloved wife, Paria, whose love, constant encouragement, patience and company has made this journey possible. I also dedicate this work to my parents and my brother (Ali) to whom I am indebted for their constant support, positive attitude and love.

# Abstract

It is evidently not trivial to analytically solve practical engineering problems due to their inherent (geometrical and/or material) nonlinearities. Moreover, experimental testing can be extremely costly, time-consuming and even dangerous, in some cases. In the past few decades, therefore, numerical techniques have been progressively developed and utilised in order to investigate complex engineering applications through computer simulations, in a cost-effective manner.

An important feature of a numerical methodology is how to approximate a physical domain into a computational domain and that, typically, can be carried out via mesh-based and particle-based approximations, either of which manifest with a different range of capabilities. Due to the geometrical complexity of many industrial applications (e.g. biomechanics, shape casting, metal forming, additive manufacturing, crash simulations), a growing attraction has been received by tetrahedral mesh generation, thanks to Delaunay and advancing front techniques [1, 2]. Alternatively, particle-based methods can be used as they offer the possibility of tackling specific applications in which mesh-based techniques may not be efficient (e.g. hyper velocity impact, astrophysics, failure simulations, blast).

In the context of fast thermo-elastodynamics, modern commercial packages are typically developed on the basis of second order displacement-based finite element formulations and, unfortunately, that introduces a series of numerical shortcomings such as reduced order of convergence for strains and stresses in comparison with displacements and the possible onset of numerical instabilities (e.g. detrimental locking, hour-glass modes, spurious pressure oscillations).

To rectify these drawbacks, a mixed-based set of first order hyperbolic conservation laws for isothermal elastodynamics was presented in [3–6], in terms of the linear momentum $\boldsymbol{p}$ per unit undeformed volume and the minors of the deformation, namely, the deformation gradient $\boldsymbol{F}$, its co-factor $\boldsymbol{H}$ and its Jacobian $J$. Taking inspiration of these works [4, 7] and in order to account for irreversible processes, the balance of total energy (also known as the first law of thermodynamics) is incorporated to the set of physical laws used to describe the deformation process. This, in general, can be expressed in terms of the entropy density $\eta$ or total energy density $E$ by which the Total Lagrangian entropy-based and total energy-based formulations $\{\boldsymbol{p}, \boldsymbol{F}, \boldsymbol{H}, J, \eta \text{ or } E\}$ are established, respectively. Interestingly, taking advantage of the conservation formulation framework, it is possible to bridge the gap between solid dynamics and Computational Fluid Dynamics (CFD) by exploiting available CFD

techniques in the context of solid dynamics.

From a computational standpoint, two distinct and extremely competitive spatial discretisations are employed, namely, mesh-based Vertex-Centred Finite Volume Method (VCFVM) and meshless Smooth Particle Hydrodynamics (SPH). A linear reconstruction procedure together with a slope limiter is employed in order to ensure second order accuracy in space whilst avoiding numerical oscillations in the vicinity of sharp gradients, respectively. Crucially, the discontinuous solution for the conservation variables across (dual) control volume interfaces or between any pair of particles is approximated via an acoustic Riemann solver. In addition, a tailor-made artificial compressibility algorithm and an angular momentum preservation scheme are also incorporated in order to assess same limiting scenarios.

The semi-discrete system of equations is then temporally discretised using a one-step two-stage Total Variation Diminishing (TVD) Runge-Kutta time integrator, providing second order accuracy in time. The geometry is also monolithically updated to be only used for post-processing purposes.

Finally, a wide spectrum of challenging examples is presented in order to assess both the performance and applicability of the proposed schemes. The new formulation is proven to be very efficient in nearly incompressible thermo-elasticity in comparison with classical finite element displacement-based approaches. The proposed computational framework provides a good balance between accuracy and speed of computation.

**Keywords:** Finite Volume Method, Vertex-Centred scheme, Smooth Particle Hydrodynamics, Riemann solver, Conservation laws, Thermoelasticity

# Research Output

## Journal publications

- ☐ C. H. Lee, A. J. Gil, **A. Ghavamian** and J. Bonet. "A Total Lagrangian upwind Smooth Particle Hydrodynamics algorithm for large strain explicit solid dynamics", *Computer Methods in Applied Mechanics and Engineering*, Vol. 344, 209–250, 2019. [DOI: 10.1016/j.cma.2018.09.033]

- ☐ O. I. Hassan, **A. Ghavamian**, C. H. Lee, A. J. Gil, J. Bonet and F. Auricchio. "An upwind vertex centred finite volume algorithm for nearly and truly incompressible explicit fast solid dynamic applications: Total and Updated Lagrangian formulations", *Journal of Computational Physics: X*, Vol. 3:100025, 2019. [DOI: 10.1016/j.jcpx.2019.100025]

- ☐ **A. Ghavamian**, C. H. Lee, A. J. Gil, J. Bonet, T. Heuze and L. Stainier. "Thermodynamically consistent Smooth Particle Hydrodynamics algorithm for large strain thermoelasticity", *Computer Methods in Applied Mechanics and Engineering*, (Under review).

- ☐ J. Bonet, C. H. Lee, A. J. Gil, and **A. Ghavamian**. "A first order hyperbolic framework for large strain computational solid dynamics. Part III: Thermo-elasticity and thermoplasticity", *Computer Methods in Applied Mechanics and Engineering*, (Under review).

## Conference publications

- ☐ C. H. Lee, **A. Ghavamian**, A. J. Gil, J. Bonet. "Development of an upwind Smooth Particle Hydrodynamics algorithm for a first order conservation law framework in large strain thermoelasticity". In proceedings of the *Asian Pacific Congress on Computational Mechanics (APCOM)*, Taipei, Taiwan, 18-21 December, 2019.

- ☐ **A. Ghavamian**, C. H. Lee, A. J. Gil, T. Heuze, J. Bonet and L. Stainier. "An entropy-stable Smooth Particle Hydrodynamcis algorithm for large strain thermoelasticity". In proceedings of the *VI International Conference on Particle-based Methods: Fundamentals and Applications, ECCOMAS Thematic Conference*, Barcelona, Spain, 28-30 October, 2019.

- ☐ **A. Ghavamian**, C. H. Lee, A. J. Gil and J. Bonet. "A first order hyperbolic framework for thermoelasticity: An upwind vertex centred Total Lagrangian scheme". In proceedings of the *Society of Engineering Science (SES)*, Madrid, Spain, 10-12 October, 2018.
- ☐ C. H. Lee, A. J. Gil, **A. Ghavamian** and J. Bonet. "A new Smooth Particle Hydrodynamics algorithm for large strain fast solid dynamics". In Proceedings of the *European Congress on Computational Methods in Applied Sciences and Engineering (ECCOMAS)*, Glasgow, United Kingdom, 11-15 June, 2018.

## Invited talks

- ☐ **A. Ghavamian**, C. H. Lee, A. J. Gil, T. Heuze, J. Bonet and L. Stainier."Large strain fast solid dynamics" at *Journée du GeM (GeM day)* conducted by *Institute of Research in Civil and Mechanical Engineering (GeM) group*, Nantes, France, $6^{th}$ June, 2019.
- ☐ **A. Ghavamian**, C. H. Lee, A. J. Gil, T. Heuze, J. Bonet and L. Stainier. "Large strain solid dynamics: from elasticity to coupled thermo-elasticity" at *VIII Congrès de la Belle et Élégante Mécanique (CBEM)*, Universite de Nantes, France, 25 january, 2019.

## Posters

- ☐ **A. Ghavamian**, C. H. Lee, A. J. Gil and J. Bonet."Large strain solid dynamics in Total Lagrangian framework" at *The Annual Zienkiewicz Centre for Computational Engineering (ZCCE) Postgraduate Workshop*, Swansea University, United Kingdom, 1-2 February, 2018. ***Awarded as the "Best poster of the 2018 ZCCE poster competition"***.

# Contents

**Title** **Page No.**

# List of Figures

**Title** **Page No.**

# List of Tables

**Title** **Page No.**

# List of Algorithms

**Title** **Page No.**

# Nomenclature

**Scalars**

| | | |
|---|---|---|
| $J$ | Jacobian of deformation | $[-]$ |
| $E$ | Total energy | $[\text{Kg m}^{-1} \text{ s}^{-2}]$ |
| $\eta$ | Entropy | $[\text{Kg K}^{-1} \text{ m}^{-1} \text{ s}^{-2}]$ |
| $\theta$ | Temperature | [K] |
| $s_R$ | Heat source terms | $[\text{Kg m}^{-1} \text{ s}^{-2}]$ |
| $p$ | Pressure | $[\text{Kg m}^{-1} \text{ s}^{-2}]$ |
| $\mathcal{E}$ | Internal energy | $[-]$ |
| $\varepsilon_p$ | Plastic strain | $[-]$ |
| $W$ | Strain energy | $[-]$ |
| $\phi$ | Slope limiter | $[-]$ |
| $\mathcal{D}$ | Dissipation | $[\text{Kg m}^{-1} \text{ s}^{-2}]$ |
| $c$ | Wave speed | $[\text{m s}^{-1}]$ |
| $c_p$ | Longitudinal or pressure wave speed | $[\text{m s}^{-1}]$ |
| $c_s$ | Transverse or shear wave speed | $[\text{m s}^{-1}]$ |
| $t$ | Time | [s] |
| $x$ | Distance | [m] |
| $\Omega_R$ | Volume in material configuration | $[\text{m}^3]$ |
| $\Omega$ | Volume in spatial configuration | $[\text{m}^3]$ |
| $\rho$ | Spatial density | $[\text{Kg m}^{-3}]$ |
| $\rho_R$ | Material density | $[\text{Kg m}^{-3}]$ |
| $\lambda$ | Lame constant | $[\text{Kg m}^{-1} \text{ s}^{-2}]$ |
| $\mu$ | Lame constant | $[\text{Kg m}^{-1} \text{ s}^{-2}]$ |

| | | |
|---|---|---|
| $\kappa$ | Bulk modulus | [Kg m$^{-1}$ s$^{-2}$] |
| $\tilde{\kappa}$ | Fictitious bulk modulus | [Kg m$^{-1}$ s$^{-2}$] |
| $\nu$ | Poisson's ratio | [–] |
| $E$ | Young's modulus | [Kg m$^{-1}$ s$^{-2}$] |
| $C_v$ | Specific heat capacity | [m$^2$ s$^{-2}$ K$^{-1}$] |
| $\alpha$ | Thermal expansion coefficient | [1/K] |
| $h$ | Thermal conduction coefficient | [Kg m K$^{-1}$ s$^{-3}$] |
| $\alpha_{CFL}$ | Courant-Fredrichs-Lewy number | [–] |
| $G$ | Amplification factor | [–] |

**Vectors**

| | | |
|---|---|---|
| $\boldsymbol{\mathcal{U}}$ | Conservative variables | |
| $\boldsymbol{\mathcal{F}}$ | Flux | |
| $\boldsymbol{\mathcal{F}}^C$ | Contact flux | |
| $\boldsymbol{\mathcal{S}}$ | Source terms | |
| $\boldsymbol{u}$ | Displacement field, $\boldsymbol{u} = \boldsymbol{x} - \boldsymbol{X}$ | [m] |
| $\boldsymbol{p}$ | Linear momentum | [Kg m$^{-2}$ s$^{-1}$] |
| $\boldsymbol{v}$ | Spatial velocity | [m s$^{-1}$] |
| $\boldsymbol{w}$ | Angular momentum | [rad/s] |
| $\boldsymbol{t}$ | traction | [Kg m$^{-1}$ s$^{-2}$] |
| $\boldsymbol{f}_R$ | Body forces | [Kg m$^{-1}$ s$^{-2}$] |
| $\boldsymbol{Q}$ | Heat flux | [Kg S$^{-3}$] |
| $\boldsymbol{x}$ | Spatial or Eulerian coordinates | [m] |
| $\boldsymbol{X}$ | Material or Lagrangian coordinates | [m] |
| $\boldsymbol{d}$ | Distance | [m] |
| $\boldsymbol{n}$ | Spatial outward unit normal | [m] |
| $\boldsymbol{N}$ | Material outward unit normal | [m] |
| $\boldsymbol{a}$ | Spatial area vector | [m$^2$] |
| $\boldsymbol{A}$ | Material area vector | [m$^2$] |
| $\boldsymbol{\lambda}$ | Lagrange multiplier | [–] |

**Tensors**

| | | |
|---|---|---|
| $\boldsymbol{\mathcal{A}}$ | Flux Jacobian matrix | |
| $\boldsymbol{F}$ | Deformation gradient | [–] |
| $\boldsymbol{C}$ | Right Cauchy-Green strain | [–] |
| $\boldsymbol{H}$ | Co-factor of the deformation | [–] |
| $\boldsymbol{\chi}$ | Set of geometric strains $\{\boldsymbol{F}, \boldsymbol{H}, J\}$ | |
| $\boldsymbol{G}$ | Gradient of a scalar | |
| $\boldsymbol{\mathcal{G}}$ | Amplification matrix | |
| $\boldsymbol{I}$ | Second order identity tensor | [–] |
| $\boldsymbol{\varepsilon}$ | Strain | [Kg m$^{-1}$ s$^{-2}$] |
| $\boldsymbol{P}$ | First Piola Kirchoff stress | [Kg m$^{-1}$ s$^{-2}$] |
| $\boldsymbol{S}$ | Second Piola Kirchoff stress | [Kg m$^{-1}$ s$^{-2}$] |
| $\boldsymbol{\delta}$ | Kronecker delta | [–] |
| $\boldsymbol{\epsilon}$ | Alternating or permutation tensor | [–] |

## Subscripts [1]

| | |
|---|---|
| $\boldsymbol{\mathcal{U}}_R$ | Property at reference temperature |
| $\boldsymbol{\mathcal{U}}_a$ | Nodal value |
| $\boldsymbol{\mathcal{U}}_b$ | Neighbour value |
| $\boldsymbol{\mathcal{U}}_{ab}$ | Property at the node associated to cell $a$ |
| $\boldsymbol{\mathcal{U}}_f$ | Property at the face |
| $\boldsymbol{\mathcal{U}}_g$ | Property at Gauss point |
| $\hat{\boldsymbol{\mathcal{U}}}$ | Deviatoric component |
| $\boldsymbol{\mathcal{U}}_{\text{vol}}$ | Volumetric component |

## Superscripts [1]

| | |
|---|---|
| $\boldsymbol{\mathcal{U}}^+$ | Right state of an interface |
| $\boldsymbol{\mathcal{U}}^-$ | Left state of an interface |
| $\boldsymbol{\mathcal{U}}^*$ | Variable associated to first Runge-Kutta stage |
| $\boldsymbol{\mathcal{U}}^{**}$ | Variable associated to second Runge-Kutta stage |

[1] $\boldsymbol{\mathcal{U}}$ represents a scalar, vector or second-order tensor.

| | |
|---|---|
| $\boldsymbol{\mathcal{U}}^C$ | Contact Riemann values |
| $\boldsymbol{\mathcal{U}}^T$ | Transpose of a tensor/matrix |
| $\boldsymbol{\mathcal{U}}^{-1}$ | Inverse of a tensor/matrix |
| $\dot{\boldsymbol{\mathcal{U}}}$ | Time derivative |

**Operators**

| | |
|---|---|
| $\nabla_0 \times [\ ]$, CURL $[\ ]$ | Material curl |
| $\nabla_0 [\ ]$, GRAD $[\ ]$ | Material gradient |
| $\nabla_0 \cdot [\ ]$, DIV $[\ ]$ | Material divergence |
| $\nabla \times [\ ]$, curl $[\ ]$ | Spatial curl |
| $\nabla [\ ]$, grad $[\ ]$ | Spatial gradient |
| $\nabla \cdot [\ ]$, div $[\ ]$ | Spatial divergence |
| $[\ ] : [\ ]$ | Double dot product |
| $[\ ] \times [\ ]$ | Cross product |
| $[\ ] \otimes [\ ]$ | Dyadic product |
| $[\ ] \boldsymbol{\times} [\ ]$ | Tensor cross product |
| det $[\ ]$ | Determinant |
| tr $[\ ]$ | Trace of tensor/matrix |
| $[\![ [\ ] ]\!]$ | Jump operator |

# Part I

# Preliminaries

Chapter 1

# Introduction

## 1.1 Motivation

Amongst real-life engineering problems, there are some applications in which extremely large deformations take place in a very short amount of time (see Figure 1.1).

These problems can be analysed with any of the following options for which a set of benefits and limitations are introduced.

**Analytical** (exact) solution: It provides a reliable closed-form solution to a mathematical expression. This option, however, is limited to the case of some simplified linear Partial Differential Equations (PDEs) and could not be a suitable choice for a comprehensive investigation, considering the inherent (geometrical and/or material) nonlinearities of most engineering problems. Nonetheless, analytical solutions can still provide a significantly useful insight into identifying the nature of a problem based on which a successive numerical algorithm can be developed [8–10]. For instance, the analytical solution for one-dimensional linear advection equation has been very useful to assess the capability of different types of (exact and approximated) Riemann solvers for shock-dominated scenarios [11].

**Experimental** solution: It has always been considered as a powerful, reliable and reasonably valid tool in order to verify the cause of a problem. In addition, it can be applied to a wide variety of disciplines. In fact, considering laboratory research, one can effectively control the experiment's environment (e.g. temperature and humidity) in comparison with natural situations and that could improve, in some cases, the sought results. That also implies that some conditions occur faster in an experimental setting that may take longer to occur in a natural environment [12]. Despite all these benefits, there are some disadvantages of using experimental testing approach. Sometimes, the experimental study conducted in a laboratory environment might not be realistic and valid due to the error generated by human mistakes and/or artificial situations. These systematic and random errors stem from different reasons such as instrumental, observational and environmental errors. For instance, one can consider a poorly calibrated thermometer that reads temperature 102° C when immersed in boiling water and 2° C when immersed in ice water at atmospheric pressure. Moreover, the construction and


(a) Car crash testing

(b) Civil airplane crash

(c) Bone fracture

(d) Forging

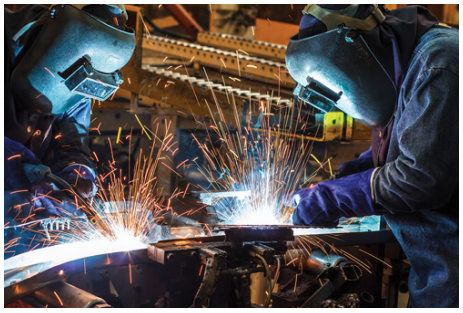

(e) Welding

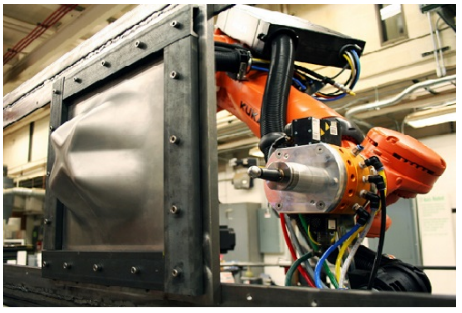

(f) Metal forming

FIGURE 1.1: Applications of computational solid dynamics

testing of the desired prototype has typically been costly, time-consuming and even in some cases impossible (soft tissue modelling) [13–15].

**Numerical** solution: During the past few decades, an extensive effort has been devoted to developing Computer-Aided Design (CAD) and Computer-Aided Engineering (CAE) tools in order to successfully tackle engineering problems (see Figure 1.2 for some examples). Although experiments will always be necessary to calibrate our models, these numerical methodologies, with the aid of powerful computers, have become an efficient and economical replacement to the experiments, in many practical applications [13]. They are capable of not only reducing the cost of constructing new machines and reducing environmental risks but also simulate many technological and natural phenomena where experiments can be far too dangerous or even impossible to be safely conducted in a laboratory. Thus far, several numerical methods have been developed in order to approximately find the solution of engineering problems. These techniques are known for their unique features and capabilities which make them desirable

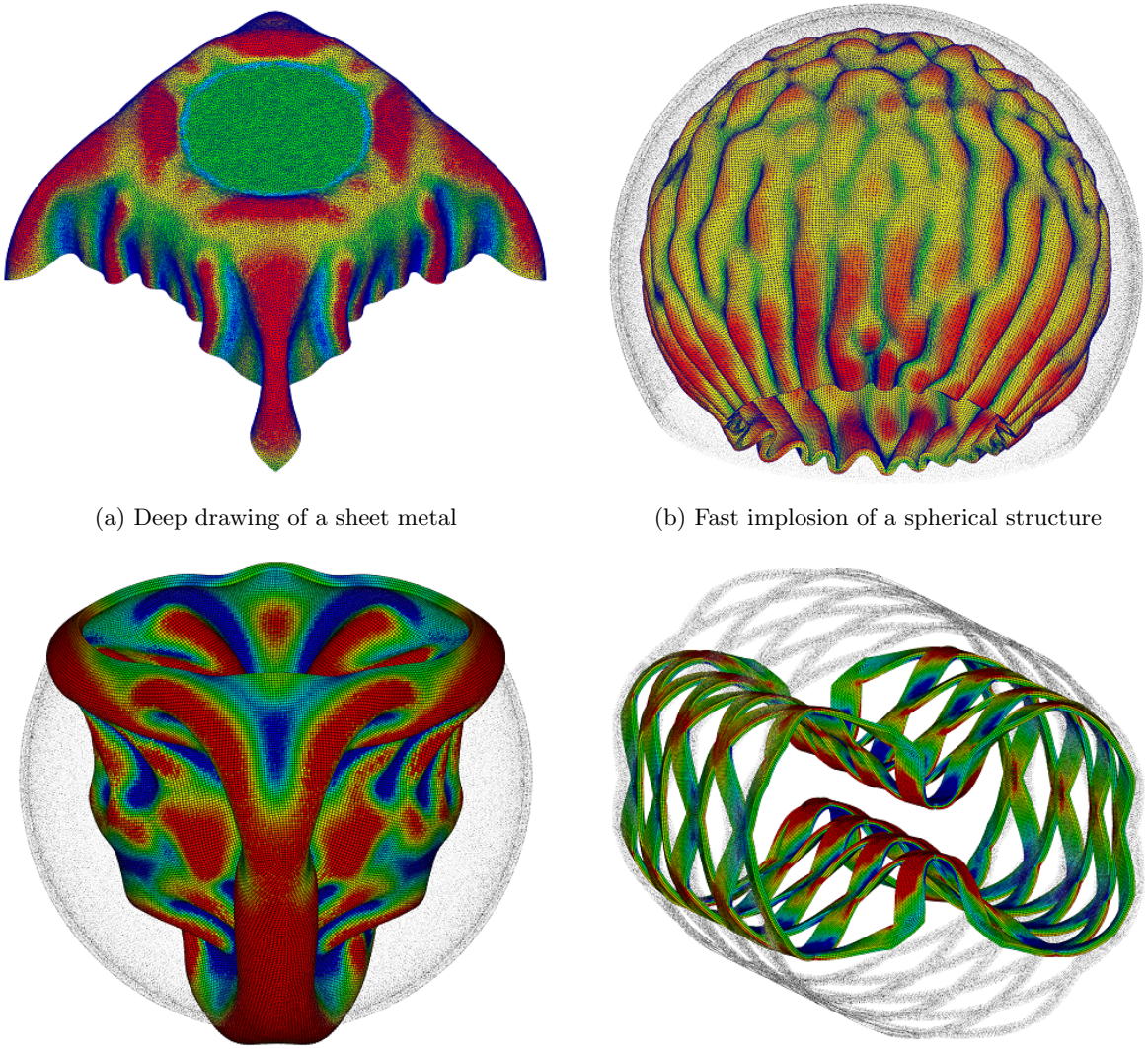

(a) Deep drawing of a sheet metal

(b) Fast implosion of a spherical structure

(c) Collapse of a thin sphere

(d) Crushing of a stent-like structure

FIGURE 1.2: Deformed states of some numerical simulations with pressure distribution using in-house mesh-based Vertex-Centred Finite Volume Method (a) and (b) and in-house mesh-free Smooth Particle Hydrodynamics (c) and (d)

for certain applications. One of these features is the way of approximating a physical domain into a computational domain as it typically consists of two categories, namely, (1) mesh-based approaches and (2) particle-based (meshless) approaches. Figure 1.3 shows an example of a physical domain approximated by mesh generation (unstructured tetrahedral elements) and particle distribution.

Taking the advantages and disadvantages of the above-mentioned proposed solutions into account, one can appropriately choose the desired approach once the problem description and its application are clarified. In this thesis, the application will be large strain fast solid dynamics. Therefore, to avoid time-consuming costly experiments and also considering the existent nonlinearities in the solution (due to large strains), numerical modelling has employed as the

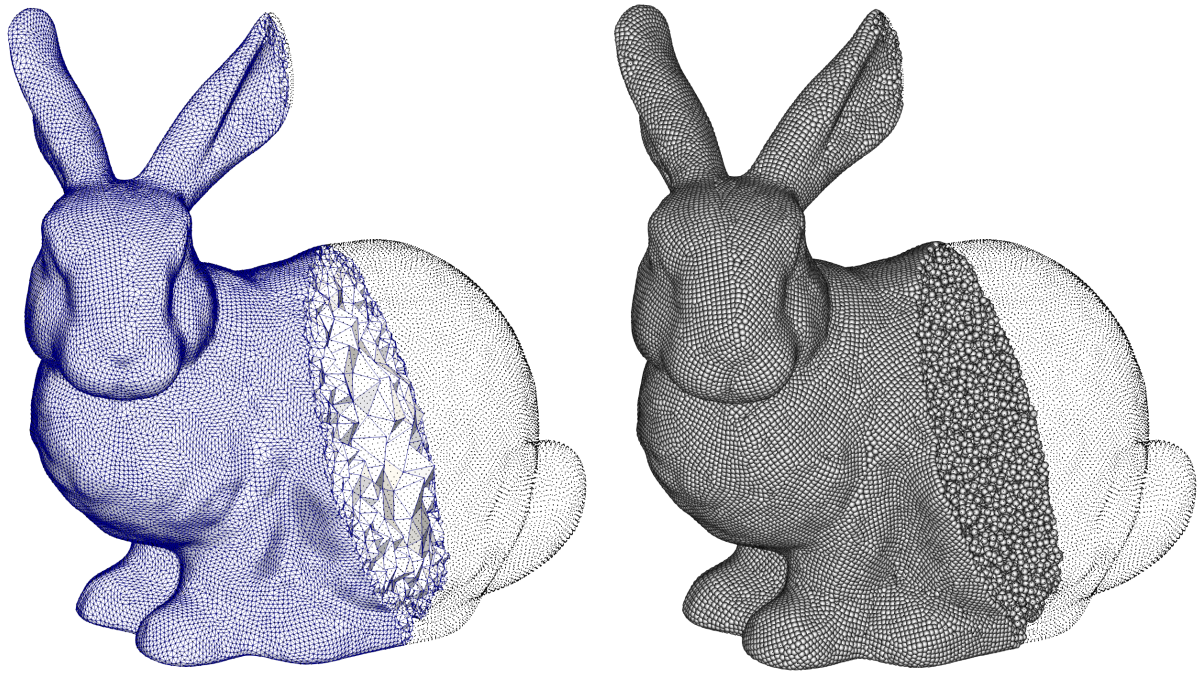

(a) (b)

FIGURE 1.3: Computational domain: Stanford bunny with (a) mesh generation; and (b) particle distribution

desired approach. Of course, some analytical analysis is also carried out to prove the validity of the proposed numerical schemes.

In general, to perform a numerical modelling in the context of solid dynamics, one might use the existing commercial packages (ANSYS AUTODYN, LS-DYNA and ABAQUS to name a few), open source software (Codeaster, FEM-based; OpenFOAM, FVM-based; and DualSPHysics, SPH-based) or in-house computer software. By using commercial software, it is possible to numerically simulate a wide range of applications, such as fracture and fragmentation, metal forming and additive manufacturing processes, contact and hypervelocity impact [16]. These numerical tools are typically developed on the basis of classical low order finite element displacement-based formulations and, consequently, suffer from a certain number of numerical difficulties (locking, hour-glass modes and spurious pressure oscillations) [7, 17, 18]. Although some modifications have been applied to commercial tools to alleviate some of these shortcomings [14, 19–21], numerical difficulties are still evident when dealing with nearly/truly incompressible materials [16, 22]. Additionally, the shock-capturing technologies are poorly developed in the context of solid dynamics [6, 7, 18, 23]. It is worthwhile noting that the development and extension of the current capabilities of these tools are not straightforward due to the closed nature of their implementation. Figure 1.4 shows the results of two test cases using classical displacement-based numerical approaches. The deformation and pressure distribution of the simulations illustrates how the aforementioned numerical difficulties could be experienced. In fact, the use of high order interpolation schemes [24] can be an alternative solution. However, the increase in the number of Gauss integration points can drastically reduce

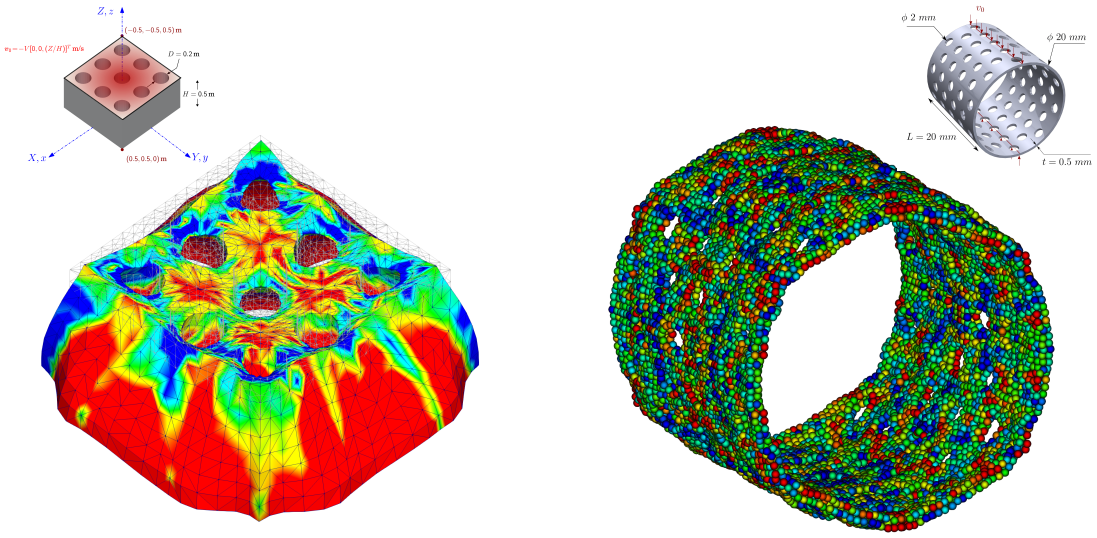


(a) Punch test on a perforated cube

(b) Crushing a stent-like structure

FIGURE 1.4: Numerical simulations based on classical displacement-based (a) vertex centred Finite Volume Method; and (b) Smooth Particle Hydrodynamics

the computational efficiency in comparison with low order schemes, especially when complex and history-dependent constitutive laws (e.g. visco-elasticity [25], visco-plasticity [26]) are of great interest. This thesis offers a unified computational framework which is adapted to two very competitive numerical methodologies capable of surpassing the above-mentioned numerical shortcomings raised by the use of the traditional displacement-based approach. Additionally, it provides a great potential to develop a robust shock capturing algorithm, thanks to the conservative nature of the equations.

## 1.2 State of the art in computational solid dynamics

### 1.2.1 Mesh-based methods

On the past few decades, a vast branch of numerical methodologies has been designed based on computational meshes. These methods have been evolving regularly and producing different approaches in order to enhance the capability of tackling engineering problems. Additionally, the mesh-based techniques provide some features where the particle-based approaches struggle such as the straightforward imposition of boundary conditions, well-defined mesh connectivity taking neighbouring elements/cells search into account and consistency of a numerical algorithm, to name a few [27]. In the context of computational mechanics, and in particular solid mechanics, Finite Element Method (FEM) [28] is the most often chosen. Shock waves propagating in a different type of materials, contact-impact problems, buckling analysis, crack propagation and dynamic fracture, mechanism-based modelling of material nonlinearities are some of the applications in which FEM method has succeeded [13]. Nonetheless, it has been shown that other well-known numerical techniques such as Finite Difference Method (FDM) [9], Finite Volume Method (FVM) [11] and Discontinuous Galerkin (DG) method [29–31] can be an

advantageous substitution to classical FEM approximation and even in some cases, outperform the FEM solution [6, 32].

In the following section, the literature of the mesh-based methodologies is explored, categorised to the classical displacement-based and mixed-based approaches.

#### 1.2.1.1 Classical displacement-based approach

Current industry codes (e.g. PAM-CRASH, LS-DYNA, ABAQUS, Altair HyperCrash) targeting on the simulation of fast solid dynamics problems (e.g. vehicle crash simulation, hypervelocity impact on honeycomb sandwich panel and the implosion of an underwater structure) are developed on the basis of classical low order (linear) finite element displacement-based formulations. However, these formulations present a number of drawbacks, namely, (1) spurious hour-glassing and pressure checkerboarding [33], (2) bending difficulty [34], (3) locking phenomena [35], (4) reduced order of convergence for strains and stresses in comparison with displacements and (5) high frequency noise in the vicinity of shocks [36, 37].

To rectify some of these shortcomings, a variety of enhanced techniques have been developed and introduced in the last few decades. A popular option to avoid locking is resorting to a Selective Reduced Integration (SRI) procedure [19–21], typically applied to (tri-linear) hexahedral elements. In this case, the volumetric component of the stress is under-integrated using a reduced number of Gauss integration points. Despite compromising accuracy and not satisfying the inf-sup Ladyzenskaja-Babuška-Brezzi condition, this approach remains very appealing to the industry as the modifications required to the existing commercial finite element codes are very minor. As an alternative, a multi-field Veubeke-Hu-Washizu(VHW) type variational principle [19, 21, 38] is introduced to avoid locking by decomposing deviatoric and volumetric components of deformation so that they can be treated independently. Mean dilatation technique (also known as B-Bar method) is a specific case of VHW approach where the volumetric part is under-integrated using constant interpolation [14]. Unfortunately, these remedies are just designated to Hexahedral element as a linear tetrahedron element cannot be under-integrated anymore.

In the past few years, effort has been devoted to tetrahedral meshing techniques as many engineering applications involve complex geometries and that the use of tetrahedral meshing will only be a practical choice for decompositions of the computational domains. The popularity of using tetrahedral mesh is progressively increasing thanks to Delaunay [1], advancing front techniques [2] and octree based method [39, 40]. In addition, it has been proven that the tetrahedral mesh generation performs in a more efficient manner in some applications such as shock hydrodynamics, optimisation and adaptive simulations [41]. The most preferred choice in the industry is the Average Nodal Pressure (ANP) procedure originally proposed by Bonet and Burton [42] in which the pressure field is under-integrated at nodes. Extensive effort has since been devoted in order to prevent the appearance of hourglassing-like modes [34, 43–46], a typical shortcoming of this type of finite element. Several variants of the original ANP approach have since followed, including the averaged nodal deformation gradient [34], the F-bar method [47], Triangular composite finite elements [48], and the Smoothed Finite Element

Method (SFEM) [35]. However, all of the enhanced methods described above still suffer from spurious pressure fluctuations when attempting to model predominantly nearly incompressible solids [42]. This specific shortcoming can be partially alleviated using the recently proposed SFEM in conjunction with the use of a non-consistent smoothing pressure procedure [49].

On another front, several attempts have also been reported at aiming to solve solid mechanics problems via the use of displacement-based finite volume discretisations [50–53]. Some interesting work has also been recently explored using the open source platform "OpenFOAM", with special attention paid to the simulation of contact mechanics [54], orthotropic materials experiencing moderate strains [55], hyperelastic and hypoelastic formulations for Eulerian non-linear elastoplasticity [56] and metal forming applications [57]. In this thesis, the focus is on **Vertex-Centred Finite Volume Method (VCFVM)** as one of the employed spatial discretisation techniques.

Fryer and his co-workers could be considered as the pioneers on presenting VCFVM in solid mechanics with the application of multiphysics modelling of metals casting process [58–60]. In [61, 62] the VCFVM and FEM techniques are compared and the connection between the weak integral form in FEM approximation procedure and strong integral form of the governing equations in FVM is expressed. In fact, the development of VCFVM is based on the work of Baliga and Patankar [63] as they proposed a locally conservative (control volume based) FEM in which the weighting function is assumed to be the identity matrix rather than being equivalent to the shape function, as we expect at the standard Galerkin FEM. Fallah and his co-workers [64] also compared VCFVM and FEM with the application of geometrically nonlinear stress analysis. Taylor et al. used VCFVM for analysing the behaviour of elastic-visco-plastic materials in multiphysics [65, 66]. Fluid-Structure Interaction (FSI), welding process, wave propagation, biomechanics, natural extrusion process, shape casting and metal forming are some of the applications where VCFVM has been employed for numerical approximation [32, 64–70]. An extensive very well organised literature review in finite volume method can be found in [71].

In extension to thermo-mechanics, Biot [72, 73] pioneered in comprehensively developing variational principles in coupled thermo-elasticity and irreversible thermodynamics. Lord and Shulman [74] introduced the concept of generalised thermo-elasticity and paradox of heat conduction versus classical (or conventional) thermo-elasticity. In fact, the paradox indicates that the heat conduction portion of the total energy conservation law has an infinite speed of propagation (diffusive behaviour) whereas the mechanical part is a wave-type motion. In this case, a time-dependent heat transport equation will be considered, leading to hyperbolic coupled equations. Nevertheless, the theory of generalised thermo-elasticity is not the main interest of this work though (an extensive literature review can be found in [75–77]).

Simo and Miehe [78] presented an associative coupled thermo-plasticity at finite strains. Chadwick et al. [79] studied the thermo-mechanics of rubber-like solids and presented a modified entropic elasticity material model. Following this work, Miehe [80] and Holzapfel [81] expressed formulations and numerical analysis on entropic thermo-elasticity of rubber-like solids at finite strains. Demirdžić and his co-workers employed FVM for different coupled thermo-mechanical problems such as thermo-elastoplastic stress analysis of a deformable solid [82], stress analysis

in complex domains [83], studying the deformation of a hygro-thermo-elastic orthotropic body [84] and linear thermo-visco-elasticity [85]. Furthermore, various applications in the context of thermo-mechanics is tackled using FVM such as thermo-elastic response of rubber-like matrix composites and electro-magneto-thermo-elastic multiphase composites [86–88], thermo-elastic wave propagation [89], analysis of nonlinear thermo-mechanical dynamics of shape memory alloys [90], one-dimensional simulation of an electrofusion welding process [91], optimisation of thermo-mechanical structural members [92], thermo-mechanical analysis of functionally graded solids [93, 94], unidimensional thermo-mechanical numerical simulations of impacts on elastic-plastic solids within the small strain framework [95], crack propagation in concrete [96] and coupled Fluid-Structured interaction [97, 98].

#### 1.2.1.2 Mixed-based methodology

The earliest attempt at employing a system of first order hyperbolic conservation laws in solid dynamics originates from the work of Trangenstein and Colella [99, 100], inspired from the work of [101], where the conservation variables of the mixed-based approach were the linear momentum $\boldsymbol{p}$ and the continuum deformation gradient tensor $\boldsymbol{F}$. Specifically, a second order Godunov-type cell centred Finite Volume Method (FVM) in combination with a Riemann based upwinding stabilisation was presented. Although the consideration of involutions was outlined as part of the paper, its numerical implementation was not fully described. Moreover, the explored examples were restricted to the case of small strain linear elasticity in two dimensions [100]. With a similar philosophy, an alternative version of cell centred FVM (via a node-based discretisation of the numerical fluxes) originally proposed by Mazeran and Després [102], and later explored in [103–105], where gas dynamics applications were adapted to the case of hyperelastic solids [106, 107]. In application of fully incompressible materials (biomedical and structural engineering), a mixed-based displacement-rotation VCFVM framework [108–110] and a displacement-pressure cell centred finite volume algorithm [53, 111] are presented in order to account for incompressibility constraint. In parallel, Scovazzi and co-authors [25, 112–115] also used a mixed-based approach for a linear tetrahedral element by utilising a Variational Multi-Scale method. In extension to coupled thermo-mechanical problems, Fallah et al. [116] pioneered in using a displacement-pressure cell centred finite volume formulation to analyse the behaviour of compressible and incompressible solids and, that, it has followed by Bejilonja et al. [117] using a segregated solution procedure to make the method computationally efficient.

In recent years, the research group at Swansea University have pursued the same $\{\boldsymbol{p}, \boldsymbol{F}\}$ system whilst exploiting a wide range of spatial discretisation techniques including upwind cell centred FVM [6, 18], Jameson-Schmidt-Turkel vertex centred FVM [118], upwind VCFVM [7, 16], two step Taylor-Galerkin FEM [119] and stabilised Petrov-Galerkin FEM [17]. In subsequent papers, the $\{\boldsymbol{p}, \boldsymbol{F}\}$ system was then augmented by incorporating a new conservation law for the Jacobian of the deformation $J$ [7, 16, 23] to effectively solve nearly incompressible deformations. Moreover, the $\{\boldsymbol{p}, \boldsymbol{F}, J\}$ formulation was also extended to account for truly incompressible materials utilising a tailor-made fractional step approach [16, 120]. Further enhancement of this framework has recently been reported [3, 120], when considering materials governed by a polyconvex constitutive law where the co-factor $\boldsymbol{H}$ of the deformation plays a dominant role.

The complete set of unknowns $\{\boldsymbol{p}, \boldsymbol{F}, \boldsymbol{H}, J\}$ yields an elegant system of conservation laws, where the existence of a generalised convex entropy function enables the derivation of a symmetric system of hyperbolic equations, dual of that expressed in terms of entropy conjugates of the conservation variables [120].

### 1.2.2 Meshless methods

An alternative way for the numerical approximation of engineering problems is particle methods (or meshless methods) as it does not require to deal with the hassles of mesh generation and connectivity matrix. This can be a great advantage on tackling specific engineering applications where the mesh-based numerical approaches struggle. For instance, many practical applications deal with extremely large deformations and using mesh-based approaches can lead to mesh distortion and consequently, introduces severe error to the numerical computations [35, 121]. In addition, adaptive mesh refinement in some applications like moving discontinuities or failure simulations (e.g. crack propagation) can cause more complicated computer implementations, extra computational costs and also degradation of accuracy due to the projection of quantities of interest between successive meshes [122, 123]. Meshless methods, however, can perform particle refinement in a more efficient procedure, due to the fact that interpolation of the solution does not depend on connectivities. The complexity of particle refinement still remains as a challenging procedure though. Furthermore, they offer easier numerical implementations in three-dimensional cases than grid-based methods [124]. The reasonable accuracy and stability of these methods [125] along with their meshfree features and computational efficiencies have made them very competitive for the past few decades.

Particle methods have been extensively used in fluid and solid mechanics such as crack growth and propagation, free surface flows, hypervelocity impact problems, metal forming, multi-physics, astrophysics and fluid-solid interaction [27, 126–128]. Smooth Particle Hydrodynamics (SPH) was the very first particle method originally initiated by the work of Lucy [129] for astrophysics applications and, then, developed by Gingold and Monaghan [130]. To improve the capability and robustness of the particle-based approaches, many other methods have been developed so far such as Corrected Smooth Particle Hydrodynamics (CSPH) [131], Element-free Galerkin (EFG) [132], Reproducible Kernel Particle Method (RKPM) [133], Meshless Local Petrov-Galerkin method (MLPG) [134], Material Point Method (MPM) [135], Discontinuous Galerkin MPM (DGMPM) [136] and Particle-In-Cell (PIC) [137], to name a few. An extensive review on the history and development of meshless methods can be found in the references [127, 138–140]. In the current work, **Smooth Particle Hydrodynamics (SPH)** is considered as an alternative spatial discretisation technique for balance principles.

#### 1.2.2.1 Classical displacement-based approaches

The first attempt on making the classical SPH more competitive among the grid-based computational approaches was perhaps carried out by Monaghan [141, 142], after the development of SPH by Lucy [129], Gingold and Monaghan [130] in 1977. Over the past decades, many efforts has been devoted to this Lagrangian particle-based numerical technique such that it has

become a powerful, competitive and relatively reliable numerical tool to tackle a vast number of practical problems such as astrophysics [143], Fluid dynamics [144, 145], wave propagation, explosion phenomena and hypervelocity impacts [126, 146], to name a few (a comprehensive review for SPH in diverse applications can be seen in reference [128]). Classical SPH has also shown its capabilities on structural mechanics applications initiated by the work of Libersky et al [147] in the subjects of high-velocity impacts on elastic-plastic solids, perforation and fragmentation and that followed by successfully using SPH for some other applications like geomechanics, machining, forging and metal forming and shell structures [148–151].

Traditionally, the displacement-based SPH Lagrangian formalism suffers from a number of well-known drawbacks, namely, (1) existence of numerical errors close to the boundaries owing to lack of consistency (lack of reproducibility of kernel interpolation function) [152, 153]; (2) numerical difficulties associated to stability such as tensile instability (non-physical clumping of particles under a tensile test) or appearance of zero-energy modes due to the rank-deficiency emerging as a result of using nodal integration [154, 155] and (3) reduced order of convergence for derived variables (e.g. strains and stresses) [42, 44–46].

To alleviate the above-mentioned shortcomings, significant efforts have been carried out to re-establish the consistency and reproducibility, improve the accuracy and enhance the robustness of the classical SPH over the last two decades. Chen et al. [156, 157] proposed a correction on kernel function based upon a Taylor series expansion in order to enhance the accuracy of solution within the domain, near and on the boundaries. Different strategies have employed to make corrections on Kernel interpolation function aimed at ensuring its reproducibility and consistency [133, 158–160], even though that has increased the risk of having negative, non-symmetric or non-monotonically decreasing kernel which results in less accurate results and representation of non-physical solutions like negative density or energy [154]. Bonet and Kulasegaram [161] presented Corrected SPH (CSPH) by the introduction of corrections in the kernel functions and in their derivatives. Dyka et al. [162, 163] introduced a stress-point approach to alleviate the tensile instability issue and improve the accuracy of the SPH algorithm. Those companion Lagrangian points have been set to carry derived field variables like stress or velocity gradient. Randles and Libersky [164] presented a normalised SPH aimed at increasing accuracy and stability. Vignjevic et al. [165] also proposed an alternative discretisation method for classical SPH to treat zero-energy modes and tensile instability. Belytschko et al. [153] made a stability analysis on particle methods and stated that using a Lagrangian kernel with stress points is the best approach for the discretisation of particle-based algorithms. In fact, the Lagrangian kernel can only remedy tensile instability but not zero-energy modes. Utilising an analogues hourglass control approach in FEM, Ganzenmuller et al. [166] introduced a stabilisation procedure to control hourglass modes and removed tensile instability inherent to the updated Lagrangian approach and also rank-deficiency inherent to the nodal integration.

In extension to coupled thermo-mechanical problems, Barta et al. [167] used a modified SPH to study shear strain localization exhibited in thermo-elasto-viscoplastic materials through a one-dimensional problem, without adding an artificial viscosity. SPH methodology is considered in [168] to exploit a thermo-visco-plasticity model accounting for damage due to fracture. Zhang et al. [169] utilised a coupled SPH-FEM computational algorithm in order to simulate

impact dynamics problems using viscoplasticity (consists of linear thermo-elasticity, von Mises yield criterion, associated flow rule, nonlinear isotropic strain hardening, strain rate hardening, temperature softening due to adiabatic heating) and isotropic ductile damage model along with Mie-Grüneisen Equation Of State (EOS). A three dimensional fully coupled thermo-mechanical approach using SPH methodology presented in the work of Fraser et al. [170, 171] to account for large plastic deformations, particularly in the application of friction stir welding, where free surfaces of arbitrary and rapidly alterable shapes are intrinsically covered by the SPH method. Hu et al. [172, 173] considered a thermoelastic material model for simulating laser welding through SPH methodology in order to predict the temperature distribution and the dimensions of welding seam during the welding process. A Total Lagrangian thermo-mechanical energy-based formalism is presented by Ba and Gakwaya [174] discretised using a corrected SPH framework aimed at tackling large deformation problems in solid mechanics. In a recent work [175], some thermo-mechanical coupled problems are simulated and compared using SPH and FEM numerical algorithm provided by LS-Dyna commercial package.

Thus far, the available improved SPH methodologies still suffer from persistent artificial mechanism (e.g. hourglassing), especially when dealing with predominant nearly incompressible behaviour [176] and that can be suppressed by the so-called non-consistent stabilisation strategies (i.e. artificial viscous fluxes [164, 177, 178] and conservative strain smoothing regularisation [42, 179]).

#### 1.2.2.2 Mixed-based methodologies

In order to rectify the shortcomings of classical SPH, Lee et al. [4, 5] recently introduced a mixed-based Total Lagrangian SPH computational framework for explicit fast solid dynamics, where the conservation of linear momentum $\boldsymbol{p}$ is solved along with conservation equations for the deformation gradient $\boldsymbol{F}$, its co-factor $\boldsymbol{H}$ and its Jacobian $J$. Specifically, the SPH discretisation of the new system of conservation laws $\{\boldsymbol{p}, \boldsymbol{F}, \boldsymbol{H}, J\}$ was introduced through a family of well-established stabilisation strategies, namely, a Jameson-Schmidt-Turkel (JST) algorithm [3, 23] and a variationally consistent Streamline Upwind Petrov Galerkin (SUPG) algorithm [5, 17]. Both computational methodologies yield in the same order of convergence is obtained for velocities, deviatoric and volumetric components of stress and were capable of eliminating spurious hourglass-like modes, tensile instability and spurious pressure oscillations in nearly incompressible scenarios.

## 1.3 Scope and outline of the thesis

The scope of this thesis is the numerical investigation on fast transient large strain solid dynamic problems consisting of reversible and irreversible processes. In this work, a system of conservation equations is expressed in terms of the linear momentum $\boldsymbol{p}$ and the minors of the deformation, namely, deformation gradient tensor $\boldsymbol{F}$, its co-factor $\boldsymbol{H}$ and its Jacobian $J$. Additionally, in order to account for irreversible processes, the above system is augmented with

an additional conservation law and variable describing the total balance of energy in the system. This is known as the first law of thermodynamics which, in general, can be expressed in terms of total energy $E$ or entropy $\eta$. For completeness, both expressions for the first law are presented and compared. For closure of the system, different constitutive models including isothermal hyper-elastic, isothermal elasto-plastic and thermo-elastic materials are employed. These constitutive models are constructed on the basis of polyconvex stored energy functionals in order to guarantee the existence of real wave speeds for the entire range of (thermo-/hyper-) elastic deformations. We then present an adapted artificial compressibility algorithm [180–182] to be able to treat near (fully) incompressible scenarios.

From the spatial discretisation standpoint, a unified computational framework is presented which consists of an upwind SPH scheme and an upwind VCFVM methodology. The distinct abilities introduced by each of the employed numerical schemes allow for tackling a wide range of applications. In addition, discontinuity of the solution at the interface of two control volumes (VCFVM scheme) or between any pair of particles (SPH scheme) leads to a Riemann problem which is solved by the aid of a very simple acoustic Riemann solver. The semi-discrete equations are advanced in time through an explicit Total Variation Diminishing (TVD) Runge-Kutta (RK) method.

The thesis is organised into the following chapters:

## Part I

In this part, preliminary material for engaging into the subject of interest (large strain explicit fast solid dynamics) is presented by illustrating how the current work can potentially contribute to industrial applications. The state of art in the context of fast solid dynamics is then studied in order to get advantages of the previous successive works.

## Part II

In this part, the mathematical description of Lagrangian Solid Dynamics is presented. It is divided into two chapters presenting the physical laws governing the deformation of a continuum and the employed constitutive models.

**Chapter 2:**

This chapter introduces the balance principles used in solid dynamics in a Total Lagrangian description. The conservation laws are presented in a mixed-based fashion, applicable to be utilised for a reversible and irreversible process. The objective of the mixed-based formalism is to alleviate some numerical difficulties encountered by traditional displacement-based formulation.

**Chapter 3:**

For closure of the system of equations presented in the previous chapter, appropriate constitutive models are introduced in this chapter including thermo-mechanical and purely mechanical models. The former consists of a (nonlinear and linear) thermo-elastic material. The latter presents isothermal hyperelastic and elasto-plastic constitutive models.

# Part III

This part deals with the numerical methodologies whose objective is to approximately translate the problem from the continuum level to the discrete level. Two distinct numerical schemes are utilised in order to discretise the conservation laws in space and, then, the conservative variables are updated in time using a time integrator. The possibility of having different choices for spatial discretisations provide a useful insight on how to choose an appropriate numerical methodology for a target problem.

**Chapter 4:**

This chapter spatially discretises the presented system of equations using the Vertex-Centred Finite Volume Method (VCFVM). The nature of the method and its computational features are initially described and, then, the semi-discretised set of equations are presented. A linear reconstruction procedure and a slope limiter are introduced in order to increase the order of accuracy whilst avoiding spurious oscillations in the vicinity of sharp gradients. In order to ensure the stability of the VCFVM algorithm, a Riemann-based upwinding stabilisation procedure is presented. To this end, the rate of local entropy production of the VCFVM algorithm is examined via the classical Coleman-Noll procedure.

**Chapter 5:**

This chapter focus on a spatial discretisation of the presented conservation laws using the Smooth Particle Hydrodynamics (SPH). The fundamental features of the method and its recent improvements are initially described and, then, the semi-discretised set of equations are presented in conjunction with a linear reconstruction procedure and a slope limiter. It is then shown that the upwind-SPH scheme produces non-negative local entropy between any pair of particles via the classical Coleman-Noll procedure. Finally, a tailor-made artificial compressibility algorithm is suitably adapted to the SPH scheme in order to accommodate nearly and truly incompressibility.

**Chapter 6:**

In this chapter, the semi-discrete set of equations are evolved in time using a one-step two-stage Total Variation Diminishing Runge-Kutta time integrator. The computational validity of the numerical algorithm is investigated using consistency and von-Neumann stability analysis. To this end, the complete flowchart of the proposed numerical algorithms is presented.

## Part VI

This part focus on analysing a series of one- and three-dimensional numerical examples in order to assess the accuracy, robustness and capability of the proposed methodologies.

**Chapter 7:**

This chapter is devoted to a series of one-dimensional benchmark examples aimed at assessing the fundamental abilities of the proposed algorithms in shock dominated scenarios. Furthermore, a convergence study is carried out using a linear thermo-elastic material to ensure the optimum accuracy of the solution.

**Chapter 8:**

In this chapter, the fundamental study on the proposed algorithms is extended to three-dimensional problems. A thorough study is carried out on the spatial convergence, conservation property, robustness and ability to handle incompressible scenarios for both VCFVM and SPH numerical methodologies.

**Chapter 9:**

In this chapter, a series of isothermal and irreversible practical test cases are analysed in order to prove the robustness of the proposed numerical algorithms. These conceivable applications involve impact scenarios, biomedical and soft robotic problems and manufacturing processes.

## Part V

This part mainly provides some conclusions and future perspectives on the accomplished work presented in this thesis.

**Chapter 10**

This chapter summarises the accomplished work in this thesis and suggests potential directions of research in order to enhance the current work.

# Part II

# Lagrangian Solid Dynamics

# Chapter 2

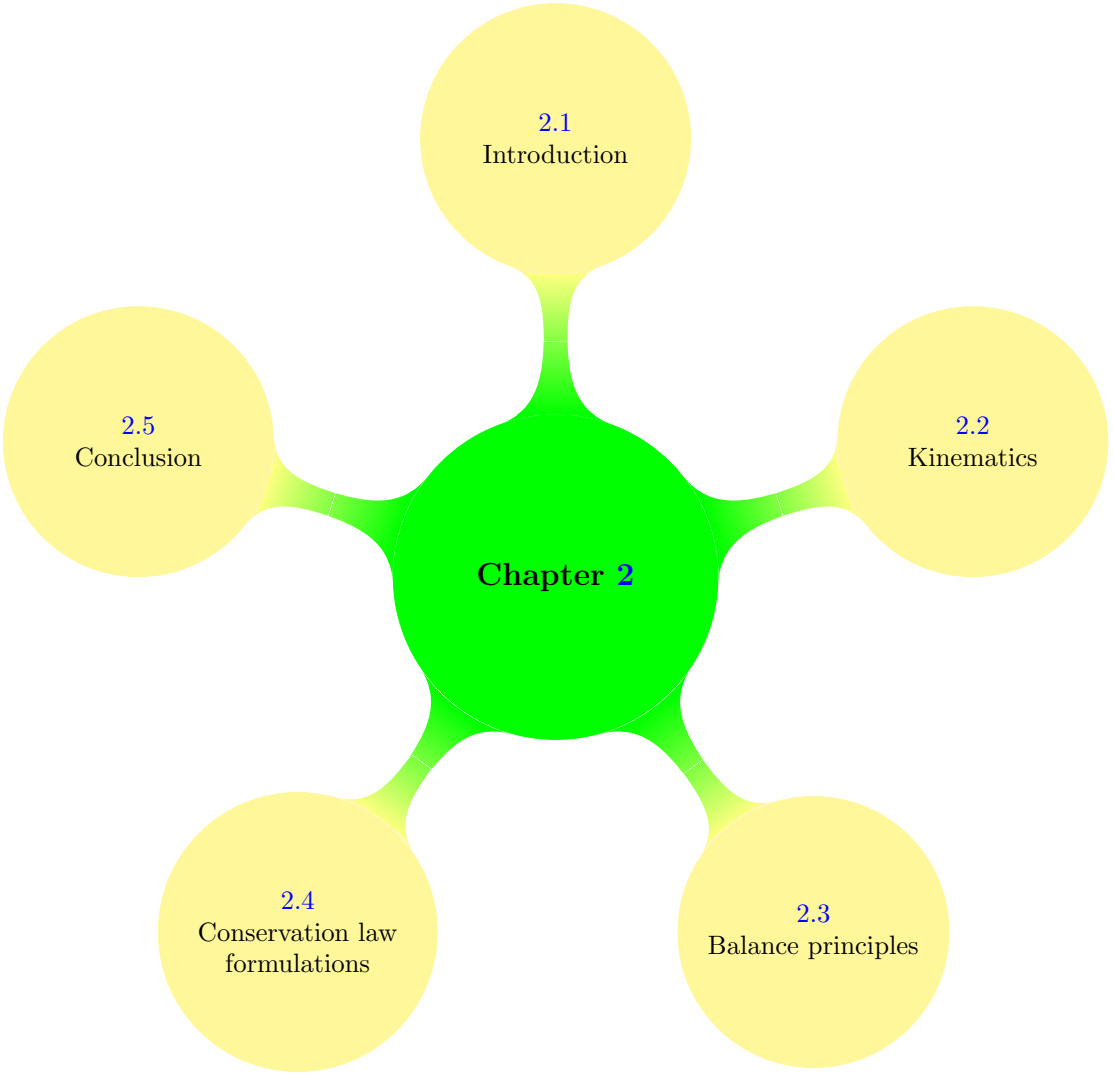


FIGURE 2.1: Structure of Chapter 2

# Governing equations

## 2.1 Introduction

This chapter is devoted to present the balance principles of nonlinear solid mechanics with a focus on thermo-elastodynamics. In Section 2.2, the kinematics of the motion of a continuum is discussed followed by the introduction of different problem descriptions. The conservation laws governing the motion of the continuum are then introduced in the form of a mixed-based formulation in Section 2.3. Finally, the presented formulations are summarised into the form of a set of first order conservation laws, applicable to both thermo-mechanical and isothermal processes. The schematic representation of the layout of this chapter is depicted in Figure 2.1.

## 2.2 Kinematics

### 2.2.1 Motion of a continuum

Consider the deformation of a continuum moving from its reference (material) configuration with volume $\Omega_R$, of boundary $\partial\Omega_R$, into a current (spatial) configuration at time $t$ occupying volume $\Omega$, of boundary $\partial\Omega$ (see Figure 2.2). The motion of the body is defined through a mapping function $\boldsymbol{x} = \boldsymbol{\phi}(\boldsymbol{X}, t)$ by which a solid particle at the reference state is transformed to the spatial configuration. Therefore, the displacement, velocity and acceleration of a particle can be obtained as

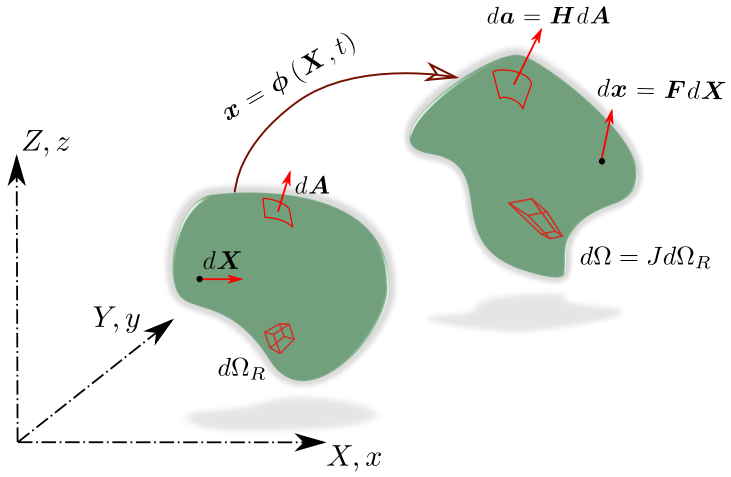


Figure 2.2: Motion of a deformable continuum

$$\boldsymbol{u}(\boldsymbol{X},t) = \boldsymbol{\phi}(\boldsymbol{X},t) - \boldsymbol{\phi}(\boldsymbol{X},0) = \boldsymbol{x} - \boldsymbol{X}; \tag{2.1a}$$

$$\boldsymbol{v}(\boldsymbol{X},t) = \frac{\partial \boldsymbol{u}(\boldsymbol{X},t)}{\partial t}; \tag{2.1b}$$

$$\boldsymbol{a}(\boldsymbol{X},t) = \frac{\partial \boldsymbol{v}(\boldsymbol{X},t)}{\partial t} = \frac{\partial^2 \boldsymbol{u}(\boldsymbol{X},t)}{\partial t^2}. \tag{2.1c}$$

Strain measurement is important for the characterisation of deformation. The deformation gradient (also so-called fibre map) is a two-point tensor by which a fibre at material configuration can be related to its spatial counterpart ($d\boldsymbol{x} = \boldsymbol{F} d\boldsymbol{X}$) and is defined as

$$\boldsymbol{F} = \frac{\partial \boldsymbol{\phi}(\boldsymbol{X},t)}{\partial \boldsymbol{X}} = \boldsymbol{I} + \boldsymbol{\nabla}_0 \boldsymbol{u}, \tag{2.2}$$

where $\boldsymbol{I}$ is the second order identity tensor and $[\boldsymbol{\nabla}_0 \boldsymbol{u}]_{IJ} = \frac{\partial u_I}{\partial X_J}$. Two additional geometric strain measurements are the area map $\boldsymbol{H}$ (co-factor of $\boldsymbol{F}$) and the volume map $J$ (Jacobian of the deformation) defined as

$$\boldsymbol{H} = J\boldsymbol{F}^{-T}; \tag{2.3}$$

$$J = \det(\boldsymbol{F}). \tag{2.4}$$

The former connects an area vector from material to spatial configuration ($d\boldsymbol{a} = \boldsymbol{H} d\boldsymbol{A}$) [2] and the latter is responsible for linking a volume element from the reference into the deformed states ($d\Omega = J d\Omega_R$).

Having the mapping defined, it is of paramount importance to ensure the fulfilment of the following conditions [13]:

- The function $\boldsymbol{\phi}(\boldsymbol{X},t)$ is continuously differentiable (smooth enough) so that the compatibility condition is satisfied (i.e. no overlaps or gaps in the deformed state).
- The function $\boldsymbol{\phi}(\boldsymbol{X},t)$ has to be one-to-one, meaning that for every point at the reference configuration $\Omega_R$, there is a unique point at spatial configuration $\Omega$ and that is necessary and sufficient for regularity of the deformation gradient $\boldsymbol{F}$.
- The volume map restrictedly satisfies $J > 0$ since a regular deformation gradient $\boldsymbol{F}$ requires non-zero determinant.

### 2.2.2 Lagrangian and Eulerian descriptions

The mathematical description of an equation, governing the deformation of a continuum can be presented in different ways and that strongly depends on the sought problem. The two very well-known approaches in continuum mechanics are Lagrangian (material) and Eulerian

[2] This relation is known as Nanson's formula [14].

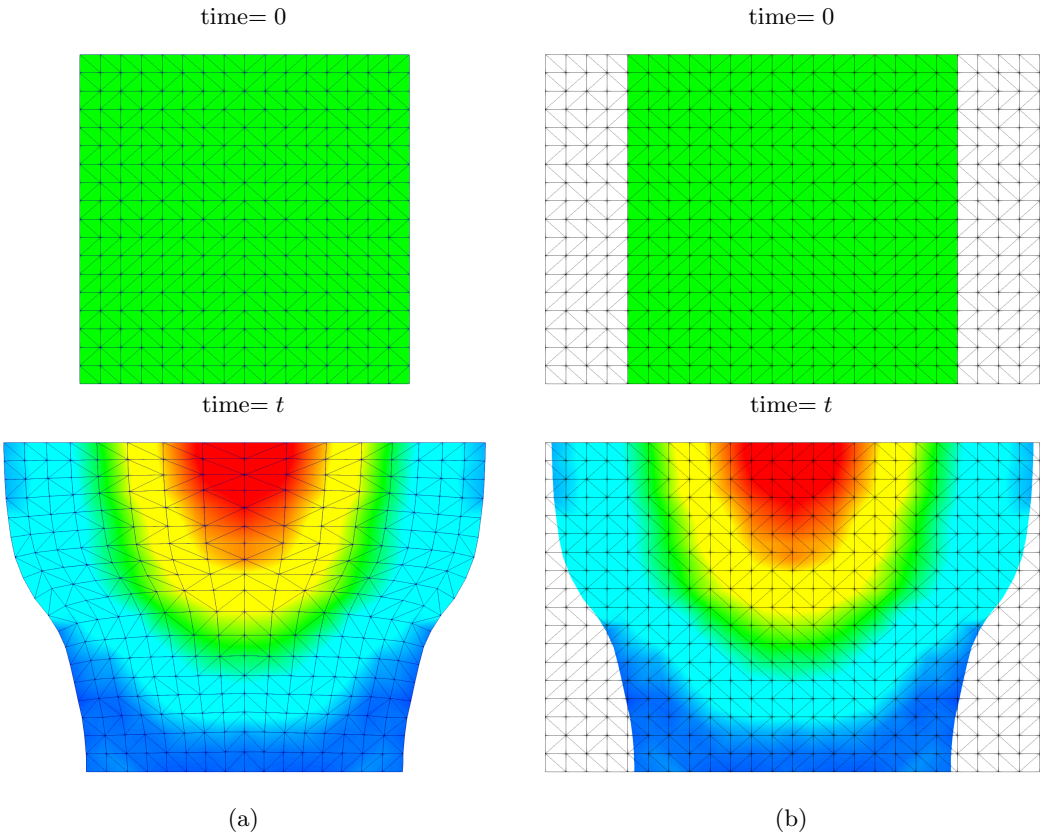


FIGURE 2.3: Schematic definition of (a) Lagrangian and (b) Eulerian descriptions

(spatial) descriptions where the former defines a problem based upon material coordinates $\boldsymbol{X}$ and time $t$ and the latter, introduces spatial coordinates $\boldsymbol{x}$ and time $t$ as the independent variables. A schematic of both frameworks is illustrated in Figure 2.3.

In the Lagrangian description, an observer follows an individual particle of a continuum (i.e. an infinitesimal portion of the continuum) while the body deforms. This means that the conservation of mass will be automatically fulfilled. Lagrangian approaches are more employed in solid mechanics since the stress generally depends on the (history of) deformation [118]. From the numerical standpoint, the computational grid moves with the deformable body and this can be very advantageous in the case of dealing with history-dependent constitutive models. In addition, the boundaries of the computational domain always lie on the physical boundaries of the deformed configuration which can be a matter of crucial importance when modelling multi-material applications [13]. Nonetheless, the Lagrangian approach may struggle when extreme deformations occur in which mesh distortion can drastically degrade the accuracy of the numerical solution. Although this can be rectified by applying adaptive mesh refinement, it brings more complexity in the computer programming, extra computational cost and numerical error to the computations [35].

In the Eulerian approach, an observer looks at a specific location in the space through which the deformable continuum moves. This feature allows handling extremely large deformations without being concerned about any mesh entanglement since the computational mesh will be

fixed in space. This is why the Eulerian approach is prevalent in fluid mechanics as the stresses and behaviour of prevalent Newtonian fluids do not depend on their histories. This, however, arises some difficulties in tracking boundary information in some cases such as simulating moving boundaries, free surface boundaries and interfaces capturing. A possible way of remedy this could be the use of Volume of Fluid (VOF) or Marker-and-Cell (MAC) method [183].

In this thesis, a Total Lagrangian framework is employed due to the type of applications under consideration.

## 2.3 Balance principles

In this Section, the governing equations required to model the motion of a solid continuum are presented in a Total Lagrangian framework. These equations traditionally consist of the conservation of mass, linear momentum, angular momentum and total energy/entropy where the last two are the first and second principles of thermodynamics. Insofar as a mixed-based approach is employed in this thesis, the balance principle is supplemented with conservation laws for geometric strains, namely, the deformation gradient, the area map and the volume map.

### 2.3.1 Conservation of mass

The mass conservation principle postulates that for any closed system (i.e. no mass transfer), the quantity of mass must remain constant over time and this can be generally written as

$$\frac{dm}{dt} = 0, \tag{2.5}$$

where $m$ stands for the mass of the system. It is then possible to write the Total Lagrangian (global) form of the mass conservation as

$$\frac{d}{dt}\int_{\Omega_R} \rho_R \, d\Omega_R = 0. \tag{2.6}$$

Here $\rho_R$ is the density in the reference configuration, with a constant value for a homogeneous continuum. This leads to the Total Lagrangian local form of mass conservation as

$$\frac{d\rho_R}{dt} = 0, \tag{2.7}$$

followed by an appropriate jump condition

$$c\,[\![\rho_R]\!] = 0. \tag{2.8}$$

where $[\![\cdot]\!] = (\cdot)^+ - (\cdot)^-$ is the jump operator denoting the jump of a variable across a moving interface with normal velocity $c$. It is evident from Eq. (2.7) that for a Total Lagrangian framework, the mass conservation is automatically satisfied and, therefore, mass or continuity equation does not need to be explicitly solved.

### 2.3.2 Conservation of linear momentum

The linear momentum equation can be derived on the basis of Newton's second law of motion where the summation of all (surface and body) forces is equivalent to the time rate of the global linear momentum. It can be written in an integral form and, then, with the application of the Gauss divergence theorem renders

$$\begin{aligned}\frac{d}{dt}\int_{\Omega_R} \boldsymbol{p}\, d\Omega_R &= \int_{\partial\Omega_R} \boldsymbol{t}\, dA + \int_{\Omega_R} \boldsymbol{f}_R\, d\Omega_R \\ &= \int_{\Omega_R} (\mathrm{DIV}\boldsymbol{P} + \boldsymbol{f}_R)\, d\Omega_R,\end{aligned} \tag{2.9}$$

where $\boldsymbol{p} = \rho_R \boldsymbol{v}$ is the linear momentum per unit undeformed volume $\Omega_R$, $\boldsymbol{t} = \boldsymbol{P}\boldsymbol{N}$ is the traction vector obtained from the multiplication of the first Piola-Kirchhohf stress tensor $\boldsymbol{P}$ and unit material outward normal vector $\boldsymbol{N}$, $\boldsymbol{f}_R = \rho_R \boldsymbol{b}$ denotes the body forces per unit of reference volume $\Omega_R$ and DIV represents the material divergence operator. Hence, the strong form of the linear momentum conservation equation reads

$$\boxed{\frac{\partial \boldsymbol{p}}{\partial t} = \mathrm{DIV}\boldsymbol{P} + \boldsymbol{f}_R,} \tag{2.10}$$

followed by an appropriate jump condition

$$c\,[\![\boldsymbol{p}]\!] = -[\![\boldsymbol{P}]\!]\boldsymbol{N}. \tag{2.11}$$

### 2.3.3 Conservation of angular momentum

Considering the definition of angular momentum about a reference point $\boldsymbol{x}_R$ as $\boldsymbol{w} = \boldsymbol{r} \times \boldsymbol{p}$ where $\boldsymbol{r} = \boldsymbol{x} - \boldsymbol{x}_R$ and using Eq. (2.9), the integral form of the angular momentum conservation, with the application of Gauss divergence theorem, can be expressed as

$$\begin{aligned}\frac{d}{dt}\int_{\Omega_R} \boldsymbol{w}\, d\Omega_R &= \int_{\partial\Omega_R} \boldsymbol{r} \times \boldsymbol{t}\, dA + \int_{\Omega_R} \boldsymbol{r} \times \boldsymbol{f}_R\, d\Omega_R \\ &= \int_{\Omega_R} \mathrm{DIV}(\boldsymbol{r} \boldsymbol{\times} \boldsymbol{P})\, d\Omega_R + \int_{\Omega_R} \boldsymbol{r} \times \boldsymbol{f}_R\, d\Omega_R,\end{aligned} \tag{2.12}$$

where the mathematical operator $\times$ is the standard cross product between two vectors and $\boldsymbol{\times}$ is defined as the tensor cross product presented in [3] (see Appendix A). This leads to the local form of the angular momentum conservation law as

$$\frac{\partial \boldsymbol{w}}{\partial t} = \mathrm{DIV}(\boldsymbol{r} \boldsymbol{\times} \boldsymbol{P}) + \boldsymbol{r} \times \boldsymbol{f}_R, \tag{2.13}$$

followed by an appropriate jump condition

$$c\,[\![\boldsymbol{w}]\!] = -\boldsymbol{r} \boldsymbol{\times} ([\![\boldsymbol{P}]\!]\boldsymbol{N})\,. \tag{2.14}$$

By the aid of alternating tensor [3] and the Gauss divergence theorem, the surface integral on the right hand side of Eq. (2.12) can be re-written as follows

$$\begin{aligned}\int_{\partial\Omega_R} \boldsymbol{r}\times\boldsymbol{t}\,dA &= \int_{\partial\Omega_R} \boldsymbol{\epsilon}:(\boldsymbol{r}\otimes\boldsymbol{t})\,dA\\ &= \int_{\partial\Omega_R} \boldsymbol{\epsilon}:(\boldsymbol{r}\otimes\boldsymbol{P}\boldsymbol{N})\,dA\\ &= \int_{\Omega_R} \left(\boldsymbol{\epsilon}:\boldsymbol{F}\boldsymbol{P}^T + \boldsymbol{r}\times \mathrm{DIV}\boldsymbol{P}\right) d\Omega_R.\end{aligned} \tag{2.15}$$

Replacing the new obtained expression from Eq. (2.15) into Eq. (2.12) results in

$$\int_{\Omega_R} \boldsymbol{r}\times\left(\frac{\partial \boldsymbol{p}}{\partial t} - \mathrm{DIV}\boldsymbol{P} - \boldsymbol{f}_R\right) d\Omega_R = \int_{\Omega_R} \boldsymbol{\epsilon}:(\boldsymbol{F}\boldsymbol{P}^T)\,d\Omega_R. \tag{2.16}$$

The balance of linear momentum Eq. (2.10) is evident on the left hand side of Eq. (2.16) and thus, the simplified equation for fulfilling the conservation of angular momentum yields

$$\int_{\Omega_R} \boldsymbol{\epsilon}:(\boldsymbol{F}\boldsymbol{P}^T)\,d\Omega_R = \boldsymbol{0}. \tag{2.17}$$

The local form of the obtained relation in Eq. (2.17) reads

$$\boldsymbol{\epsilon}:(\boldsymbol{F}\boldsymbol{P}^T) = \boldsymbol{0}, \tag{2.18}$$

which requires the fulfillment of $\boldsymbol{F}\boldsymbol{P}^T = \boldsymbol{P}\boldsymbol{F}^T$. In addition, considering the definition of second Piola-Kirchhoff stress tensor as $\boldsymbol{S} = \boldsymbol{F}^{-1}\boldsymbol{P}$, it is possible to simply define the condition of the conservation of angular momentum as the symmetry of second Piola-Kirchhoff stress tensor

$$\boldsymbol{S} = \boldsymbol{S}^T. \tag{2.19}$$

### 2.3.4 Conservation of deformation gradient

Considering the deformation gradient $\boldsymbol{F}$ as an independent conservative variable, the integral form of the conservation of deformation gradient reads

$$\frac{d}{dt}\int_{\Omega_R} \boldsymbol{F}\,d\Omega_R = \int_{\partial\Omega_R} \frac{1}{\rho_R}\boldsymbol{p}\otimes\boldsymbol{N}\,dA, \tag{2.20}$$

which has been obtained by integrating the time derivative of Eq. (2.2) over a reference volume $\Omega_R$. Applying the Gauss divergence theorem on the right hand side of Eq. (2.20) enables us to

[3] The alternating tensor (or the so-called permutation operator) is defined as $\epsilon_{IJK} = \hat{\boldsymbol{e}}_i \cdot (\hat{\boldsymbol{e}}_j \times \hat{\boldsymbol{e}}_k)$.

express the local differential form for the conservation of deformation gradient

$$\boxed{\frac{\partial \boldsymbol{F}}{\partial t} = \mathrm{DIV}\left(\frac{1}{\rho_R}\boldsymbol{p}\otimes\boldsymbol{I}\right),} \tag{2.21}$$

followed by an appropriate jump condition

$$c\,[\![\,\boldsymbol{F}\,]\!] = -\frac{1}{\rho_R}[\![\boldsymbol{p}]\!]\otimes\boldsymbol{N}. \tag{2.22}$$

Crucially, the evolution of the fibre map $\boldsymbol{F}$ must be advanced in time satisfying a compatibility condition (known as the so-called involution [184])

$$\mathrm{CURL}(\boldsymbol{F}) = \nabla\times\boldsymbol{F} = \boldsymbol{0}; \tag{2.23a}$$

$$[\mathrm{CURL}(\boldsymbol{F})]_{iI} = \epsilon_{IJK}\frac{\partial F_{iK}}{\partial X_J} \tag{2.23b}$$

where $\epsilon_{IJK}$ is the alternating (or permutation) tensor. This ensures that the deformation gradient $\boldsymbol{F}$ corresponds to the material gradient of a real mapping [18, 106]. It is mathematically evident that CURL of a gradient field is null. However, as the deformation gradient is considered here to be an independent variable, its gradient will be computed in a weakly manner at a discrete level. Hence, an appropriate approximation for the gradient of the (velocity) field has to be taken into account such that the compatibility condition would not get violated.

### 2.3.5 Conservation of area map

An alternative expression for the co-factor of deformation gradient Eq. (2.3) is [185]

$$\boldsymbol{H} = \frac{1}{2}\,\boldsymbol{F}\boldsymbol{\times}\boldsymbol{F} = \frac{1}{2}\,\mathrm{CURL}\,(\boldsymbol{x}\boldsymbol{\times}\boldsymbol{F})\,. \tag{2.24}$$

By integrating the time derivative of Eq. (2.24), the integral form of conservation of area map reads

$$\frac{d}{dt}\int_{\Omega_R}\boldsymbol{H}\,d\Omega_R = \int_{\Omega_R}\mathrm{CURL}\,(\boldsymbol{v}\boldsymbol{\times}\boldsymbol{F})\,d\Omega_R, \tag{2.25}$$

from which the strong form of the conservation of the area map can be extracted

$$\boxed{\frac{\partial \boldsymbol{H}}{\partial t} = \mathrm{CURL}\left(\frac{1}{\rho_R}\boldsymbol{p}\boldsymbol{\times}\boldsymbol{F}\right),} \tag{2.26}$$

followed by an appropriate jump condition

$$c\,[\![\,\boldsymbol{H}\,]\!] = -\boldsymbol{F}^{\mathrm{Ave}}\boldsymbol{\times}\left(\frac{1}{\rho_R}[\![\boldsymbol{p}]\!]\otimes\boldsymbol{N}\right), \tag{2.27}$$

where $\boldsymbol{F}^{\text{Ave}} := \frac{1}{2}\left(\boldsymbol{F}^{+} + \boldsymbol{F}^{-}\right)$ denotes the average state of deformation gradient between the left and right states of a discontinuous surface. The fulfillment of a compatibility condition for evolution of area map $\boldsymbol{H}$ is also required as

$$\text{DIV}\boldsymbol{H} = \boldsymbol{0}; \tag{2.28a}$$

$$\left(\text{DIV}\boldsymbol{H}\right)_i = \frac{\partial H_{iI}}{\partial X_I}. \tag{2.28b}$$

Notice that, if necessary, the conservation form of the area map Eq. (2.26) can be re-expressed in non-conservation form by the aid of compatibility condition Eq. (2.23)

$$\frac{\partial \boldsymbol{H}}{\partial t} = \boldsymbol{F} \times \boldsymbol{\nabla}_R \left(\frac{\boldsymbol{p}}{\rho_R}\right). \tag{2.29}$$

### 2.3.6 Conservation of volume map

The Jacobian of deformation can be evaluated using Eq. (2.4) or as follows

$$J = \frac{1}{3}\left(\boldsymbol{H} : \boldsymbol{F}\right) = \frac{1}{3}\text{DIV}\left(\boldsymbol{H}^T\boldsymbol{x}\right). \tag{2.30}$$

Integration of time derivative of Eq. (2.30) with the aid of the Gauss divergence theorem leads to the integral form of the conservation of volume map

$$\frac{d}{dt}\int_{\Omega_R} J\, d\Omega_R = \int_{\Omega_R} \text{DIV}\left(\boldsymbol{H}^T\frac{\boldsymbol{p}}{\rho_R}\right) d\Omega_R, \tag{2.31}$$

where the local form yields

$$\boxed{\frac{\partial J}{\partial t} = \text{DIV}\left(\boldsymbol{H}^T\frac{\boldsymbol{p}}{\rho_R}\right),} \tag{2.32}$$

followed by an appropriate jump condition

$$c\left[\!\left[J\right]\!\right] = -\boldsymbol{H}^{\text{Ave}} : \left(\frac{1}{\rho_R}\left[\!\left[\boldsymbol{p}\right]\!\right] \otimes \boldsymbol{N}\right), \tag{2.33}$$

with $\boldsymbol{H}^{\text{Ave}} := \frac{1}{2}\left(\boldsymbol{H}^{+} + \boldsymbol{H}^{-}\right)$ standing for the average state of area map between the left and right states of a discontinuous surface. The conservation form of volume map Eq. (2.32) can be re-written, if necessary, in non-conservation form using involution Eq. (2.28)

$$\frac{\partial J}{\partial t} = \boldsymbol{H} : \boldsymbol{\nabla}_R\left(\frac{\boldsymbol{p}}{\rho_R}\right). \tag{2.34}$$

*Remark* 1: Notice that the geometric strains $\{\boldsymbol{F}, \boldsymbol{H}, J\}$, in the case of displacement-based formulation, are not independent variables anymore and will be computed as a function of the material gradient of a current geometry as

$$\boldsymbol{F} = \boldsymbol{\nabla}_0 \boldsymbol{x}; \qquad J = \det \boldsymbol{F}; \qquad \boldsymbol{H} = J\boldsymbol{F}^{-T}. \tag{2.35}$$

### 2.3.7 Conservation of total energy (first law of thermodynamics)

Conservation of total energy postulates that the rate of change of total energy is equivalent to the volume ($\mathbb{B}$) and surface ($\mathbb{S}$) energies (and/or works) applied on a continuum and its integral form can be expressed in a Total Lagrangian framework as

$$\frac{d}{dt}\int_{\Omega_R} E \, d\Omega_R = \int_{\partial\Omega_R} \mathbb{S} \, dA + \int_{\Omega_R} \mathbb{B} \, d\Omega_R, \tag{2.36}$$

where $E$ is the total energy density per unit of the reference volume, $\mathbb{S}$ includes the surface forces (tractions $\boldsymbol{t} = \boldsymbol{P}\boldsymbol{N}$ and heat fluxes $\boldsymbol{Q}$) and $\mathbb{B}$ comprises the body forces ($\boldsymbol{f}_R$) and heat source terms ($s_R$). Applying the Gauss divergence theorem, Eq. (2.36) can be re-written as

$$\begin{aligned} \frac{d}{dt}\int_{\Omega_R} E \, d\Omega_R &= \int_{\partial\Omega_R} \left(\boldsymbol{t}\cdot\boldsymbol{v} - \boldsymbol{Q}\cdot\boldsymbol{N}\right) dA + \int_{\Omega_R} \left(\boldsymbol{f}_R\cdot\boldsymbol{v} + s_R\right) d\Omega_R \\ &= \int_{\Omega_R} \left(\mathrm{DIV}\left(\boldsymbol{P}^T\boldsymbol{v} - \boldsymbol{Q}\right) + \boldsymbol{f}_R\cdot\boldsymbol{v} + s_R\right) d\Omega_R, \end{aligned} \tag{2.37}$$

with heat flux $\boldsymbol{Q}$ defined by Fourier's law [186] in Total Lagrangian description as

$$\boldsymbol{Q} = -\frac{h}{J}\boldsymbol{H}^T\boldsymbol{H}\boldsymbol{\nabla}_R\theta. \tag{2.38}$$

Here $h$ denotes the heat conduction coefficient. By virtue of Eq. (2.37), we can now express the local differential form of the conservation of total energy

$$\boxed{\frac{\partial E}{\partial t} = \mathrm{DIV}\left(\boldsymbol{P}^T\boldsymbol{v} - \boldsymbol{Q}\right) + \boldsymbol{f}_R\cdot\boldsymbol{v} + s_R,} \tag{2.39}$$

which is also considered as the first law of thermodynamics and followed by an appropriate jump condition

$$c\,[\![E]\!] = -\left(\frac{1}{\rho_R}[\![\boldsymbol{P}^T\boldsymbol{p}]\!]\cdot\boldsymbol{N}\right) + [\![\boldsymbol{Q}]\!]\cdot\boldsymbol{N}. \tag{2.40}$$

Alternatively, it is possible to define the total energy of a system per unit of the reference volume as a combination of its internal energy $\mathcal{E}$ and kinetic energy

$$E = \mathcal{E} + \frac{1}{2}\rho_R\boldsymbol{v}\cdot\boldsymbol{v}. \tag{2.41}$$

This allows expressing the non-conservative form of the first law of thermodynamics in terms of the internal energy as

$$\frac{\partial \mathcal{E}}{\partial t} + \boldsymbol{v} \cdot \underbrace{\left( \frac{\partial \boldsymbol{p}}{\partial t} - \mathrm{DIV}\boldsymbol{P} - \boldsymbol{f}_R \right)}_{\text{Balance of linear momentum}} = \boldsymbol{P} : \boldsymbol{\nabla}_R \boldsymbol{v} - \mathrm{DIV}\boldsymbol{Q} + s_R. \tag{2.42}$$

It can be seen from Eq. (2.42) that the second term on the left hand side will vanish as it represents Eq. (2.10). Therefore, the non-conservative local form of the first law of thermodynamics reads

$$\frac{\partial \mathcal{E}}{\partial t} = \boldsymbol{P} : \boldsymbol{\nabla}_R \boldsymbol{v} - \mathrm{DIV}\boldsymbol{Q} + s_R. \tag{2.43}$$

### 2.3.8 Entropy inequality principle (second law of thermodynamics)

The second law of thermodynamics broadly states that the total entropy of an isolated system (no mass and energy transfer out of/into the system) must increase over time. The second law is responsible for the direction of energy transfer whereas the first law of thermodynamics is not capable of [78, 80]. Let us consider the internal energy of a general thermo-mechanical system defined as $\mathcal{E} = \mathcal{E}(\boldsymbol{\chi}, \eta, \boldsymbol{\alpha})$ where $\boldsymbol{\chi} = \{\boldsymbol{F}, \boldsymbol{H}, J\}$ represents the set of geometric strains, $\eta$ stands for entropy and $\boldsymbol{\alpha}$ denotes a possible vector/tensor of the internal state variables which can describe phenomena such as plastic deformation. We can now obtain the time rate of the internal energy by the aid of chain rule as

$$\frac{\partial \mathcal{E}}{\partial t} = \frac{\partial \mathcal{E}}{\partial \boldsymbol{F}} : \dot{\boldsymbol{F}} + \frac{\partial \mathcal{E}}{\partial \boldsymbol{H}} : \dot{\boldsymbol{H}} + \frac{\partial \mathcal{E}}{\partial J}\dot{J} + \frac{\partial \mathcal{E}}{\partial \eta}\dot{\eta} + \frac{\partial \mathcal{E}}{\partial \boldsymbol{\alpha}} \cdot \dot{\boldsymbol{\alpha}}. \tag{2.44}$$

Defining temperature $\theta$ as the conjugate variable of entropy $\theta = \frac{\partial \mathcal{E}}{\partial \eta}$ and substituting Eq. (2.44) into the non-conservative form of the first law of thermodynamics Eq. (2.43) reads

$$\left( \frac{\partial \mathcal{E}}{\partial \boldsymbol{F}} + \frac{\partial \mathcal{E}}{\partial \boldsymbol{H}} \times \boldsymbol{F} + \frac{\partial \mathcal{E}}{\partial \boldsymbol{J}}\boldsymbol{H} - \boldsymbol{P} \right) : \dot{\boldsymbol{F}} + \frac{\partial \mathcal{E}}{\partial \boldsymbol{\alpha}} \cdot \dot{\boldsymbol{\alpha}} + \theta\dot{\eta} + \mathrm{DIV}\boldsymbol{Q} - s_R = \boldsymbol{0}. \tag{2.45}$$

In the absence of any internal state variables $\frac{\partial \mathcal{E}}{\partial \boldsymbol{\alpha}} = \boldsymbol{0}$ and introducing the elastic first Piola-Kirchhoff stress tensor $\boldsymbol{P} = \frac{\partial \mathcal{E}}{\partial \boldsymbol{F}} + \frac{\partial \mathcal{E}}{\partial \boldsymbol{H}} \times \boldsymbol{F} + \frac{\partial \mathcal{E}}{\partial \boldsymbol{J}}\boldsymbol{H}$, Eq. (2.45) reduces to

$$\boxed{\theta\dot{\eta} + \mathrm{DIV}\boldsymbol{Q} - s_R = 0,} \tag{2.46}$$

which is another form of the first law of thermodynamics in the absence of internal state variables. This equation can be a replacement for conservation of total energy in the case of smooth solutions.

In order to obtain the entropy inequality, let us manipulate $\mathrm{DIV}\boldsymbol{Q}$ as follows

$$\begin{aligned}\mathrm{DIV}\boldsymbol{Q} &= \theta\,\frac{1}{\theta}\,\mathrm{DIV}\boldsymbol{Q} \\ &= \theta\left[\mathrm{DIV}\left(\frac{\boldsymbol{Q}}{\theta}\right)+\frac{1}{\theta^2}\boldsymbol{\nabla}_R\theta\cdot\boldsymbol{Q}\right] \\ &= \theta\,\mathrm{DIV}\left(\frac{\boldsymbol{Q}}{\theta}\right)+\frac{1}{\theta}\,\boldsymbol{\nabla}_R\theta\cdot\boldsymbol{Q}.\end{aligned} \tag{2.47}$$

This can lead to an alternative conservation type law for the entropy as

$$\frac{\partial\eta}{\partial t}+\mathrm{DIV}\left(\frac{\boldsymbol{Q}}{\theta}\right)=\frac{s_R}{\theta}-\frac{1}{\theta^2}\boldsymbol{Q}\cdot\boldsymbol{\nabla}_R\theta, \tag{2.48}$$

followed by an appropriate jump condition

$$c\,[\![\eta]\!]=[\![\frac{\boldsymbol{Q}}{\theta}]\!]\cdot\boldsymbol{N}. \tag{2.49}$$

By substituting Eq. (2.47) into Eq. (2.45), after rearranging the last three terms

$$-\mathcal{D}_{int}+\theta\left[\dot{\eta}+\mathrm{DIV}\left(\frac{\boldsymbol{Q}}{\theta}\right)-\frac{s_R}{\theta}\right]+\frac{1}{\theta}\,\boldsymbol{\nabla}_R\theta\cdot\boldsymbol{Q}=\boldsymbol{0}, \tag{2.50}$$

where $\mathcal{D}_{int}$ is the so-called internal dissipation expressed as

$$\mathcal{D}_{int}=\left(\boldsymbol{P}-\left[\frac{\partial\mathcal{E}}{\partial\boldsymbol{F}}+\frac{\partial\mathcal{E}}{\partial\boldsymbol{H}}\boldsymbol{\times}\boldsymbol{F}+\frac{\partial\mathcal{E}}{\partial\boldsymbol{J}}\boldsymbol{H}\right]\right):\dot{\boldsymbol{F}}-\frac{\partial\mathcal{E}}{\partial\boldsymbol{\alpha}}\cdot\dot{\boldsymbol{\alpha}}. \tag{2.51}$$

It generally measures the amount of energy that has been lost through either a viscous type behaviour or internal friction. In a particular case where internal state variables and viscous type effects are absent, the internal dissipation vanishes $\mathcal{D}_{int}=0$ since $\boldsymbol{P}=\frac{\partial\mathcal{E}}{\partial\boldsymbol{F}}+\frac{\partial\mathcal{E}}{\partial\boldsymbol{H}}\boldsymbol{\times}\boldsymbol{F}+\frac{\partial\mathcal{E}}{\partial\boldsymbol{J}}\boldsymbol{H}$ and $\frac{\partial\mathcal{E}}{\partial\boldsymbol{\alpha}}=\boldsymbol{0}$. As the Fourier's law of conduction states that

$$\boldsymbol{\nabla}_R\theta\cdot\boldsymbol{Q}\leq 0, \tag{2.52}$$

Eq. (2.50) leads to

$$\dot{\eta}+\mathrm{DIV}\left(\frac{\boldsymbol{Q}}{\theta}\right)-\frac{s_R}{\theta}\geq 0, \tag{2.53}$$

which represents the entropy inequality (or the second law of thermodynamics).

In a general case where internal state variables exist, based on the entropy inequality Eq. (2.53) and Fourier's law Eq. (2.52), Eq. (2.50) gives

$$\mathcal{D}_{int}-\frac{1}{\theta}\,\boldsymbol{\nabla}_R\theta\cdot\boldsymbol{Q}\geq 0, \tag{2.54}$$

which represents the well-known Clasius-Duhem inequality [78]. It is also easy to prove that the internal dissipation must be always positive ($\mathcal{D}_{int}\geq 0$) considering Clasius-Duhem inequality (2.54) and Fourier's law (2.52).

## 2.4 Conservation law formulations

In general, the integral form of a conservation law is expressed as

$$\frac{d}{dt}\int_{\Omega_R} \boldsymbol{\mathcal{U}}\, d\Omega_R + \int_{\partial\Omega_R} \boldsymbol{\mathcal{F}_N}\, dA = \int_{\Omega_R} \boldsymbol{\mathcal{S}}\, d\Omega_R, \tag{2.55}$$

with $\boldsymbol{\mathcal{U}}$ representing the set of conservation variables, $\boldsymbol{\mathcal{F}_N}$ their corresponding flux vectors and $\boldsymbol{\mathcal{S}}$ is the set of possible source terms [3]. In the case of a smooth function, the integral form Eq. (2.55) can be expressed in the form of a first order set of differential equations

$$\frac{\partial \boldsymbol{\mathcal{U}}}{\partial t} + \underbrace{\frac{\partial \boldsymbol{\mathcal{F}}_I}{\partial X_I}}_{\mathrm{DIV}(\boldsymbol{\mathcal{F}})} = \boldsymbol{\mathcal{S}}. \tag{2.56}$$

Crucially, in the case of a non-smooth solution, the local conservation form (2.56) will be followed by an appropriate Rankine-Hugoniot jump condition (2.57) [17, 22, 187] across a discontinuity surface with outward unit normal $\boldsymbol{N}$ propagating with speed $c$ as reads

$$c\,[\![\boldsymbol{\mathcal{U}}]\!] = [\![\boldsymbol{\mathcal{F}}]\!]\,\boldsymbol{N}, \tag{2.57}$$

In order to concisely define the required conservation laws to be employed for tackling a problem, two different processes have been considered which will be discussed in the following sections.

### 2.4.1 Irreversible process

In an irreversible process the energy equation is coupled to the rest of conservation laws and has to be solved in conjunction with conservation of linear momentum and geometric strains. Therefore, re-calling conservation equations presented in Section 2.3 (Eq. (2.10), Eq. (2.21), Eq. (2.26), Eq. (2.32), Eq. (2.39) and Eq. (2.48)), it is now possible to define the conservative variables, their corresponding fluxes and the source terms as

$$\boldsymbol{\mathcal{U}} = \begin{bmatrix} \boldsymbol{p} \\ \boldsymbol{F} \\ \boldsymbol{H} \\ J \\ E \\ \eta \end{bmatrix}; \qquad \boldsymbol{\mathcal{F}_N} = \boldsymbol{\mathcal{F}}_I N_I = - \begin{bmatrix} \boldsymbol{t} \\ \frac{1}{\rho_R}\boldsymbol{p}\otimes\boldsymbol{N} \\ \boldsymbol{F}\times\left(\frac{1}{\rho_R}\boldsymbol{p}\otimes\boldsymbol{N}\right) \\ \boldsymbol{H} : \left(\frac{1}{\rho_R}\boldsymbol{p}\otimes\boldsymbol{N}\right) \\ \frac{1}{\rho_R}\boldsymbol{p}\cdot\boldsymbol{t} - \boldsymbol{Q}\cdot\boldsymbol{N} \\ -\frac{\boldsymbol{Q}}{\theta}\cdot\boldsymbol{N} \end{bmatrix}; \qquad \boldsymbol{\mathcal{S}} = \begin{bmatrix} \boldsymbol{f}_R \\ \boldsymbol{0} \\ \boldsymbol{0} \\ 0 \\ \boldsymbol{f}_R\cdot\frac{\boldsymbol{p}}{\rho_R} + s_R \\ \frac{s_R}{\theta} - \frac{1}{\theta^2}\boldsymbol{Q}\cdot\boldsymbol{\nabla}_R\theta \end{bmatrix}. \tag{2.58}$$

Here the first law of thermodynamics is expressed in terms of both total energy and entropy conservation laws such that either of them can be used to form the system of equations. The former is known here as the total energy-based formulations whereas the latter is known as the entropy-based system of equations. In addition, the appropriate jump condition for each

conservation law, using Eq. (2.57) and Eq. (2.58), can be expressed as

$$c\,[\![\boldsymbol{p}]\!] = -[\![\boldsymbol{P}]\!]\boldsymbol{N}; \tag{2.59a}$$

$$c\,[\![\boldsymbol{F}]\!] = -\frac{1}{\rho_R}[\![\boldsymbol{p}]\!] \otimes \boldsymbol{N}; \tag{2.59b}$$

$$c\,[\![\boldsymbol{H}]\!] = -\boldsymbol{F}^{\text{Ave}} \times \left(\frac{1}{\rho_R}[\![\boldsymbol{p}]\!] \otimes \boldsymbol{N}\right); \tag{2.59c}$$

$$c\,[\![J]\!] = -\boldsymbol{H}^{\text{Ave}} : \left(\frac{1}{\rho_R}[\![\boldsymbol{p}]\!] \otimes \boldsymbol{N}\right); \tag{2.59d}$$

$$c\,[\![E]\!] = -\left(\frac{1}{\rho_R}[\![\boldsymbol{P}^T\boldsymbol{p}]\!] \cdot \boldsymbol{N}\right) + [\![\boldsymbol{Q}]\!] \cdot \boldsymbol{N}; \tag{2.59e}$$

$$c\,[\![\eta]\!] = [\![\frac{\boldsymbol{Q}}{\theta}]\!] \cdot \boldsymbol{N}. \tag{2.59f}$$

---

*Remark* 2: Nonetheless, Eq. (2.13) will not be solved along with other conservation equations in this thesis because it introduces an extra variable $\boldsymbol{r}$ which cannot be obtained directly by using any of the existing conservation laws. Therefore, a global a-posteriori angular momentum projection procedure is considered for conserving the angular momentum of the system (see Appendix D).

---

### 2.4.2 Isothermal process

For an isothermal process where we deal with a purely mechanical case, the total energy equation (2.39) will be decoupled from the rest of conservation laws and is not necessary to be solved. However, form a computational standpoint, the evolution of total energy can still provide useful information on tracking the numerical dissipation of the algorithm. It is worthwhile noting that the heat flux will be neglected due to the lack of temperature gradient. The rest of the conservation laws will be treated as it is explained in Section 2.4.1, neglecting the coupling effects.

Having the complete set of conservation laws, it is now possible to close the system of equations by using an appropriate constitutive model (which will be introduced in chapter 3), initial and boundary conditions.

## 2.5 Conclusion

In this chapter, the equations governing the motion of a deformable solid have been presented with the focus on thermo-elastodynamics. The balance principles have been introduced in a Total Lagrangian description. Finally, the general set of (total energy-based or entropy-based) $\{\boldsymbol{p}, \boldsymbol{F}, \boldsymbol{H}, J, E \text{ or } \eta\}$ formulations are presented in the form of a first-order system of

conservation laws to be utilised for either irreversible or isothermal isothermal process. In the case of a discontinuous solution, the set of equations is accompanied by an appropriate Rankine-Hugoniot jump condition.

Chapter 3

# Constitutive models

## 3.1 Introduction

A constitutive model, in general, describes the material behaviour through a mathematical model. It might simply be an empirical (phenomenological) relation between two physical quantities, especially kinematic and kinetic, or derived based upon first principles (theoretical work). In fact, a constitutive equation generally provides a relation between stresses, strains and internal variables by which the principles of objectivity [14] and thermodynamic consistency (via Coleman-Noll procedure [188]) have to be satisfied. The former, which is also known as the principle of frame invariance, states that a rigid body motion must not generate strains and, consequently, no stresses. The latter requires satisfaction of the second principle of thermodynamics through the entropy inequality Eq. (2.54).

This chapter introduces the employed constitutive laws in the present work in two main categories: isothermal models (Section 3.2) and the general case of coupled thermo-mechanical models (Section 3.3). To this end, Section 3.4 investigates the hyperbolicity of the system of equations, expressed in Eq. (2.58), for the case of the employed material models. The schematic representation of the layout of this chapter is depicted in Figure 3.1.

## 3.2 Isothermal model

A constitutive relation for an isothermal material model can be mathematically derived from its strain energy functional $\psi$. The term strain energy stands for the energy stored by a material undergoing deformation. In the case of reversible isothermal elasticity, the strain energy functional $\psi_R$ per unit of undeformed volume can alternatively be re-expressed via a polyconvex function $W_R$ as [120]

$$\psi_R(\boldsymbol{\nabla}_0 \boldsymbol{x}) = W_R(\boldsymbol{\chi}), \tag{3.1}$$

where $W_R$ is convex with respect to its 19 variables, namely, $3 \times 3$ components of $\boldsymbol{F}$ and $\boldsymbol{H}$ and the scalar $J$. This condition, which is strongly related to the material stability of the

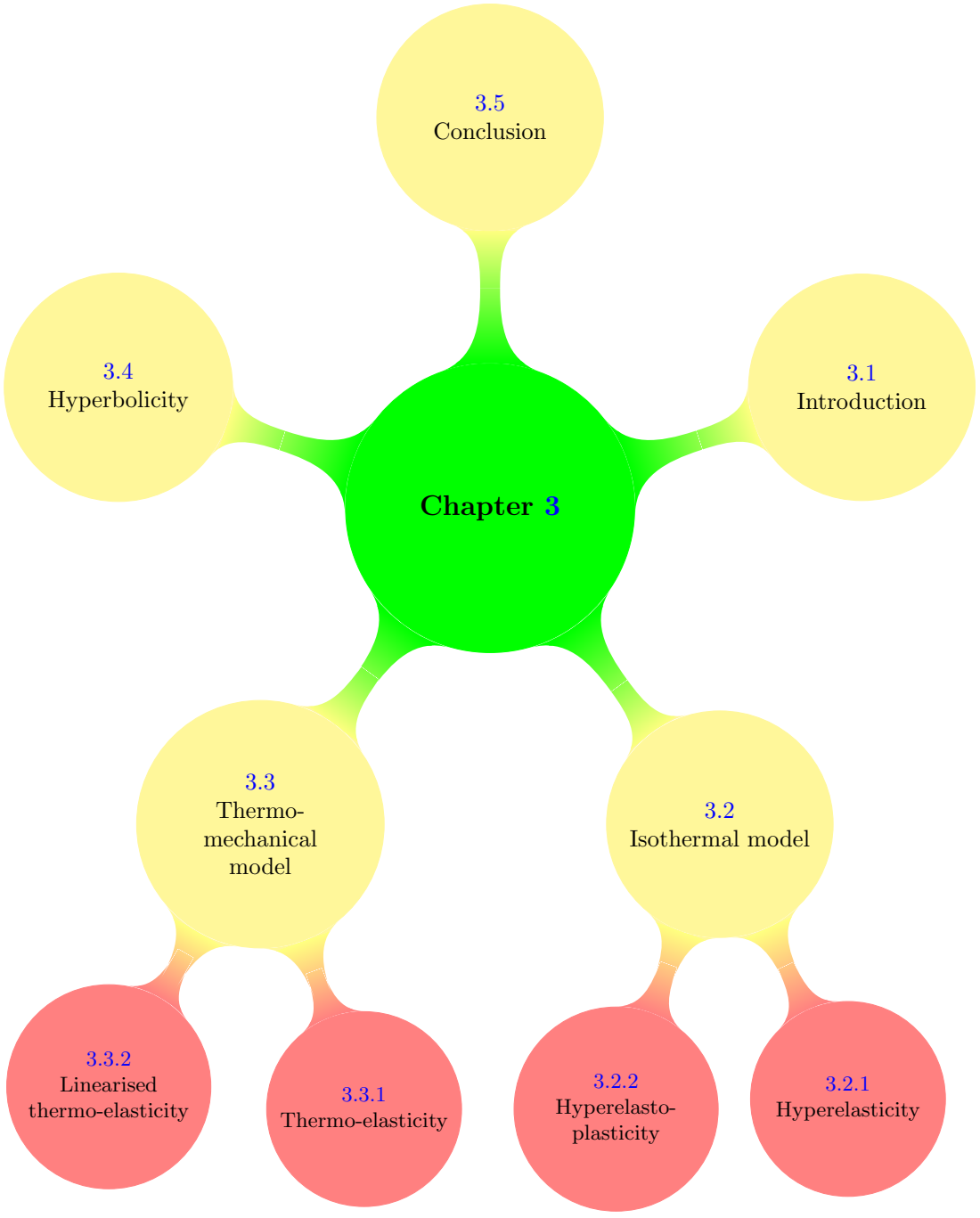


FIGURE 3.1: Structure of Chapter 3

constitutive equations, ensures the well-posedness of the governing equations. An extensive discussion about polyconvexity can be found in [189].

For isotropic materials, expression of $W_R$ can be further simplified through the use of the invariants $\{I_1, I_2, I_3\}$ defined as [120, 185]

$$I_1 = \boldsymbol{F} : \boldsymbol{F}; \qquad I_2 = \boldsymbol{H} : \boldsymbol{H}; \qquad I_3 = J^2. \tag{3.2}$$

### 3.2.1 Hyperelasticity

#### Compressible polyconvex model

For a compressible Mooney–Rivlin model, an admissible polyconvex strain energy can be defined as [3]

$$W_R(\boldsymbol{\chi}) = \alpha I_1 + \beta I_2 + f(J), \tag{3.3}$$

where $\alpha$ and $\beta$ are positive material parameters. Appropriate values for $\alpha$ and $\beta$ and a suitable function for $f(J)$ must be chosen such that, at the reference configuration, the stress vanishes and the usual linear elasticity tensor in terms of the Lame coefficients $\lambda$ and $\mu$ is recovered. This leads to the following set of conditions

$$\begin{aligned} f'(1) &= -2(\alpha + 2\beta); \\ f''(1) &= \lambda + 2\alpha; \\ \mu &= 2(\alpha + \beta). \end{aligned} \tag{3.4}$$

The following convex expression for $f(J)$ is employed here

$$f(J) = -4\beta J - 2\alpha \ln J + \frac{\lambda}{2}(J-1)^2. \tag{3.5}$$

The first Piola-Kirchoff stress tensor can then be defined as [3]

$$\boldsymbol{P}_R(\boldsymbol{\chi}) = \frac{\partial W_R}{\partial \boldsymbol{F}} + \frac{\partial W_R}{\partial \boldsymbol{H}} \times \boldsymbol{F} + \frac{\partial W_R}{\partial J}\boldsymbol{H} \tag{3.6}$$

$$= \boldsymbol{\Sigma}_{\boldsymbol{F}} + \boldsymbol{\Sigma}_{\boldsymbol{H}} \times \boldsymbol{F} + \Sigma_J \boldsymbol{H}. \tag{3.7}$$

Notice here that $\boldsymbol{\Sigma}_{\boldsymbol{F}}$, $\boldsymbol{\Sigma}_{\boldsymbol{H}}$, $\Sigma_J$ are defined as the corresponding work conjugate stresses to the geometric strains $\{\boldsymbol{F}, \boldsymbol{H}, J\}$, respectively. By substituting Eq. (3.3) into the above equation, the first Piola-Kirchoff stress tensor for a compressible Mooney-Rivlin (MR) material model reads

$$\boldsymbol{P}_R = 2\alpha\boldsymbol{F} + 2\beta\boldsymbol{H} \times \boldsymbol{F} + \left(-4\beta - \frac{2\alpha}{J} + \lambda(J-1)\right)\boldsymbol{H}. \tag{3.8}$$

It is worth to mention that the Mooney-Rivlin model degenerates to the neo-Hookean (NH) material model if $\alpha = \frac{\mu}{2}$ and $\beta = 0$ and, therefore, the first Piola-Kirchoff stress tensor for the neo-Hookean material model can be expressed as

$$\boldsymbol{P}_R = \mu\boldsymbol{F} + \left(-\frac{\mu}{J} + \lambda(J-1)\right)\boldsymbol{H}. \tag{3.9}$$

### Nearly incompressible polyconvex model

The strain energy $W_R$ for polyconvex nearly incompressible Mooney-Rivlin material model can be decomposed into the deviatoric $\hat{W}_R(\boldsymbol{\chi})$ and volumetric $U_R(J)$ contributions [16, 120, 185]

$$W(\boldsymbol{\chi}) = \underbrace{\zeta J^{-2/3}\left(\boldsymbol{F}:\boldsymbol{F}\right) + \xi J^{-2}\left(\boldsymbol{H}:\boldsymbol{H}\right)^{3/2} - 3\zeta - 3^{3/2}\xi}_{\hat{W}_R} + \underbrace{\frac{\kappa}{2}(J-1)^2}_{U_R}, \tag{3.10}$$

where $\zeta$, $\xi$ and $\kappa$ (bulk modulus) are positive material parameters. By comparison of the tangent elasticity operator at the initial undeformed configuration with that of classical linear elasticity [185], appropriate values for the material parameters $\zeta$ and $\xi$ can be defined in terms of the shear modulus $\mu$, that is, $2\zeta + 3\sqrt{3}\xi = \mu$ [4, 16, 120]. To obtain the expression for the first Piola (3.6), the following derivatives are required as follows

$$\frac{\partial \hat{W}_R}{\partial \boldsymbol{F}} := \boldsymbol{\Sigma}_{\boldsymbol{F}} = 2\zeta J^{-2/3}\boldsymbol{F}; \tag{3.11a}$$

$$\frac{\partial \hat{W}_R}{\partial \boldsymbol{H}} := \boldsymbol{\Sigma}_{\boldsymbol{H}} = 3\xi J^{-2}\left(\boldsymbol{H}:\boldsymbol{H}\right)^{1/2}\boldsymbol{H}; \tag{3.11b}$$

$$\frac{\partial W_R}{\partial J} := \Sigma_J = \underbrace{\frac{\partial \hat{W}_R}{\partial J}}_{\hat{\Sigma}_J} + \underbrace{\frac{dU_R}{dJ}}_{\text{Pressure}(p)}, \tag{3.11c}$$

with

$$\hat{\Sigma}_J = -\frac{2}{3}\zeta J^{-5/3}(\boldsymbol{F}:\boldsymbol{F}) - 2\xi J^{-3}(\boldsymbol{H}:\boldsymbol{H})^{3/2}; \qquad p = \kappa(J-1). \tag{3.12}$$

Hence, the first Piola-Kirchhoff stress tensor, decomposed here into deviatoric ($\hat{\boldsymbol{P}}$) and volumetric ($\boldsymbol{P}_{\text{vol}}$) contributions, for nearly incompressible Mooney-Rivlin model reads

$$\boldsymbol{P}_R = \hat{\boldsymbol{P}}_R + \boldsymbol{P}_{R,\text{vol}}, \tag{3.13}$$

where

$$\begin{aligned}\hat{\boldsymbol{P}}_R &= 2\zeta J^{-2/3}\boldsymbol{F} + \left(3\xi J^{-2}\left(\boldsymbol{H}:\boldsymbol{H}\right)^{1/2}\boldsymbol{H}\right)\boldsymbol{\times}\boldsymbol{F} + \left(-\frac{2}{3}\zeta J^{-5/3}(\boldsymbol{F}:\boldsymbol{F}) - 2\xi J^{-3}(\boldsymbol{H}:\boldsymbol{H})^{3/2}\right)\boldsymbol{H};\\ \boldsymbol{P}_{R,\text{vol}} &= p\boldsymbol{H}; \quad p = \kappa(J-1).\end{aligned} \tag{3.14}$$

By consideration of the material parameters $\zeta = \frac{\mu}{2}$ and $\xi = 0$, it is possible to retrieve the strain energy functional for nearly incompressible neo-Hookean model and, therefore, its Piola-Kirchhoff stress tensor as

$$\boldsymbol{P}_R = \underbrace{\mu J^{-2/3}\boldsymbol{F} - \frac{\mu}{3}J^{-5/3}(\boldsymbol{F}:\boldsymbol{F})\boldsymbol{H}}_{\hat{\boldsymbol{P}}_R} + \underbrace{p\boldsymbol{H}}_{\boldsymbol{P}_{R,\text{vol}}}; \qquad p = \kappa(J-1). \tag{3.15}$$

*Remark* 3: It is worth to mention that the classical nearly incompressible neo-Hookean model [14] can be simply recovered through Eq. (3.15) as

$$\hat{\boldsymbol{P}}_R = \mu J_{\boldsymbol{F}}^{-2/3}\left(\boldsymbol{F} - \frac{1}{3}(\boldsymbol{F}:\boldsymbol{F})\boldsymbol{F}^{-T}\right); \qquad \boldsymbol{P}_{R,\text{vol}} = p\boldsymbol{H}; \qquad p = \kappa(J-1). \tag{3.16}$$

where $J = \det \boldsymbol{F}$ is the Jacobian of deformation and $\boldsymbol{H} = \frac{1}{2}\boldsymbol{F} \times \boldsymbol{F}$ is the area map, both evaluated on the basis of the deformation gradient tensor $\boldsymbol{F} = \boldsymbol{\nabla}_0 \boldsymbol{x}$. It must be noted that in continuum level, Eq. (3.16) is exactly equivalent to Eq. (3.15). However, in discrete level, they will not be the same due to the different definition of the geometric strains.

### 3.2.2 Hyperelasto-plasticity

The standard rate-independent [4] von Mises plasticity with isotropic hardening [5] is considered to be utilised here in order to model an isothermal hyperelasto-plastic behaviour [190]. In this case, the deformation gradient tensor $\boldsymbol{F}$ can be multiplicatively decomposed into elastic $\boldsymbol{F}_e$ and plastic $\boldsymbol{F}_p$ components such that

$$\boldsymbol{F} = \boldsymbol{F}_e\,\boldsymbol{F}_p, \tag{3.17}$$

It is also possible to define elastic left strain tensor as

$$\boldsymbol{b}_e = \boldsymbol{F}\,\boldsymbol{C}_p^{-1}\boldsymbol{F}^T; \qquad \boldsymbol{C}_p = \boldsymbol{F}_p^T\boldsymbol{F}_p, \tag{3.18}$$

where $\boldsymbol{C}_p$ is the plastic right Cauchy Green tensor. In addition, the strain energy functional should be essentially defined in terms of the elastic principal stretches $(\lambda_e^1,\, \lambda_e^2,\, \lambda_e^3)$

$$\psi(\lambda_e^1,\, \lambda_e^2,\, \lambda_e^3, J) = \hat{\psi}\left(J^{-1/3}\lambda_e^1,\, J^{-1/3}\lambda_e^2,\, J^{-1/3}\lambda_e^3\right) + \psi_{\text{vol}}(J), \tag{3.19}$$

where

$$\begin{aligned} \hat{\psi} &= \mu\left[(\ln\lambda_e^1)^2 + (\ln\lambda_e^2)^2 + (\ln\lambda_e^3)^2\right] - \frac{\mu}{3}(\ln J)^2; \\ \psi_{\text{vol}} &= \frac{\kappa}{2}(\ln J)^2; \quad \kappa = \lambda + \frac{2}{3}\mu; \quad \ln J = \sum_{\alpha=1}^{3}\ln\lambda_e^\alpha. \end{aligned} \tag{3.20}$$

The algorithmic structure of how to update first Piola-Kirchhoff stress tensor for this particular material model is shown in Algorithm 3.1.

[4] A 'rate-independent' model postulates that given a deformation history for the material will lead to a specific state of stress irrespective of the speed at which this path is followed [14]. In other words, the stress is not a function of the strain rate.

[5] The feature of 'isotropic hardening' indicates that the yield stress increases equally in all directions due to tensile or compressive loading [14].

**Algorithm 3.1:** Time update of the first Piola Kirchoff stress tensor - Hyperelasto-plasticity

**Input** : $\boldsymbol{F}^{n+1}, J^{n+1}, \left[\boldsymbol{C}_p^{-1}\right]^n, \varepsilon_p^n$

**Output:** $\boldsymbol{P}^{n+1}$

(1) Evaluate Jacobian of deformation: $J_{\boldsymbol{F}}^{n+1} = \det\left(\boldsymbol{F}^{n+1}\right)$.

(2) Compute trial elastic left strain tensor: $\bar{\boldsymbol{b}}_e^{n+1} = \boldsymbol{F}^{n+1}\left[\boldsymbol{C}_p^{-1}\right]^n\left[\boldsymbol{F}^T\right]^{n+1}$.

(3) Obtain pressure: $p^{n+1} = \kappa\,\frac{\ln\left(J^{n+1}\right)}{J^{n+1}}$.

(4) Spectral decomposition of $\bar{\boldsymbol{b}}_e^{n+1}$ to obtain stretches and spatial normal vectors: $\bar{\lambda}_e^i\ ,\ \bar{\boldsymbol{n}}_i \leftarrow \bar{\boldsymbol{b}}_e^{n+1} = \sum_{i=1}^3 \left(\bar{\lambda}_e^i\right)^2 (\bar{\boldsymbol{n}}_i \otimes \bar{\boldsymbol{n}}_i)$.

(5) Set spatial normals: $\boldsymbol{n}_i^{n+1} = \bar{\boldsymbol{n}}_i$.

(6) Compute trial deviatoric Kirchoff stress tensor: $\bar{\boldsymbol{\tau}}' = \sum_{i=1}^3 \bar{\tau}'_{ii}\,(\bar{\boldsymbol{n}}_i \otimes \bar{\boldsymbol{n}}_i)\,;\qquad \bar{\tau}'_{ii} = 2\mu\,\ln\left(\bar{\lambda}_e^i\right) - \frac{2}{3}\mu\,\ln\left(J_{\boldsymbol{F}}^{n+1}\right)$.

(7) Evaluate yield criterion: $f\left(\bar{\boldsymbol{\tau}}', \varepsilon_p^n\right) = \sqrt{\frac{3}{2}(\bar{\boldsymbol{\tau}}' : \bar{\boldsymbol{\tau}}')} - \left(\tau_y^0 + H\varepsilon_p^n\right)$.

(8) Compute direction vector, plastic multiplier and elastic stretch:

**if** $f\left(\bar{\boldsymbol{\tau}}', \varepsilon_p^n\right) > 0$ **then**

(8.1) Direction vector: $\boldsymbol{\upsilon}_i^{n+1} = \frac{\bar{\tau}'_{ii}}{\sqrt{\frac{2}{3}(\bar{\boldsymbol{\tau}}':\bar{\boldsymbol{\tau}}')}}$.

(8.2) Plastic multiplier: $\Delta\gamma = \frac{f\left(\bar{\boldsymbol{\tau}}', \varepsilon_p^n\right)}{3\mu + H}$.

(8.3) Elastic stretch: $\lambda_e^{i,n+1} = \exp\left(\ln(\bar{\lambda}_e^i) - \Delta\gamma\,\boldsymbol{\upsilon}_i^{n+1}\right)$.

**else**

(8.1) $\boldsymbol{\upsilon}_i^{n+1} = \Delta\gamma = 0$.

**end**

(9) Update elastic left strain tensor: $\boldsymbol{b}_e^{n+1} = \sum_{i=1}^3 \left(\lambda_e^{i,n+1}\right)^2 \left(\boldsymbol{n}_i^{n+1} \otimes \boldsymbol{n}_i^{n+1}\right)$.

(10) Update plastic right Cauchy Green tensor: $\left[\boldsymbol{C}_p^{-1}\right]^{n+1} = \left[\boldsymbol{F}^{-1}\right]^{n+1}\boldsymbol{b}_e^{n+1}\left[\boldsymbol{F}^{-T}\right]^{n+1}$.

(11) Update plastic strain: $\varepsilon_p^{n+1} = \varepsilon_p^n + \Delta\gamma$.

(12) Compute Kirchoff stresss tensor: $\boldsymbol{\tau}^{n+1} = \sum_{i=1}^3 \tau_{ii}\left(\boldsymbol{n}_i^{n+1} \otimes \boldsymbol{n}_i^{n+1}\right)$;

$\tau_{ii} = \tau'_{ii} + J_{\boldsymbol{F}}^{n+1} p^{n+1};\qquad \tau'_{ii} = \left(1 - \frac{2\mu\,\Delta\gamma}{\sqrt{\frac{2}{3}(\bar{\boldsymbol{\tau}}':\bar{\boldsymbol{\tau}}')}}\right)\bar{\tau}'_{ii}$.

(13) Evaluate first Piola Kirchoff stress tensor: $\boldsymbol{P}_R^{n+1} = \boldsymbol{\tau}^{n+1}\left[\boldsymbol{F}^{-T}\right]^{n+1}$.

## 3.3 Thermo-mechanical model

Considering an irreversible process, a general thermo-mechanical constitutive model is required to account for mechanical and thermal effects altogether. In this case, the stress is generally a function of the strains, temperature or entropy of the system and possibly, an internal state variable.

### 3.3.1 Thermo-elasticity

For strict thermo-elasticity[6], the internal energy of a system can be expressed by a convex multi-variable (polyconvex) function as [191]

$$\mathcal{E} = \mathcal{E}\left(\boldsymbol{\chi}, \eta\right), \tag{3.21}$$

where $\boldsymbol{\chi} = \{\boldsymbol{F}, \boldsymbol{H}, J\}$ represents the set of geometric strains and $\eta$ denotes the entropy, that is the energy dual conjugate variable to the temperature described as

$$\theta = \frac{\partial \mathcal{E}}{\partial \eta}. \tag{3.22}$$

Taking time derivative of equation Eq. (3.21) for the internal energy, in combination with the geometric conservation laws for $\boldsymbol{\chi}$, gives

$$\frac{\partial \mathcal{E}}{\partial t} = \frac{\partial \mathcal{E}}{\partial \boldsymbol{\chi}} : \frac{\partial \boldsymbol{\chi}}{\partial t} + \frac{\partial \mathcal{E}}{\partial \eta}\frac{\partial \eta}{\partial t} \tag{3.23a}$$

$$= \frac{\partial \mathcal{E}}{\partial \boldsymbol{F}} : \frac{\partial \boldsymbol{F}}{\partial t} + \frac{\partial \mathcal{E}}{\partial \boldsymbol{H}} : \left(\boldsymbol{F} \times \frac{\partial \boldsymbol{F}}{\partial t}\right) + \frac{\partial \mathcal{E}}{\partial J}\left(\boldsymbol{H} : \frac{\partial \boldsymbol{F}}{\partial t}\right) + \theta\frac{\partial \eta}{\partial t} \tag{3.23b}$$

$$= \left(\frac{\partial \mathcal{E}}{\partial \boldsymbol{F}} + \frac{\partial \mathcal{E}}{\partial \boldsymbol{H}} \times \boldsymbol{F} + \frac{\partial \mathcal{E}}{\partial J}\boldsymbol{H}\right) : \frac{\partial \boldsymbol{F}}{\partial t} + \theta\frac{\partial \eta}{\partial t}. \tag{3.23c}$$

Note that the expression in the above parenthesis represents the components of the first Piola, that is

$$\boldsymbol{P} = \frac{\partial \mathcal{E}}{\partial \boldsymbol{F}} + \frac{\partial \mathcal{E}}{\partial \boldsymbol{H}} \times \boldsymbol{F} + \frac{\partial \mathcal{E}}{\partial J}\boldsymbol{H}. \tag{3.24}$$

#### General thermal relationships

In general, (Calorimetry) relationships between internal energy $\mathcal{E}$, temperature $\theta$ and entropy $\eta$ can be derived from the definition of the heat capacity at constant volume $c_v$

$$\frac{\partial \tilde{\mathcal{E}}}{\partial \theta} = c_v; \qquad \tilde{\mathcal{E}}\left(\boldsymbol{\chi}, \theta\right) = \mathcal{E}\left(\boldsymbol{\chi}, \eta\left(\boldsymbol{\chi}, \theta\right)\right), \tag{3.25}$$

[6] In the absence of other state variables such as plastic strain.

where $c_v = \rho_R C_v$ and $C_v$ is the specific heat capacity at constant volume. Insofar as the internal energy $\mathcal{E}$ presented in Eq. (3.21) is expressed as a function of the entropy $\eta$ and deformation $\boldsymbol{\chi}$, Eq. (3.25) can be recast using the chain rule to yield

$$\frac{\partial \mathcal{E}}{\partial \eta}\frac{\partial \eta}{\partial \theta} = c_v. \tag{3.26}$$

With the aid of Eq. (3.22), a constitutive relationship between the temperature $\theta$ and the entropy $\eta$ at constant deformation can be established

$$\frac{d\theta}{d\eta} = \frac{\theta}{c_v}. \tag{3.27}$$

Assuming constant $C_v$ for all temperatures allows the relationship between entropy and temperature to be integrated for $\theta$ as

$$\theta\left(\boldsymbol{\chi}, \eta\right) = \theta_R \exp\left(\frac{\eta - \eta_R\left(\boldsymbol{\chi}\right)}{c_v}\right); \qquad \eta_R\left(\boldsymbol{\chi}\right) = \eta\left(\boldsymbol{\chi}, \theta_R\right). \tag{3.28}$$

with $\theta_R$ defined as the reference temperature.

---

*Remark* 4: It is useful to note that

$$\theta\left(\boldsymbol{\chi}, \eta\right) = \theta_0\left(\boldsymbol{\chi}\right) e^{\frac{\eta}{c_v}}; \qquad \theta_0\left(\boldsymbol{\chi}\right) = \theta\left(\boldsymbol{\chi}, 0\right), \tag{3.29}$$

where $\theta_0\left(\boldsymbol{\chi}\right)$ denotes the temperature of the material if entropy is kept constant at zero whilst the deformation is changed. Both $\theta_0\left(\boldsymbol{\chi}\right)$ and $\eta_R\left(\boldsymbol{\chi}\right)$ describe the thermal-mechanical couplings and are related by

$$\theta_0\left(\boldsymbol{\chi}\right) = \theta_R \exp\left(-\frac{\eta_R\left(\boldsymbol{\chi}\right)}{c_v}\right); \qquad \eta_R\left(\boldsymbol{\chi}\right) = -c_v \ln\left(\frac{\theta_0\left(\boldsymbol{\chi}\right)}{\theta_R}\right). \tag{3.30}$$

Moreover, the relation between $\mathcal{E}_R$ (internal energy at reference temperature) and $\mathcal{E}_0$ (internal energy for zero entropy) can be established

$$\mathcal{E}_R\left(\boldsymbol{\chi}\right) = \mathcal{E}_0\left(\boldsymbol{\chi}\right) + c_v\left(\theta_R - \theta_0\left(\boldsymbol{\chi}\right)\right), \tag{3.31}$$

where

$$\mathcal{E}_0 = \mathcal{E}(\boldsymbol{\chi}, 0); \qquad \theta_0\left(\boldsymbol{\chi}\right) = \theta_R e^{-\frac{\eta_R(\boldsymbol{\chi})}{c_v}}. \tag{3.32}$$

---

For completeness, Eq. (3.28) can also be alternatively expressed for $\eta$ as

$$\eta\left(\boldsymbol{\chi}, \theta\right) = \eta_R\left(\boldsymbol{\chi}\right) + c_v \ln\left(\frac{\theta}{\theta_R}\right). \tag{3.33}$$

Finally, assuming constant heat capacity $c_v$, it is possible to write an explicit relationship for

the internal energy $\mathcal{E}$. Integrating Eq. (3.25) with respect to temperature $\theta$ between the limits $\theta = \theta_R$ and a given value $\theta$

$$\underbrace{\tilde{\mathcal{E}}(\boldsymbol{\chi}, \theta)}_{\mathcal{E}(\boldsymbol{\chi},\eta)} = \mathcal{E}_R(\boldsymbol{\chi}) + c_v \underbrace{(\theta - \theta_R)}_{\Delta\theta} \tag{3.34a}$$

$$= \mathcal{E}_R(\boldsymbol{\chi}) + c_v \theta_R \left[ \exp\left( \frac{\eta - \eta_R(\boldsymbol{\chi})}{c_v} \right) - 1 \right], \tag{3.34b}$$

where $\Delta\theta = \theta - \theta_R$ represents the temperature increment.

### Helmholtz's free energy functional

It is now possible to express the first Piola in terms of deformation $\boldsymbol{\chi}$ and temperature $\theta$. To achieve this, by the aid of Legendre transform, the Helmholtz's free energy (also called strain energy functional in the isothermal case) per unit of undeformed volume can be introduced as

$$W(\boldsymbol{\chi}, \theta) = \underbrace{\mathcal{E}(\boldsymbol{\chi}, \eta)}_{\tilde{\mathcal{E}}(\boldsymbol{\chi},\theta)} - \theta\eta(\boldsymbol{\chi}, \theta). \tag{3.35}$$

Moreover, based on Eq. (3.24), the state of stress at a given temperature can be obtained in a direct manner as

$$\boxed{\boldsymbol{P}(\boldsymbol{\chi}, \theta) = \frac{\partial W}{\partial \boldsymbol{F}} + \frac{\partial W}{\partial \boldsymbol{H}} \times \boldsymbol{F} + \frac{\partial W}{\partial J} \boldsymbol{H}.} \tag{3.36}$$

Substituting Eq. (3.34a) and Eq. (3.33) into Eq. (3.35) gives a final expression for the strain energy functional $W$ as [78]

$$W(\boldsymbol{\chi}, \theta) = \underbrace{W_R(\boldsymbol{\chi})}_{\text{Mechanical}} - \underbrace{\Delta\theta\eta_R(\boldsymbol{\chi})}_{\text{Coupling}} + \underbrace{T(\theta)}_{\text{Thermal}}; \qquad T(\theta) = c_v \left[ \Delta\theta - \theta \ln \frac{\theta}{\theta_R} \right]. \tag{3.37}$$

More generally, a wide range of materials relies on the assumption that the distortional behaviour of the material can be split from the volumetric response. Mathematically, these assumptions are expressed by means of an additive decomposition of $W_R$ into distortional $\hat{W}_R$ and volumetric components $U_R$, namely, $W_R(\boldsymbol{\chi}) = \hat{W}_R(\boldsymbol{\chi}) + U_R(J)$. Similarly, the same decomposition between volumetric and distortional components can be established in terms of entropy such that $\eta_R(\boldsymbol{\chi}) = \hat{\eta}_R(\boldsymbol{\chi}) + \eta_{R,\text{vol}}(J)$. Equation Eq. (3.37) then becomes

$$W(\boldsymbol{\chi}, \theta) = \hat{W}_R(\boldsymbol{\chi}) + U_R(J) - \Delta\theta \left[ \hat{\eta}_R(\boldsymbol{\chi}) + \eta_{R,\text{vol}}(J) \right] + T(\theta). \tag{3.38}$$

In addition, a complementary relation to the energy dual conjugate variable described in Eq. (3.22) is in the form of

$$\eta(\boldsymbol{\chi}, \theta) = -\frac{\partial W}{\partial \theta}. \tag{3.39}$$

Using Eq. (3.36), the first Piola becomes

$$\boldsymbol{P}(\boldsymbol{\chi},\theta) = \hat{\boldsymbol{P}}_R(\boldsymbol{\chi}) + p_R\boldsymbol{H} - \Delta\theta\left[\frac{\partial\hat{\eta}_R}{\partial\boldsymbol{F}} + \frac{\partial\hat{\eta}_R}{\partial\boldsymbol{H}} \boldsymbol{\times} \boldsymbol{F} + \left(\frac{\partial\hat{\eta}_R}{\partial J} + \frac{d\eta_{R,\mathrm{vol}}}{dJ}\right)\boldsymbol{H}\right], \tag{3.40}$$

where

$$\hat{\boldsymbol{P}}_R = \frac{\partial\hat{W}_R}{\partial\boldsymbol{F}} + \frac{\partial\hat{W}_R}{\partial\boldsymbol{H}} \boldsymbol{\times} \boldsymbol{F} + \frac{\partial\hat{W}_R}{\partial J}\boldsymbol{H}; \qquad p_R = \frac{dU_R(J)}{dJ}. \tag{3.41}$$

Moreover, re-arranging equation Eq. (3.34a) and combining Eq. (3.35) defined at reference temperature yields an alternative expression for $\theta$ using Eq. (2.41) to give

$$\theta = \theta_R + \frac{1}{c_v}\left[E - \frac{\rho_R}{2}(\boldsymbol{v}\cdot\boldsymbol{v}) - \mathcal{E}_R(\boldsymbol{\chi})\right]; \qquad \mathcal{E}_R(\boldsymbol{\chi}) = W_R(\boldsymbol{\chi}) + \theta_R\eta_R(\boldsymbol{\chi}). \tag{3.42}$$

Looking at Eq. (3.40), we need to define the thermo-mechanical coupling term $\eta_R(\boldsymbol{\chi})$ in order to obtain the explicit expression for the first Piola-Kirchhoff stress tensor.

In order to ensure the existence of real wave speeds for all values of $\{\boldsymbol{\chi},\eta\}$, that is regardless of the amount of deformation and thermal state, sufficient conditions for the function $\mathcal{E}(\boldsymbol{\chi},\eta)$[7] Eq. (3.34a) to be convex in $\boldsymbol{\chi}$ and $\eta$ are [191]

(1) $\mathcal{E}_R(\boldsymbol{\chi})$ is convex in $\boldsymbol{\chi}$;
(2) $-\eta_R(\boldsymbol{\chi})$ is convex in $\boldsymbol{\chi}$.

#### 3.3.1.1 Mie-Grüneisen equation of state

A particular case of an elastic material with Mie-Grüneisen Equation Of State (EOS) is considered here where only the volumetric mechanical component is coupled with the thermal effects, that is $\eta_R(\boldsymbol{\chi}) \approx \eta_{R,\mathrm{vol}}(J)$ by assuming $\hat{\eta}_R(\boldsymbol{\chi}) = 0$. This is described as

$$J\frac{\partial p(J,\eta)}{\partial\mathcal{E}} = -\Gamma_0 J^q, \tag{3.43}$$

where $\Gamma_0$ and $q$ are material constant parameters. It is now possible to obtain explicit expression for $\eta_R(J)$ starting from equation Eq. (3.43). This is achieved by combing equations Eq. (3.22) and Eq. (3.34a) such that

$$\frac{\partial p(J,\eta)}{\partial\mathcal{E}} = \frac{1}{\frac{\partial\mathcal{E}}{\partial\eta}}\frac{\partial p}{\partial\eta} = \frac{1}{\theta}\frac{\partial p}{\partial\eta} = -\frac{1}{c_v}\frac{d\eta_R(J)}{dJ} = -\Gamma_0 J^{q-1}, \tag{3.44}$$

[7] This is an extension of the usual polyconvexity condition for non-thermal processes where the internal energy is required to be convex on the extended set of deformation variables $\boldsymbol{\chi}$ and the entropy density $\eta$.

from which $\eta_R(J)$ can be integrated to give[8]

$$-\eta_R(J) = \frac{c_v \Gamma_0}{q}\left(1 - J^q\right). \tag{3.45}$$

Differentiating Eq. (3.44) with respect to $J$ implies the convexity of $-\eta_R(J)$ such that

$$-\frac{d^2\eta_R(J)}{dJ^2} = (1-q)c_v\Gamma_0 J^{q-2} \geq 0 \qquad \forall\, 0 \leq q \leq 1. \tag{3.46}$$

This ensures the satisfaction of Condition 2, presented in the previous section, one of the two conditions that must be fulfilled for a convex thermo-mechanical model.

Moreover, in order to complete the constitutive model, it is now necessary to ensure that $\tilde{\mathcal{E}}_R(\boldsymbol{\chi})$ is also convex (refer to Condition 1). Due to the nature of a Mie-Grüneisen model, $\tilde{\mathcal{E}}_R(\boldsymbol{\chi})$ is additively decomposed into the summation of a deviatoric contribution and a volumetric contribution, namely $\mathcal{E}_R(\boldsymbol{\chi}) = \hat{\mathcal{E}}_R(\boldsymbol{\chi}) + \mathcal{E}_{R,vol}(J)$. For this reason, it would be tempting to choose a function $\mathcal{E}_R(\boldsymbol{\chi})$ similar to those of $W_R$.

However, this would lead to a non-vanishing state of stress for $\boldsymbol{F} = \boldsymbol{H} = \boldsymbol{I}, J = 1, \eta = 0$, which is contrary to the definition of a stress-free reference configuration. In order to resolve this problem, it is important that $\mathcal{E}_R(\boldsymbol{\chi})$ satisfies appropriate initial conditions at $\boldsymbol{\chi}_I = \{\boldsymbol{F} = \boldsymbol{I}, \boldsymbol{H} = \boldsymbol{I}, J = 1\}$. In particular, the first Piola Kirchhoff stress tensor at reference state vanishes, and therefore differentiating equation Eq. (3.34a) gives

$$\left.\frac{\partial \hat{\mathcal{E}}_R}{\partial \boldsymbol{F}}\right|_{\boldsymbol{\chi}_I} + \left.\frac{\partial \hat{\mathcal{E}}_R}{\partial \boldsymbol{H}}\right|_{\boldsymbol{\chi}_I} \boldsymbol{\times}\, \boldsymbol{I} + \left.\frac{\partial \hat{\mathcal{E}}_R}{\partial J}\right|_{\boldsymbol{\chi}_I} \boldsymbol{I} = \boldsymbol{0}; \qquad \left.\frac{d\mathcal{E}_{R,vol}}{dJ}\right|_{J=1} = \theta_R \left.\frac{d\eta_R}{dJ}\right|_{J=1} = c_v\Gamma_0\theta_R. \tag{3.47}$$

The simplest convex function for $\hat{\mathcal{E}}_R(\boldsymbol{\chi})$ and $\mathcal{E}_{R,vol}(J)$ that satisfies the above conditions Eq. (3.47) are

$$\hat{\mathcal{E}}_R(\boldsymbol{\chi}) = \zeta J^{-2/3} I_1 + \xi J^{-2} I_2^{3/2} - 3\left(\zeta + \sqrt{3}\xi\right) \tag{3.48}$$

and

$$\mathcal{E}_{R,vol}(J) = \frac{\kappa}{2}(J-1)^2 + c_v\Gamma_0\theta_R(J-1), \tag{3.49}$$

respectively. By making use of equations Eq. (3.48), Eq. (3.49), Eq. (3.45) and Eq. (3.34a), the first Piola Kirchhoff stress tensor becomes

$$\boldsymbol{P}\left(\boldsymbol{\chi}, \theta(\boldsymbol{\chi}, \eta)\right) = \hat{\boldsymbol{P}}(\boldsymbol{\chi}) + p\boldsymbol{H}. \tag{3.50}$$

Here,

$$\hat{\boldsymbol{P}}(\boldsymbol{\chi}) := \boldsymbol{\Sigma}_{\boldsymbol{F}} + \boldsymbol{\Sigma}_{\boldsymbol{H}} \boldsymbol{\times} \boldsymbol{F} + \hat{\Sigma}_J \boldsymbol{H}; \qquad p = p_R + c_v\Gamma_0\left(\theta_R - \theta J^{q-1}\right), \tag{3.51}$$

where $\boldsymbol{\Sigma}_{\boldsymbol{F}}$, $\boldsymbol{\Sigma}_{\boldsymbol{H}}$, $\Sigma_J$ and $p_R$ are already presented in Eq. (3.11). It is worth pointing out that the material parameters $\{\zeta, \xi, \kappa\}$ used above in general are not the same as those defined in Section 3.2). However, in this Mie-Grüneisen model, the deviatoric mechanical response is

[8] For the limiting case of $q = 0$, expression Eq. (3.45) becomes $-\eta_R(J) = -c_v\Gamma_0 \ln J$.

completely decoupled from thermal effects, which implies that $\zeta$ and $\xi$ remains the same as those presented in Section 3.2.

Finally, it is interesting to find the relationship between $\kappa$ as in equation Eq. (3.51) and the traditional $\kappa_R$ defined as

$$\kappa_R = \left.\frac{d^2U_R}{dJ^2}\right|_{J=1}, \tag{3.52}$$

that is the initial bulk modulus at constant temperature (i.e. the bulk modulus defined in the mechanical models). To achieve this, particularising Eq. (3.42)b to the volumetric component of the Helmholtz free energy potential gives

$$U_R(J) = \mathcal{E}_{R,vol}(J) - \theta_R \eta_R(J). \tag{3.53}$$

Simple double differentiation of Eq. (3.53) gives at $J = 1$ the following bulk moduli relationship

$$\kappa_R = \kappa + c_v \theta_R \Gamma_0 (1 - q). \tag{3.54}$$

Notice that for the particular case of $q = 1$, then $\kappa = \kappa_R$.

---

*Remark* 5: It is worth to mention that in the case of gas dynamics where $q = 0$, only the volumetric part of the stress will be taken into account and, therefore, the first Piola will simply reduces to

$$\boldsymbol{P} = p\boldsymbol{H}; \qquad p = -\frac{\Gamma_0 \mathcal{E}}{J}. \tag{3.55}$$

In the particular case of an ideal gas using Mie-Grüneisen EOS, and following Eq. (3.45), pressure yields

$$p(J,\theta) = -\Delta\theta \frac{d\eta_{R,\mathrm{vol}}}{dJ} = -c_v \Gamma_0 J^{-1} \Delta\theta. \tag{3.56}$$

---

#### 3.3.1.2 Modified entropic elasticity

Another type of thermo-mechanical model is the so-called modified entropic elasticity model in which the internal energy at the reference temperature, that is $\mathcal{E}_R(\boldsymbol{\chi})$, is assumed to be a function of the volume ratio such that

$$\mathcal{E}_R(\boldsymbol{\chi}) \approx \mathcal{E}_{R,\mathrm{vol}}(J). \tag{3.57}$$

Specifically, and following the work of Chadwick and Creasy [79], an empirical expression for the volumetric energy functional $\mathcal{E}_{R,\mathrm{vol}}(J)$ is

$$\mathcal{E}_{R,\mathrm{vol}}(J) = 3\theta_R \alpha \kappa G(J); \qquad G(J) = \gamma^{-1}(J^\gamma - 1), \tag{3.58}$$

where $\gamma > 0$ is a positive non-dimensional parameter and $\alpha$ represents the so-called linear thermal expansion coefficient defined at the reference temperature. In this thesis, the value of $\gamma = 1$ identical to that of presented in [79] by Ogden is used, which implies that

$$\mathcal{E}_{R,\text{vol}}(J) = 3\theta_R \alpha \kappa (J-1). \tag{3.59}$$

In this case, by using equation Eq. (3.35), both the deviatoric and volumetric components of Helmholtz's free energy at the reference temperature are

$$\hat{W}_R(\boldsymbol{\chi}) = -\theta_R \hat{\eta}_R(\boldsymbol{\chi}); \qquad U_R(J) = \mathcal{E}_{R,\text{vol}}(J) - \theta_R \eta_{R,\text{vol}}(J), \tag{3.60}$$

respectively. Re-arrangement of the above expressions for $\hat{\eta}_R$ and $\eta_{R,\text{vol}}$ yields

$$\hat{\eta}_R(\boldsymbol{\chi}) = -\frac{1}{\theta_R}\hat{W}_R(\boldsymbol{\chi}); \qquad \eta_{R,\text{vol}}(J) = \frac{1}{\theta_R}\left[\mathcal{E}_{R,\text{vol}}(J) - U_R(J)\right]. \tag{3.61}$$

Taking derivative of Eq. (3.61) with respect to $\boldsymbol{\chi}$, and, then, substituting into equation Eq. (3.40) for $\boldsymbol{P}$ yields

$$\boldsymbol{P}(\boldsymbol{\chi},\theta) = \frac{\theta}{\theta_R}\hat{\boldsymbol{P}}_R + p\boldsymbol{H}; \qquad p = \frac{\theta}{\theta_R}p_R - \frac{\Delta\theta}{\theta_R}\frac{d\mathcal{E}_{R,\text{vol}}}{dJ} = p_R - \Delta\theta\frac{d\eta_{R,\text{vol}}}{dJ}. \tag{3.62}$$

available for total energy-based formulations. The first Piola relation for the case of entropy-based system of equations can be simply obtained by replacing temperature as a function of entropy (3.28). In addition, the temperature described in Eq. (3.42) reduces to

$$\theta = \theta_R + \frac{1}{c_v}\left[E - \frac{\rho_R}{2}(\boldsymbol{v}\cdot\boldsymbol{v}) - U_R(J) - \theta_R\eta_{R,\text{vol}}(J)\right]. \tag{3.63}$$

---

*Remark* 6: In strict entropic elasticity [81], the internal energy is entirely associated with the generation of heat in the material. This can be mathematically described as $\hat{\mathcal{E}}_R(\boldsymbol{\chi}) = \mathcal{E}_{R,\text{vol}} = 0$, which implies that

$$\boldsymbol{P}(\boldsymbol{\chi},\theta) = \frac{\theta}{\theta_R}\boldsymbol{P}_R(\boldsymbol{\chi}); \qquad \boldsymbol{P}_R(\boldsymbol{\chi}) = \hat{\boldsymbol{P}}_R(\boldsymbol{\chi}) + p_R\boldsymbol{H}, \tag{3.64}$$

and

$$\theta = \theta_R + \frac{1}{c_v}\left[E - \frac{\rho_R}{2}(\boldsymbol{v}\cdot\boldsymbol{v})\right]. \tag{3.65}$$

---

### 3.3.2 Linearised thermo-elasticity

In this thesis, for mesh convergence study purposes on the numerical schemes, defined in Chapters 4 and 5, the linearised thermo-elastic material model is derived. This can also be useful in the case of problems introducing infinitesimal strains. In order to linearise the general

nonlinear Helmholtz's free energy Eq. (3.37), directional derivative about a reference state defined by $\{\boldsymbol{\chi}, \theta\} = \{\boldsymbol{I}, 1, \theta_R\}$ is carried out as follows

$$\begin{aligned} W(\boldsymbol{\chi}, \theta) &\simeq W^{lin}(\Delta\boldsymbol{\chi}, \Delta\theta) \\ &= \underbrace{W(\boldsymbol{I}, 1, \theta_R)}_{0} + DW(\boldsymbol{I}, 1, \theta_R)\left[\Delta\boldsymbol{\chi}, \Delta\theta\right] + \frac{1}{2} D^2 W(\boldsymbol{I}, 1, \theta_R) \begin{bmatrix} \Delta\boldsymbol{\chi}, \Delta\theta \\ \Delta\boldsymbol{\chi}, \Delta\theta \end{bmatrix}, \end{aligned} \tag{3.66}$$

Evaluating the derivatives appeared in Eq. (3.66), allows us to obtain the linearised Helmholtz's free energy as follows

$$W^{lin}(\Delta\boldsymbol{\chi}, \Delta\theta) = \frac{\lambda}{2} (\boldsymbol{\varepsilon} : \boldsymbol{I})^2 + \mu (\boldsymbol{\varepsilon} : \boldsymbol{\varepsilon}) - \frac{c_v}{2\theta_R} (\Delta\theta)^2 - c_v \Gamma_0 (\boldsymbol{\varepsilon} : \boldsymbol{I}) \Delta\theta, \tag{3.67}$$

where $\boldsymbol{\varepsilon} = \frac{1}{2}\left(\boldsymbol{F} + \boldsymbol{F}^T - 2\boldsymbol{I}\right)$. Therefore, it is now convenient to derive the linear expression for first Piola-Kirchhoff stress tensor by taking derivative of linearised Helmholtz's free energy with respect to their corresponding conjugate variables

$$\boldsymbol{P} = \frac{\partial W^{lin}}{\partial \boldsymbol{\varepsilon}} = (\lambda \boldsymbol{I} \otimes \boldsymbol{I} + 2\mu \boldsymbol{\mathcal{I}}) : \boldsymbol{\varepsilon} - c_v \Gamma_0 (\theta - \theta_R) \boldsymbol{I}, \tag{3.68}$$

where $\boldsymbol{\mathcal{I}}$ is unit fourth order tensor. Alternatively, the first Piola can be re-expressed as a function of the deformation gradient as

$$\boldsymbol{P} = \lambda (\boldsymbol{F} : \boldsymbol{I}) \boldsymbol{I} + \mu \left(\boldsymbol{F} + \boldsymbol{F}^T\right) - c_v \Gamma_0 (\theta - \theta_R) \boldsymbol{I} - (3\lambda + 2\mu) \boldsymbol{I}. \tag{3.69}$$

Recalling Eq. (3.39), the linear expression for entropy can be computed as follows

$$\eta = -\frac{\partial W^{lin}}{\partial \theta} = \frac{c_v}{\theta_R} (\theta - \theta_R) + c_v \Gamma_0 (\boldsymbol{F} : \boldsymbol{I} - 3). \tag{3.70}$$

Having the first Piola and entropy, it is now possible to obtain temperature, according to the chosen coupling procedure.

---

*Remark* 7: It is useful to note that the Mie-Grüneisen constant $\Gamma_0$ can be related to the material properties as [192]

$$\Gamma_0 = \frac{3\kappa\alpha}{c_v}, \tag{3.71}$$

where $\kappa$ stands for the bulk modulus, $\alpha$ is the thermal expansion coefficient and $c_v$ represents the heat capacity of the material.

---

## 3.4 Hyperbolicity

As it is well known, the study of the eigenvalue structure of the (entropy-based) system (2.58) is crucial in order to guarantee its hyperbolicity. In Reference [7], the authors verified the

hyperbolic nature of the problem only for a Mie-Grüneisen equation of state. However, the procedure presented in [7] requires the formation of flux Jacobian matrix $\frac{\partial \boldsymbol{\mathcal{F}}_{\boldsymbol{N}}}{\partial \boldsymbol{\mathcal{U}}}$, whereby the evaluation of this matrix sometimes can be quite challenging. It is interesting to show that the use of tensor cross product allows for simple expressions for the resulting tangent operator which neatly separates material from geometrical dependencies, and, finally, the satisfaction of Legendre-Hadamard condition [193]. The same methodology is then extended to the case of a modified entropic elasticity.

To achieve this, the eigenvalues (or wave speeds) of the entropy-based system (2.58) can be determined by identifying possible plane wave solutions (in the absence of source terms) of the type [3]

$$\boldsymbol{\mathcal{U}} = \phi(\boldsymbol{X}\cdot\boldsymbol{N} - c_\alpha t)\boldsymbol{\mathcal{U}}_\alpha = \phi(\boldsymbol{X}\cdot\boldsymbol{N} - c_\alpha t)\begin{bmatrix} \rho_R \boldsymbol{v}_\alpha \\ \boldsymbol{F}_\alpha \\ \boldsymbol{H}_\alpha \\ J_\alpha \\ \eta_\alpha \end{bmatrix}, \tag{3.72}$$

where $\phi$ denotes a scalar real-valued function, $c_\alpha$ is the wave speed corresponding to the eigenmode $\boldsymbol{\mathcal{U}}_\alpha$ and $\boldsymbol{N}$ is the direction of propagation. Substitution of the above expression into Eq. (2.56) leads to a characteristic equation of the system given by

$$\boldsymbol{\mathcal{A}}_{\boldsymbol{N}}\boldsymbol{\mathcal{U}}_\alpha = c_\alpha \boldsymbol{\mathcal{U}}_\alpha; \qquad \boldsymbol{\mathcal{A}}_{\boldsymbol{N}} = \frac{\partial \boldsymbol{\mathcal{F}}_{\boldsymbol{N}}}{\partial \boldsymbol{\mathcal{U}}}. \tag{3.73}$$

However, above eigenvalue problem Eq. (3.73) unfortunately requires the explicit expression for the (convective) flux Jacobian matrix $\boldsymbol{\mathcal{A}}_{\boldsymbol{N}}$. To avoid this, it is important to note that the above equation can be re-written by utilising the definition of the directional derivative to give

$$D\boldsymbol{\mathcal{F}}_{\boldsymbol{N}}[\boldsymbol{\mathcal{U}}_\alpha] = c_\alpha \boldsymbol{\mathcal{U}}_\alpha. \tag{3.74}$$

Considering each individual component of this system (2.58) gives

$$-\begin{bmatrix} D\left(\boldsymbol{P}\boldsymbol{N}\right)\left[\boldsymbol{F}_\alpha, \boldsymbol{H}_\alpha, J_\alpha, \eta_\alpha\right] \\ D\left(\boldsymbol{v}\otimes\boldsymbol{N}\right)\left[\boldsymbol{v}_\alpha\right] \\ D\left(\boldsymbol{F}\times(\boldsymbol{v}\otimes\boldsymbol{N})\right)\left[\boldsymbol{v}_\alpha, \boldsymbol{F}_\alpha\right] \\ D\left(\boldsymbol{H}:(\boldsymbol{v}\otimes\boldsymbol{N})\right)\left[\boldsymbol{v}_\alpha, \boldsymbol{H}_\alpha\right] \\ 0 \end{bmatrix} = c_\alpha \begin{bmatrix} \rho_R \boldsymbol{v}_\alpha \\ \boldsymbol{F}_\alpha \\ \boldsymbol{H}_\alpha \\ J_\alpha \\ \eta_\alpha \end{bmatrix}. \tag{3.75}$$

For the case where $c_\alpha \neq 0$, the geometric equations $\{\boldsymbol{F}_\alpha, \boldsymbol{H}_\alpha, J_\alpha\}$, as well as the entropy equation $\eta_\alpha$, of the system, result in

$$\boldsymbol{F}_\alpha = -\frac{1}{c_\alpha}\boldsymbol{v}_\alpha \otimes \boldsymbol{N}; \tag{3.76a}$$

$$\boldsymbol{H}_\alpha = -\frac{1}{c_\alpha}\left[\boldsymbol{F}_\alpha \boldsymbol{\times} (\boldsymbol{v} \otimes \boldsymbol{N}) + \boldsymbol{F} \boldsymbol{\times} (\boldsymbol{v}_\alpha \otimes \boldsymbol{N})\right]; \tag{3.76b}$$

$$J_\alpha = -\frac{1}{c_\alpha}\left[\boldsymbol{H}_\alpha : (\boldsymbol{v} \otimes \boldsymbol{N}) + \boldsymbol{H} : (\boldsymbol{v}_\alpha \otimes \boldsymbol{N})\right]; \tag{3.76c}$$

$$\eta_\alpha = 0. \tag{3.76d}$$

Substitution Eq. (3.76a) into Eq. (3.76b) yields

$$\boldsymbol{H}_\alpha = -\frac{1}{c_\alpha}\left[\underbrace{(\boldsymbol{v}_\alpha \otimes \boldsymbol{N}) \boldsymbol{\times} (\boldsymbol{v} \otimes \boldsymbol{N})}_{\mathbf{0}} + \boldsymbol{F} \boldsymbol{\times} (\boldsymbol{v}_\alpha \otimes \boldsymbol{N})\right] = -\frac{1}{c_\alpha}\boldsymbol{F} \boldsymbol{\times} (\boldsymbol{v}_\alpha \otimes \boldsymbol{N}). \tag{3.77}$$

It is possible to demonstrate after some algebra that the first term on the right hand side of Eq. (3.76c) is zero, yielding the reduced equation

$$J_\alpha = -\frac{1}{c_\alpha}\boldsymbol{H} : (\boldsymbol{v}_\alpha \otimes \boldsymbol{N}). \tag{3.78}$$

Substitution Eq. (3.76a), Eq. (3.77) and Eq. (3.78) into Eq. (3.75) results in

$$\rho_R c_\alpha^2 \boldsymbol{v}_\alpha = D(\boldsymbol{PN})\left[\boldsymbol{v}_\alpha \otimes \boldsymbol{N}, \boldsymbol{F} \boldsymbol{\times} (\boldsymbol{v}_\alpha \otimes \boldsymbol{N}), \boldsymbol{H} : (\boldsymbol{v}_\alpha \otimes \boldsymbol{N}), 0\right]. \tag{3.79}$$

For convenience, the above expression can also be pre-multiplied by a generic virtual velocity field $\delta\boldsymbol{v}$ to give

$$\rho_R c_\alpha^2 \delta\boldsymbol{v} \cdot \boldsymbol{v}_\alpha = (\delta\boldsymbol{v} \otimes \boldsymbol{N}) : D\boldsymbol{P}\left[\boldsymbol{v}_\alpha \otimes \boldsymbol{N}, \boldsymbol{F} \boldsymbol{\times} (\boldsymbol{v}_\alpha \otimes \boldsymbol{N}), \boldsymbol{H} : (\boldsymbol{v}_\alpha \otimes \boldsymbol{N}), 0\right] \tag{3.80a}$$

$$= (\delta\boldsymbol{v} \otimes \boldsymbol{N}) : D\left(\frac{\partial \mathcal{E}}{\partial \boldsymbol{F}} + \frac{\partial \mathcal{E}}{\partial \boldsymbol{H}} \boldsymbol{\times} \boldsymbol{F} + \frac{\partial \mathcal{E}}{\partial J}\boldsymbol{H}\right)\left[\boldsymbol{v}_\alpha \otimes \boldsymbol{N}, \boldsymbol{F} \boldsymbol{\times} (\boldsymbol{v}_\alpha \otimes \boldsymbol{N}), \boldsymbol{H} : (\boldsymbol{v}_\alpha \otimes \boldsymbol{N}), 0\right] \tag{3.80b}$$

$$= \underbrace{\begin{bmatrix} (\delta\boldsymbol{v} \otimes \boldsymbol{N}) : \\ \boldsymbol{F} \boldsymbol{\times} (\delta\boldsymbol{v} \otimes \boldsymbol{N}) : \\ \boldsymbol{H} : (\delta\boldsymbol{v} \otimes \boldsymbol{N}) \\ 0 \end{bmatrix}^T [\mathbb{H}_e] \begin{bmatrix} : (\boldsymbol{v}_\alpha \otimes \boldsymbol{N}) \\ : \boldsymbol{F} \boldsymbol{\times} (\boldsymbol{v}_\alpha \otimes \boldsymbol{N}) \\ \boldsymbol{H} : (\boldsymbol{v}_\alpha \otimes \boldsymbol{N}) \\ 0 \end{bmatrix}}_{\text{Constitutive term}} \tag{3.80c}$$

$$+ \underbrace{\left(\frac{\partial \mathcal{E}}{\partial \boldsymbol{H}} + \frac{\partial \mathcal{E}}{\partial J}\boldsymbol{F}\right) : \left[(\delta\boldsymbol{v} \otimes \boldsymbol{N}) \boldsymbol{\times} (\boldsymbol{v}_\alpha \otimes \boldsymbol{N})\right]}_{\text{Geometric term becomes 0}}.$$

Taking $\delta\boldsymbol{v} = \boldsymbol{v}_\alpha$ leads to the well-known Legendre-Hadamard condition, but this time written as

$$\rho_R c_\alpha^2 = \begin{bmatrix} (\boldsymbol{v}_\alpha \otimes \boldsymbol{N}) : \\ \boldsymbol{F} \boldsymbol{\times} (\boldsymbol{v}_\alpha \otimes \boldsymbol{N}) : \\ \boldsymbol{H} : (\boldsymbol{v}_\alpha \otimes \boldsymbol{N}) \\ 0 \end{bmatrix}^T [\mathbb{H}_e] \begin{bmatrix} : (\boldsymbol{v}_\alpha \otimes \boldsymbol{N}) \\ : \boldsymbol{F} \boldsymbol{\times} (\boldsymbol{v}_\alpha \otimes \boldsymbol{N}) \\ \boldsymbol{H} : (\boldsymbol{v}_\alpha \otimes \boldsymbol{N}) \\ 0 \end{bmatrix} > 0. \tag{3.81}$$

Notice that the eigenstructure of the system only depends on $[\mathbb{H}_e]$, which contains full information about the physics of the problem.

---

*Remark* 8: With the help of equation (3.80c), it is interesting to show that the fourth order elasticity tensor $\mathbf{C}$ is additively decomposed into a material contribution $\mathbf{C}_m$ (depending upon second derivatives of $e$) and a geometrical contribution $\mathbf{C}_g$, namely, $\mathbf{C} = \mathbf{C}_m + \mathbf{C}_g$, with

$$\begin{aligned} \mathbf{C}_m &= \mathcal{E}_{\boldsymbol{FF}} + \boldsymbol{F} \boldsymbol{\times} \mathcal{E}_{\boldsymbol{HH}} \boldsymbol{\times} \boldsymbol{F} + \mathcal{E}_{JJ} \boldsymbol{H} \otimes \boldsymbol{H} + \mathcal{E}_{\boldsymbol{FH}} \boldsymbol{\times} \boldsymbol{F} + \boldsymbol{F} \boldsymbol{\times} \mathcal{E}_{\boldsymbol{HF}} + \mathcal{E}_{\boldsymbol{F}J} \otimes \boldsymbol{H} \\ &\quad + \boldsymbol{H} \otimes \mathcal{E}_{J\boldsymbol{F}} + \boldsymbol{F} \boldsymbol{\times} \mathcal{E}_{\boldsymbol{H}J} \otimes \boldsymbol{H} + \boldsymbol{H} \otimes \mathcal{E}_{J\boldsymbol{H}} \boldsymbol{\times} \boldsymbol{F}; \\ \mathbf{C}_g &= \boldsymbol{\mathcal{I}} \boldsymbol{\times} \left( \frac{\partial \mathcal{E}}{\partial \boldsymbol{H}} + \frac{\partial \mathcal{E}}{\partial J} \boldsymbol{F} \right), \end{aligned} \tag{3.82a}$$

where $[\boldsymbol{\mathcal{I}}]_{iIjJ} = \delta_{ij}\delta_{IJ}$. Utilising the Legendre-Hadamard condition expressed in Eq. (3.81) can be alternatively represented as

$$\rho_R c_\alpha^2 = (\boldsymbol{v}_\alpha \otimes \boldsymbol{N}) : \mathbf{C} : (\boldsymbol{v}_\alpha \otimes \boldsymbol{N}) = (\boldsymbol{v}_\alpha \otimes \boldsymbol{N}) : \mathbf{C}_m : (\boldsymbol{v}_\alpha \otimes \boldsymbol{N}) = \boldsymbol{v}_\alpha \cdot (\mathbf{C}_{\boldsymbol{NN}} \boldsymbol{v}_\alpha), \tag{3.83}$$

where the acoustic tensor $\mathbf{C}_{\boldsymbol{NN}}$ being defined as

$$[\mathbf{C}_{\boldsymbol{NN}}]_{ij} = [\mathbf{C}_m]_{iIjJ} N_I N_J. \tag{3.84}$$

Instead of deriving a close form solution for the expression above Eq. (3.83), it is sufficient to obtain bounds of the wave speeds by assuming $\boldsymbol{N}$ is a principal direction. In this particular case, the first two eigenvalues correspond to pressure waves are obtained by taking $\boldsymbol{v}_\alpha = \boldsymbol{n}$, where $\boldsymbol{n}$ is a unit vector orthogonal to the vectors $\boldsymbol{F}\boldsymbol{T}_{1,2} = \boldsymbol{t}_{1,2}$ lie on the propagation surface. Similarly, the next four eigenvalues correspond to shear waves by taking $\boldsymbol{v}_\alpha = \boldsymbol{t}_{1,2}$.

---

In order to obtain the Hessian $[\mathbb{H}_e]$ for both models presented in this work, we can use the entropy as the thermal variable to allow the convex entropy function of the hyperbolic set of equations to be chosen as the convex energy function $S$ [191]

$$S(\boldsymbol{\chi}, \eta) = \frac{\rho_R}{2} \boldsymbol{v} \cdot \boldsymbol{v} + \mathcal{E}(\boldsymbol{\chi}, \eta) - \theta_R \eta, \tag{3.85}$$

which gives conjugate entropy variables as

$$\boldsymbol{\mathcal{V}} = \frac{\partial S}{\partial \boldsymbol{\mathcal{U}}} = \begin{bmatrix} \frac{\partial S}{\partial (\rho_R \boldsymbol{v})} \\ \frac{\partial S}{\partial \boldsymbol{F}} \\ \frac{\partial S}{\partial \boldsymbol{H}} \\ \frac{\partial S}{\partial J} \\ \frac{\partial S}{\partial \eta} \end{bmatrix} = \begin{bmatrix} \boldsymbol{v} \\ \boldsymbol{\Sigma_F} \\ \boldsymbol{\Sigma_H} \\ \Sigma_J \\ \Delta\theta \end{bmatrix}. \tag{3.86}$$

The Hessian operator $[\mathbb{H}_S]$ associated with the convex entropy function $S$ is obtained as

$$[\mathbb{H}_S] = \frac{\partial \boldsymbol{\mathcal{V}}}{\partial \boldsymbol{\mathcal{U}}} = \frac{\partial S}{\partial \boldsymbol{\mathcal{U}} \partial \boldsymbol{\mathcal{U}}} = \left[\begin{array}{c|c} \frac{1}{\rho_R}\boldsymbol{I} & \boldsymbol{0} \\ \hline \boldsymbol{0} & [\mathbb{H}_{\mathcal{E}}] \end{array}\right] = \left[\begin{array}{c|cccc} \frac{1}{\rho_R}\boldsymbol{I} & \multicolumn{4}{c}{\boldsymbol{0}} \\ \hline \boldsymbol{0} & \frac{\partial^2 \mathcal{E}}{\partial \boldsymbol{F} \partial \boldsymbol{F}} & \frac{\partial^2 \mathcal{E}}{\partial \boldsymbol{F} \partial \boldsymbol{H}} & \frac{\partial^2 \mathcal{E}}{\partial \boldsymbol{F} \partial J} & \frac{\partial^2 \mathcal{E}}{\partial \boldsymbol{F} \partial \eta} \\ & \frac{\partial^2 \mathcal{E}}{\partial \boldsymbol{H} \partial \boldsymbol{F}} & \frac{\partial^2 \mathcal{E}}{\partial \boldsymbol{H} \partial \boldsymbol{H}} & \frac{\partial^2 \mathcal{E}}{\partial \boldsymbol{H} \partial J} & \frac{\partial^2 \mathcal{E}}{\partial \boldsymbol{H} \partial \eta} \\ & \frac{\partial^2 \mathcal{E}}{\partial J \partial \boldsymbol{F}} & \frac{\partial^2 \mathcal{E}}{\partial J \partial \boldsymbol{H}} & \frac{\partial^2 \mathcal{E}}{\partial J \partial J} & \frac{\partial^2 \mathcal{E}}{\partial J \partial \eta} \\ & \frac{\partial^2 \mathcal{E}}{\partial \eta \partial \boldsymbol{F}} & \frac{\partial^2 \mathcal{E}}{\partial \eta \partial \boldsymbol{H}} & \frac{\partial^2 \mathcal{E}}{\partial \eta \partial J} & \frac{\partial^2 \mathcal{E}}{\partial \eta \partial \eta} \end{array}\right]. \tag{3.87}$$

### Mie Grüneisen model

The Hessian operator $[\mathbb{H}_{\mathcal{E}}]$ for the Mie Grüneisen model reads as follows [191]

$$[\mathbb{H}_{\mathcal{E}}] = \begin{bmatrix} \mathcal{E}_{\boldsymbol{FF}} & \boldsymbol{0} & \mathcal{E}_{\boldsymbol{F}J} & \boldsymbol{0} \\ \boldsymbol{0} & \mathcal{E}_{\boldsymbol{HH}} & \mathcal{E}_{\boldsymbol{H}J} & \boldsymbol{0} \\ \mathcal{E}_{J\boldsymbol{F}} & \mathcal{E}_{J\boldsymbol{H}} & \mathcal{E}_{JJ} & \mathcal{E}_{J\eta} \\ \boldsymbol{0} & \boldsymbol{0} & \mathcal{E}_{\eta J} & \mathcal{E}_{\eta\eta} \end{bmatrix}, \tag{3.88}$$

where the components are

$$\mathcal{E}_{J,\eta} = \mathcal{E}_{\eta J} = -\Gamma_0 J^{q-1}\theta; \qquad \mathcal{E}_{\eta\eta} = \frac{\theta}{c_v}; \qquad \mathcal{E}_{JJ} = \gamma_R + \kappa + \mathcal{E}_{JJ}^{\Delta T} + \theta c_v \Gamma_0 J^{q-2}\left[\Gamma_0 J^q + (1-q)\right], \tag{3.89}$$

and $\mathcal{E}_{\boldsymbol{FF}} = W_{\boldsymbol{FF}}$, $\mathcal{E}_{\boldsymbol{HH}} = W_{\boldsymbol{HH}}$, $\mathcal{E}_{\boldsymbol{F}J} = \mathcal{E}_{J\boldsymbol{F}} = W_{J\boldsymbol{F}}$ and $\mathcal{E}_{\boldsymbol{H}J} = \mathcal{E}_{J\boldsymbol{H}} = W_{J\boldsymbol{H}}$. These components are defined as [191]

$$W_{\boldsymbol{FF}} = 2\zeta_R J^{-2/3}\boldsymbol{\mathcal{I}}; \quad W_{\boldsymbol{HH}} = 3\xi_R J^{-2} II_{\boldsymbol{H}}^{1/2}\left[II_{\boldsymbol{H}}^{-1}\boldsymbol{H}\otimes\boldsymbol{H} + \boldsymbol{\mathcal{I}}\right]; \quad W_{JJ} = \gamma_R + \kappa, \tag{3.90a}$$

$$W_{\boldsymbol{F}J} = W_{J\boldsymbol{F}} = -\frac{4\zeta_R}{3}J^{-5/3}\boldsymbol{F}; \qquad W_{\boldsymbol{H}J} = W_{J\boldsymbol{H}} = -6\xi_R J^{-3} II_{\boldsymbol{H}}^{1/2}\boldsymbol{H}, \tag{3.90b}$$

with

$$\gamma_R = \frac{10\zeta_R}{9}J^{-8/3}II_{\boldsymbol{F}} + 6\xi_R J^{-4} II_{\boldsymbol{H}}^{3/2}. \tag{3.91}$$

### Modified entropic elasticity

In the case of modified entropic elasticity, the Hessian operator $[\mathbb{H}_S]$ yields [191]

$$[\mathbb{H}_{\mathcal{E}}] = \begin{bmatrix} \mathcal{E}_{\boldsymbol{FF}} & \mathcal{E}_{\boldsymbol{FH}} & \mathcal{E}_{\boldsymbol{F}J} & \mathcal{E}_{\boldsymbol{F}\eta} \\ \mathcal{E}_{\boldsymbol{HF}} & \mathcal{E}_{\boldsymbol{HH}} & \mathcal{E}_{\boldsymbol{H}J} & \mathcal{E}_{\boldsymbol{H}\eta} \\ \mathcal{E}_{J\boldsymbol{F}} & \mathcal{E}_{J\boldsymbol{H}} & \mathcal{E}_{JJ} & \mathcal{E}_{J\eta} \\ \mathcal{E}_{\eta\boldsymbol{F}} & \mathcal{E}_{\eta\boldsymbol{H}} & \mathcal{E}_{\eta J} & \mathcal{E}_{\eta\eta} \end{bmatrix}, \tag{3.92}$$

where

$$\mathcal{E}_{\boldsymbol{FF}} = \frac{\theta}{\theta_R}\left[2\alpha_{\boldsymbol{\mathcal{I}}} + \frac{4\alpha_R^2}{c_v\theta_R}\boldsymbol{F}\otimes\boldsymbol{F}\right]; \quad \mathcal{E}_{\boldsymbol{HH}} = \frac{\theta}{\theta_R}\left[2\beta_R\boldsymbol{\mathcal{I}} + \frac{4\beta_R^2}{c_v\theta_R}\boldsymbol{H}\otimes\boldsymbol{H}\right]; \tag{3.93a}$$

$$\mathcal{E}_{JJ} = \frac{\theta}{\theta_R}\left[f'' + \frac{1}{c_v\theta_R}(f' - \hat{\kappa}_R)^2\right]; \quad \mathcal{E}_{\boldsymbol{FH}} = \frac{\theta}{\theta_R}\frac{4\alpha\beta_R}{c_v\theta_R}\boldsymbol{F}\otimes\boldsymbol{H}; \quad \mathcal{E}_{\boldsymbol{HF}} = \frac{\theta}{\theta_R}\frac{4\alpha\beta_R}{c_v\theta_R}\boldsymbol{H}\otimes\boldsymbol{F}; \tag{3.93b}$$

$$\mathcal{E}_{\boldsymbol{F}J} = \mathcal{E}_{J\boldsymbol{F}} = \frac{\theta}{\theta_R}\frac{2\alpha}{c_v\theta_R}\left(f' - \hat{\kappa}_R\right)\boldsymbol{F}; \quad \mathcal{E}_{\boldsymbol{H}J} = \mathcal{E}_{J\boldsymbol{H}} = \frac{\theta}{\theta_R}\frac{2\beta_R}{c_v\theta_R}\left(f' - \hat{\kappa}_R\right)\boldsymbol{H}; \tag{3.93c}$$

$$\mathcal{E}_{\boldsymbol{F}\eta} = \mathcal{E}_{\eta\boldsymbol{F}} = \frac{\theta}{c_v\theta_R}2\alpha\boldsymbol{F}; \quad \mathcal{E}_{\boldsymbol{H}\eta} = \mathcal{E}_{\eta\boldsymbol{H}} = \frac{\theta}{c_v\theta_R}2\beta_R\boldsymbol{H}; \quad \mathcal{E}_{J\eta} = \mathcal{E}_{\eta J} = \frac{\theta}{c_v\theta_R}\left(f' - \hat{\kappa}_R\right); \tag{3.93d}$$

$$\mathcal{E}_{\eta\eta} = \frac{\theta}{c_v}. \tag{3.93e}$$

The positive definite Hessian operators, obtained for both models, can ensure the existence of real wave speeds (and, hence,material stability) for all values of $\{\boldsymbol{\chi}, \eta\}$, that is regardless of the amount of deformation and thermal state[9].

## 3.5 Conclusion

In this chapter, a set of constitutive models have been presented aimed at describing the non-linear material behaviour in the context of large strain fast solid dynamics. To close the system of equations introduced in Chapter 2, purely mechanical and thermo-mechanical constitutive models have been presented by which the principle of objectivity and thermodynamical consistency are satisfied. To this end, the hyperbolicity of the presented first-order conservation laws is proved for the particular case of the employed constitutive models.

[9] This is an extension of the usual polyconvexity condition for non-thermal processes where the energy is required to be convex on the extended set of deformation variables $\boldsymbol{\chi}$ and and the entropy density $\eta$.

# Part III

# Numerical Methodology

Chapter 4

# Spatial discretisation: Finite Volume Method

## 4.1 Introduction

Thus far, the conservation laws governing the motion of a continuum are presented in chapter 2 and for the closure of the system of equations, appropriate constitutive models (discussed in chapter 3), initial and boundary conditions are provided. In the following chapter, the governing equations are spatially discretised using a Vertex-Centred Finite Volume Method (VCFVM). The nature of the numerical scheme is discussed in Section 4.2 and, therefore, the discretised formulations are presented in Section 4.3. The contact flux approximations are then introduced in Section 4.3.2, through the application of an acoustic Riemann solver. To this end, the local entropy production of the VCFVM scheme is examined in Section 4.4. The schematic representation of the layout of this chapter is depicted in Figure 4.1.

## 4.2 Finite Volume Method

The main idea for the Finite Volume Method (FVM) is initially introduced by the fundamental works of Godunov [194] and Preissmann [195] in the 1960s. The method is then officially introduced by McDonald [196], and MacCormack and Paullay [197] into the field of Computational Fluid Dynamics (CFD) and later extended to three-dimensional cases in [198]. They used the method to approximate the hyperbolic conservation laws corresponding to the Euler equations of gas dynamics. Nowadays, FVM is not only the most widely spread numerical methodology implemented in (open-source, commercial and industrial) CFD solvers, but it has also attracted a great interest of solid mechanics community [71, 199].

Basically, FVM splits a physical domain into a number of sub-domains known as control volumes/cells (visualised in Figure 4.2) in which the value of a conservative quantity is stored at the centre of the control volume. This is also known as cell averaged quantity $\boldsymbol{\mathcal{U}}_i$ meaning the

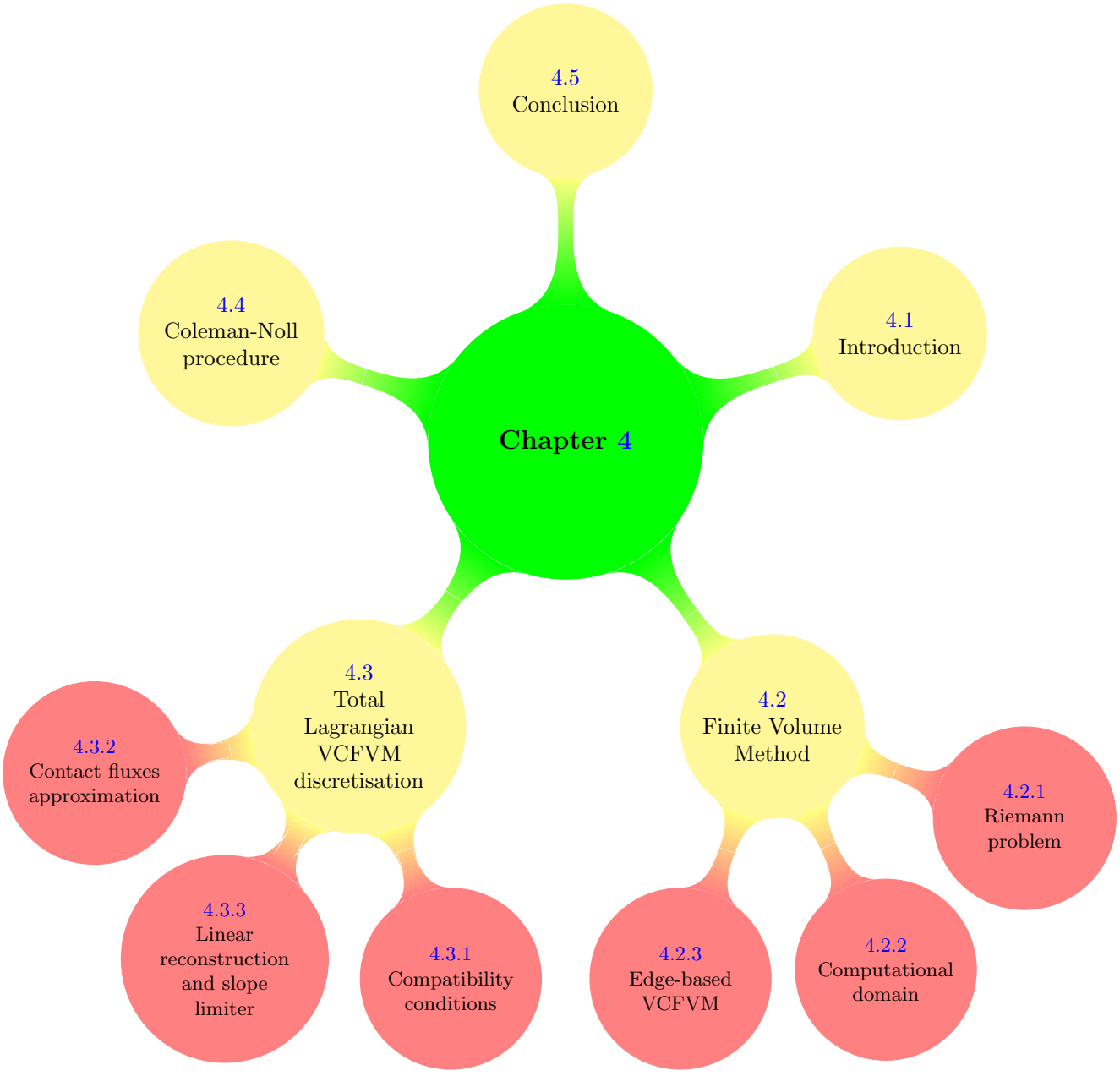


FIGURE 4.1: Structure of Chapter 4

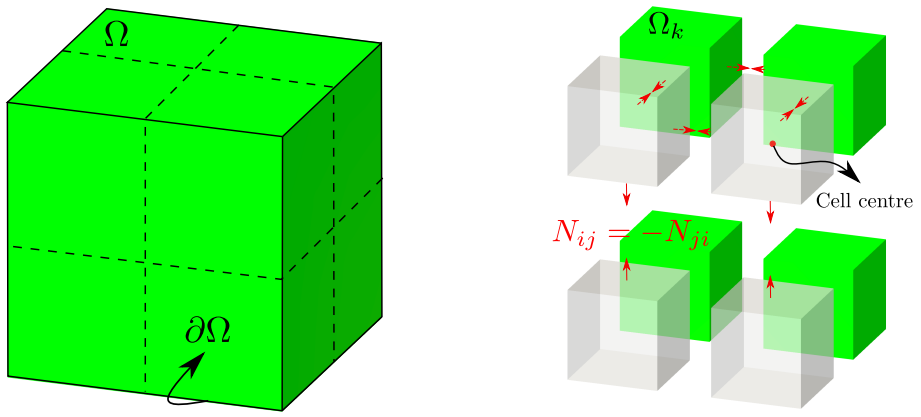


(a) Continuum (b) Sub-domains $\Omega_k(\Omega_1 \cup ... \cup \Omega_8 = \Omega)$

FIGURE 4.2: A physical domain divided into control volumes

total integral of the conserved quantity over each cell, expressed as

$$\boldsymbol{\mathcal{U}}_i = \frac{1}{\Omega_R^i} \int_{\Omega_R^i} \boldsymbol{\mathcal{U}} \, d\Omega_R. \tag{4.1}$$

Recalling the general form of a conservation law Eq. (2.55), the cell averages will then advance in time based upon the update of the flux vectors $\boldsymbol{\mathcal{F}}_N$ through the boundary of the control volume

$$\frac{d\boldsymbol{\mathcal{U}}_i}{dt} = -\frac{1}{\Omega_R^i} \int_{\partial\Omega_R^i} \boldsymbol{\mathcal{F}}_N \, dA. \tag{4.2}$$

Evaluating those flux vectors through an appropriate approximation has always been considered as a significant numerical challenge in the context of finite volume methodology. The derivation of numerical flux vectors corresponding to the current study is discussed in Section 4.3.2.

### 4.2.1 Riemann problem

A (Godunov-type) finite volume methodology can genuinely introduce a Riemann problem which is defined by a conservation equation together with piecewise constant initial data, introducing a single discontinuity into the domain of interest. Naturally, discontinuity of the conservation variables across control volume interfaces leads to a Riemann problem, whose approximated solution can be derived by means of a Riemann solution [11]. Figure 4.3 illustrates the discontinuous solution at the interface of each control volume for a one-dimensional problem. In addition, it must be noted that the flux entering into a control volume is identical to that leaving the adjacent control volume and that is known as the conservation property of the finite volume method. This property is of paramount importance when dealing with solution discontinuities and shock dominated scenarios [200].

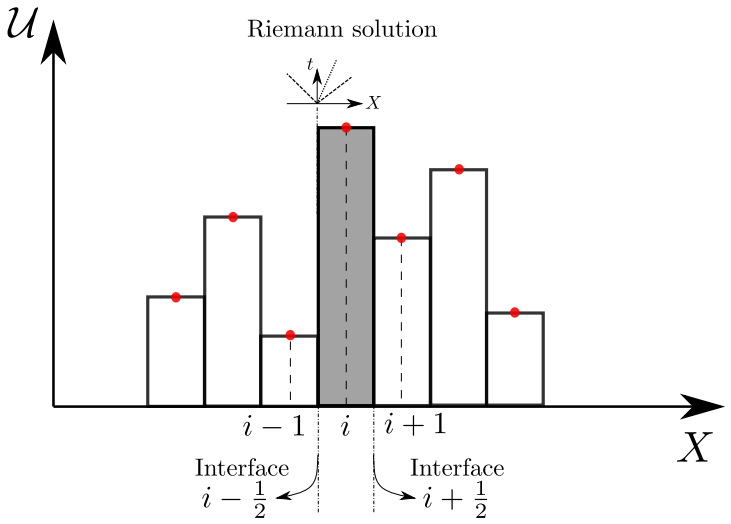


FIGURE 4.3: One-dimensional Godunov type Finite Volume Method: Riemann problem at the interfaces

### 4.2.2 Computational domain

The computational domain in the finite volume method is tessellated into a set of non-overlapping control volumes that entirely cover the domain. The two very well-known control volume tessellations are Cell-Centred Finite Volume Method (CCFVM) and Vertex-Centred Finite Volume Method (VCFVM), among several variations of the original FVM (e.g. staggered, periodic heterogeneous microstructural, matrix-free, meshless). In the case of the CCFVM, the control volumes are identical to the computational mesh with the conservative quantities stored at their centres; whereas the VCFVM stores the conservative quantities at the computational mesh vertices and the control volumes are constructed by median dual approach. This approach connects edge midpoints with element centroids in two dimensions and edge midpoints with face centroids and element centroids in three dimensions [118, 199] and that ensures non-overlapping control volumes. These constructed cells (based on the computational grid) at the VCFVM is also known as dual control volumes. Figure 4.4 illustrates the computational stencil for the CCFVM and the VCFVM schemes such that a representative prism with four tetrahedral elements is selected through which a cell-centred control volume (or a tetrahedral element) and a vertex-centred dual control volume are depicted. For intuitive purposes, the two-dimensional stencil for CCFVM and VCFVM is also shown where it is evident how the number of control volumes in the VCFVM stencil, in particular case of triangular elements, is less than the case of the CCFVM. However each control volume in CCFVM has more edges than in CCFVM. Roughly speaking, there is a transfer of the location of the computational cost between CCFVM and VCFVM which is still a matter of debate between both communities.It must be also noted that the FVM is well-suited to structured and unstructured meshes and this feature makes the method quite suitable for representing complex geometries [8, 113, 118].

In this thesis, Vertex-Centred Finite Volume Method is considered as one of the employed spatial discretisation methods and will be explored in the following sections.

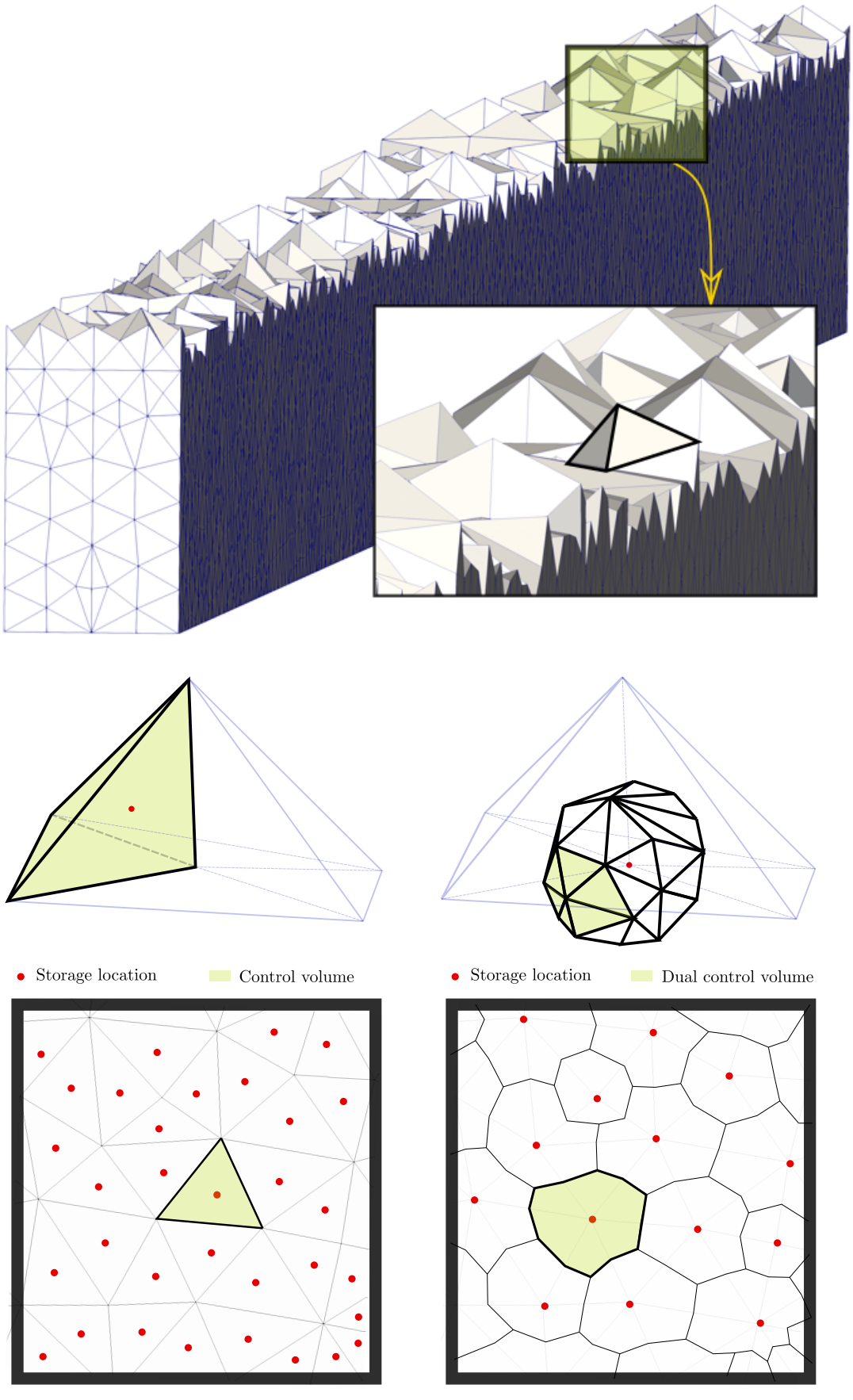


(a) CCFVM (b) VCFVM

FIGURE 4.4: The schematic definition of control volume in two and three dimensions for (a) Cell-Centred Finite Volume Method (CCFVM) and (b) Vertex-Centred Finite Volume Method (VCFVM)

### 4.2.3 Edge-based VCFVM

As it is mentioned earlier, the cell averaged value within a control volume will be updated by the flux vectors ($\boldsymbol{\mathcal{F}}_{\boldsymbol{N}}$) passing through the surface of the control volume (known as control surface). The direction of those flux vectors will be defined by area vectors associated with each control surface (facet). Using VCFVM, one classical approach is to loop over all the facets associated with a dual control volume in order to compute the area vector as

$$\boldsymbol{\mathcal{C}}_a = \sum_{k \in \Gamma_a} A_k \boldsymbol{N}_k, \tag{4.3}$$

where $\Gamma_a$ is the set of facets associated with the dual control volume $a$, $A_k$ is the area of a given facet $k$ and $\boldsymbol{N}_k$ denotes its outward unit normal vector (see Figure 4.5a). In this case, the integral form of a conservation law Eq. (2.55) over an undeformed control volume $\Omega_R^a$ can be discretised as follows

$$\Omega_R^a \frac{d\boldsymbol{\mathcal{U}}_a}{dt} = -\left( \sum_{b \in \Lambda_a} \sum_{k \in \Gamma_{ab}} \boldsymbol{\mathcal{F}}^C_{\boldsymbol{N}_k} A_k + \sum_{\gamma \in \Lambda_a^B} \boldsymbol{\mathcal{F}}_a^{\gamma} \boldsymbol{\mathcal{C}}^{\gamma} \right) + \Omega_R^a \boldsymbol{\mathcal{S}}_a, \tag{4.4}$$

with $\boldsymbol{\mathcal{F}}^C_{\boldsymbol{N}_k}$ denoting the contact flux vectors, as yet to be defined in Section 4.3.2, and where $b \in \Lambda_a$ denotes the set of neighbouring control volumes associated with the dual control volume $\Omega_R^a$. Notice that the classical approach Eq. (4.4) clearly shows a substantial increase in computational cost due to an extra loop over the facets of the dual control volume $\Omega_R^a$.

An alternative way for evaluation of the area vectors is an edge-based approach [199, 201] which results in a more efficient stencil. In this approach, node $a$ denoting the centre of dual control volume $\Omega^a$ is connected to a set of neighbouring interior nodes $b$ or boundary nodes $B$ through edges. For a given edge connecting nodes $a$ and $b$, the area vector is defined as

$$\boldsymbol{C}_{ab} = \underbrace{\sum_{k \in \Gamma_{ab}}}_{\text{Edges}} A_k \boldsymbol{N}_k, \tag{4.5}$$

where $\Gamma_{ab}$ stands for the set of facets associated with the edge $ab$, $A_k$ denotes the area of a given facet $k$ and $\boldsymbol{N}_k$ is its outward unit normal vector. The contribution of the boundary faces $\Gamma_a^B$ associated with a boundary edge $(aB)$ should also be taken into account. It must be noted that due to the definition of the dual mesh, the area vectors satisfy $\boldsymbol{C}_{ab} = -\boldsymbol{C}_{ba}$. The main assumption of the edge-based approach indicates that the integral of the flux over facets associated with an edge is approximated by assuming the flux to be constant over the facets and equal to its computed value at the midpoint of the edge. In fact, the outward normal vector associated with an edge ($\boldsymbol{N}_k$) is the mean approximation of two outward normals ($\boldsymbol{N}_1$ and $\boldsymbol{N}_2$) associated to the two facets through which the edge is crossed (see Figure 4.5b). It must be noted that this assumption will not affect the order of convergence [118]. Consequently, using the area vectors $\boldsymbol{C}_{ab}$ (rather than $\boldsymbol{\mathcal{C}}_a$) can substantially reduce the computational cost when computing the approximated boundary integral presented in Eq. (4.2). In this thesis, the edge-based approach will be utilised through VCFVM approximation.

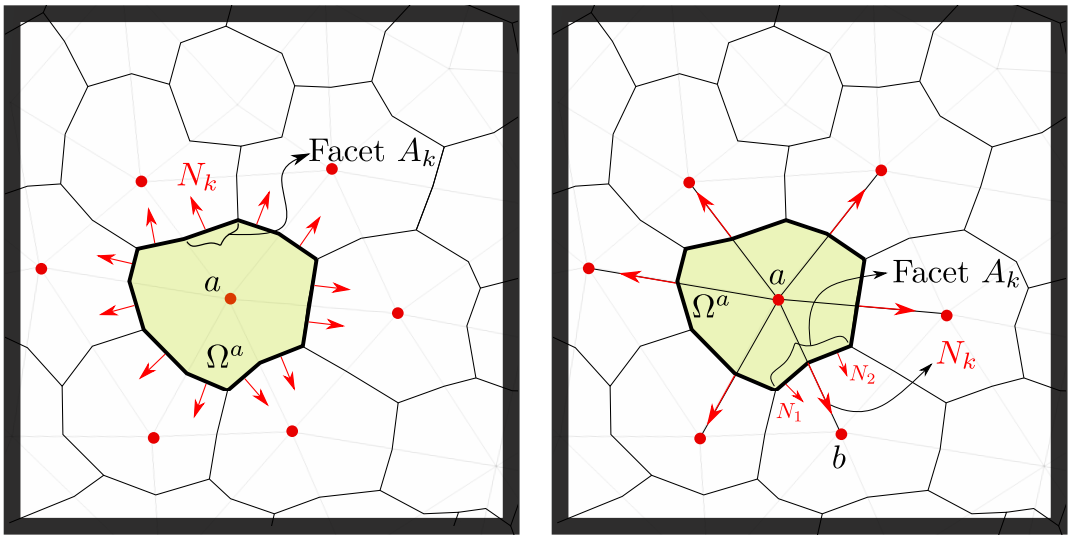


(a) (b)

FIGURE 4.5: Area vector approximation in VCFVM using (a) classical and (b) edge-based approaches

## 4.3 Total Lagrangian VCFVM discretisation

In general, the integral form of a conservation law Eq. (2.55) over an undeformed control volume $\Omega_R^a$ can be spatially discretised using VCFVM as

$$\Omega_R^a \frac{d\boldsymbol{\mathcal{U}}_a}{dt} = -\left( \sum_{b \in \Lambda_a} \boldsymbol{\mathcal{F}}^C_{\boldsymbol{N}_{ab}} \|\boldsymbol{C}_{ab}\| + \sum_{\gamma \in \Gamma_a^B} \boldsymbol{\mathcal{F}}_a^\gamma \boldsymbol{C}^\gamma \right) + \Omega_R^a \boldsymbol{\mathcal{S}}_R^a, \tag{4.6}$$

where $\boldsymbol{\mathcal{U}}_a$ is the cell averaged conservative quantity within the dual control volume $\Omega_R^a$ and $\boldsymbol{\mathcal{S}}_a$ denotes the source term. The term presented in the big parenthesis in Eq. (4.6) is the approximation for the flux vector $\boldsymbol{\mathcal{F}}_{\boldsymbol{N}}$ defined in Eq. (2.58) and consists of two terms. The first term evaluates the contact flux $\boldsymbol{\mathcal{F}}^C$, yet to be defined in Section 4.3.2, by summing over all the edges through which the center of dual control volume $\Omega^a$ is connected to its neighbours $\Omega_b$ (see Figure 4.5b). The second term computes the fluxes $\boldsymbol{\mathcal{F}}_a^\gamma$ by summing over all the boundary faces associated with the dual control volume $\Omega^a$. Luo et al. [202] proposed to evaluate the boundary fluxes through a weighted average stencil in two and three dimensions such that

$$\text{(2D)}\ \boldsymbol{\mathcal{F}}_a^\gamma = \frac{5\boldsymbol{\mathcal{F}}_a + \boldsymbol{\mathcal{F}}_b}{6}; \qquad \text{(3D)}\ \boldsymbol{\mathcal{F}}_a^\gamma = \frac{6\boldsymbol{\mathcal{F}}_a + \boldsymbol{\mathcal{F}}_b + \boldsymbol{\mathcal{F}}_c}{8}, \tag{4.7}$$

wherein the three-dimensional case, $a$ and $b$ and $c$ represents the three nodes of a triangular face. It must be reminded that $a$ is also the centre of the dual control volume located on the physical boundary (see Figure 4.6). In addition, the (tributary) boundary area vector is approximated as $\boldsymbol{C}^\gamma = \frac{A^\gamma \boldsymbol{N}^\gamma}{3}$ [11, 118].

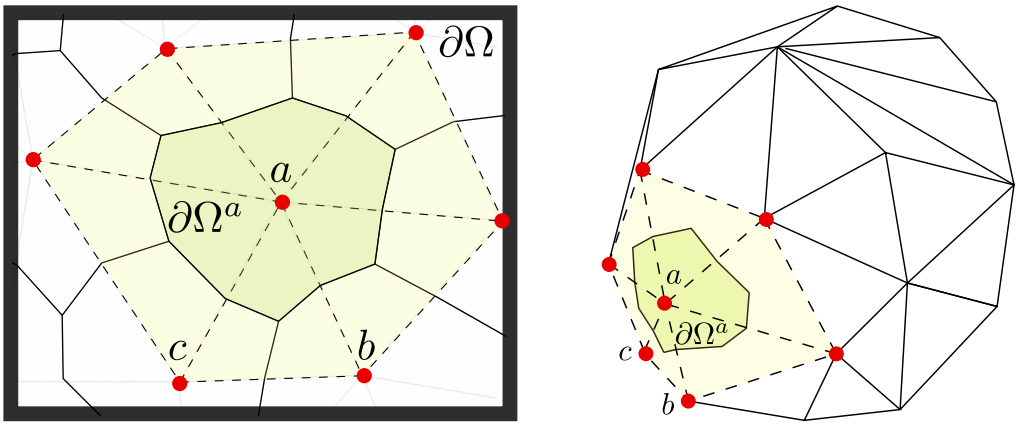


(a) (b)

FIGURE 4.6: VCFVM approximation for the boundary contribution of the flux vectors represented in (a) two and (b) three dimensions

It is now possible to spatially discretise the system of conservation laws Eq. (2.58) using the edge-based VCFVM and the application of the Green-Gauss divergence theorem

$$\Omega_R^a \frac{d\boldsymbol{p}_a}{dt} = \sum_{b\in\Lambda_a} \boldsymbol{t}^C \|\boldsymbol{C}_{ab}\| + \sum_{\gamma\in\Gamma_a^B} \boldsymbol{t}_a^\gamma \|\boldsymbol{C}^\gamma\| + \Omega_R^a \boldsymbol{f}_R^a; \tag{4.8a}$$

$$\Omega_R^a \frac{d\boldsymbol{F}_a}{dt} = \sum_{b\in\Lambda_a} \frac{1}{\rho_R}\boldsymbol{p}^C \otimes \boldsymbol{C}_{ab} + \sum_{\gamma\in\Gamma_a^B} \frac{1}{\rho_R}\boldsymbol{p}_a^\gamma \otimes \boldsymbol{C}^\gamma; \tag{4.8b}$$

$$\Omega_R^a \frac{d\boldsymbol{H}_a}{dt} = \sum_{b\in\Lambda_a} \boldsymbol{F}_{ab}^{\text{Ave}} \times \left(\frac{1}{\rho_R}\boldsymbol{p}^C \otimes \boldsymbol{C}_{ab}\right) + \sum_{\gamma\in\Gamma_a^B} \boldsymbol{F}_a^\gamma \times \left(\frac{1}{\rho_R}\boldsymbol{p}_a^\gamma \otimes \boldsymbol{C}^\gamma\right); \tag{4.8c}$$

$$\Omega_R^a \frac{dJ_a}{dt} = \sum_{b\in\Lambda_a} \frac{1}{\rho_R}\boldsymbol{p}^C \cdot \left(\boldsymbol{H}_{ab}^{\text{Ave}}\boldsymbol{C}_{ab}\right) + \sum_{\gamma\in\Gamma_a^B} \frac{1}{\rho_R}\boldsymbol{p}_a^\gamma \cdot \left(\boldsymbol{H}_a^\gamma \boldsymbol{C}^\gamma\right); \tag{4.8d}$$

$$\begin{aligned}\Omega_R^a \frac{dE_a}{dt} = &\sum_{b\in\Lambda_a} \left(\frac{1}{\rho_R}\left(\boldsymbol{p}^C \cdot \boldsymbol{t}^C\right)\|\boldsymbol{C}_{ab}\| - \boldsymbol{Q}^C \cdot \boldsymbol{C}_{ab}\right) \\ &+ \sum_{\gamma\in\Gamma_a^B} \left(\frac{1}{\rho_R}\boldsymbol{t}_a^\gamma \cdot \boldsymbol{p}_a^\gamma \|\boldsymbol{C}_{ab}\| - \boldsymbol{Q}_a^\gamma \cdot \boldsymbol{C}^\gamma\right) + \Omega_R^a \boldsymbol{f}_R^a \cdot \frac{\boldsymbol{p}_a}{\rho_R} + \Omega_R^a s_R^a,\end{aligned} \tag{4.8e}$$

where the averaged values are defined as $[\cdot]_{ab}^{\text{Ave}} := \frac{1}{2}\left([\cdot]_a + [\cdot]_b\right)$ and $\{\boldsymbol{t}^C, \boldsymbol{p}^C, \boldsymbol{Q}^C\}$ are the contact traction, contact linear momentum and contact heat flux, respectively, as yet to be defined in Section 4.3.2. In the case of entropy-based formulations where the equation of entropy evolution replaces the conservation of total energy, the semi-discrete set of $\{\boldsymbol{p}, \boldsymbol{F}, \boldsymbol{H}, J\}$ equations, as described in Eq. (4.8a)-Eq. (4.8d), remains exactly the same, whilst the entropy equation can

be spatially discretised as

$$\Omega_R^a \theta_a \frac{d\eta_a}{dt} = -\sum_{b\in\Lambda_a} \left(\boldsymbol{Q}^C \cdot \boldsymbol{C}_{ab}\right) - \sum_{\gamma\in\Gamma_a^B} \left(\boldsymbol{Q}_a^\gamma \cdot \boldsymbol{C}^\gamma\right) + \Omega_R^a s_R^a. \tag{4.9}$$

In addition, the spatial (deformed) geometry can be updated through the discrete nodal linear momentum field as

$$\frac{d\boldsymbol{x}_a}{dt} = \frac{\boldsymbol{p}_a}{\rho_R}. \tag{4.10}$$

Note that in this thesis, the geometry update is only required for post-processing purposes.

### 4.3.1 Compatibility conditions

Crucially, the evolution of the fibre map $\boldsymbol{F}$ and area map $\boldsymbol{H}$ must be advanced in time satisfying a set of compatibility conditions Eq. (2.23) and Eq. (2.28). In discrete level, these intrinsic constraints must ensure that $\boldsymbol{F}$ and $\boldsymbol{H}$ evolve in time through a material discrete gradient of a continuous velocity field [18]. To achieve this, a central difference approximation is employed for discretisation of the contact linear momentum $\boldsymbol{p}^C = \frac{1}{2}\left(\boldsymbol{p}_a + \boldsymbol{p}_b\right)$ in Eq. (4.8b) and Eq. (4.8c). It has been proven that a central difference approximation in VCFVM is equivalent to a linear Bubnov-Galerkin Finite Element Method and that guarantees the enforcement of the involutions [7, 8]. Hence, the complete semi-discrete form of fibre map (2.21) and area map (2.29) equations can now be expressed as

$$\Omega_R^a \frac{d\boldsymbol{F}_a}{dt} = \sum_{b\in\Lambda_a} \frac{1}{2\rho_R}(\boldsymbol{p}_a + \boldsymbol{p}_b) \otimes \boldsymbol{C}_{ab} + \sum_{\gamma\in\Gamma_a^B} \frac{1}{\rho_R}\left(\boldsymbol{p}_a^\gamma \otimes \boldsymbol{N}^\gamma\right)\frac{A^\gamma}{3}; \tag{4.11a}$$

$$\Omega_R^a \frac{d\boldsymbol{H}_a}{dt} = \boldsymbol{F}_a \times \left( \sum_{b\in\Lambda_a} \frac{1}{2\rho_R}(\boldsymbol{p}_a + \boldsymbol{p}_b) \otimes \boldsymbol{C}_{ab} + \sum_{\gamma\in\Gamma_a^B} \frac{1}{\rho_R}\left(\boldsymbol{p}_a^\gamma \otimes \boldsymbol{N}^\gamma\right)\frac{A^\gamma}{3} \right). \tag{4.11b}$$

### 4.3.2 Contact fluxes approximation

From the viewpoint of Vertex-Centred Finite Volume Method (VCFVM) as one of the employed spatial discretisation in this thesis, discontinuity of the conservation variables across (dual) control volume interfaces crucially leads to a Riemann problem. That problem, therefore, requires to be approximately solved through the use of a (nonlinear) Riemann solver. There are several approaches to evaluate the approximated contact fluxes $\{\boldsymbol{t}, \boldsymbol{p}, \boldsymbol{Q}\}^C$ presented in Eq. (4.8) [200]. Classically, The flux vector along the direction of outward unit normal vector $\boldsymbol{N}$ can be written as [11, 199]

$$\boldsymbol{\mathcal{F}}_{\boldsymbol{N}}^C = \underbrace{\frac{1}{2}\left[\boldsymbol{\mathcal{F}}_{\boldsymbol{N}}(\boldsymbol{\mathcal{U}}^-) + \boldsymbol{\mathcal{F}}_{\boldsymbol{N}}(\boldsymbol{\mathcal{U}}^+)\right]}_{\text{Unstable flux}} \underbrace{- \frac{1}{2}\int_{\boldsymbol{\mathcal{U}}^-}^{\boldsymbol{\mathcal{U}}^+} |\boldsymbol{\mathcal{A}}_{\boldsymbol{N}}| \, \mathrm{d}\boldsymbol{\mathcal{U}}}_{\text{Upwinding stabilisation}}; \qquad \boldsymbol{\mathcal{A}}_{\boldsymbol{N}} = \frac{\partial \boldsymbol{\mathcal{F}}_{\boldsymbol{N}}}{\partial \boldsymbol{\mathcal{U}}}, \tag{4.12}$$

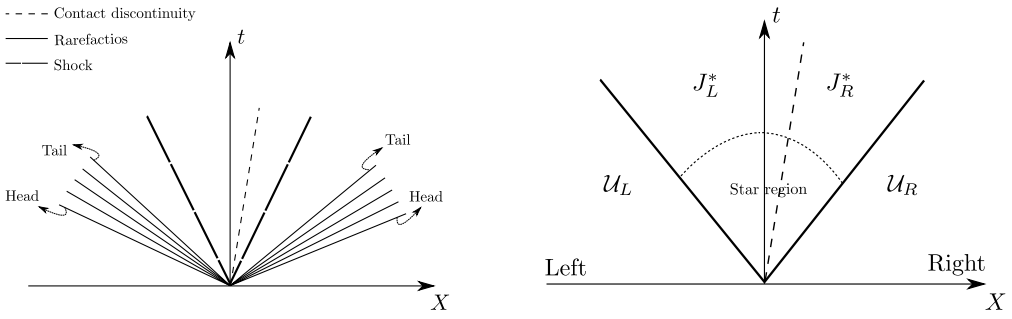


FIGURE 4.7: Representative solution of a Riemann problem: (a) possible wave patterns; and (b) structure of the solution

with $\boldsymbol{\mathcal{A}_N}$ denoting the flux Jacobian matrix to the system of conservation laws and $\boldsymbol{\mathcal{U}}^{-,+}$ are representing the linearly reconstructed left and right states conservative variables (see Section 4.3.3), defining the limit of the above integral along an arbitrary pass. The unstable flux term is simply a central difference approximation between the left and right states, similar to the Bubnov-Galerkin term in Finite Element Method, which suffers from severe numerical instabilities [45, 155, 161]. Therefore, the upwinding stabilisation has played the significant role of damping the instabilities and to achieve this, an Eigen structure analysis (as it is already performed in Ref. [6]) is required.

#### 4.3.2.1 Acoustic Riemann solver

Riemann solver is a numerical technique to solve Riemann problems. It is the most used and developed in the context of Computational Fluid Dynamics (CFD) for solving time-dependent hyperbolic Partial Differential Equations (PDEs). In fact, the solution structure of a Riemann problem, for hyperbolic conservation laws in particular, strongly depends on the wave propagation pattern of the solution. In general, three types of waves possibly appear at a contact interface, namely, (1) shock wave, (2) contact discontinuity, and/or (3) rarefaction (smooth transition) wave (see Figure 4.7a). The problem solution is evident at the left ($\boldsymbol{\mathcal{U}}_L$) and right ($\boldsymbol{\mathcal{U}}_R$) states of a wave pattern and the challenge remains at how to obtain the solution at the star region (see Figure 4.7b) distinguished by the waves [11, 200]. To achieve this, the two types of exact or approximated Riemann solver can be employed. The formers, initiated by the work of Godunov [194], is fundamentally useful to provide an invaluable insight into the physical sense of the Riemann problem and can be considered as an excellent reference solution to better develop the approximated Riemann solvers. However, its design strongly depends on the variables selected (conservative or primitive), the (number of) equations and the technique for the iterative procedure, to name a few [200]. These restrictions, therefore, entails that the exact Riemann solver is not effectively applied in some cases where the use of non-iterative approximated Riemann solvers could be an advantageous alternative.

Considering an acoustic Riemann solver, Eq. (4.12) reduces to

$$\boldsymbol{\mathcal{F}}_{\boldsymbol{N}}^{C} = \boldsymbol{\mathcal{F}}_{\boldsymbol{N}}^{\text{Ave}} + \boldsymbol{\mathcal{F}}_{\boldsymbol{N}}^{\text{Stab}} = \underbrace{\frac{1}{2}\left[\boldsymbol{\mathcal{F}}_{\boldsymbol{N}}(\boldsymbol{\mathcal{U}}^{+}) + \boldsymbol{\mathcal{F}}_{\boldsymbol{N}}(\boldsymbol{\mathcal{U}}^{-})\right]}_{\text{Unstable flux}} - \underbrace{\frac{1}{2}|\boldsymbol{\mathcal{A}}_{\boldsymbol{N}}|\left(\boldsymbol{\mathcal{U}}^{+} - \boldsymbol{\mathcal{U}}^{-}\right)}_{\text{Upwinding stabilisation}(\boldsymbol{\mathcal{D}}^{\boldsymbol{\mathcal{U}}})}, \tag{4.13}$$

with a further assumption of [200]

$$\boldsymbol{\mathcal{F}}_{\boldsymbol{N}}(\boldsymbol{\mathcal{U}}^{+,-}) = \boldsymbol{\mathcal{F}}_{\boldsymbol{N}}^{+,-}. \tag{4.14}$$

Following Ref. [6, 7], the explicit expression of the absolute value of the flux Jacobian matrix $|\boldsymbol{\mathcal{A}}_{\boldsymbol{N}}| = \left|\frac{\partial \boldsymbol{\mathcal{F}}_{\boldsymbol{N}}}{\partial \boldsymbol{\mathcal{U}}}\right|$ (see Ref. [6], Section 4.3.1, Eq. (32)) has to be utilised. Thus, the application of Rankine-Hugoniot jump condition for the linear momentum conservation law yields

$$c_p\,(\boldsymbol{n}\otimes\boldsymbol{n})\,[\![\boldsymbol{p}]\!] = -(\boldsymbol{n}\otimes\boldsymbol{n})\,[\![\boldsymbol{t}]\!]; \tag{4.15a}$$

$$c_s\,(\boldsymbol{I}-\boldsymbol{n}\otimes\boldsymbol{n})\,[\![\boldsymbol{p}]\!] = -(\boldsymbol{I}-\boldsymbol{n}\otimes\boldsymbol{n})\,[\![\boldsymbol{t}]\!], \tag{4.15b}$$

where $(\boldsymbol{n}\otimes\boldsymbol{n})$ and $(\boldsymbol{I}-\boldsymbol{n}\otimes\boldsymbol{n})$ are the normal and tangential projection tensors and with $\boldsymbol{n}$ denoting the outward unit normal vector across the interface of the deformed configuration defined as

$$\boldsymbol{n} = \frac{\boldsymbol{H}\boldsymbol{N}}{\|\boldsymbol{H}\boldsymbol{N}\|}. \tag{4.16}$$

Eq. (4.15a) can be decomposed into the left and right states as

$$c_p^{-}\,(\boldsymbol{n}\otimes\boldsymbol{n})\,\left(\boldsymbol{p}^{-}-\boldsymbol{p}^{C}\right) = (\boldsymbol{n}\otimes\boldsymbol{n})\,\left(\boldsymbol{t}^{-}-\boldsymbol{t}^{C}\right); \tag{4.17a}$$

$$c_p^{+}\,(\boldsymbol{n}\otimes\boldsymbol{n})\,\left(\boldsymbol{p}^{+}-\boldsymbol{p}^{C}\right) = -(\boldsymbol{n}\otimes\boldsymbol{n})\,\left(\boldsymbol{t}^{+}-\boldsymbol{t}^{C}\right). \tag{4.17b}$$

where the $[\cdot]^{-}$ and $[\cdot]^{+}$ are denoting the linearly reconstructed values at the left and right states of a contact interface, respectively. This can also be done for Eq. (4.15b) in a similar manner. Thus, and after some simple algebraic manipulations, the contact flux vectors $\{\boldsymbol{p},\boldsymbol{t}\}^{C}$ yield

$$\boldsymbol{t}^{C} = (\boldsymbol{n}\otimes\boldsymbol{n})\left[\frac{c_p^{+}\boldsymbol{t}^{-}+c_p^{-}\boldsymbol{t}^{+}}{c_p^{-}+c_p^{+}} + \frac{c_p^{-}c_p^{+}(\boldsymbol{p}^{+}-\boldsymbol{p}^{-})}{c_p^{-}+c_p^{+}}\right] + (\boldsymbol{I}-\boldsymbol{n}\otimes\boldsymbol{n})\left[\frac{c_s^{+}\boldsymbol{t}^{-}+c_s^{-}\boldsymbol{t}^{+}}{c_s^{-}+c_s^{+}} + \frac{c_s^{-}c_s^{+}(\boldsymbol{p}^{+}-\boldsymbol{p}^{-})}{c_s^{-}+c_s^{+}}\right]; \tag{4.18a}$$

$$\boldsymbol{p}^{C} = (\boldsymbol{n}\otimes\boldsymbol{n})\left[\frac{c_p^{-}\boldsymbol{p}^{-}+c_p^{+}\boldsymbol{p}^{+}}{c_p^{-}+c_p^{+}} + \frac{\boldsymbol{t}^{+}-\boldsymbol{t}^{-}}{c_p^{-}+c_p^{+}}\right] + (\boldsymbol{I}-\boldsymbol{n}\otimes\boldsymbol{n})\left[\frac{c_s^{-}\boldsymbol{p}^{-}+c_s^{+}\boldsymbol{p}^{+}}{c_s^{-}+c_s^{+}} + \frac{\boldsymbol{t}^{+}-\boldsymbol{t}^{-}}{c_s^{-}+c_s^{+}}\right], \tag{4.18b}$$

with $c_p$ and $c_s$ representing the pressure and shear wave speeds.

It is worth noting that for the case of a homogeneous linear elastic material model, we have $c_p = c_p^{+} = c_p^{-}$ and $c_s = c_s^{+} = c_s^{-}$. As a result, and following the structure of contact flux presented in Eq. (4.13), the contact linear momentum and contact traction presented in Eq. (4.18) reduce

to

$$\boldsymbol{t}^C = \frac{1}{2}\left(\boldsymbol{t}^+ + \boldsymbol{t}^-\right) + \frac{1}{2}\left[c_p(\boldsymbol{n}\otimes\boldsymbol{n}) + c_s(\boldsymbol{I} - \boldsymbol{n}\otimes\boldsymbol{n})\right]\left(\boldsymbol{p}^+ - \boldsymbol{p}^-\right); \tag{4.19a}$$

$$\boldsymbol{p}^C = \frac{1}{2}\left(\boldsymbol{p}^+ + \boldsymbol{p}^-\right) + \frac{1}{2}\left[\frac{1}{c_p}(\boldsymbol{n}\otimes\boldsymbol{n}) + \frac{1}{c_s}(\boldsymbol{I} - \boldsymbol{n}\otimes\boldsymbol{n})\right]\left(\boldsymbol{t}^+ - \boldsymbol{t}^-\right), \tag{4.19b}$$

where $c_p$ and $c_s$ represent the elastic pressure and shear wave speeds, respectively

$$c_p = \sqrt{\frac{\lambda + 2\mu}{\rho_R}}; \qquad c_s = \sqrt{\frac{\mu}{\rho_R}}. \tag{4.20}$$

Having obtained the contact fluxes in Eq. (4.19), it is now possible to define the upwinding stabilisation terms $\boldsymbol{\mathcal{D}}^{\boldsymbol{\mathcal{U}}}_{ab}$. This is carried out by following the structure of Eq. (4.13) where we have an averaged term named unstable flux and an upwinding stabilisation term. The latter can be expressed, considering the corresponding flux of each conservation law (see Eq. (4.8)), as

$$\boldsymbol{\mathcal{D}}^{\boldsymbol{p}}_{ab} = \boldsymbol{t}^{\text{Stab}}_{ab} = \boldsymbol{P}^{\text{Stab}}_{ab}\boldsymbol{C}_{ab}; \tag{4.21a}$$

$$\mathcal{D}^{J}_{ab} = \boldsymbol{v}^{\text{Stab}}_{ab} \cdot \left(\boldsymbol{H}^{\text{Ave}}_{ab}\boldsymbol{C}_{ab}\right); \tag{4.21b}$$

$$\mathcal{D}^{E}_{ab} = \left(\boldsymbol{t}^{\text{Stab}}_{ab} \cdot \boldsymbol{v}^{\text{Ave}}_{ab} + \boldsymbol{t}^{\text{Ave}}_{ab} \cdot \boldsymbol{v}^{\text{Stab}}_{ab}\right)\|\boldsymbol{C}_{ab}\|, \tag{4.21c}$$

with the stabilised contact fluxes

$$\boldsymbol{P}^{\text{Stab}}_{ab} := \boldsymbol{S}^{\boldsymbol{p}}_{ab}\left[(\boldsymbol{v}_b - \boldsymbol{v}_a)\otimes\boldsymbol{N}_{ab}\right]; \qquad \boldsymbol{v}^{\text{Stab}}_{ab} := \boldsymbol{S}^{J}_{ab}\left[\left(\Sigma^b_J - \Sigma^a_J\right)\boldsymbol{H}^{\text{Ave}}_{ab}\boldsymbol{N}_{ab}\right], \tag{4.22}$$

where $\Sigma_J$ is defined in Eq. (3.11c) and with positive definite stabilisation matrices $\{\boldsymbol{S}^{\boldsymbol{p}}_{ab}, \boldsymbol{S}^{J}_{ab}\}$, defined as

$$\boldsymbol{S}^{\boldsymbol{p}}_{ab} = \frac{\rho_R}{2}\left[c_p\boldsymbol{n}_{ab}\otimes\boldsymbol{n}_{ab} + c_s\left(\boldsymbol{I} - \boldsymbol{n}_{ab}\otimes\boldsymbol{n}_{ab}\right)\right]; \quad \boldsymbol{S}^{J}_{ab} = \frac{1}{2\rho_R}\left[\frac{1}{c_p}\boldsymbol{n}_{ab}\otimes\boldsymbol{n}_{ab} + \frac{1}{c_s}\left(\boldsymbol{I} - \boldsymbol{n}_{ab}\otimes\boldsymbol{n}_{ab}\right)\right]. \tag{4.23}$$

Notice here that the stabilisation terms for deformation gradient and area map equations are defined $\boldsymbol{\mathcal{D}}^{\boldsymbol{F}}_{ab} = \boldsymbol{0}$ and $\boldsymbol{\mathcal{D}}^{\boldsymbol{H}}_{ab} = \boldsymbol{0}$, as the necessary requirement for satisfying the involutions. Additionally, the contact heat flux at the total energy conservation law is considered with no stabilisation (i.e. $\boldsymbol{Q}^{C}_{ab} = \boldsymbol{Q}^{\text{Ave}}_{ab}$) since it naturally introduces a diffusive behaviour.

### 4.3.3 Linear reconstruction and slope limiter

In the classical Godunov's type FVM [194], a piecewise constant approximation is considered for conservative quantities $\mathcal{U}$ within each dual control volume. This results in a first order accurate solution for the semi-discrete system of equations (4.6). This will introduce an excessive numerical viscosity (due to its diffusive nature) and, therefore, smeared results with poor accuracy, especially in the presence of sharp gradients [11, 199, 200]. To rectify this shortcoming

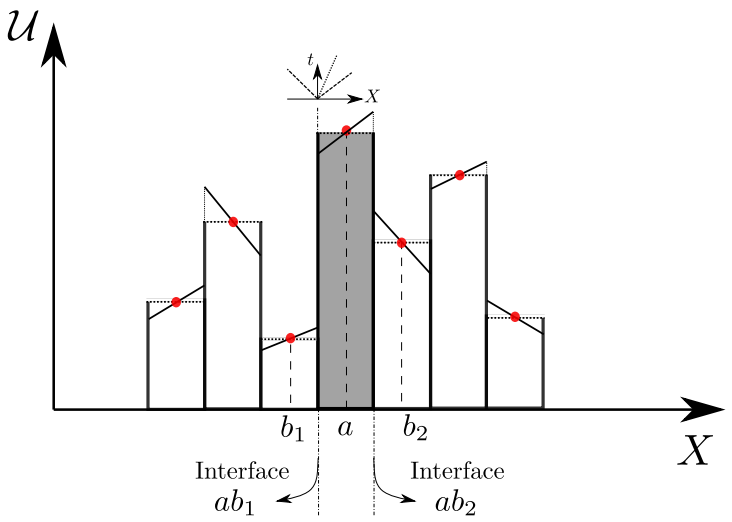


FIGURE 4.8: One-dimensional solution representing a piecewise linear reconstruction

and following the work of [6, 7], a conservative linear reconstruction procedure is employed here in order to obtain second order accurate solution in space (see Figure 4.8). To do so, a linear field is assumed for the conservative quantity $\mathcal{U}_a$ within an arbitrary dual control volume $\Omega^a$

$$\mathcal{U}_a(\boldsymbol{X}) = \mathcal{U}_a + \boldsymbol{G}_a \cdot (\boldsymbol{X} - \boldsymbol{X}_a), \tag{4.24}$$

where $\boldsymbol{X}$ belongs to any position of the dual control volume $\Omega^a$, $\boldsymbol{X}_a$ is its centroid position and $\boldsymbol{G}_a$ is the gradient operator.

### Gradient operator

The local gradient operator $\boldsymbol{G}_a$ can be obtained using a least squares minimisation process [6, 18]. To do so, an objective functional $\Pi$ with the unknowns $\mathcal{U}_a$ and $\boldsymbol{G}_a$ is defined as

$$\Pi(\mathcal{U}_a, \boldsymbol{G}_a) = \sum_{b \in \Lambda_a^b} \left[ \underbrace{\mathcal{U}_b - (\mathcal{U}_a + \boldsymbol{G}_a \cdot \Delta\boldsymbol{X})}_{\Delta\mathcal{U}} \right]^2 ; \qquad \Delta\boldsymbol{X} = \boldsymbol{X}_b - \boldsymbol{X}_a, \tag{4.25}$$

where $\mathcal{U}_b$ is the centroid value of the neighbouring cells $\Omega_b$ (with positions $\boldsymbol{X}_b$) to the cell $\Omega^a$ and $\Delta\mathcal{U}$ stands for the difference between the $\mathcal{U}_b$ and the value obtained by linear extrapolation of $\mathcal{U}_a$ from cell $a$ to $b$.

The directional derivative of the functional $\Pi$ with respect to $\mathcal{U}_a$ and $\boldsymbol{G}_a$ reads

$$D\Pi[\delta\mathcal{U}_a] = \sum_{b \in \Lambda_a^b} -2\left[\mathcal{U}_b - (\mathcal{U}_a + \boldsymbol{G}_a \cdot \Delta\boldsymbol{X})\right] \delta\mathcal{U}_a = 0; \tag{4.26a}$$

$$D\Pi[\delta\boldsymbol{G}_a] = \sum_{b \in \Lambda_a^b} -2\left[\mathcal{U}_b - (\mathcal{U}_a + \boldsymbol{G}_a \cdot \Delta\boldsymbol{X})\right] (\Delta\boldsymbol{X} \cdot \delta\boldsymbol{G}_a) = 0, \tag{4.26b}$$

in which considering arbitrary values for $\delta\,\mathcal{U}_a$ and $\delta\,\boldsymbol{G}_a$, yields

$$\sum_{b\in\Lambda_a^b}\mathcal{U}_a+\sum_{b\in\Lambda_a^b}\Delta\boldsymbol{X}\cdot\boldsymbol{G}_a=\sum_{b\in\Lambda_a^b}\mathcal{U}_b; \tag{4.27a}$$

$$\mathcal{U}_a\sum_{b\in\Lambda_a^b}\Delta\boldsymbol{X}+\sum_{b\in\Lambda_a^b}\left(\Delta\boldsymbol{X}\otimes\Delta\boldsymbol{X}\right)\boldsymbol{G}_a=\sum_{b\in\Lambda_a^b}\mathcal{U}_b\Delta\boldsymbol{X}. \tag{4.27b}$$

Eq. (4.27) is now a system of equations that can be solved for the unknowns $\mathcal{U}_a$ and $\boldsymbol{G}_a$ representing as

$$\begin{bmatrix} n_b & \left[\sum_{b\in\Lambda_a^b}\Delta\boldsymbol{X}\right]^T \\ \sum_{b\in\Lambda_a^b}\Delta\boldsymbol{X} & \sum_{b\in\Lambda_a^b}\left(\Delta\boldsymbol{X}\otimes\Delta\boldsymbol{X}\right) \end{bmatrix}\begin{bmatrix}\mathcal{U}_a\\ \boldsymbol{G}_a\end{bmatrix}=\begin{bmatrix}\sum_{b\in\Lambda_a^b}\mathcal{U}_b\\ \sum_{b\in\Lambda_a^b}\mathcal{U}_b\,\Delta\boldsymbol{X}\end{bmatrix}. \tag{4.28}$$

The case of which the position $\boldsymbol{X}_a$ is the centre of gravity (barycentre) of neighbouring positions $\boldsymbol{X}_b$ leads to

$$\boldsymbol{X}_{cg}=\boldsymbol{X}_a=\frac{1}{b}\sum_{b\in\Lambda_a^b}\boldsymbol{X}_b;\qquad\sum_{b\in\Lambda_a^b}\Delta\boldsymbol{X}=\boldsymbol{0}. \tag{4.29}$$

Consequently, the solution of the system of equations (4.28) is obtained as follows

$$\mathcal{U}_a=\frac{1}{b}\sum_{b\in\Lambda_a^b}\mathcal{U}_b;\qquad\boldsymbol{G}_a=\left[\sum_{b\in\Lambda_a^b}\Delta\boldsymbol{X}\otimes\Delta\boldsymbol{X}\right]^{-1}\sum_{b\in\Lambda_a^b}\mathcal{U}_b\,\Delta\boldsymbol{X}. \tag{4.30}$$

---

*Remark* 9: Alternatively, in the case of $\mathcal{U}_a$ being a known quantity, the objective functional $\Pi$ depends only on $\boldsymbol{G}_a$ as

$$\Pi(\boldsymbol{G}_a)=\sum_{b\in\Lambda_a^b}\left[\mathcal{U}_b-\left(\mathcal{U}_a+\boldsymbol{G}_a\cdot\Delta\boldsymbol{X}\right)\right]^2. \tag{4.31}$$

Minimisation of this functional leads to the following expression for the gradient operator

$$\boldsymbol{G}_a=\left[\sum_{b\in\Lambda_a^b}\Delta\boldsymbol{X}\otimes\Delta\boldsymbol{X}\right]^{-1}\sum_{b\in\Lambda_a^b}\left(\mathcal{U}_b-\mathcal{U}_a\right)\Delta\boldsymbol{X}, \tag{4.32}$$

which is identical to Eq. (4.30) when $\sum_{b\in\Lambda_a^b}\Delta\boldsymbol{X}=\boldsymbol{0}$ [6, 18, 118].

Having the gradient operator at (4.30) or (4.32), it is now possible to obtain the reconstructed solution $\mathcal{U}_{a\beta}$ at the flux integration point $\beta$ associated with the cell $\Omega^a$ as

$$\mathcal{U}_{a\beta} = \mathcal{U}_a + \boldsymbol{G}_a \cdot (\boldsymbol{X}_\beta - \boldsymbol{X}_a). \tag{4.33}$$

It must be noticed that the linear reconstruction procedure is conservative if and only if the gradient is obtained at the cell centroid location $\boldsymbol{X}_a$. However, this procedure, unfortunately, violates the principle of monotonicity and, therefore, an appropriate slope limiter is required in order to avoid spurious oscillations (wiggles) in the vicinity of sharp gradients.

#### Slope limiter

The employed linear reconstruction presented in Section 4.3.3 allows for constructing a high order (second order) scheme. However, it is well known that these schemes show an oscillatory behaviour in the vicinity of sharp (high) gradients [11, 200]. Hence, slope limiters are employed in order to ensure robustness and preserve mesh symmetries which are on the basis of classical slope limiters [203] for scalar fields and frame-invariant limiters for vector fields [204]. In addition, these limiters guarantees monotonicity preserving numerical scheme fulfilling a set of conditions, namely, (1) local extrema must not be created during the time evolution; and (2) an existing local minimum must be non-decreasing and a local maximum non-increasing [183].

In this thesis, a priori component by component limiting procedure is adapted for vectors and tensors since the definition of extrema is unclear for these fields. Hence, the local slope limiter at flux integration point $\beta$ reads [205]

$$\mathcal{U}_{a\beta} = \mathcal{U}_a + \phi_a \boldsymbol{G}_a \cdot (\boldsymbol{X}_\beta - \boldsymbol{X}_a). \tag{4.34}$$

It is worth noting that the lack of mesh symmetry when employing component-by-component velocity limiting has led to the development of frame-invariant tensorial limiting for vector fields [204, 206]. An alternative proposed procedure is to limit the vector fields using convex hull methodology [207, 208]. In the event that a reconstructed vector lies within the convex hull of a neighbouring vector, it is shown that monotonicity is satisfied in all directions. This procedure has been successfully tested in two dimensions, however, its extension to three-dimensional scenarios is quite complex [206].

In this study, the conventional Barth and Jespersen limiter [209], described by Algorithm 4.1, is used in order to obtain a monotonic solution.

## 4.4 Coleman-Noll procedure

In this section, we present a procedure to obtain consistent and locally conservative stabilisation terms by utilising the concept of the rate of entropy production [16], which can be understood as a discrete version of the classical Coleman-Noll procedure. We first start by multiplying the

**Algorithm 4.1:** Barth and Jespersen slope limiter

**Input :** $\mathcal{U}_a,\ \mathcal{U}_b$

**Output:** $\phi_a$

(1) Compute minimum and maximum values:

$$\mathcal{U}_a^{\min} = \min_{b\in\Lambda_a^b}(\mathcal{U}_a,\mathcal{U}_b); \qquad \mathcal{U}_a^{\max} = \max_{b\in\Lambda_a^b}(\mathcal{U}_a,\mathcal{U}_b).$$

(2) Compute an unlimited reconstruction at the flux integration point $\beta$:

$$\mathcal{U}_{a\beta} = \mathcal{U}_a + \boldsymbol{G}_a\cdot(\boldsymbol{X}_\beta - \boldsymbol{X}_a); \qquad \forall\,\beta\in\Lambda_a^\beta.$$

(3) Obtain a maximum allowable value of $\phi_{a\beta}$ at each flux integration point:

$$\phi_{a\beta} = \begin{cases} \min\left(1, \frac{\mathcal{U}_a^{\max}-\mathcal{U}_a}{\mathcal{U}_{a\beta}-\mathcal{U}_a}\right), & \text{if} \quad \mathcal{U}_{a\beta}-\mathcal{U}_a > 0; \\ \min\left(1, \frac{\mathcal{U}_a^{\min}-\mathcal{U}_a}{\mathcal{U}_{a\beta}-\mathcal{U}_a}\right), & \text{if} \quad \mathcal{U}_{a\beta}-\mathcal{U}_a < 0; \\ 1, & \text{if} \quad \mathcal{U}_{a\beta}-\mathcal{U}_a = 0. \end{cases}$$

(4) Select the limiter associated with the cell:

$$\phi_a = \min_{\beta\in\Lambda_a^\beta}(\phi_{a\beta}).$$

complete set of $\{\boldsymbol{p}_a, \boldsymbol{F}_a, \boldsymbol{H}_a, J_a\}$ semi-discrete equations (expressed in Eq. (4.8a)-Eq. (4.8d)) by their dual conjugate variables $\{\boldsymbol{v}_a, \boldsymbol{\Sigma}_{\boldsymbol{F}}^a, \boldsymbol{\Sigma}_{\boldsymbol{H}}^a, \Sigma_J^a\}$, subtracting them from Eq. (4.8e) and adding over all nodes $a$ of the computational mesh, gives, after some simple algebra,

$$\dot{\mathcal{D}}_p(t) := \sum_a \Omega_R^a \left[\frac{dE_a}{dt} - \frac{\boldsymbol{p}_a}{\rho_R}\cdot\frac{d\boldsymbol{p}_a}{dt} - \boldsymbol{\Sigma}_{\boldsymbol{F}}^a : \frac{d\boldsymbol{F}_a}{dt} - \boldsymbol{\Sigma}_{\boldsymbol{H}}^a : \frac{d\boldsymbol{H}_a}{dt} - \Sigma_J^a\frac{dJ_a}{dt}\right] \tag{4.35a}$$

$$= \sum_a\sum_{b\in\Lambda_a}\left[\left(\boldsymbol{P}_{ab}^{\text{Ave}}\boldsymbol{C}_{ab}\right)\cdot\frac{\boldsymbol{p}_{ab}^{\text{Ave}}}{\rho_R} - \left(\boldsymbol{P}_{ab}^{\text{Ave}}\boldsymbol{C}_{ab}\right)\cdot\frac{\boldsymbol{p}_a}{\rho_R} - \boldsymbol{P}_a : \left(\frac{\boldsymbol{p}_{ab}^{\text{Ave}}}{\rho_R}\otimes\boldsymbol{C}_{ab}\right)\right]$$

$$- \sum_a\sum_{b\in\Lambda_a^b}\left(\boldsymbol{Q}_{ab}^{\text{Ave}}\cdot\boldsymbol{\mathcal{C}}_{ab}\right) + \sum_a \Omega_R^a s_R^a - \sum_a\sum_{b\in\Lambda_a}\left(\frac{\boldsymbol{p}_a}{\rho_R}\cdot\boldsymbol{\mathcal{D}}_{ab}^{\boldsymbol{p}} + \Sigma_J^a\mathcal{D}_{ab}^J - \mathcal{D}_{ab}^E\right) \tag{4.35b}$$

$$= \sum_a \frac{1}{2\rho_R}\left[\sum_{b\in\Lambda_a}\left(\boldsymbol{P}_{ab}^{\text{Ave}}\boldsymbol{C}_{ab}\right)\cdot(\boldsymbol{p}_b-\boldsymbol{p}_a) - \sum_{b\in\Lambda_a}\left(\boldsymbol{P}_a\boldsymbol{C}_{ab}\right)\cdot(\boldsymbol{p}_a+\boldsymbol{p}_b)\right]$$

$$- \sum_a\sum_{b\in\Lambda_a^b}\left(\boldsymbol{Q}_{ab}^{\text{Ave}}\cdot\boldsymbol{\mathcal{C}}_{ab}\right) + \sum_a \Omega_R^a s_R^a - \sum_a\sum_{b\in\Lambda_a}\left(\frac{\boldsymbol{p}_a}{\rho_R}\cdot\boldsymbol{\mathcal{D}}_{ab}^{\boldsymbol{p}} + \Sigma_J^a\mathcal{D}_{ab}^J - \mathcal{D}_{ab}^E\right), \tag{4.35c}$$

with $\dot{\mathcal{D}}_p(t)$ defined as the time rate of numerical entropy (diffusion), $\boldsymbol{P}_a = \boldsymbol{\Sigma}_{\boldsymbol{F}}^a + \boldsymbol{\Sigma}_{\boldsymbol{H}}^a\boldsymbol{\times}\boldsymbol{F}_a + \Sigma_J^a\boldsymbol{H}_a$ and the upwinding stabilisation terms are already introduced in Eq. (4.21). Since $\sum_{b\in\Lambda_a}\boldsymbol{C}_{ab} = \boldsymbol{0}$, we could then add the redundant term $\frac{1}{\rho_R}\sum_{b\in\Lambda_a}(\boldsymbol{P}_a\boldsymbol{C}_{ab})\cdot\boldsymbol{p}_a - \sum_{b\in\Lambda_a}\boldsymbol{Q}_a\cdot\boldsymbol{\mathcal{C}}_{ab}$ to the above

expression, yielding

$$\dot{\mathcal{D}}_p(t) = \sum_a \frac{1}{2\rho_R}\left[\sum_{b\in\Lambda_a}\left(\boldsymbol{P}_{ab}^{\mathrm{Ave}}\boldsymbol{C}_{ab}\right)\cdot(\boldsymbol{p}_b-\boldsymbol{p}_a) - \sum_{b\in\Lambda_a}(\boldsymbol{P}_a\boldsymbol{C}_{ab})\cdot(\boldsymbol{p}_a+\boldsymbol{p}_b) + \sum_{b\in\Lambda_a} 2\,(\boldsymbol{P}_a\boldsymbol{C}_{ab})\cdot\boldsymbol{p}_a\right] + \sum_a \Omega_R^a s_R^a - \sum_a\sum_{b\in\Lambda_a}\left(\boldsymbol{Q}_{ab}^{\mathrm{Ave}}-\boldsymbol{Q}_a\right)\cdot\boldsymbol{\mathcal{C}}_{ab} - \sum_a\sum_{b\in\Lambda_a}\left(\frac{\boldsymbol{p}_a}{\rho_R}\cdot\boldsymbol{\mathcal{D}}_{ab}^{\boldsymbol{p}} + \Sigma_J^a\mathcal{D}_{ab}^J - \mathcal{D}_{ab}^E\right). \tag{4.36}$$

Using Eq. (4.22) and after substitution of Eq. (4.21) into Eq. (4.36), in the absence of source terms, it gives

$$\begin{aligned}\dot{\mathcal{D}}_p(t) = {}& \frac{1}{4\rho_R}\sum_a\sum_{b\in\Lambda_a}\left[\left(\boldsymbol{P}_b-\boldsymbol{P}_a\right)\boldsymbol{C}_{ab}\right]\cdot(\boldsymbol{p}_b-\boldsymbol{p}_a) - \frac{1}{2}\sum_a\sum_{b\in\Lambda_a}(\boldsymbol{Q}_b-\boldsymbol{Q}_a)\cdot\boldsymbol{\mathcal{C}}_{ab}\\ & - \frac{1}{2}\sum_a\sum_{b\in\Lambda_a}\|\boldsymbol{C}_{ab}\|\,(\boldsymbol{v}_b-\boldsymbol{v}_a)\cdot\left[\boldsymbol{\mathcal{S}}_{ab}^{\boldsymbol{p}}\,(\boldsymbol{v}_b-\boldsymbol{v}_a)\right]\\ & - \sum_a\sum_{b\in\Lambda_a}\Sigma_J^a\|\boldsymbol{C}_{ab}\|\left(\Sigma_J^b-\Sigma_J^a\right)(\boldsymbol{H}_{ab}^{\mathrm{Ave}}\boldsymbol{N}_{ab})\cdot\left[\boldsymbol{\mathcal{S}}_{ab}^J\left(\boldsymbol{H}_{ab}^{\mathrm{Ave}}\boldsymbol{N}_{ab}\right)\right].\end{aligned} \tag{4.37a}$$

Notice here that the evaluation of $\{\boldsymbol{\mathcal{D}}_{ab}^{\boldsymbol{p}}, \mathcal{D}_{ab}^J, \mathcal{D}_{ab}^E\}$ is carried out by utilising a piecewise constant representation for $\{\boldsymbol{p}, \Sigma_J\}$ and, more importantly, the summation is carried out over control volumes. Rearranging the above summation over edges connecting $a$ and $b$ gives

$$\dot{\mathcal{D}}_p(t) = \sum_{\substack{\text{edges}\\ a\leftrightarrow b}}\dot{\mathcal{D}}_p^{ab}(t), \tag{4.38a}$$

where the edge-based entropy production is defined as

$$\dot{\mathcal{D}}_p^{ab}(t) := \|\boldsymbol{C}_{ab}\|\left[(\boldsymbol{v}_b-\boldsymbol{v}_a)\cdot\left[\boldsymbol{\mathcal{S}}_{ab}^{\boldsymbol{p}}\,(\boldsymbol{v}_b-\boldsymbol{v}_a)\right] + \left(\Sigma_J^b-\Sigma_J^a\right)^2(\boldsymbol{H}_{ab}^{\mathrm{Ave}}\boldsymbol{N}_{ab})\cdot\left[\boldsymbol{\mathcal{S}}_{ab}^J\left(\boldsymbol{H}_{ab}^{\mathrm{Ave}}\boldsymbol{N}_{ab}\right)\right]\right]. \tag{4.39}$$

It is now easy to show that both positive definite stabilisation matrices $\{\boldsymbol{S}_{ab}^{\boldsymbol{p}}, \boldsymbol{S}_{ab}^J\}$, expressed in terms of the physical pressure $c_p$ and shear wave $c_s$ speeds (refer to Eq. (4.20)), guarantee non-negative local entropy production for every edge, that is $\dot{\mathcal{D}}_p^{ab}(t) \geq 0$. This demonstrates the entropy production for the semi-discrete scheme.

## 4.5 Conclusion

In this chapter, the mixed-based system of $\{\boldsymbol{p}, \boldsymbol{F}, \boldsymbol{H}, J, E \text{ or } \eta\}$ conservation laws, introduced in Chapter 2, is spatially discretised using a Vertex-Centred Finite Volume Method (VCFVM). A linear reconstruction procedure in conjunction with a slope limiter is presented with the objective of ensuring second order accuracy in space whilst avoiding numerical oscillations in the vicinity of sharp gradients, respectively. The contact flux approximations are introduced by means of an acoustic Riemann solver and, to this end, the non-negative local entropy production for every edge is ensured via the classical Coleman-Noll procedure.

Chapter 5

# Spatial discretisation: Smooth Particle Hydrodynamics

## 5.1 Introduction

This chapter provides a meshfree numerical methodology aimed at spatially discretising the set of mixed-based conservation laws Eq. (2.58) introduced in chapter 2. Firstly, the weak forms of the system of equations are expressed in Section 5.2 as the building blocks for the discretisation procedure. An introduction on the numerical scheme along with its features and capabilities is then presented in Section 5.3. The mixed-based formulations are then spatially discretised using both classical and edge-based Smooth Particle Hydrodynamics methodology in Section 5.4. The rate of entropy production of the SPH scheme is investigated in Section 5.5. Finally, a tailor-made artificial compressibility algorithm is suitably adapted to the SPH scheme aimed at extending the capability of the numerical algorithm to the limiting case of incompressibility. The schematic representation of the layout of this chapter is depicted in Figure 5.1.

## 5.2 Principle of Virtual Work

In general, a standard weak variational statement for the mixed-based system $\{\boldsymbol{p}, \boldsymbol{F}, \boldsymbol{H}, J, E \text{ or } \eta\}$ Eq. (2.58) (known as the Bubnov-Galerkin contribution $\mathcal{A}_{\text{Gal}}$) is established by multiplying the local form of the conservation laws Eq. (2.56) by appropriate work conjugate virtual fields $\delta\boldsymbol{\mathcal{V}}$ and integrating over the volume $\Omega_R$ of a continuum, to give

$$0 = \mathcal{A}_{\text{Gal}}(\boldsymbol{\mathcal{U}}, \delta\boldsymbol{\mathcal{V}}) := \int_{\Omega_R} \delta\boldsymbol{\mathcal{V}} \bullet \frac{\partial \boldsymbol{\mathcal{U}}}{\partial t}\, d\Omega_R - \int_{\Omega_R} \delta\boldsymbol{\mathcal{V}} \bullet \boldsymbol{\mathcal{S}}\, d\Omega_R + \int_{\Omega_R} \delta\boldsymbol{\mathcal{V}} \bullet \frac{\partial \boldsymbol{\mathcal{F}}_I}{\partial X_I}\, d\Omega_R. \tag{5.1}$$

The symbol $\bullet$ is used to denote the inner (dual) product of conjugate pairs, $\delta\boldsymbol{\mathcal{V}}$ represent the virtual power conjugates of the conservation variables $\boldsymbol{\mathcal{U}}$. In detail, $\delta\boldsymbol{\mathcal{V}}$ consists of $\delta\boldsymbol{v}$ as the virtual velocity field, $\{\delta\boldsymbol{\Sigma}_{\boldsymbol{F}}, \delta\boldsymbol{\Sigma}_{\boldsymbol{H}}, \delta\Sigma_J\}$ as appropriate conjugate stresses to $\{\boldsymbol{F}, \boldsymbol{H}, J\}$, $\delta\Sigma_E = C$ with $C$ representing a constant value and $\delta\theta$ as the conjugate variable of entropy, respectively.


FIGURE 5.1: Structure of Chapter 5

Application of the Green-Gauss divergence theorem on the last term of Eq. (5.1) results in

$$0 = \mathcal{A}_{\text{Gal}}(\boldsymbol{\mathcal{U}}, \delta\boldsymbol{\mathcal{V}}) := \int_{\Omega_R} \delta\boldsymbol{\mathcal{V}} \bullet \frac{\partial \boldsymbol{\mathcal{U}}}{\partial t}\, d\Omega_R - \int_{\Omega_R} \delta\boldsymbol{\mathcal{V}} \bullet \boldsymbol{\mathcal{S}}\, d\Omega_R - \int_{\Omega_R} \boldsymbol{\mathcal{F}}_I \bullet \frac{\partial \delta\boldsymbol{\mathcal{V}}}{\partial X_I}\, d\Omega_R + \int_{\partial\Omega_R} \delta\boldsymbol{\mathcal{V}} \bullet \boldsymbol{\mathcal{F}}_{\boldsymbol{N}}\, dA. \tag{5.2}$$

Above Galerkin representation (5.2) can be particularised to the case of the linear momentum $\boldsymbol{p}$, the extended set of geometric strain measures $\{\boldsymbol{F}, \boldsymbol{H}, J\}$ and the total energy $(E)$ of the system as

$$0 = \mathcal{A}^{\boldsymbol{p}}_{\text{Gal}} := \overbrace{\int_{\Omega_R} \delta\boldsymbol{v} \cdot \frac{\partial \boldsymbol{p}}{\partial t}\, d\Omega_R}^{\delta\mathcal{W}_{iner}} + \overbrace{\int_{\Omega_R} \boldsymbol{P} : \boldsymbol{\nabla}_R \delta\boldsymbol{v}\, d\Omega_R}^{\delta\mathcal{W}_{int}} - \overbrace{\left( \int_{\Omega_R} \delta\boldsymbol{v} \cdot \boldsymbol{f}_R\, d\Omega_R + \int_{\partial\Omega_R} \delta\boldsymbol{v} \cdot \boldsymbol{t}_B\, dA \right)}^{\delta\mathcal{W}_{ext}}; \tag{5.3a}$$

$$0 = \mathcal{A}^{\boldsymbol{F}}_{\text{Gal}} := \int_{\Omega_R} \delta\boldsymbol{\Sigma}_{\boldsymbol{F}} : \left[ \frac{\partial \boldsymbol{F}}{\partial t} - \boldsymbol{\nabla}_R \left( \frac{\boldsymbol{p}}{\rho_R} \right) \right] d\Omega_R; \tag{5.3b}$$

$$0 = \mathcal{A}^{\boldsymbol{H}}_{\text{Gal}} := \int_{\Omega_R} \delta\boldsymbol{\Sigma}_{\boldsymbol{H}} : \left[ \frac{\partial \boldsymbol{H}}{\partial t} - \boldsymbol{F} \times \boldsymbol{\nabla}_R \left( \frac{\boldsymbol{p}}{\rho_R} \right) \right] d\Omega_R; \tag{5.3c}$$

$$0 = \mathcal{A}^{J}_{\text{Gal}} := \int_{\Omega_R} \delta\Sigma_J \left[ \frac{\partial J}{\partial t} - \boldsymbol{H} : \boldsymbol{\nabla}_R \left( \frac{\boldsymbol{p}}{\rho_R} \right) \right] d\Omega_R; \tag{5.3d}$$

$$0 = \mathcal{A}^{E}_{\text{Gal}} := \int_{\Omega_R} \delta\Sigma_E \left[ \frac{\partial E}{\partial t} - \text{DIV}\left( \boldsymbol{P}^T \boldsymbol{v} - \boldsymbol{Q} \right) - \boldsymbol{f}_R \cdot \boldsymbol{v} - s_R \right] d\Omega_R; \tag{5.3e}$$

$$= \int_{\Omega_R} \delta\Sigma_E \frac{\partial E}{\partial t} - \int_{\partial\Omega_R} \delta\Sigma_E \left( \boldsymbol{v} \cdot \boldsymbol{t} - \boldsymbol{Q} \cdot \boldsymbol{N} \right) dA - \int_{\Omega_R} \delta\Sigma_E \left( \boldsymbol{f}_R \cdot \boldsymbol{v} + s_R \right) d\Omega_R,$$

with $\boldsymbol{t}_B$ being a possible boundary traction vector, $\delta\mathcal{W}_{iner}$ represents the inertial virtual power and $\delta\mathcal{W}_{int}$ and $\delta\mathcal{W}_{ext}$ stand for internal and external virtual powers, respectively. Notice that only the linear momentum conservation equation Eq. (5.3a) has been integrated by parts in order to enable the imposition of boundary tractions [3]. Alternatively, the total energy conservation, Eq. (5.3e), can be expressed in terms of entropy as

$$0 = \mathcal{A}^{\eta}_{\text{Gal}} := \int_{\Omega_R} \delta\theta \left[ \frac{\partial \eta}{\partial t} + \frac{1}{\theta} \text{DIV}\left( \boldsymbol{Q} \right) - \frac{s_R}{\theta} \right] d\Omega_R. \tag{5.4}$$

## 5.3 Smooth Particle Hydrodynamics

Smooth Particle Hydrodynamics (SPH) can be considered as the oldest modern particle method, initially developed by Lucy [129] and Gingold and Monaghan [130] in the 1970s. The method was first employed to tackle astrophysical and cosmological problems during the 1980s due to the resemblance between particle movements and liquid/gas flow movements. Therefore, it was considered suitable to model classical Newtonian hydrodynamics equations. The method is then becoming greatly mature as a result of the increased scrutiny and exploration during 1990s [178]. The Lagrangian mesh-free SPH method has been evolving since then and became a strong and reliable numerical tool to tackle several diverse ranges of applications in fluid mechanics such as free surface flows [210]. Considerable attention has also been shown on using

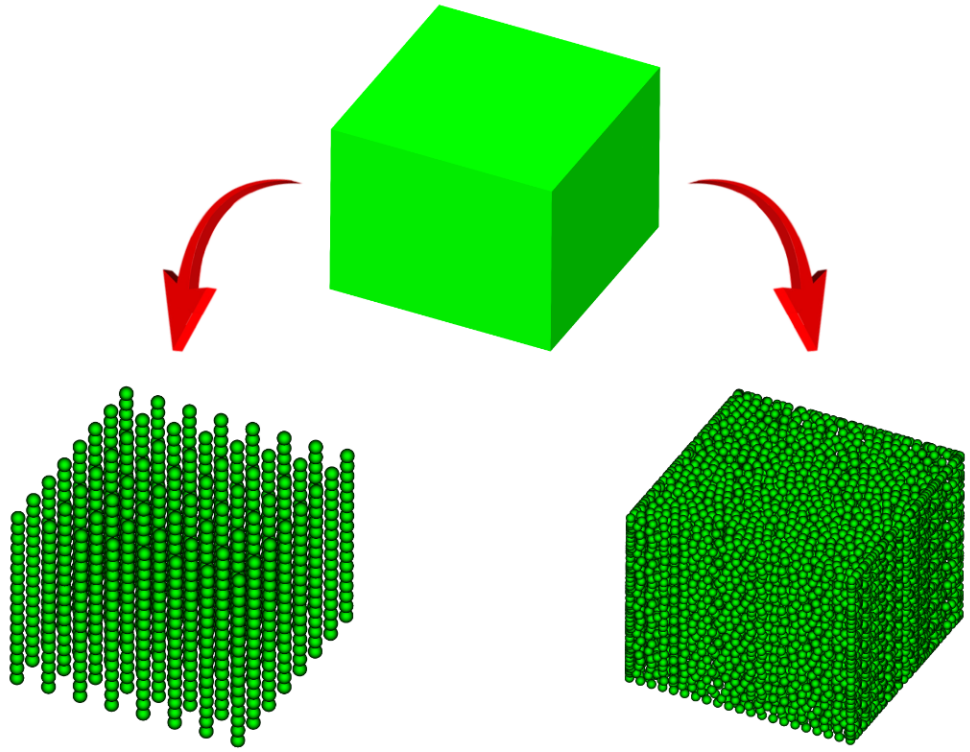

(a) Isometric view

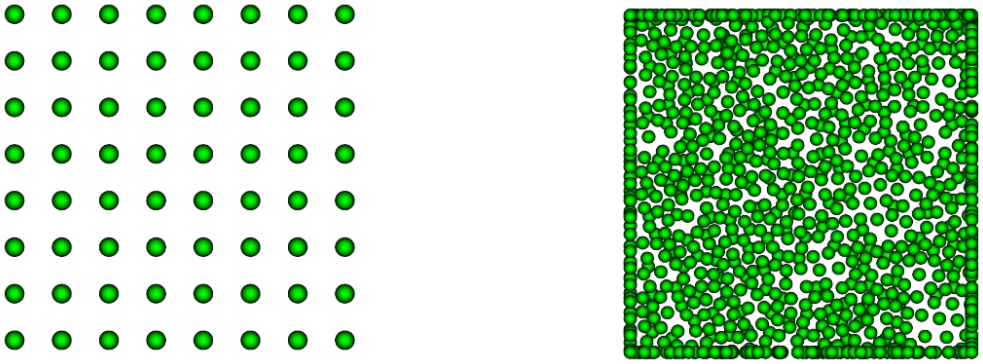

(b) Top view

FIGURE 5.2: Particle approximation of a physical domain using regular (left column) and irregular (right column) particle distributions

the SPH method in simulation of solid mechanic problems, application in metal forming, fracture and fragmentation, biomechanics and hypervelocity impacts [42, 124, 126, 147, 178, 211], to name a few.

The SPH method basically approximate a continuum into a number of scattered particles as it is illustrated in Figure 5.2. The particle distribution could be in a regular or an irregular order, which would affect the accuracy of the solution (see [27] for an extensive discussion). Once the domain is discretised, the value of a conservative quantity at a target particle will then be approximated based on the information stored at its neighbours through a kernel

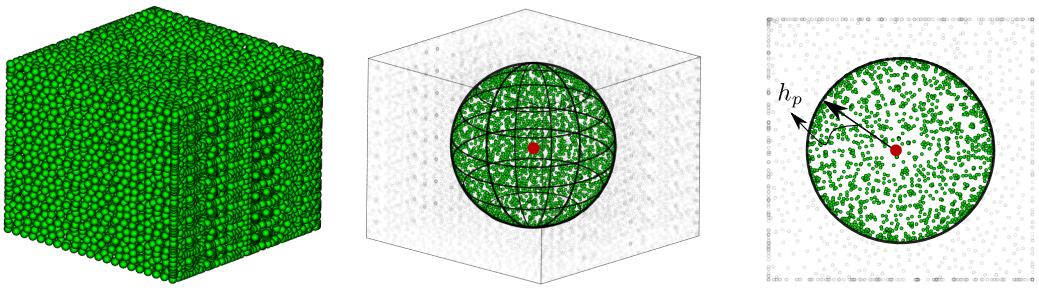


(a) Computational domain (b) Tributary volume (c) Compact support

FIGURE 5.3: Neighbouring particles associated to a target particle by a tributary volume

approximation. The neighbouring particles are those whose locations lie within the kernel's compact support of that particular target particle (see Figure 5.3).

### 5.3.1 Kernel approximation

The concept of interpolation in the SPH method can be expressed by following first the definition of the Dirac delta distribution

$$\delta(\boldsymbol{X}-\boldsymbol{X}') = \begin{cases} +\infty & \boldsymbol{X}=\boldsymbol{X}' \\ 0 & \boldsymbol{X}\neq\boldsymbol{X}' \end{cases} \qquad \forall \boldsymbol{X}\in\Omega_R, \tag{5.5}$$

which obeys the following useful properties

$$\begin{gathered} \int_{\Omega_R} \delta(\boldsymbol{X})d\Omega_R = 1; \\ \int_{\Omega'_R} \boldsymbol{\mathcal{U}}(\boldsymbol{X}')\,\delta(\boldsymbol{X}'-\boldsymbol{X})\,d\Omega'_R = \boldsymbol{\mathcal{U}}(\boldsymbol{X}). \end{gathered} \tag{5.6}$$

As the Dirac delta function is infinitely sharp and not integrable, it cannot be used for approximation purposes. Therefore and as an alternative, a smooth kernel function $W$ can be employed for approximating the value of a field $\boldsymbol{\mathcal{U}}(\boldsymbol{X}_a)$ as

$$\boldsymbol{\mathcal{U}}(\boldsymbol{X}) = \int_{\Omega'_R} \boldsymbol{\mathcal{U}}(\boldsymbol{X}')\,W(\boldsymbol{X}-\boldsymbol{X}',h_p)\,d\Omega'_R, \tag{5.7}$$

where $h_p$ is the so-called smoothing length defining the size of the compact support (or tributary volume) for the kernel interpolant (see Figure 5.3). This parameter is of paramount importance as it controls the accuracy of the interpolation in the SPH scheme [27]. By comparing Eq. (5.5) and Eq. (5.7), it is evident that if the kernel function tends to the Dirac delta, the approximated solution $\boldsymbol{\mathcal{U}}$ tends to the exact solution $\boldsymbol{\mathcal{U}}$. It is worth noticing that if the density of particle distribution varies in space, the smoothing length shall change accordingly to maintain the designated numerical accuracy. Nonetheless, this is not the case of the current work in which

the density of a continuum is regularly distributed between all the particles and therefore, a constant smoothing length will be required.

By virtue of Eq. (2.56), it is required to evaluate the derivative of a field variable using kernel approximation. In the case of the SPH methodology, the integral form of Eq. (5.7) will be approximated using particle (nodal) integration such that the value of quantity $\boldsymbol{\mathcal{U}}$ and its derivative at a material point $\boldsymbol{X}_a$ will be computed as

$$\boldsymbol{\mathcal{U}}(\boldsymbol{X}_a) \approx \sum_{b \in \Lambda_b^a} \Omega_R^b \boldsymbol{\mathcal{U}}(\boldsymbol{X}_b)\, W(\boldsymbol{X}_a - \boldsymbol{X}_b, h_p); \tag{5.8}$$

$$\nabla_R \boldsymbol{\mathcal{U}}(\boldsymbol{X}_a) \approx \sum_{b \in \Lambda_b^a} \Omega_R^b \boldsymbol{\mathcal{U}}(\boldsymbol{X}_b) \otimes \nabla_R W(\boldsymbol{X}_a - \boldsymbol{X}_b, h_p), \tag{5.9}$$

where, $b$ denotes the neighbouring particles associated to the tributary volume of the target particle $a$. For the rest of this thesis, $W(\boldsymbol{X}_a - \boldsymbol{X}_b, h_p)$ is replaced with $W_b(\boldsymbol{X}_a)$ for simplicity. In addition, a further assumptions are made on the interpolation described in Eq. (5.8) and Eq. (5.9) for computational efficiency, namely[125, 161],

$$\boldsymbol{\mathcal{U}}(\boldsymbol{X}_a) \approx \boldsymbol{\mathcal{U}}_a; \qquad \delta\boldsymbol{\mathcal{V}}(\boldsymbol{X}_a) \approx \delta\boldsymbol{\mathcal{V}}_a. \tag{5.10}$$

#### 5.3.1.1 Kernel functions

Since the development of the SPH method, a wide variety of kernel functions with different features are proposed. At the original SPH paper by Lucy [129], a smooth bell-shaped kernel function was employed. Gingold and Monaghan [130] utilised a Gaussian kernel which was sufficiently smooth even for high order derivatives. It is actually considered as a golden choice due to its reliable stability and accuracy, specifically for irregular particle distributions. However, this kernel function requires a large number of particles to shape its compact support and that leads to an expensive computational cost. Fulk and Quinn [212] investigated twenty kernel functions in one-dimensional space and concluded that the obtained results are well established for smooth data. They indicated, by contrast, that in the case of non-smooth data, the type of kernel plays a much less important role on the accuracy of the solution and the obtained results are generally not quite accurate. Morris [213] studied the effects of different kernels on the accuracy and stability of the SPH scheme and showed that its stability property will generally improve if higher order spline kernel interpolants are employed. Johnson et al. [214] used a quadratic smoothing kernel function to simulate high-velocity impact problems. Liu et al. [210] studied the kernel function mathematically and proposed a systematical way to construct a smoothing function that may meet different needs. Jin and Ding [215] analysed ten different kernels on a stable field and showed that Gaussian and Q-spline kernels can be considered as the most computationally accurate kernel functions among the others. Omang and his co-workers [216] presented an alternative kernel function for cylindrically symmetric systems and tested it on shock-dominated problems, resulting in a more efficient computational framework. The most frequently used kernel function can be considered as the Schoenberg cubic B-spline

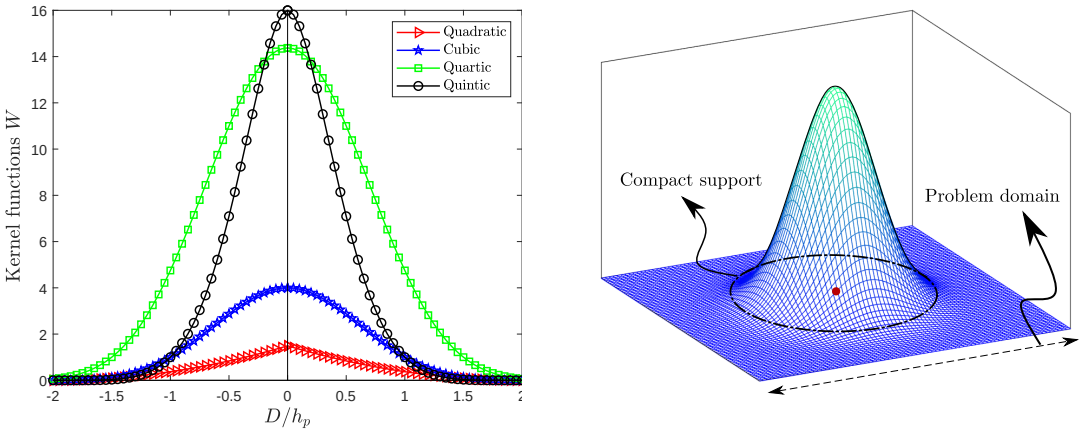


(a) (b)

FIGURE 5.4: Kernel interpolant function: (a) Different types of kernel functions and (b) a representative 3D kernel function

functions [217]. The cubic spline has narrow compact support along with the features of the Gaussian kernel. However, the second derivative of the cubic spline is a piecewise linear function which makes its stability inferior to those smoother kernels. Bonet et al. [161] proposed a fifth-order polynomial aimed at eliminating the spurious oscillations introduced by the classical cubic kernels.

In this thesis, a quadratic kernel function in three-dimensions is employed [214] as

$$W(\boldsymbol{X}, h_p) = \frac{\zeta}{\pi h_p^3}\left(1 - D + \frac{D^2}{4}\right), \tag{5.11}$$

where $D = \frac{||\boldsymbol{X}-\boldsymbol{X}_b||}{h_p}$ is the distance between a target particle and its neighbours and $\zeta = \frac{15}{16}$ is a user supplied coefficient usually considered within the range of $0.8 \leq \zeta \leq 1.5$. Figure 5.4a compares the employed quadratic kernel against some of the existing higher order kernel functions in the literature (quintic [161], quartic [218], cubic [217]). Additionally, an intuitive three-dimensional representative kernel is depicted in Figure 5.4b.

#### 5.3.1.2 Kernel properties

Crucially, an appropriate kernel function has to fulfil the following properties

- *Compact support*: the kernel function must have a compact support, shown in Figure 5.4b, as

$$W(\boldsymbol{X} - \boldsymbol{X}_b, h_p) = 0 \quad \text{for} \quad ||\boldsymbol{X} - \boldsymbol{X}_b|| > h_p. \tag{5.12}$$

- *Unity condition*: This condition indicates that the smooth kernel function must be normalised over its supported domain (analogous to the Dirac delta function property presented at Eq. (5.6)a),

$$\int_{\Omega_R^b} W(\boldsymbol{X} - \boldsymbol{X}', h_p) d\Omega_R' = 1. \tag{5.13}$$

- *Dirac delta condition*: The kernel interpolant must tend to Dirac delta function when the smoothing length tends to zero

$$\lim_{h_p \to 0} W(\boldsymbol{X} - \boldsymbol{X}_b, h_p) = \delta(\boldsymbol{X} - \boldsymbol{X}_b). \tag{5.14}$$

- *Positivity*: The kernel function has to be non-negative ($W(\boldsymbol{X} - \boldsymbol{X}_b) \geq 0$) within the compact support of a particle located at material point $\boldsymbol{X}$ for any material point $\boldsymbol{X}_b$. This is important to ensure a meaningful (or stable) representation of some physical phenomena like density in hydrodynamical simulations [27].
- *Monotonicity*: the kernel function must be monotonically decreasing while the interpolation is getting far away from a target particle. This means that the approximation of a variable in the target particle is more affected by the closer neighbouring particles.
- *Symmetry*: The kernel should be an even function meaning that neighbouring particles with the same distance but different locations form a target particle should have an equivalent effect on it. Although this property is useful for interpolation purposes, it is not a necessary condition.

#### 5.3.1.3 Kernel drawbacks

It is well-known that the basic kernel functions introduce a number of shortcomings into the SPH methodology [27, 161, 210], namely, (1) lack of consistency (or completeness); and (2) boundary inadequacy. The former stands for the capability of the kernel to accurately reproduce a polynomial of order $n$ ($n^{th}$ order reproducibility). The classical kernel functions are not even zeroth-order reproducible and that leads to an inaccurate interpolation. The latter entails that the basic SPH approximations are derived on the basis of an assumption where a full distribution of neighbouring particles is taken into account. This, however, is not the case when a target particle is located close to the boundary of the physical domain. In this occasion, the kernel is truncated by the physical boundary of the domain and, therefore, an inaccurate interpolation will be performed due to an insufficient number of neighbouring particles (i.e. no particle lies within the truncated compact support, see Figure 5.5). This can be interpreted as the lack of unity property for the kernel function. To rectify these shortcomings, a correction procedure is required for the kernel interpolant and its derivatives.

### 5.3.2 Consistent kernel approximation

During the past few decades, a considerable effort was devoted into proposing different correction approaches for the kernel interpolant and its gradients [133, 158, 159, 161, 177, 211, 217]. Moving Least Square (MLS) [219] and enforcing consistency condition [133] are two usual

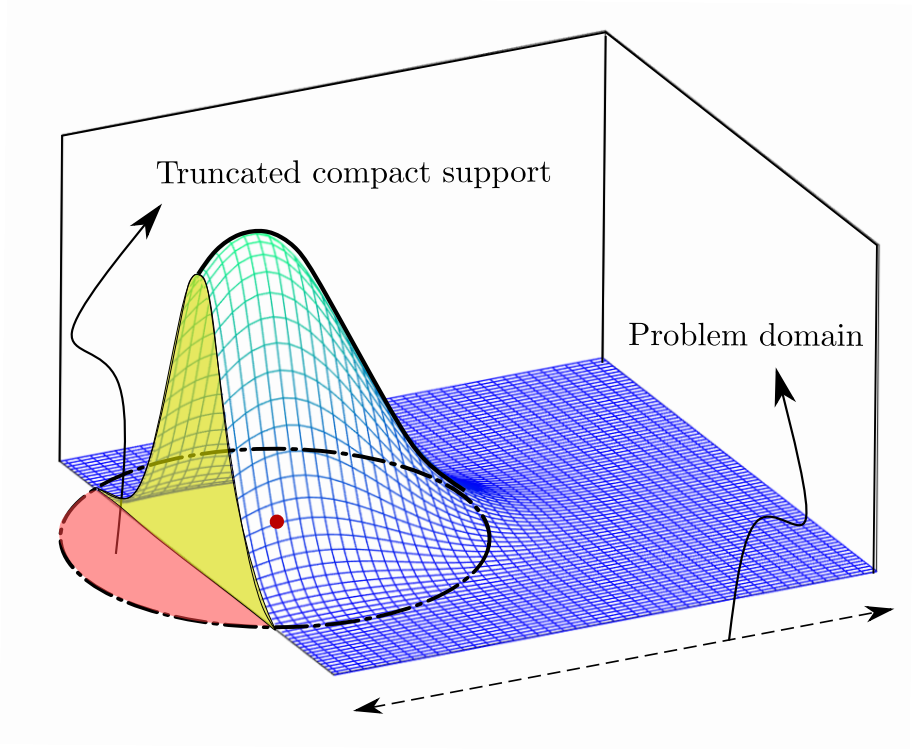


FIGURE 5.5: Boundary inadequacy in particle approximations

strategies to be employed for the kernel correction. The former basically approximate the kernel function using a least-square polynomial with a set of complete basis and that ensures the reproducibility of the kernel interpolant up to a certain order of accuracy. The latter is the interest of the current thesis and will be discussed in the following section.

#### 5.3.2.1 Corrected kernel

Liu et al. [133] introduced a set of adjusting factors ($\alpha$, $\boldsymbol{\beta}$) in the kernel function $W$ aimed at obtaining a reproducible kernel $\tilde{W}$ up to first order accuracy

$$\tilde{W}_b(\boldsymbol{X}) = W_b(\boldsymbol{X})\,\alpha(\boldsymbol{X})\,(1 + \boldsymbol{\beta}(\boldsymbol{X}) \cdot (\boldsymbol{X} - \boldsymbol{X}_b))\,. \tag{5.15}$$

The general integral form of constant and linear reproducibility constraints for the kernel function can be expressed as

$$\int_{\Omega_R} \tilde{W}(\boldsymbol{X}) d\Omega_R = 1; \tag{5.16a}$$

$$\int_{\Omega_R} \boldsymbol{X}\tilde{W}(\boldsymbol{X}) d\Omega_R = \boldsymbol{0}. \tag{5.16b}$$

Notice that the first consistency condition Eq. (5.16a) for constant reproducibility is equivalent to the unity condition Eq. (5.13). Considering the application of particle integration, as the

typical case in the SPH methodology, the above integrals can be discretised as

$$\sum_{b\in\Lambda_b^a} \Omega_R^b \tilde{W}_b(\boldsymbol{X}_a) = 1; \tag{5.17a}$$

$$\sum_{b\in\Lambda_b^a} \Omega_R^b \left(\boldsymbol{X}_a - \boldsymbol{X}_b\right) \tilde{W}_b(\boldsymbol{X}_a) = \boldsymbol{0}, \tag{5.17b}$$

where $a$ stands for a target particle and $b$ represents its neighbouring particles. Enforcing the consistency conditions (Eq. (5.17a)) into Eq. (5.15) leads to evaluation of the adjusting factor $\boldsymbol{\beta}(\boldsymbol{X})$ and subsequently $\alpha(\boldsymbol{X})$ as

$$\boldsymbol{\beta}(\boldsymbol{X}_a) = \left[\sum_{b\in\Lambda_a^b} \Omega_R^b (\boldsymbol{X}_a - \boldsymbol{X}_b) \otimes (\boldsymbol{X}_a - \boldsymbol{X}_b)\, W_b(\boldsymbol{X}_a)\right]^{-1} \sum_{b\in\Lambda_a^b} \Omega_R^b (\boldsymbol{X}_a - \boldsymbol{X}_b)\, W_b(\boldsymbol{X}_a); \tag{5.18a}$$

$$\alpha(\boldsymbol{X}_a) = \left(\sum_{b\in\Lambda_a^b} \Omega_R^b W_b(\boldsymbol{X}_a)\left[1 + \boldsymbol{\beta}(\boldsymbol{X})\cdot(\boldsymbol{X}_a - \boldsymbol{X}_b)\right]\right)^{-1}. \tag{5.18b}$$

The corrected kernel obtained with this strategy guarantees a reliable interpolation for a linear function and exact evaluation of its gradients. For simplicity, one may only consider the constant reproducibility in which $\boldsymbol{\beta}(\boldsymbol{X}) = \boldsymbol{0}$ and thus, the corrected kernel suitable for perfectly interpolating a constant function yields

$$\tilde{W}_b(\boldsymbol{X}_a) = \frac{W_b(\boldsymbol{X}_a)}{\underbrace{\sum_{b\in\Lambda_a^b} \Omega_R^b W_b(\boldsymbol{X}_a)}_{\alpha(\boldsymbol{X})}}. \tag{5.19}$$

#### 5.3.2.2 Corrected gradient of the standard kernel

Corrected Gradient of the Standard Kernel (CGSK) can be introduced using a correction matrix $\boldsymbol{L}$ as [211],

$$\tilde{\nabla}_R W_b(\boldsymbol{X}_a) = \boldsymbol{L}_a \nabla_R W_b(\boldsymbol{X}_a). \tag{5.20}$$

By enforcing that the following consistency condition is fulfilled by the corrected gradient of the standard kernel

$$\sum_{b\in\Lambda_a^b} \Omega_R^b (\boldsymbol{X}_b - \boldsymbol{X}_a) \otimes \nabla_R W_b(\boldsymbol{X}_a) = \boldsymbol{I}. \tag{5.21}$$

The correction matrix $\boldsymbol{L}_a$ can be evaluated for each particle as

$$\boldsymbol{L}_a = \left(\sum_{b\in\Lambda_a^b} \Omega_R^b (\boldsymbol{X}_b - \boldsymbol{X}_a) \otimes \nabla_R W_b(\boldsymbol{X}_a)\right)^{-1}. \tag{5.22}$$

This correction strategy ensures that the gradient of any linear (but not constant) field is exactly evaluated.

#### 5.3.2.3 Corrected gradient of the corrected kernel

An alternative correction approach is to combine the constant correction presented at Eq. (5.19) with the CGSK Eq. (5.20) [211]. To do so, the Corrected Gradient of the Corrected Kernel (CGCK) reads

$$\tilde{\nabla}_R \tilde{W}_b(\boldsymbol{X}_a) = \boldsymbol{L}_a \nabla_R \tilde{W}_b(\boldsymbol{X}_a), \tag{5.23}$$

where the gradient of the corrected kernel $\nabla_R \tilde{W}_b(\boldsymbol{X}_a)$ can be evaluated easily by differentiation of Eq. (5.19) which yields

$$\nabla_R \tilde{W}_b(\boldsymbol{X}_a) = \frac{\nabla_R W_b(\boldsymbol{X}_a) - \gamma(\boldsymbol{X}_a)}{\sum_{b\in\Lambda_a^b} \Omega_R^b W_b(\boldsymbol{X}_a)}; \qquad \gamma(\boldsymbol{X}_a) = \frac{\sum_{b\in\Lambda_a^b} \Omega_R^b \nabla_R W_b(\boldsymbol{X}_a)}{\sum_{b\in\Lambda_a^b} \Omega_R^b W_b(\boldsymbol{X}_a)}. \tag{5.24}$$

In addition, enforcing the consistency condition Eq. (5.20), this time in terms of CGCK, the correction matrix ($\boldsymbol{L}$) renders

$$\boldsymbol{L}_a = \left( \sum_{b\in\Lambda_a^b} \Omega_R^b \nabla_R \tilde{W}_b(\boldsymbol{X}_a) \otimes \boldsymbol{X}_b \right)^{-1}. \tag{5.25}$$

The CGCK strategy guarantees the perfect interpolation of a constant or a linear function and the exact evaluation of its derivatives. In other word, the CGCK is reproducible up to second order accuracy.

Having the corrected kernel and its corrected gradient, it is now possible to consistently approximate a field variable and its derivative using the SPH methodology as

$$\boldsymbol{\mathcal{U}}(\boldsymbol{X}_a) \approx \sum_{b\in\Lambda_b^a} \Omega_R^b \boldsymbol{\mathcal{U}}_b \tilde{W}_b(\boldsymbol{X}_a); \tag{5.26}$$

$$\nabla_R \boldsymbol{\mathcal{U}}(\boldsymbol{X}_a) \approx \sum_{b\in\Lambda_b^a} \Omega_R^b \left[\boldsymbol{\mathcal{U}}_b - \boldsymbol{\mathcal{U}}_a\right] \otimes \tilde{\nabla}_R W_b(\boldsymbol{X}_a). \tag{5.27}$$

It is worth noticing that the term $\boldsymbol{\mathcal{U}}_a$ is added into Eq. (5.27) in order to guarantee that the gradient vanishes for a uniform field (constant reproducibility) [177]. Alternatively, the gradient of a field variable can be evaluated using the CGCK approximation as

$$\nabla_R \boldsymbol{\mathcal{U}}(\boldsymbol{X}_a) \approx \sum_{b\in\Lambda_b^a} \Omega_R^b \boldsymbol{\mathcal{U}}_b \otimes \tilde{\nabla}_R \tilde{W}_b(\boldsymbol{X}_a). \tag{5.28}$$

## 5.4 Total Lagrangian SPH discretisation

Typically, in the context of Element Free Galerkin schemes [122, 220], the Galerkin weak statements described in Eq. (5.3) are accurately evaluated using the necessary distribution of (Gauss) quadrature points in order to avoid spurious hourglass (or zero-energy) modes [42, 155]. In general, the positions of these quadrature points do not coincide with those of the

material particles [220, 221]. This is, however, not the case when employing a mesh-free SPH discretisation in which above integrands Eq. (5.3) are under-integrated at the cloud of particles regarded as quadrature points [4, 107, 125, 176, 178].

The internal virtual power $\delta\mathcal{W}_{iner}$ (5.3a) can now be approximated using the SPH technique as

$$\delta\mathcal{W}_{iner} \approx \sum_a \Omega_R^a \delta\boldsymbol{v}(\boldsymbol{X}_a) \cdot \frac{\partial \boldsymbol{p}(\boldsymbol{X}_a, t)}{\partial t} \approx \Omega_R^a \sum_a \delta\boldsymbol{v}_a \cdot \frac{\partial \boldsymbol{p}_a}{\partial t}. \tag{5.29}$$

This clearly results in the introduction of a lumped mass matrix which is usually preferred in the application of explicit solid dynamics [4]. It is worth noticing that the lumped mass matrix does not alter the order of convergence of the algorithm [17, 23]. The external virtual power $\delta\mathcal{W}_{ext}$ comprised of external boundary tractions and body forces reads

$$\delta\mathcal{W}_{ext} \approx \sum_B A_B \delta\boldsymbol{v}_B \cdot \boldsymbol{t}_B + \sum_B \Omega_R^a \delta\boldsymbol{v}_a \cdot \boldsymbol{f}_R^a \tag{5.30a}$$

$$\approx \sum_a \Omega_R^a \delta\boldsymbol{v}_a \cdot \left( \underbrace{\frac{A_a}{\Omega_R^a}\boldsymbol{t}_a + \boldsymbol{f}_R^a}_{\boldsymbol{E}_a} \right), \tag{5.30b}$$

where $B$ represents a particle placed on the physical boundary, $A_B$ its material tributary area and $\boldsymbol{t}_B$ its traction vector computed directly from the given traction boundary conditions [6, 18, 118]. It must be noted that $A_a = 0$ for those particles not lying on the physical boundary. Finally, the approximation of the internal virtual power renders

$$\delta\mathcal{W}_{int} \approx \sum_b \Omega_R^b \boldsymbol{P}_b : \boldsymbol{\nabla}_R \delta\boldsymbol{v}(\boldsymbol{X}_b) \tag{5.31a}$$

$$\approx \sum_b \Omega_R^b \boldsymbol{P}_b : \left( \sum_{a \in \Lambda_a^b} \Omega_R^a \, (\delta\boldsymbol{v}_a - \delta\boldsymbol{v}_b) \otimes \tilde{\nabla}_R W_a(\boldsymbol{X}_b) \right) \tag{5.31b}$$

$$\approx \sum_a \Omega_R^a \delta\boldsymbol{v}_a : \left( \underbrace{\sum_{b \in \Lambda_b^a} \Omega_R^b \left( \boldsymbol{P}_b \tilde{\nabla}_R W_a(\boldsymbol{X}_b) - \boldsymbol{P}_a \tilde{\nabla}_R W_b(\boldsymbol{X}_a) \right)}_{\boldsymbol{T}_a} \right), \tag{5.31c}$$

where $\boldsymbol{P}_{a,b} := \boldsymbol{P}(\boldsymbol{F}_{a,b}, \boldsymbol{H}_{a,b}, J_{a,b})$ and the internal force representation $\boldsymbol{T}_a$ described in Eq. (5.31c) satisfies the global conservation of linear momentum, that is $\sum_a \Omega_R^a \boldsymbol{T}_a = \boldsymbol{0}$.

The extended set of geometric conservation laws along with conservation of total energy/entropy can analogously be approximated to yield the semi-discrete equations as

$$\frac{d\boldsymbol{p}_a}{dt} = \sum_{b\in\Lambda_a^b} \Omega_R^b \left(\boldsymbol{P}_a\tilde{\nabla}_R W_b(\boldsymbol{X}_a) - \boldsymbol{P}_b\tilde{\nabla}_R W_a(\boldsymbol{X}_b)\right) + \frac{A_a}{\Omega_R^a}\boldsymbol{t}_a + \boldsymbol{f}_R^a + \boldsymbol{\mathcal{D}}^{\boldsymbol{p}}; \tag{5.32a}$$

$$\frac{d\boldsymbol{F}_a}{dt} = \sum_{b\in\Lambda_a^b} \frac{1}{\rho_R}\Omega_R^b \left(\boldsymbol{p}_b - \boldsymbol{p}_a\right)\otimes\tilde{\nabla}_R W_b(\boldsymbol{X}_a); \tag{5.32b}$$

$$\frac{d\boldsymbol{H}_a}{dt} = \boldsymbol{F}_a \times \left(\sum_{b\in\Lambda_a^b} \frac{1}{\rho_R}\Omega_R^b \left(\boldsymbol{p}_b - \boldsymbol{p}_a\right)\otimes\tilde{\nabla}_R W_b(\boldsymbol{X}_a)\right); \tag{5.32c}$$

$$\frac{dJ_a}{dt} = \boldsymbol{H}_a : \left(\sum_{b\in\Lambda_a^b} \frac{1}{\rho_R}\Omega_R^b \left(\boldsymbol{p}_b - \boldsymbol{p}_a\right)\otimes\tilde{\nabla}_R W_b(\boldsymbol{X}_a)\right) + \mathcal{D}^J; \tag{5.32d}$$

$$\begin{aligned}\frac{dE_a}{dt} = &\sum_{b\in\Lambda_a^b} \frac{1}{\rho_R}\Omega_R^b \left[\left(\boldsymbol{P}_a\tilde{\nabla}_R W_b(\boldsymbol{X}_a)\right)\cdot\boldsymbol{p}_b - \left(\boldsymbol{P}_b\tilde{\nabla}_R W_a(\boldsymbol{X}_b)\right)\cdot\boldsymbol{p}_a\right] \\ &- \sum_{b\in\Lambda_a^b} \Omega_R^b \left(\boldsymbol{Q}_a\cdot\tilde{\nabla}_R W_b(\boldsymbol{X}_a) - \boldsymbol{Q}_b\cdot\tilde{\nabla}_R W_a(\boldsymbol{X}_b)\right) \\ &+ \boldsymbol{f}_R^a\cdot\frac{\boldsymbol{p}_a}{\rho_R} + s_R^a + \frac{A_a}{\Omega_R^a}\boldsymbol{t}_B^a\cdot\frac{\boldsymbol{p}_B^a}{\rho_R} - \frac{A_a}{\Omega_R^a}Q_B^a + \mathcal{D}^E,\end{aligned} \tag{5.32e}$$

where $\tilde{\nabla}_R W_b(\boldsymbol{X}_a)^{\text{Ave}} := \frac{1}{2}\left(\tilde{\nabla}_R W_b(\boldsymbol{X}_a) - \tilde{\nabla}_R W_a(\boldsymbol{X}_b)\right)$. Notice that Eq. (5.32c) and Eq. (5.32d) are the discrete form for Eq. (2.29) and Eq. (2.34), respectively. Additionally, the stabilisation terms for $\{\boldsymbol{p}, J, E\}$ equations reads

$$\boldsymbol{\mathcal{D}}^{\boldsymbol{p}} = \sum_{b\in\Lambda_a^b} \Omega_R^b \boldsymbol{P}_{ab}^{\text{Stab}}\tilde{\nabla}_R W_b(\boldsymbol{X}_a)^{\text{Ave}} + \boldsymbol{f}_R^a + \frac{A_a}{\Omega_R^a}\boldsymbol{t}_B^a; \tag{5.33a}$$

$$\mathcal{D}^J = \sum_{b\in\Lambda_a^b} \frac{1}{\rho_R}\Omega_R^b \boldsymbol{p}_{ab}^{\text{Stab}}\cdot\left(\boldsymbol{H}_a\tilde{\nabla}_R W_b(\boldsymbol{X}_a) - \boldsymbol{H}_b\tilde{\nabla}_R W_a(\boldsymbol{X}_b)\right); \tag{5.33b}$$

$$\mathcal{D}^E = \sum_{b\in\Lambda_a^b} \frac{1}{\rho_R}\Omega_R^b \left(\boldsymbol{p}_a + \boldsymbol{p}_b\right)\cdot\left(\boldsymbol{P}_{ab}^{\text{Stab}}\tilde{\nabla}_R W_b(\boldsymbol{X}_a)^{\text{Ave}}\right) + \sum_{b\in\Lambda_a^b} \frac{1}{\rho_R}\Omega_R^b \left(\Sigma_J^a + \Sigma_J^b\right)\tilde{\nabla}_R W_b(\boldsymbol{X}_a)^{\text{Ave}}\cdot\boldsymbol{p}_{ab}^{\text{Stab}}. \tag{5.33c}$$

In the case of entropy-based formulations where the equation of entropy evolution replaces the conservation of total energy, the semi-discrete set of $\{\boldsymbol{p}, \boldsymbol{F}, \boldsymbol{H}, J\}$ equations, as described in Eq. (5.32a)-Eq. (5.32d), remains exactly the same and the entropy equation can be spatially discretised as

$$\theta_a\frac{d\eta_a}{dt} = -\sum_{b\in\Lambda_a^b}\left(\Omega_R^b\boldsymbol{Q}_a\cdot\boldsymbol{\mathcal{C}}_{ab} - \boldsymbol{Q}_b\cdot\boldsymbol{\mathcal{C}}_{ba}\right) + \left[s_R^a - \frac{A_a}{\Omega_R^a}Q_B^a\right]. \tag{5.34}$$

Notice that no stabilisation is considered for the contact heat flux (i.e. $\boldsymbol{Q}_{ab}^C = \boldsymbol{Q}_{ab}^{\text{Ave}}$) due to its natural diffusive behaviour. The stabilisation terms $\{\boldsymbol{p}, \boldsymbol{P}\}$, as yet to be defined in Section 5.5,

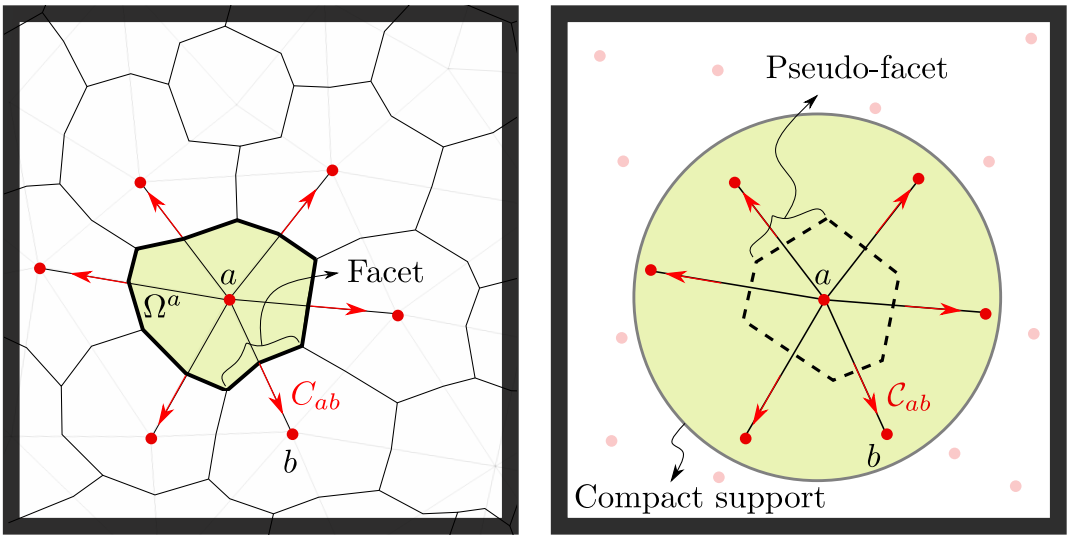


(a) (b)

FIGURE 5.6: Edge-based approach: (a) Vertex-Centred Finite Volume Method and (b) Smooth Particle Hydrodynamics

are the necessary requirements for the semi-discrete system of equations in order for numerical stability of the algorithm [7, 16, 17, 22, 32]. In addition, the spatial (deformed) geometry can be updated through the discrete nodal linear momentum field as

$$\frac{d\boldsymbol{x}_a}{dt} = \frac{\boldsymbol{p}_a}{\rho_R}. \tag{5.35}$$

Notice that the geometry update here is only for the post-processing purposes.

### 5.4.1 Alternative framework: Edge-based SPH

To approximate a field variable in the computational domain using the conventional SPH approach, a nested loop is required where the first (outer) loop is over the (target) particles and the second (inner) loop is over the neighbouring particles associated to a target particle. This, however, degrades the computational efficiency of the SPH algorithm. An alternative approach is the so-called edge-based SPH implementation which is somehow analogous to the edge-based FVM approach presented in the previous chapter (section 4.2.3). Figure 5.6 depicts the conceptual similarity of the edge-based approaches in the FVM and the SPH methodologies. In this case, two representative particles are connected together with a line (edges) along the direction of a pseudo-area vector, as yet to be defined. Hence, the approximation of a field variable only needs one loop over the edges and that results in ease of implementation and a computationally faster algorithm. To achieve this, it is first required to recall the VCFVM methodology where the discrete gradient evaluation within a dual control volume associated with node $a$ reads

$$\nabla_R \boldsymbol{\mathcal{U}}(\boldsymbol{X}_a) \approx \frac{1}{\Omega_R^a} \int_{\partial\Omega_R^a} \boldsymbol{\mathcal{U}}(\boldsymbol{X}) \otimes \boldsymbol{N} dA, \tag{5.36}$$

with $\boldsymbol{N}$ being the outward unit normal vector on the boundary of the dual control volume $\partial\Omega_R^a$. Above discrete boundary integral (5.36) can then be discretised by means of the Finite Volume Method where a (second order) central difference approximation is utilised for the discretisation of the vectorial function $\boldsymbol{\mathcal{U}}$, to give

$$\nabla_R \boldsymbol{\mathcal{U}}(\boldsymbol{X}_a) \approx \frac{1}{\Omega_R^a} \sum_{b \in \Lambda_b^a} \boldsymbol{\mathcal{U}}^{\mathrm{Ave}} \otimes \boldsymbol{C}_{ab}; \qquad \boldsymbol{\mathcal{U}}^{\mathrm{Ave}} = \frac{1}{2} \left[ \boldsymbol{\mathcal{U}}_a + \boldsymbol{\mathcal{U}}_b \right], \tag{5.37}$$

where $\boldsymbol{C}_{ab}$ is the area vector already defined in Eq. (4.5).

In addition, it has been proven in Ref. [211] that the CGSK reproduces exactly the gradient of any linear function and thus, Eq. (5.28), if necessary, can be alternatively expressed by artificially including the redundant term $-\boldsymbol{\mathcal{U}}_a$ as

$$\nabla_R \boldsymbol{\mathcal{U}}(\boldsymbol{X}_a) \approx \sum_{b \in \Lambda_b^a} 2\Omega_R^b \left( \frac{1}{2} \left[ \boldsymbol{\mathcal{U}}_b - \boldsymbol{\mathcal{U}}_a \right] \right) \otimes \tilde{\nabla}_R \tilde{W}_b(\boldsymbol{X}_a). \tag{5.38}$$

In this case, the term $(\boldsymbol{\mathcal{U}}_b - \boldsymbol{\mathcal{U}}_a)$ vanishes the gradient for a constant field and thus, the correction of the kernel function itself that ensures the constant reproducibility would be unnecessary. Hence, the CGCK at above expression (5.28) can be replaced with CGSK which is responsible for the linear reproducibility

$$\nabla_R \boldsymbol{\mathcal{U}}(\boldsymbol{X}_a) \approx \sum_{b \in \Lambda_b^a} 2\Omega_R^b \boldsymbol{\mathcal{U}}^{\mathrm{Ave}} \otimes \tilde{\nabla}_R W_b(\boldsymbol{X}_a); \qquad \boldsymbol{\mathcal{U}}^{\mathrm{Ave}} = \frac{1}{2} \left[ \boldsymbol{\mathcal{U}}_b + (-\boldsymbol{\mathcal{U}}_a) \right]. \tag{5.39}$$

Comparing Eq. (5.39) and Eq. (5.37), a useful relationship arises relating the (mesh-based) material outward normal area vector with the (mesh-free) SPH kernel gradient evaluation, defined as

$$\boxed{\boldsymbol{\mathcal{C}}_{ab}^{\mathrm{CGSK}} = 2\Omega_R^a \Omega_R^b \tilde{\nabla}_R W_b(\boldsymbol{X}_a),} \tag{5.40}$$

which can be known as the material pseudo-area vector where its reciprocal relationship can be defined as $\boldsymbol{\mathcal{C}}_{ba}^{\mathrm{CGSK}} = 2\Omega_R^a \Omega_R^b \tilde{\nabla}_R W_a(\boldsymbol{X}_b)$. Due to the anti-symmetric nature of the SPH gradient correction [161, 211], notice here that $\boldsymbol{\mathcal{C}}_{ab}^{\mathrm{CGSK}} \neq -\boldsymbol{\mathcal{C}}_{ba}^{\mathrm{CGSK}}$. It is imperative to remind that using $\boldsymbol{\mathcal{C}}_{ab}^{\mathrm{CGSK}}$ requires the application of $\boldsymbol{\mathcal{U}}^{\mathrm{Ave}}$ presented at Eq. (5.39).

*Remark* 10: An alternative representation for the evaluation of a kernel gradient can be formulated by adding the redundant term $\boldsymbol{\mathcal{U}}_a$ to Eq. (5.28), to give

$$\nabla_R \boldsymbol{\mathcal{U}}(\boldsymbol{X}_a) \approx \sum_{b \in \Lambda_b^a} 2\Omega_R^b \boldsymbol{\mathcal{U}}^{\mathrm{Ave}} \otimes \tilde{\nabla}_R \tilde{W}_b(\boldsymbol{X}_a); \qquad \boldsymbol{\mathcal{U}}^{\mathrm{Ave}} = \frac{1}{2}\left[\boldsymbol{\mathcal{U}}_a + \boldsymbol{\mathcal{U}}_b\right]. \tag{5.41}$$

By comparison of Eq. (5.38) with Eq. (5.37), one can present an alternative material pseudo-area vector constructed on the basis of the CGCK correction procedure as

$$\boxed{\boldsymbol{\mathcal{C}}_{ab}^{\mathrm{CGCK}} = 2\Omega_R^a \Omega_R^b \tilde{\nabla}_R \tilde{W}_b(\boldsymbol{X}_a),} \tag{5.42}$$

with its reciprocal relation defined as $\boldsymbol{\mathcal{C}}_{ba}^{\mathrm{CGCK}} = 2\Omega_R^a \Omega_R^b \tilde{\nabla}_R \tilde{W}_a(\boldsymbol{X}_b)$.

Considering the definition of the pseudo-area vectors, it is now possible to re-express the system of equations (5.32) as

$$\Omega_R^a \frac{d\boldsymbol{p}_a}{dt} = \sum_{b \in \Lambda_a^b} \frac{1}{2}\left(\boldsymbol{P}_a \boldsymbol{\mathcal{C}}_{ab} - \boldsymbol{P}_b \boldsymbol{\mathcal{C}}_{ba}\right) + \left[\Omega_R^a \boldsymbol{f}_R^a + A_a \boldsymbol{t}_B^a\right] + \boldsymbol{\mathcal{D}}_{ab}^{\boldsymbol{p}}; \tag{5.43a}$$

$$\Omega_R^a \frac{d\boldsymbol{F}_a}{dt} = \sum_{b \in \Lambda_a^b} \frac{1}{2\rho_R}\left(\boldsymbol{p}_b - \boldsymbol{p}_a\right) \otimes \boldsymbol{\mathcal{C}}_{ab}; \tag{5.43b}$$

$$\Omega_R^a \frac{d\boldsymbol{H}_a}{dt} = \boldsymbol{F}_a \times \left( \sum_{b \in \Lambda_a^b} \frac{1}{2\rho_R}\left(\boldsymbol{p}_b - \boldsymbol{p}_a\right) \otimes \boldsymbol{\mathcal{C}}_{ab} \right); \tag{5.43c}$$

$$\Omega_R^a \frac{dJ_a}{dt} = \boldsymbol{H}_a : \left( \sum_{b \in \Lambda_a^b} \frac{1}{2\rho_R}\left(\boldsymbol{p}_b - \boldsymbol{p}_a\right) \otimes \boldsymbol{\mathcal{C}}_{ab} \right) + \mathcal{D}_{ab}^{J}; \tag{5.43d}$$

$$\begin{aligned} \Omega_R^a \frac{dE_a}{dt} = & \sum_{b \in \Lambda_a^b} \frac{1}{2\rho_R}\left[\left(\boldsymbol{P}_a \boldsymbol{\mathcal{C}}_{ab}\right) \cdot \boldsymbol{p}_b - \left(\boldsymbol{P}_b \boldsymbol{\mathcal{C}}_{ba}\right) \cdot \boldsymbol{p}_a\right] + \Omega_R^a \boldsymbol{f}_R^a \cdot \frac{\boldsymbol{p}_a}{\rho_R} + \Omega_R^a s_R^a \\ & - \sum_{b \in \Lambda_a^b} \frac{1}{2}\left(\boldsymbol{Q}_a \cdot \boldsymbol{\mathcal{C}}_{ab} - \boldsymbol{Q}_b \cdot \boldsymbol{\mathcal{C}}_{ba}\right) - A_a Q_B^a + A_a \boldsymbol{t}_B^a \cdot \frac{\boldsymbol{p}_B^a}{\rho_R} + \mathcal{D}_{ab}^{E}, \end{aligned} \tag{5.43e}$$

where material and spatial pseudo-area vectors being defined as $\boldsymbol{\mathcal{C}}_{ab}^{\mathrm{Ave}} := \frac{1}{2}\left(\boldsymbol{\mathcal{C}}_{ab} - \boldsymbol{\mathcal{C}}_{ba}\right)$ and $\boldsymbol{c}_{ab}^{\mathrm{Ave}} := \frac{1}{2}\left(\boldsymbol{H}_a \boldsymbol{\mathcal{C}}_{ab} - \boldsymbol{H}_b \boldsymbol{\mathcal{C}}_{ba}\right)$, respectively. In addition, the chosen pseudo-area vector here is $\boldsymbol{\mathcal{C}}_{ab} = \boldsymbol{\mathcal{C}}_{ab}^{\mathrm{CGSK}}$, expressed at Eq. (5.40). Notice that Eq. (5.43c) and Eq. (5.43d) are the discrete form for Eq. (2.29) and Eq. (2.34), respectively. Moreover, the entropy evolution Eq. (5.34)

with the application of the pseudo-area vector ($\boldsymbol{\mathcal{C}}_{ab}^{\text{CGSK}}$) is re-written as

$$\Omega_R^a \theta_a \frac{d\eta_a}{dt} = -\sum_{b\in\Lambda_a^b} \frac{1}{2}\left(\boldsymbol{Q}_a \cdot \boldsymbol{\mathcal{C}}_{ab} - \boldsymbol{Q}_b \cdot \boldsymbol{\mathcal{C}}_{ba}\right) + \left[\Omega_R^a s_R^a - A_a Q_B^a\right]. \tag{5.44}$$

It is quite clear that the new mathematical representation of the system of conservation laws Eq. (5.43) is much more elegant than the classical version expressed at Eq. (5.32).

---

*Remark* 11: An alternative semi-discrete form of the system of equations (5.43a-5.43e) can be expressed on the basis of the CGCK correction procedure. In this case, the discrete form of the linear momentum Eq. (5.43a), entropy Eq. (5.44) and total energy Eq. (5.43e) remains identical as presented before whilst the geometric strains take the format of

$$\Omega_R^a \frac{d\boldsymbol{F}_a}{dt} = \sum_{b\in\Lambda_a^b} \frac{\boldsymbol{p}_b}{\rho_R} \otimes \boldsymbol{\mathcal{C}}_{ab}; \tag{5.45a}$$

$$\Omega_R^a \frac{d\boldsymbol{H}_a}{dt} = \boldsymbol{F}_a \times \left(\sum_{b\in\Lambda_a^b} \frac{\boldsymbol{p}_b}{\rho_R} \otimes \boldsymbol{\mathcal{C}}_{ab}\right); \tag{5.45b}$$

$$\Omega_R^a \frac{dJ_a}{dt} = \boldsymbol{H}_a : \left(\sum_{b\in\Lambda_a^b} \frac{\boldsymbol{p}_b}{\rho_R} \otimes \boldsymbol{\mathcal{C}}_{ab}\right) + \mathcal{D}_{ab}^J, \tag{5.45c}$$

where $\boldsymbol{\mathcal{C}}_{ab} = \boldsymbol{\mathcal{C}}_{ab}^{\text{CGCK}}$ is defined at Eq. (5.42).

---

The upwinding stabilisation terms $\{\boldsymbol{\mathcal{D}}_{ab}^{\boldsymbol{p}}, \mathcal{D}_{ab}^J, \mathcal{D}_{ab}^E\}$, presented in Eq. (5.43) can be obtained through the same procedure used in Section 4.3.2 which yields

$$\boldsymbol{\mathcal{D}}_{ab}^{\boldsymbol{p}} = \sum_{b\in\Lambda_a^b} \boldsymbol{P}_{ab}^{\text{Stab}} \boldsymbol{\mathcal{C}}_{ab}^{\text{Ave}}; \tag{5.46a}$$

$$\mathcal{D}_{ab}^J = \sum_{b\in\Lambda_a^b} \frac{1}{\rho_R} \boldsymbol{p}_{ab}^{\text{Stab}} \cdot \boldsymbol{c}_{ab}^{\text{Ave}}; \tag{5.46b}$$

$$\mathcal{D}_{ab}^E = \sum_{b\in\Lambda_a^b} \frac{1}{\rho_R} \boldsymbol{p}_{ab}^{\text{Ave}} \cdot \left(\boldsymbol{P}_{ab}^{\text{Stab}} \boldsymbol{\mathcal{C}}_{ab}^{\text{Ave}}\right) + \sum_{b\in\Lambda_a^b} \frac{1}{2\rho_R} \left(\Sigma_J^a + \Sigma_J^b\right) \boldsymbol{c}_{ab}^{\text{Ave}} \cdot \boldsymbol{p}_{ab}^{\text{Stab}}, \tag{5.46c}$$

where the stabilised contact fluxes are defined as

$$\boldsymbol{P}_{ab}^{\text{Stab}} := \boldsymbol{S}_{ab}^{\boldsymbol{p}} \left[(\boldsymbol{v}_b - \boldsymbol{v}_a) \otimes \frac{\boldsymbol{\mathcal{C}}_{ab}^{\text{Ave}}}{\|\boldsymbol{\mathcal{C}}_{ab}^{\text{Ave}}\|}\right]; \qquad \boldsymbol{v}_{ab}^{\text{Stab}} := \boldsymbol{S}_{ab}^J \left[\left(\Sigma_J^b - \Sigma_J^a\right) \frac{\boldsymbol{c}_{ab}^{\text{Ave}}}{\|\boldsymbol{c}_{ab}^{\text{Ave}}\|}\right], \tag{5.47}$$

and with the positive definite stabilisation matrices $\{\boldsymbol{S}_{ab}^{\boldsymbol{p}}, \boldsymbol{S}_{ab}^J\}$, already defined in Eq. (4.23).

The compatibility condition will be satisfied here by considering no stabilisations for the fluxes associated with the deformation gradient and the area map conservation laws (see Section 4.3.1). In addition, a linear reconstruction procedure and a slope limiter are utilised for the SPH scheme, identical to what has already been presented in Section 4.3.3. The former ensures second order accurate solution in space and the latter avoids the spurious oscillations of the solution in the vicinity of sharp gradients.

## 5.5 Coleman-Noll procedure

Following the same procedure as presented in Section 4.4, multiplying the semi-discrete equations (5.43) by their dual energy conjugate variables $\{\boldsymbol{v}, \boldsymbol{\Sigma}^a_{\boldsymbol{F}}, \boldsymbol{\Sigma}^a_{\boldsymbol{H}}, \Sigma^a_J, \theta_a\}$, and then summing up over all particles $a$ within the computational domain, which gives,

$$\sum_a \Omega^a_R \left[ \boldsymbol{v}_a \cdot \frac{d(\rho_R \boldsymbol{v}_a)}{dt} + \boldsymbol{\Sigma}^a_{\boldsymbol{F}} : \frac{d\boldsymbol{F}_a}{dt} + \boldsymbol{\Sigma}^a_{\boldsymbol{H}} : \frac{d\boldsymbol{H}_a}{dt} + \Sigma^a_J \frac{dJ_a}{dt} + \theta_a \frac{d\eta_a}{dt} \right] \tag{5.48a}$$

$$= \sum_a \sum_{b \in \Lambda^b_a} \frac{1}{2} \left[ (\boldsymbol{P}_a \boldsymbol{\mathcal{C}}_{ab}) \cdot \boldsymbol{v}_b - (\boldsymbol{P}_b \boldsymbol{\mathcal{C}}_{ba}) \cdot \boldsymbol{v}_a \right] - \sum_a \sum_{b \in \Lambda^b_a} \frac{1}{2} \left( \boldsymbol{Q}_a \cdot \boldsymbol{\mathcal{C}}_{ab} - \boldsymbol{Q}_b \cdot \boldsymbol{\mathcal{C}}_{ba} \right)$$

$$+ \sum_a \Omega^a_R \boldsymbol{v}_a \cdot \boldsymbol{f}^a_R + \sum_a \Omega^a_R s^a_R$$

$$+ \sum_a \sum_{b \in \Lambda^b_a} \left[ \boldsymbol{v}_a \cdot \left( \boldsymbol{P}^{\text{Stab}}_{ab} \boldsymbol{\mathcal{C}}^{\text{Ave}}_{ab} \right) + \Sigma^a_J \boldsymbol{v}^{\text{Stab}}_{ab} \cdot \boldsymbol{c}^{\text{Ave}}_{ab} - \boldsymbol{Q}^{\text{Stab}}_{ab} \cdot \boldsymbol{\mathcal{C}}^{\text{Ave}}_{ab} \right] \tag{5.48b}$$

$$= \sum_a \Omega^a_R \boldsymbol{v}_a \cdot \boldsymbol{f}^a_R + \sum_a \Omega^a_R s^a_R + \sum_a \sum_{b \in \Lambda^b_a} \left[ \boldsymbol{v}_a \cdot \left( \boldsymbol{P}^{\text{Stab}}_{ab} \boldsymbol{\mathcal{C}}^{\text{Ave}}_{ab} \right) + \Sigma^a_J \boldsymbol{v}^{\text{Stab}}_{ab} \cdot \boldsymbol{c}^{\text{Ave}}_{ab} \right], \tag{5.48c}$$

where $\boldsymbol{P}_a = \boldsymbol{\Sigma}^a_{\boldsymbol{F}} + \boldsymbol{\Sigma}^a_{\boldsymbol{H}} \times \boldsymbol{F}_a + \Sigma^a_J \boldsymbol{H}_a$. Notice here the nested summation carried out over particles, which implies that the summation over the non-stabilised terms in Eq. (5.48b) vanish as a result of their anti-symmetric nature and reduces into Eq. (5.48c).

Noticing that the rate of total energy is

$$\frac{dE_a}{dt} = \underbrace{\left[ \boldsymbol{v}_a \cdot \frac{d(\rho_R \boldsymbol{v}_a)}{dt} \right]}_{\frac{d\psi^a_{\text{kin}}}{dt}} + \underbrace{\left[ \boldsymbol{P}_a : \frac{d\boldsymbol{F}_a}{dt} \right]}_{\frac{d\psi^a_{\text{ela}}}{dt}} + \underbrace{\left[ \theta_a \frac{d\eta_a}{dt} \right]}_{\frac{d\psi^a_{\text{heat}}}{dt}} + \underbrace{[-\boldsymbol{v}_a \cdot \boldsymbol{f}^a_R - s^a_R]}_{\frac{d\psi^a_{\text{ext}}}{dt}}, \tag{5.49}$$

and re-arranging the above nested particle summation into a summation over edges by connecting neighbouring particles $a$ and $b$ (within a given compact support) yields

$$\sum_a \Omega^a_R \frac{dE_a}{dt} = - \sum_{\substack{\text{edges} \\ a \leftrightarrow b}} \left[ \boldsymbol{P}^{\text{Stab}}_{ab} : \left( (\boldsymbol{v}_b - \boldsymbol{v}_a) \otimes \boldsymbol{\mathcal{C}}^{\text{Ave}}_{ab} \right) + \boldsymbol{v}^{\text{Stab}}_{ab} \cdot \left( \left( \Sigma^b_J - \Sigma^a_J \right) \boldsymbol{c}^{\text{Ave}}_{ab} \right) \right]. \tag{5.50}$$

To guarantee non-negative (numerical) entropy production for every edge, which in this case is to ensure that the square bracket terms of Eq. (5.50) $\leq 0$, appropriate numerical stabilisation $\{\boldsymbol{P}^{\text{Stab}}_{ab}, \boldsymbol{v}^{\text{Stab}}_{ab}\}$ are utilised, expressed at Eq. (5.47). It is very interesting to observe how these

stabilisation terms are directly related to the difference in velocity $(\boldsymbol{v}_b - \boldsymbol{v}_a)$ and stress $(\Sigma_J^b - \Sigma_J^a)$ between neighbouring particles, typical of Riemann solver based upwinding terms.

## 5.6 Artificial compressibility: Isothermal hyperelasticity

### 5.6.1 General remark

In the case of nearly incompressible or truly incompressible materials, the volumetric wave speed $c_p$ reaches very large values yielding to restrictive small time steps [222]. This can substantially degrade the computational efficiency of any time-explicit algorithm. One relevant approach to rectify this issue is to employ artificial compressibility method, originally developed for the Navier-Stokes equations [180]. Considering an isothermal process, the artificial compressibility approach [23, 120] is here adapted to the system of Total Lagrangian conservation equations (described in Section 2.4.2) and then spatially discretised using the SPH scheme.

To do so, we initially require to re-express the volume map conservation law Eq. (2.34) in terms of its entropy conjugate, pressure, as

$$\frac{1}{\kappa}\frac{\partial p}{\partial t} = \boldsymbol{H} : \boldsymbol{\nabla}_R \left( \frac{\boldsymbol{p}}{\rho_R} \right). \tag{5.51}$$

Thus, the new unknown variables of the problem are $\{\boldsymbol{p}, \boldsymbol{F}, \boldsymbol{H}, p\}$ and this allows the consideration of the degenerate case of strict incompressibility.

Pursuing a similar procedure as fractional step type approach, it is necessary to first temporally discretise the continuum equations (2.10,2.21,2.29,2.34 and 5.51) and then proceed with their spatial discretisation. Additionally, the $\{\boldsymbol{p}, p\}$ will now be updated in a semi-implicit manner in order to enforce the incompressibility constraints without compromising the size of the time step as

$$\frac{\boldsymbol{p}^{n+1} - \boldsymbol{p}^n}{\Delta t} - \mathrm{DIV}\boldsymbol{P}(\boldsymbol{F}^n, \boldsymbol{H}^n, p^{n+1}) - \boldsymbol{f}_R^n = \boldsymbol{0}; \tag{5.52a}$$

$$\frac{p^{n+1} - p^n}{\kappa \Delta t} - \boldsymbol{H}^n : \boldsymbol{\nabla}_R \left( \frac{\boldsymbol{p}^{n+1}}{\rho_R} \right) = 0. \tag{5.52b}$$

It must be noted that both $\{\boldsymbol{F}, \boldsymbol{H}\}$ conservation equations are still going to be solved explicitly.

In order to solve Eq. (5.52), a predictor-corrector algorithm is used. The algorithm is first advanced explicitly yielding intermediate variables $\{\boldsymbol{p}^{\mathrm{int}}, p^{\mathrm{int}}\}$ which are then projected after

iteratively solving an implicit system known as pressure correction. Therefore, the first (predictor or intermediate) step of the scheme over a time step $\Delta t$ is defined as

$$\frac{\left(\boldsymbol{p}^{\text{int}} - \boldsymbol{p}^{n}\right)}{\Delta t} - \text{DIV}\boldsymbol{P}(\boldsymbol{F}^{n}, \boldsymbol{H}^{n}, p^{n}) - \boldsymbol{f}_{R}^{n} = \boldsymbol{0}; \tag{5.53a}$$

$$\frac{\boldsymbol{F}^{n+1} - \boldsymbol{F}^{n}}{\Delta t} - \boldsymbol{\nabla}_{R}\left(\frac{\boldsymbol{p}^{n}}{\rho_{R}}\right) = \boldsymbol{0}; \tag{5.53b}$$

$$\frac{\boldsymbol{H}^{n+1} - \boldsymbol{H}^{n}}{\Delta t} - \boldsymbol{F}^{n} \times \boldsymbol{\nabla}_{R}\left(\frac{\boldsymbol{p}^{n}}{\rho_{R}}\right) = \boldsymbol{0}; \tag{5.53c}$$

$$\frac{1}{\kappa}\frac{p^{\text{int}} - p^{n}}{\Delta t} - \boldsymbol{H}^{n} : \boldsymbol{\nabla}_{R}\left(\frac{\boldsymbol{p}^{n}}{\rho_{R}}\right) = 0. \tag{5.53d}$$

The second (corrector or projection) step reads

$$\frac{\left(\boldsymbol{p}^{n+1} - \boldsymbol{p}^{\text{int}}\right)}{\Delta t} - \text{DIV}\left[\left(p^{n+1} - p^{n}\right)\boldsymbol{H}^{n}\right] = \boldsymbol{0}; \tag{5.54a}$$

$$\frac{1}{\kappa}\frac{\left(p^{n+1} - p^{\text{int}}\right)}{\Delta t} - \boldsymbol{H}^{n} : \boldsymbol{\nabla}_{R}\left(\frac{\boldsymbol{p}^{n+1}}{\rho_{R}} - \frac{\boldsymbol{p}^{n}}{\rho_{R}}\right) = 0. \tag{5.54b}$$

It is of paramount importance to note that addition of equations (5.53a) and (5.54a) (and 5.53d and 5.54b) recovers the original equations (5.52a and 5.52b). For nearly and truly incompressible materials, the bulk modulus present in the first term of equation Eq. (5.53d) can potentially reach very high values (even infinite), leading to extremely small time steps. This will then destroy the explicit nature of the predictor step of the scheme. Consequently, that has replaced with a fictitious bulk modulus $\tilde{\kappa}$, yielding

$$\frac{1}{\tilde{\kappa}}\frac{p^{\text{int}} - p^{n}}{\Delta t} - \boldsymbol{H}^{n} : \boldsymbol{\nabla}_{R}\left(\frac{\boldsymbol{p}^{n}}{\rho_{R}}\right) = 0. \tag{5.55}$$

As a result of this, the projection step of the pressure equation Eq. (5.54b) consistently turns to

$$\frac{1}{\kappa}\frac{\left(p^{n+1} - p^{n}\right)}{\Delta t} - \frac{1}{\tilde{\kappa}}\frac{p^{\text{int}} - p^{n}}{\Delta t} - \boldsymbol{H}^{n} : \boldsymbol{\nabla}_{R}\left(\frac{\boldsymbol{p}^{n+1}}{\rho_{R}} - \frac{\boldsymbol{p}^{n}}{\rho_{R}}\right) = 0. \tag{5.56}$$

Finally, in order to solve the implicit system for the correction step (refer to (5.54a) and (5.56)) through a matrix-free approach, the artificial compressibility algorithm is further exploited. This is obtained through the introduction of "pseudo-time" derivative terms ($\frac{\partial}{\partial \tau}$) allowing the explicit evolution of the corrector equations in pseudo-time until convergence. Hence,

$$\frac{\partial \boldsymbol{p}}{\partial \tau} = \text{DIV}\left[\left(p^{n+1} - p^{n}\right)\boldsymbol{H}^{n}\right] - \frac{\left(\boldsymbol{p}^{n+1} - \boldsymbol{p}^{\text{int}}\right)}{\Delta t}; \tag{5.57a}$$

$$\frac{1}{\gamma}\frac{\partial p}{\partial \tau} = \frac{1}{\tilde{\kappa}}\frac{p^{\text{int}} - p^{n}}{\Delta t} + \boldsymbol{H}^{n} : \boldsymbol{\nabla}_{R}\left(\frac{\boldsymbol{p}^{n+1}}{\rho_{R}} - \frac{\boldsymbol{p}^{n}}{\rho_{R}}\right) - \frac{1}{\kappa}\frac{\left(p^{n+1} - p^{n}\right)}{\Delta t}, \tag{5.57b}$$

where $\gamma$ represents the artificial compressibility parameter. In this thesis, the pseudo-time terms are advanced in time using exactly the same time integrator described in Eq. (6.1)-Eq. (6.3). The upwind SPH spatial discretisation for the predictor-corrector system (5.53a, 5.53b, 5.53c, 5.55, 5.57a, 5.57b) will be presented in the following section.

---

*Remark* 12: An alternative approach for treating truly incompressibility is also presented here for completeness. In this approach which is on the basis of a pressure Poisson equation [23, 120], the pressure correction can be re-expressed by substituting Eq. (5.54b) into Eq. (5.52b) for $\boldsymbol{p}^{n+1}$ as

$$\frac{1}{\kappa}\frac{\left(p^{n+1}-p^{n}\right)}{\Delta t}-\Delta t\boldsymbol{H}^{n}:\boldsymbol{\nabla}_{R}\left(\frac{\boldsymbol{p}^{\text{int}}}{\rho_{R}}\right)-\boldsymbol{H}^{n}:\boldsymbol{\nabla}_{R}\left[\text{DIV}\left(\frac{1}{\rho_{R}}\left(p^{n+1}-p^{n}\right)\boldsymbol{H}^{n}\right)\right]=0. \tag{5.58}$$

To obtain the pressure increment, Eq. (5.58) needs the solution of a system of nonlinear equations at each time step. This is indeed not computationally efficient when aiming for large scale simulations, hence not pursued in this thesis.

---

It is worthwhile to remind that the presented artificial compressibility algorithm is just suited for the particular case of a reversible isothermal process and, therefore, the set of equations should be derived appropriately, in the other cases such as thermo-elasticity.

### 5.6.2 SPH artificial compressibility algorithm

For treatment of nearly incompressible and truly incompressible materials, analogous to what has already been described in Section 5.6.1, an artificial compressibility algorithm is presented. Hence, and considering SPH discretisation technique presented at Eq. (5.32), the predictor step of the mixed-based system $\{\boldsymbol{p},\boldsymbol{F},\boldsymbol{H},p\}$ reads

$$\frac{\boldsymbol{p}_{a}^{\text{int}}-\boldsymbol{p}_{a}^{n}}{\Delta t}=\boldsymbol{E}_{a}^{n}-\boldsymbol{T}_{a}^{n}+\boldsymbol{\mathcal{D}}(\boldsymbol{p}_{a}^{n}); \tag{5.59a}$$

$$\Omega_{R}^{a}\frac{\boldsymbol{F}_{a}^{n+1}-\boldsymbol{F}_{a}^{n}}{\Delta t}=\sum_{b\in\Lambda_{a}^{b}}\frac{1}{2}\left(\frac{\boldsymbol{p}_{b}^{n}}{\rho_{R}}\right)\otimes\boldsymbol{\mathcal{C}}_{ab}; \tag{5.59b}$$

$$\Omega_{R}^{a}\frac{\boldsymbol{H}_{a}^{n+1}-\boldsymbol{H}_{a}^{n}}{\Delta t}=\boldsymbol{F}_{a}^{n}\boldsymbol{\times}\sum_{b\in\Lambda_{a}^{b}}\frac{1}{2}\left(\frac{\boldsymbol{p}_{b}^{n}}{\rho_{R}}\right)\otimes\boldsymbol{\mathcal{C}}_{ab}; \tag{5.59c}$$

$$\Omega_{R}^{a}\frac{1}{\tilde{\kappa}}\frac{p_{a}^{\text{int}}-p_{a}^{n}}{\Delta t}=\boldsymbol{H}_{a}^{n}:\sum_{b\in\Lambda_{a}^{b}}\frac{1}{2}\left(\frac{\boldsymbol{p}_{b}^{n}}{\rho_{R}}\right)\otimes\boldsymbol{\mathcal{C}}_{ab}+\mathcal{D}(J_{a}^{n}), \tag{5.59d}$$

where the external and internal force vectors $\{\boldsymbol{E}_{a},\boldsymbol{T}_{a}\}$ are defined in Eq. (5.30) and Eq. (5.31), respectively. Moreover, $\{\boldsymbol{\mathcal{D}}(\boldsymbol{p}_{a}^{n}),\mathcal{D}(J_{a}^{n})\}$ are the stabilising terms, already defined in Eq. (5.46).

Furthermore, the corrector step of the discrete system $\{\boldsymbol{p},\boldsymbol{F},\boldsymbol{H},p\}$ renders

$$\frac{d\boldsymbol{p}_{a}}{d\tau}=\frac{1}{2\Omega_{R}^{a}}\sum_{b\in\Lambda_{a}^{b}}\left[\left(p_{b}^{n+1}-p_{b}^{n}\right)\boldsymbol{H}_{b}^{n}\right]\boldsymbol{\mathcal{C}}_{ab}-\frac{\left(\boldsymbol{p}_{a}^{n+1}-\boldsymbol{p}_{a}^{\text{int}}\right)}{\Delta t}; \tag{5.60a}$$

$$\frac{1}{\gamma}\frac{dp_{a}}{d\tau}=\frac{1}{\tilde{\kappa}}\frac{p_{a}^{\text{int}}-p_{a}^{n}}{\Delta t}-\frac{1}{\kappa}\frac{\left(p_{a}^{n+1}-p_{a}^{n}\right)}{\Delta t}+\frac{1}{2\Omega_{R}^{a}}\boldsymbol{H}_{a}^{n}:\sum_{b\in\Lambda_{a}^{b}}\left(\frac{\boldsymbol{p}_{b}^{n+1}}{\rho_{R}}-\frac{\boldsymbol{p}_{b}^{n}}{\rho_{R}}\right)\otimes\boldsymbol{\mathcal{C}}_{ab}. \tag{5.60b}$$

At each time step $\Delta t$, above system (5.60) is iteratively solved for the linear momentum and pressure within the pseudo time integration in order to obtain convergence to a pseudo steady state (e.g. $\frac{d\boldsymbol{p}_a}{d\tau} \approx \mathbf{0}$ and $\frac{dp_a}{d\tau} \approx 0$).

### 5.6.3 Iteration speed-up procedure

It is possible to incorporate an additional Laplacian (or harmonic) dissipative operator to Eq. (5.60b) in order to speed-up the convergence within the iterative process

$$\frac{1}{\gamma}\frac{dp_a}{d\tau} = \frac{1}{\tilde{\kappa}}\frac{p_a^{\text{int}} - p_a^n}{\Delta t} - \frac{1}{\kappa}\frac{\left(p_a^{n+1} - p_a^n\right)}{\Delta t} + \frac{1}{2\Omega_R^a}\boldsymbol{H}_a^n : \sum_{b\in\Lambda_a^b}\left(\frac{\boldsymbol{p}_b^{n+1}}{\rho_R} - \frac{\boldsymbol{p}_b^n}{\rho_R}\right)\otimes\boldsymbol{\mathcal{C}}_{ab} + \mathcal{D}_{\text{PSE}}(p_a). \quad (5.61)$$

The discrete pseudo viscosity term at particle $a$ can be expressed as

$$\mathcal{D}_{\text{PSE}}(p_a) := \eta\mathcal{L}\left[p(\boldsymbol{X}_a)\right]; \qquad \eta = \alpha_{\mathcal{D}}\frac{c_s^2\Delta t}{\mu}, \quad (5.62)$$

where $\alpha_{\mathcal{D}}$ is a dimensionless user-defined parameter in the range of $[0, 1]$. It is now crucially important to know how the (particle-based) Laplacian dissipative operator should be approximated such that the satisfaction of global conservation requirement, that is $\sum_a \Omega_R^a\mathcal{D}_{\text{PSE}}(p_a) = 0$, is guaranteed. To do so, consider the Laplacian of any arbitrary scalar function $\mathcal{U}$ to be numerically approximated as

$$\mathcal{L}\left[\mathcal{U}(\boldsymbol{X}_a)\right] := \boldsymbol{\nabla}_R\cdot\left[\boldsymbol{\nabla}_R\mathcal{U}(\boldsymbol{X}_a)\right] \approx \sum_{b\in\Lambda_a^b}\Omega_R^b\boldsymbol{\nabla}_R\mathcal{U}(\boldsymbol{X}_b)\cdot\tilde{\boldsymbol{\nabla}}_R\tilde{W}_b(\boldsymbol{X}_a). \quad (5.63)$$

Addition of the redundant term $\boldsymbol{\nabla}_R\mathcal{U}(\boldsymbol{X}_a)$ to Eq. (5.63) yields an alternative expression as

$$\mathcal{L}\left[\mathcal{U}(\boldsymbol{X}_a)\right] \approx \sum_{b\in\Lambda_a^b} 2\Omega_R^b\left[\frac{\boldsymbol{\nabla}_R\mathcal{U}(\boldsymbol{X}_a) + \boldsymbol{\nabla}_R\mathcal{U}(\boldsymbol{X}_b)}{2}\right]\cdot\tilde{\boldsymbol{\nabla}}_R\tilde{W}_b(\boldsymbol{X}_a). \quad (5.64)$$

It is worth mentioning that the squared bracket term, shown in Eq. (5.64) denotes the gradient approximation at the mid-edge connecting particles $a$ and $b$. This can be further approximated via a second order central difference scheme as [223]

$$\left[\frac{\boldsymbol{\nabla}_R\mathcal{U}(\boldsymbol{X}_a) + \boldsymbol{\nabla}_R\mathcal{U}(\boldsymbol{X}_b)}{2}\right] \approx \frac{\mathcal{U}_b - \mathcal{U}_a}{\|\boldsymbol{X}_b - \boldsymbol{X}_a\|}\boldsymbol{N}_{ab}, \qquad \boldsymbol{N}_{ab} := \frac{\boldsymbol{X}_b - \boldsymbol{X}_a}{\|\boldsymbol{X}_b - \boldsymbol{X}_a\|}. \quad (5.65)$$

The normal $\boldsymbol{N}_{ab}$ is defined here as a direction vector connecting particles $a$ to $b$ (see Figure 5.6).

Finally, substitution of Eq. (5.65) into Eq. (5.64) and replacing the scalar function $\mathcal{U}$ with pressure $p$ result in the discrete version of the Laplacian evaluation

$$\mathcal{L}\left[p(\boldsymbol{X}_a)\right] \approx 2\sum_{b\in\Lambda_a^b}\Omega_R^b\left[\frac{p_b - p_a}{\|\boldsymbol{X}_b - \boldsymbol{X}_a\|}\boldsymbol{N}_{ab}\right]\cdot\tilde{\boldsymbol{\nabla}}_R\tilde{W}_b(\boldsymbol{X}_a). \quad (5.66)$$

Unfortunately, the evaluation of Laplacian operator prevents the exact global conservation due to the lack of symmetry of the kernel gradient correction, that is $\tilde{\boldsymbol{\nabla}}_R \tilde{W}_b(\boldsymbol{X}_a) \neq \tilde{\boldsymbol{\nabla}}_R \tilde{W}_a(\boldsymbol{X}_b)$. This issue can also be addressed by replacing $\tilde{\boldsymbol{\nabla}}_R \tilde{W}_b(\boldsymbol{X}_a)$ with $\tilde{\boldsymbol{\nabla}}_R \tilde{W}_b^{\mathrm{Ave}}(\boldsymbol{X}_a)$ defined as

$$\tilde{\boldsymbol{\nabla}}_R \tilde{W}_b^{\mathrm{Ave}}(\boldsymbol{X}_a) := \frac{1}{2}\left(\tilde{\boldsymbol{\nabla}}_R \tilde{W}_b(\boldsymbol{X}_a) - \tilde{\boldsymbol{\nabla}}_R \tilde{W}_a(\boldsymbol{X}_b)\right). \tag{5.67}$$

---

*Remark* 13: An alternative approach to approximate the (globally conservative) Laplacian evaluation of the pressure variable $p$ can be expressed as [4]

$$\mathcal{L}\left[p(\boldsymbol{X}_a)\right] \approx \sum_{b \in \Lambda_a^b} \Omega_R^b \left[p_b - p_a\right] \tilde{\Delta}_R W_b^{\mathrm{Ave}}(\boldsymbol{X}_a), \tag{5.68}$$

where $\tilde{\Delta}_R W_b^{\mathrm{Ave}}(\boldsymbol{X}_a)$ reads

$$\tilde{\Delta}_R W_b^{\mathrm{Ave}}(\boldsymbol{X}_a) := \frac{1}{2}\left[\tilde{\Delta}_R W_b(\boldsymbol{X}_a) + \tilde{\Delta}_R W_a(\boldsymbol{X}_b)\right], \tag{5.69}$$

where the corrected Laplacian approximation $\tilde{\Delta}_R$ can be obtained through a least-square minimisation procedure (see Appendix A in [4] for further details). This, however, needs the solution of a system of equations and, therefore not pursued in this thesis.

---

Hence, the discrete pseudo viscosity operator can be described as

$$\mathcal{D}_{\mathrm{PSE}}(p_a) \approx 2\eta \sum_{b \in \Lambda_a^b} \Omega_R^b \left[\frac{p_b - p_a}{\|\boldsymbol{X}_b - \boldsymbol{X}_a\|} \boldsymbol{N}_{ab}\right] \cdot \tilde{\boldsymbol{\nabla}}_R \tilde{W}_b^{\mathrm{Ave}}(\boldsymbol{X}_a). \tag{5.70}$$

For completeness, the artificial compressibility algorithm for the VCFVM scheme is also presented in details at Appendix C.

## 5.7 Conclusion

In this chapter, the mixed-based system of $\{\boldsymbol{p}, \boldsymbol{F}, \boldsymbol{H}, J, E \text{ or } \eta\}$ equations (see Chapter 2), is spatially discretised using a Smooth Particle Hydrodynamics (SPH) scheme. Both the classical and edge-based SPH implementations are introduced where the latter has resulted in a dramatical decrease in computational cost. A linear reconstruction procedure and a slope limiter are presented in order to guarantee second order accuracy in space and avoiding spurious numerical oscillations in the vicinity of sharp gradients, respectively. The rate of local entropy production is guaranteed via a classical Coleman-Noll procedure. Finally, a tailor-made artificial compressibility algorithm is adapted to the SPH methodology in order for the limiting case of isothermal incompressibility.

Chapter 6

# Temporal discretisation

## 6.1 Introduction

The semi-discrete system of equations given in Chapter 4 for Vertex-Centred Finite Volume Method (VCFVM) and Chapter 5 for Smooth Particle Hydrodynamics scheme has to be updated in time using an appropriate time integrator, as discussed in Section 6.2. To achieve this, Section 6.3 introduces an explicit one-step two-stage Total Variation Diminishing (TVD) Runge-Kutta scheme by which second order accuracy in time is guaranteed. Due to the explicit nature of the time integrator, a stability condition is provided in Section 6.3.1. Additionally, a consistency and a von Neumann stability analyses are performed in Section 6.5. Finally, a complete algorithmic description of the proposed VCFVM and SPH schemes is presented in Section 6.4. The schematic representation of this chapter is depicted in Figure 6.1.

## 6.2 Time integrator

The objective of the current thesis is to simulate the solution of fast transient large strain solid dynamics problems. This entails a time integrator for the evolution of the semi-discrete system of equations, already presented in Eq. (4.8) for VCFVM scheme and Eq. (5.43) for SPH scheme. The selection between an explicit or an implicit time integrator can depend on several factors such as the physics of a problem, the chosen material model and the type of governing Partial Differential Equations (PDEs). For instance, hyperbolic PDEs interested in modelling wave propagation and favour the use of an explicit scheme. On the other hand, an implicit time integrator could be more suitable for a parabolic PDE due to its diffusive nature.

As the problems of interest in this thesis focus on fast transient phenomena, this favours the utilisation of an explicit scheme. Considering the rather large set of semi-discrete equations in this thesis, choosing an explicit time integrator is preferable for computational efficiency. With this in mind, in this thesis, we advocate for the use of a Runge-Kutta type method, due to its excellent results in the context of Euler equations [224, 225]. A multi-stage Runge-Kutta method is employed here and discussed in the next section.


FIGURE 6.1: Structure of Chapter 6

## 6.3 Total Variation Diminishing Runge-Kutta scheme

In order to ensure second order accuracy in time, to be consistent with second order spatial discretisation[10], a one-step two-stage Total Variation Diminishing (TVD) Runge-Kutta is utilised in this thesis, already explored in [6, 7, 16, 18, 23]. This is described by the following time

[10] For a steady state problem, a discretisation with first order accuracy in time along with second order accuracy in space will eventually converge to a second order accurate solution [11].

update equations from time step $t^n$ to $t^{n+1}$

$$\boldsymbol{\mathcal{U}}_e^{\star} = \boldsymbol{\mathcal{U}}_e^n + \Delta t\, \dot{\boldsymbol{\mathcal{U}}}_e^n(\boldsymbol{\mathcal{U}}_e^n, t^n); \tag{6.1}$$

$$\boldsymbol{\mathcal{U}}_e^{\star\star} = \boldsymbol{\mathcal{U}}_e^{\star} + \Delta t\, \dot{\boldsymbol{\mathcal{U}}}_e^{\star}(\boldsymbol{\mathcal{U}}_e^{\star}, t^{n+1}); \tag{6.2}$$

$$\boldsymbol{\mathcal{U}}_e^{n+1} = \frac{1}{2}(\boldsymbol{\mathcal{U}}_e^n + \boldsymbol{\mathcal{U}}_e^{\star\star}), \tag{6.3}$$

where the conservation variables $\boldsymbol{\mathcal{U}} = \{\boldsymbol{p}, \boldsymbol{F}, \boldsymbol{H}, J, \eta \text{ or } E\}$ and geometry $\boldsymbol{x}$ are all monolithically updated through Eqs. (6.1) to (6.3).

It must be noted that the TVD concept, initially proposed by Harten [226], guarantees the monotonicity of the first-order solution meaning that the appearance of any new local extrema will be prevented within the solution domain. In the case of the second-order solution, although a monotonic solution can be ensured by a slope limiter during the spatial reconstruction process, it will not be automatically ensured by evolving in time and that is why the TVD concept is required in order to avoid spurious oscillations in the solution [199].

### 6.3.1 Stability condition

As an explicit time integrator is utilised, the selected time step $\Delta t = t^{n+1} - t^n$ must lie within the range of the stability condition and that is governed by the standard Courant-Friedrichs-Lewy (CFL) condition [222] given as

$$\Delta t = \alpha_{\text{CFL}} \frac{h_{\min}}{c_{p,\max}}, \tag{6.4}$$

where $c_{p,\max}$ is the maximum pressure wave speed, $h_{\min}$ is the minimum characteristic length within the computational domain (defined in our case as the smallest mesh element length) and $\alpha_{\text{CFL}}$ is the CFL stability number. For the multi-dimensional numerical examples presented in this thesis, a value of $\alpha_{\text{CFL}} = 0.3$ has been selected to ensure both the accuracy and stability of the proposed algorithms.

Notice that the proposed algorithms does not necessarily ensure the conservation of angular momentum of the system due to the fact that the minors of the deformation gradient tensor, namely, $\{\boldsymbol{F}, \boldsymbol{H}, J\}$, are no longer computed on the basis of the material gradient of a current geometry (e.g. $\boldsymbol{F} \neq \boldsymbol{F}_{\boldsymbol{x}} := \boldsymbol{\nabla}_0 \boldsymbol{x}$, $\boldsymbol{H} \neq \boldsymbol{H}_{\boldsymbol{x}} := \frac{1}{2}\boldsymbol{F}_{\boldsymbol{x}} \times \boldsymbol{F}_{\boldsymbol{x}}$, $J \neq J_{\boldsymbol{x}} := \frac{1}{6}\boldsymbol{F}_{\boldsymbol{x}} : (\boldsymbol{F}_{\boldsymbol{x}} \times \boldsymbol{F}_{\boldsymbol{x}})$) [3]. This can become problematic only in those problems involving very large and sustained rotations [16]. To alleviate this, and taking inspiration from the work of [6], a global least-square angular momentum projection procedure is carried out. The linear momentum update (see Eq. (4.8a) or Eq. (5.43a)) is suitably modified (in the least squares sense) in order to preserve the total angular momentum whilst still ensuring the conservation of the overall linear momentum. Details of this projection technique can be found in Appendix D.

*Remark* 14: It is worthwhile noting that the satisfaction of Coleman-Noll procedure, presented in Sections 4.4 and 5.5, for both VCFVM and SPH schemes, respectively, is also respected in the fully discrete case for the particular TVD Runge-Kutta time integration scheme used in this work. Indeed, Eq. (6.1)-Eq. (6.3) can be combined to give (after replacing $\boldsymbol{\mathcal{U}}_a$ with $\mathcal{D}_p^{ab}$)

$$\frac{\mathcal{D}_p^{ab,n+1} - \mathcal{D}_p^{ab,n}}{\Delta t} = \frac{1}{2}\left( \dot{\mathcal{D}}_p^{ab,n} + \dot{\mathcal{D}}_p^{ab,\star} \right). \tag{6.5}$$

By noticing that both terms on the right hand side of the above equation are positive each (as demonstrated in Eq. (4.39)), it is immediate to conclude the satisfaction of entropy production in the discrete setting.

## 6.4 Algorithmic description

For ease of understanding, Algorithm 6.1 summarises the complete algorithmic description of the mixed-based $\{\boldsymbol{p}, \boldsymbol{F}, \boldsymbol{H}, J, E \text{ or } \eta\}$ Upwind VCFVM and SPH methodologies, with all the necessary numerical ingredients.

**Algorithm 6.1:** Complete stabilised Upwind-VCFVM and Upwind-SPH mixed methodologies

**Input** : $\boldsymbol{\mathcal{U}}_a^n$ where $\boldsymbol{\mathcal{U}} = [\boldsymbol{p}, \boldsymbol{F}, \boldsymbol{H}, J, E \text{ or } \eta]^T$

**Output:** $\boldsymbol{\mathcal{U}}_a^{n+1}$, $\boldsymbol{P}_a^{n+1}$, $\boldsymbol{x}_a^{n+1}$

(1) ASSIGN old primary variables: $\boldsymbol{\mathcal{U}}_a^{\text{old}} = \boldsymbol{\mathcal{U}}_a^n$ and $\boldsymbol{x}_a^{\text{old}} = \boldsymbol{x}_a^n$.

(2) EVALUATE $p$-wave speed: $c_p$ (see References [6, 120])

(3) COMPUTE time increment: $\Delta t$

**for** *TVD Runge-Kutta time integrator* $= 1$ **to** $2$ **do**

(4) COMPUTE right-hand-side of the mixed-based system: $\dot{\boldsymbol{p}}_a$ (4.8a or 5.43a), $\dot{\boldsymbol{F}}_a$ (4.8b or 5.43b), $\dot{\boldsymbol{H}}_a$ (4.8c or 5.43c), $\dot{J}_a$ (4.8d or 5.43d) and $\dot{E}_a$ (4.8e or 5.43e) or $\dot{\eta}_a$ (4.9 or 5.44)

(5) APPLY discrete angular momentum preserving algorithm (see Section 6 of [4, 16])

(6) EVOLVE $\{\boldsymbol{\mathcal{U}}_a, \boldsymbol{x}_a\}$ via TVD Runge-Kutta Eqs. (6.1) to (6.3)

(7) IMPOSE essential boundary conditions directly on particles $\boldsymbol{p}_a$ and $E_a$

(8) COMPUTE first Piola $\boldsymbol{P}_a$ (see Eq. (12) on pg. 75 in Reference [4, 16])

**end**

(8) UPDATE $\{\boldsymbol{\mathcal{U}}_a^{n+1}, \boldsymbol{x}_a^{n+1}\}$ (see Eq. (6.3))

(9) COMPUTE first Piola $\boldsymbol{P}_a^{n+1}$ (see Equation Eq. (3.40))

## 6.5 Consistency and stability analysis

One of the main challenges in computational analysis is demonstrating the validity of the numerical strategies. Although verifying a numerical methodology can be analytically achieved up to a certain order of accuracy, it is just limited to some simple linear Partial Differential Equations (PDEs) [10, 11, 183, 227]. Nonetheless, those analyses can provide a good insight into the behaviour of the numerical methodology. To do so, it is firstly required to define a set of concepts, namely, consistency, stability and convergence [11, 183],

- *Consistency*: A numerical methodology is said to be consistent if its solution for a PDE tends to the analytical solution by refining the mesh size $\Delta x$. In other words, using a numerical approximation instead of an exact mathematical procedure, the so-called *truncation error* ($\tau^n$) will be introduced at each time step $\Delta t$ and, therefore, that numerical scheme can be considered consistent if

$$\tau^n \to 0 \quad \text{when} \quad \Delta x \to 0 \ \text{ and/or } \ \Delta t \to 0. \tag{6.6}$$

- *Stability*: A numerical scheme is stable if it does not magnify the error introduced by its approximation procedure. In other words, if an initial hypothetical perturbation gets imposed on the solution of a numerical method, it will be stable if the solution remains bounded.
- *Convergence*: The very well-known Lax-Equivalence theorem [11] states that given a properly posed linear partial differential equation, discretised with a consistent Finite Difference (FD) approximation, the the approximated solution converges to the correct solution if and only if the numerical scheme is stable.

In the current thesis, the focus is on the coupled thermo-elastodynamics problems. Looking at the system of equations (2.58), and (2.39) in particular, both advective and diffusive terms can be recognised. Therefore, by considering the nature of the problems of interest in this work, the consistency and stability analyses are carried out for the linear advection-diffusion equation which reads

$$\frac{\partial \mathcal{U}}{\partial t} + a\frac{\partial \mathcal{U}}{\partial x} = \alpha \frac{\partial^2 \mathcal{U}}{\partial x^2}, \tag{6.7}$$

where $\mathcal{U}$ stands for the problem variable, $a$ is the wave speed (assumed to be constant) and $\alpha = \frac{h}{c_v}$ denotes the diffusivity coefficient. Eq. (6.7) is spatially discretised here using central difference approximation

$$\left(\frac{\partial \mathcal{U}}{\partial t}\right)_i = -\mathcal{R}_i; \qquad \mathcal{R}_i = -a\frac{\mathcal{U}_{i+1} - \mathcal{U}_{i-1}}{2\Delta x} + \alpha \frac{\mathcal{U}_{i+1} - 2\mathcal{U}_i + \mathcal{U}_{i-1}}{\Delta x^2}, \tag{6.8}$$

and also temporally discretised using the one-step two-stage Total Variation Diminishing (TVD) Runge-Kutta time integrator

$$\begin{aligned} \mathcal{U}_i^* &= \mathcal{U}_i^n - \Delta t\, \mathcal{R}_i(\mathcal{U}_i^n, t^n); \\ \mathcal{U}_i^{**} &= \mathcal{U}_i^* - \Delta t\, \mathcal{R}_i(\mathcal{U}_i^*, t^{n+1}); \\ \mathcal{U}_i^{n+1} &= \frac{1}{2}\left(\mathcal{U}_i^n + \mathcal{U}_i^{**}\right). \end{aligned} \tag{6.9}$$

### 6.5.1 Consistency analysis

The truncation error of a numerical scheme is typically defined as $\tau^n = \mathcal{O}(\Delta x^a, \Delta t^b)$ representing the order of accuracy of the numerical scheme in space (of order $a$) and time (of order $b$) [8, 11]

$$\tau^n = \frac{1}{\Delta t}(\tilde{\mathcal{U}}^{n+1} - \mathcal{U}^{n+1}), \tag{6.10}$$

where $\mathcal{U}$ stands for the exact solution of the partial differential equation (6.7) and $\tilde{\mathcal{U}}$ denotes the approximated solution obtained by the numerical scheme. Using Eq. (6.8) and Eq. (6.9), it is now possible to find out the expression for $\mathcal{U}_i^{n+1}$ as for the first stage of the TVD Runge-Kutta time integrator

$$\mathcal{U}_i^* = \mathcal{U}_i^n - \Delta t\, a \frac{\mathcal{U}_{i+1}^n - \mathcal{U}_{i-1}^n}{2\Delta x} + \Delta t\, \alpha \frac{\mathcal{U}_{i+1} - 2\mathcal{U}_i + \mathcal{U}_{i-1}}{\Delta x^2}. \tag{6.11}$$

Using Taylor series expansion of the terms $\mathcal{U}_{i+1}$ and $\mathcal{U}_{i-1}$ and replacing them into the above equation yields

$$\mathcal{U}_i^* = \mathcal{U}_i^n - a\,\Delta t \left(\frac{\partial \mathcal{U}}{\partial x}\right)_i^n - a\frac{\Delta t\,\Delta x^2}{6}\left(\frac{\partial^3 \mathcal{U}}{\partial x^3}\right)_i^n + \alpha\,\Delta t \left(\frac{\partial^2 \mathcal{U}}{\partial x^2}\right)_i^n + \alpha\frac{\Delta t\,\Delta x^2}{12}\left(\frac{\partial^4 \mathcal{U}}{\partial x^4}\right)_i^n + \mathcal{O}(\Delta x^3). \tag{6.12}$$

Following Eq. (6.12) and looking at Eq. (6.9), the second stage of the time integrator can be easily written as

$$\mathcal{U}_i^{**} = \mathcal{U}_i^* - a\,\Delta t \left(\frac{\partial \mathcal{U}}{\partial x}\right)_i^* - a\frac{\Delta t\,\Delta x^2}{6}\left(\frac{\partial^3 \mathcal{U}}{\partial x^3}\right)_i^* + \alpha\,\Delta t \left(\frac{\partial^2 \mathcal{U}}{\partial x^2}\right)_i^* + \alpha\frac{\Delta t\,\Delta x^2}{12}\left(\frac{\partial^4 \mathcal{U}}{\partial x^4}\right)_i^* + \mathcal{O}(\Delta x^3), \tag{6.13}$$

in which space derivatives can be computed on the basis of Eq. (6.12). After some simple but tedious algebraic manipulations

$$\begin{aligned} \mathcal{U}_i^{**} = \mathcal{U}_i^n &+ \Delta t \left(-2a\frac{\partial \mathcal{U}}{\partial x} + 2\alpha\frac{\partial^2 \mathcal{U}}{\partial x^2}\right)_i^n + \Delta t^2 \left(a^2\frac{\partial^2 \mathcal{U}}{\partial x^2} - 2a\,\alpha\frac{\partial^3 \mathcal{U}}{\partial x^3} + \alpha^2\frac{\partial^4 \mathcal{U}}{\partial x^4}\right)_i^n \\ &+ \Delta t \Delta x^2 \left(-\frac{a}{3}\frac{\partial^3 \mathcal{U}}{\partial x^3} + \frac{\alpha}{6}\frac{\partial^4 \mathcal{U}}{\partial x^4}\right)_i^n + \Delta t^2 \Delta x^2 \left(\frac{a^2}{3}\frac{\partial^4 \mathcal{U}}{\partial x^4} - \frac{a\,\alpha}{2}\frac{\partial^5 \mathcal{U}}{\partial x^5} + \frac{\alpha^2}{6}\frac{\partial^6 \mathcal{U}}{\partial x^6}\right)_i^n + \mathcal{O}(\Delta x^3). \end{aligned} \tag{6.14}$$

This leads to the evaluation of the numerical solution at time $n+1$ on the basis of Eq. (6.9)c

$$\begin{aligned}\tilde{\mathcal{U}}_i^{n+1} &= \frac{1}{2}\left(\mathcal{U}_i^n + \mathcal{U}_i^{**}\right)\\ &= \mathcal{U}_i^n + \Delta t\left(-a\frac{\partial \mathcal{U}}{\partial x} + \alpha\frac{\partial^2 \mathcal{U}}{\partial x^2}\right)_i^n + \Delta t^2\left(\frac{a^2}{2}\frac{\partial^2 \mathcal{U}}{\partial x^2} - a\,\alpha\frac{\partial^3 \mathcal{U}}{\partial x^3} + \frac{\alpha^2}{2}\frac{\partial^4 \mathcal{U}}{\partial x^4}\right)_i^n\\ &+ \Delta t\Delta x^2\left(-\frac{a}{6}\frac{\partial^3 \mathcal{U}}{\partial x^3} + \frac{\alpha}{12}\frac{\partial^4 \mathcal{U}}{\partial x^4}\right)_i^n + \Delta t^2\Delta x^2\left(\frac{a^2}{6}\frac{\partial^4 \mathcal{U}}{\partial x^4} - \frac{a\,\alpha}{4}\frac{\partial^5 \mathcal{U}}{\partial x^5} + \frac{\alpha^2}{12}\frac{\partial^6 \mathcal{U}}{\partial x^6}\right)_i^n + \text{H.O.T.}\end{aligned} \tag{6.15}$$

Here H.O.T denotes the High Order Terms. Having the numerical solution $\tilde{\mathcal{U}}_i^{n+1}$, we can now expand the analytical solution $\mathcal{U}_i^{n+1}$ about $\mathcal{U}_i^n$ in order to evaluate the truncation error using Eq. (6.10),

$$\begin{aligned}\tau^n = &\overbrace{\left(\frac{\partial \mathcal{U}}{\partial t} - a\frac{\partial \mathcal{U}}{\partial x} + \alpha\frac{\partial^2 \mathcal{U}}{\partial x^2}\right)_i^n}^{0\text{ based on Eq. (6.7)}}\\ &+ \Delta t\left(\frac{a^2}{2}\frac{\partial^2 \mathcal{U}}{\partial x^2} - a\,\alpha\frac{\partial^3 \mathcal{U}}{\partial x^3} + \frac{\alpha^2}{2}\frac{\partial^4 \mathcal{U}}{\partial x^4} - \frac{1}{2}\frac{\partial^2 \mathcal{U}}{\partial t^2}\right)_i^n\\ &+ \frac{\Delta x^2}{6}\left(-a\frac{\partial^3 \mathcal{U}}{\partial x^3} + \frac{\alpha}{2}\frac{\partial^4 \mathcal{U}}{\partial x^4}\right)_i^n + \Delta t\Delta x^2\left(\frac{a^2}{6}\frac{\partial^4 \mathcal{U}}{\partial x^4} - \frac{a\,\alpha}{4}\frac{\partial^5 \mathcal{U}}{\partial x^5} + \frac{\alpha^2}{12}\frac{\partial^6 \mathcal{U}}{\partial x^6}\right)_i^n\\ &- \frac{\Delta t^2}{6}\frac{\partial^3 \mathcal{U}}{\partial t^3} + \mathcal{O}(\Delta x^3, \Delta t^3),\end{aligned} \tag{6.16}$$

where the first term vanishes as it is just expressing the differential equation Eq. (6.7) and the second term represents the definition of $\mathcal{U}_{tt} + a^2\mathcal{U}_{xx} - 2a\alpha\mathcal{U}_{xxx} + \alpha^2\mathcal{U}_{xxxx} = 0$. Therefore Eq. (6.16) shows how the numerical methodology satisfies the consistency requirement (see Eq. (6.6)). Having the consistency requirement fulfilled, the stability analysis is the next step of demonstrating the validity of the numerical methodology.

### 6.5.2 Stability analysis

The von Neumann (also know as Fourier) stability analysis [203] is employed here to assess the stability limit of the numerical scheme applied on linear PDEs. This method is established based on Fourier decomposition of numerical error and can be necessary and sufficient followed by a certain number of assumptions, namely, (1) The PDE and the employed numerical methodology should be linear; (2) assuming periodic boundary conditions; and (3) the scheme should not utilise more than two time levels [9, 228]. This analysis can provide a good insight into approximating the stability limit for numerical schemes applied to nonlinear PDEs. As stated earlier, stability indicates that the generated error associated with a numerical scheme should not grow in time and that, this defines the key idea on von Neumann stability analysis. In this method, the unknown variable(s) will be replaced by an arbitrary harmonic function

$$\mathcal{U}_i^n = \sum_{m=1}^{M} A_m^n e^{Ii\phi_m}, \tag{6.17}$$

such that its amplitude ($A_m$) must not grow in time. Note that $e^{I i \phi_m} = e^{I k_m x_i}$ where $I = \sqrt{-1}$, $\phi_m$ are the phase angles with the range of $[-\pi, \pi]$ and $k_m = \frac{\pi m}{\Delta x M}$ are the wave numbers. The time dependence of the proposed function is considered through its amplitude for which an exponential function is assumed ($A_m(t) = e^{bt}$). This would be logical as the harmonic function itself has an exponential behaviour

$$\mathcal{U}_i^n = \sum_{m=1}^{M} e^{bt} e^{I i \phi_m}, \tag{6.18}$$

where $b$ is assumed to be a constant. In order to track the variation of amplitude in time, the so-called *amplification factor* is introduced

$$G = \frac{A_m^{n+1}}{A_m^n} = \frac{e^{(bt+b\Delta t)} e^{I i \phi_m}}{e^{bt} e^{I i \phi_m}} = e^{b\Delta t}, \tag{6.19}$$

and, therefore, the stability of the numerical scheme is ensured if

$$|G| \leq 1 \qquad \forall\, \phi_m \in [-\pi, \pi]. \tag{6.20}$$

In this work, the one-dimensional linear advection-diffusion equation (6.7) and the one-dimensional linearised system of equations (6.33) are considered for von Neumann stability analysis as explored in the following sections.

#### 6.5.2.1 One-dimensional linear advection-diffusion equation

In this section, the stability of the one-dimensional linear advection-diffusion equation Eq. (6.7) is analysed. For simplicity, this equation is discretised using the explicit forward Euler in time and the second order upwind method in space [229, 230]

$$\left(\frac{\partial \mathcal{U}}{\partial t}\right)_i^n = \frac{\mathcal{U}_i^{n+1} - \mathcal{U}_i^n}{\Delta t}; \tag{6.21}$$

$$\begin{aligned}\left(\frac{\partial \mathcal{U}}{\partial x}\right)_i^n = &\left(\frac{4k - 2\alpha_{CFL} + 3\alpha_{CFL}^2}{4\alpha_{CFL}}\right)\left(\frac{\mathcal{U}_i^n - \mathcal{U}_{i-2}^n}{2\Delta x}\right) \\ &+ \left(\frac{4k - 2\alpha_{CFL} + \alpha_{CFL}^2}{4\alpha_{CFL}}\right)\left(\frac{\mathcal{U}_{i+2}^n - \mathcal{U}_i^n}{2\Delta x}\right) \\ &+ \left(\frac{2\alpha_{CFL} - \alpha_{CFL}^2 - 2k}{2k}\right)\left(\frac{\mathcal{U}_{i+1}^n - \mathcal{U}_{i-1}^n}{2\Delta x}\right);\end{aligned} \tag{6.22}$$

$$\begin{aligned}\left(\frac{\partial^2 \mathcal{U}}{\partial x^2}\right)_i^n = &\left(\frac{2\alpha_{CFL} - \alpha_{CFL}^2 - 2k}{2k}\right)\left(\frac{\mathcal{U}_{i+1}^n - 2\mathcal{U}_i^n + \mathcal{U}_{i-1}^n}{\Delta x^2}\right) \\ &+ \left(\frac{4k - 2\alpha_{CFL} + \alpha_{CFL}^2}{2k}\right)\left(\frac{\mathcal{U}_{i+2}^n - 2\mathcal{U}_i^n + \mathcal{U}_{i-2}^n}{4\Delta x^2}\right),\end{aligned} \tag{6.23}$$

where

$$\alpha_{CFL} = \frac{a\Delta t}{\Delta x}; \qquad k = \frac{h}{c_v}\frac{\Delta t}{\Delta x^2}. \tag{6.24}$$

Substituting the above equations into Eq. (6.7), after some tedious algebraic manipulations, the numerical solution at time $(n+1)$ can be obtained as

$$\mathcal{U}_i^{n+1} = \frac{1}{2}\left(2k - \alpha_{CFL} + \alpha_{CFL}^2\right)\mathcal{U}_{i-2}^n + \left(2\alpha_{CFL} - 2k - \alpha_{CFL}^2\right)\mathcal{U}_{i-1}^n + \frac{1}{2}\left(2 + 2k - 3\alpha_{CFL} + \alpha_{CFL}^2\right)\mathcal{U}_i^n. \tag{6.25}$$

Substituting Eq. (6.18) into the above equation and using Eq. (6.19), the amplification factor yields

$$G = \frac{1}{2}\left(2k - \alpha_{CFL} + \alpha_{CFL}^2\right)e^{-2I\phi_m} + \left(2\alpha_{CFL} - 2k - \alpha_{CFL}^2\right)e^{-I\phi_m} + \frac{1}{2}\left(2 + 2k - 3\alpha_{CFL} + \alpha_{CFL}^2\right). \tag{6.26}$$

Considering the stability requirement at Eq. (6.20), the stability condition for one-dimensional linear advection-diffusion equation reads [230]

$$0 < k \leq \frac{\alpha_{CFL}\left(2 - \alpha_{CFL}\right)}{2}. \tag{6.27}$$

In order to check the above stability condition, it is possible to consider an extreme case in which the problem becomes thermally dominant. That indicates the heat conduction will rule on the stability condition of the numerical methodology and, therefore, one could follow the stability limit for the heat conduction equation, which is $0 < k \leq 0.5$ [8]. Consequently, it can be concluded from Eq. (6.27) that

$$0 < k \leq \overbrace{\frac{\alpha_{CFL}\left(2 - \alpha_{CFL}\right)}{2}}^{\frac{1}{2}} \qquad \Rightarrow \qquad \alpha_{CFL}\left(2 - \alpha_{CFL}\right) \leq 1. \tag{6.28}$$

It is then simple to show that

$$\left(\alpha_{CFL} - 1\right)^2 \leq 0 \qquad \Rightarrow \qquad \alpha_{CFL} \leq 1, \tag{6.29}$$

which is actually the stability condition for the linear advection equation. In this particular case, we have $\alpha_{CFL} = 1$ and that, this simply shows how the general stability condition for the one-dimensional linear advection-diffusion equation (6.27) can be recovered in the extreme cases of a purely conductive or a purely advective phenomenon.

It is also useful to decompose the real and imaginary parts of the obtained amplification factor (Eq. (6.26)) as

$$\begin{aligned}
\mathrm{Re}(G) &= \frac{1}{2}\left(2k - \alpha_{CFL} + \alpha_{CFL}^2\right)\cos(2\phi_m) + \left(2\alpha_{CFL} - 2k - \alpha_{CFL}^2\right)\cos(\phi_m) \\
&\quad + \frac{1}{2}\left(2 + 2k - 3\alpha_{CFL} + \alpha_{CFL}^2\right); \\
\mathrm{Im}(G) &= -\frac{1}{2}\left(2k - \alpha_{CFL} + \alpha_{CFL}^2\right)\sin(2\phi_m) - \left(2\alpha_{CFL} - 2k - \alpha_{CFL}^2\right)\sin(\phi_m).
\end{aligned} \tag{6.30}$$

This allows to plot the stability region for one-dimensional linear advection-diffusion equation discretised using forward Euler in time and second order upwind method in space. Figure 6.2 illustrates the stability limit on the basis of three stability parameters. Firstly, the stability

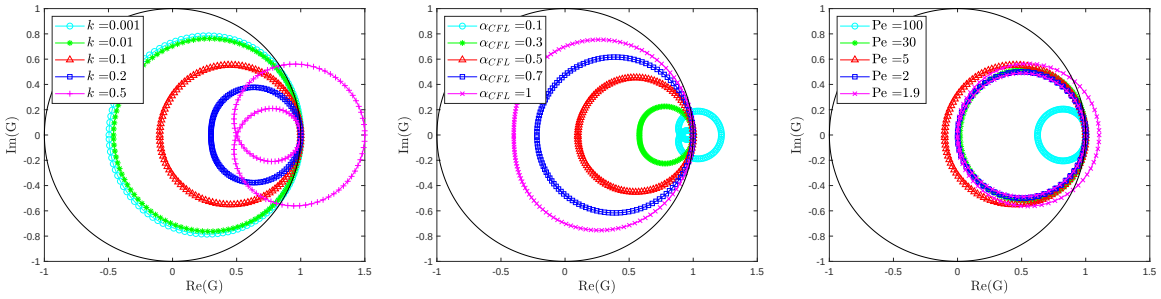


(a) (b) (c)

FIGURE 6.2: Stability limits for the one-dimensional linear advection-diffusion equation discretised using forward Euler in time and second order upwind in space for different (a) $k$ with a fixed $\alpha_{CFL} = 0.5$; (b) $\alpha_{CFL}$ with a fixed $k = 0.2$; and (c) Pe

area is depicted for different values of $k$ whilst $\alpha_{CFL} = 0.5$ is fixed, shown in Figure 6.2a. This can be useful to study the diffusive behaviour of Eq. (6.27). In fact, the only case where the amplification factor crossed out the stability limit (unit radius circle) is $k = 0.5$. This can be justified using Eq. (6.27) such that $0 < 0.5 \nleq \frac{0.5(2-0.5)}{2} = 0.375$. The other values of $k$ showed a stable behaviour since they are all placed within the stability limit.

Figure 6.2b shows the stability range for different values of $\alpha_{CFL}$ whilst $k = 0.2$ is fixed. This can help to study the stability with the focus on the advective behaviour of Eq. (6.27). As it is shown, all amplification factors placed within the stability limit (unit radius circle) except the case of $\alpha_{CFL} = 0.1$ and that, this can be justified through Eq. (6.27). Notice here that all values selected for $\alpha_{CFL}$ are on the basis of stability limit for the linear advection equation, that is $0 < \alpha_{CFL} \leq 1$ [11].

A more general way of performing the stability analysis is through the dimensionless Peclet number defined as

$$\text{Pe} = \frac{\alpha_{CFL}}{k}, \tag{6.31}$$

which introduces the ratio of the advective to the diffusive transport rate. In fact, a large Peclet number indicates an advectively dominated problem whereas a small Peclect number describes a diffusion dominated problem. It is possible to obtain the stability condition presented in Eq. (6.27) on the basis of the Peclet number and $\alpha_{CFL}$ as

$$\text{Pe}(2 - \alpha_{CFL}) \geq 2. \tag{6.32}$$

Figure 6.2c shows the stability limit for different values of the Peclet number. As it is clear, the amplification factor remains in the stability region for $\text{Pe} \geq 2$ and becomes unstable once $\text{Pe} < 2$.

#### 6.5.2.2 One-dimensional system of equations

In general, the entropy-based system of equations presented in Eq. (2.58) can be reduced, in the absence of source terms, into the one-dimensional case as

$$\rho_R \frac{\partial v}{\partial t} = \frac{\partial P}{\partial X}; \tag{6.33a}$$

$$\frac{\partial J}{\partial t} = \frac{\partial v}{\partial X}; \tag{6.33b}$$

$$\theta \frac{\partial \eta}{\partial t} = -\frac{\partial Q}{\partial X} = h \frac{\partial^2 \theta}{\partial X^2}. \tag{6.33c}$$

Notice here that the one-dimensional strain assumption, that is $J = F_{11}$, is considered. Additionally, $Q = -h\frac{\partial \theta}{\partial X}$ is the linearised heat flux with the assumption of a constant heat conduction coefficient. The one-dimensional system of equations (6.33) can be presented on the basis of three primary variables of $\{v, J, \eta\}$ and to achieve this, we need to replace temperature as a function of the variables of interest. Recalling Eq. (3.33) and with the aid of Eq. (3.45) with $q = 1$, it is possible to obtain the explicit expression of temperature as

$$\theta = \theta_R e^{\left(\frac{\eta}{c_v} - \Gamma_0 (J-1)\right)}. \tag{6.34}$$

Using Eq. (6.34) and Eq. (3.69), it is possible to express the one-dimensional linearised first Piola as

$$\begin{aligned} P &= (\lambda + 2\mu)\, J - c_v \Gamma_0 \left(\theta - \theta_R\right) \\ &= \left(\lambda + 2\mu + c_v \Gamma_0^2 \theta_R\right) J - \Gamma_0 \theta_R \eta - c_v \Gamma_0 \theta_R (\Gamma_0 - 1), \end{aligned} \tag{6.35}$$

which is obtained for the particular case of a linear thermo-elastic material model along with Mie-Grüneisen equation of state.

Also, the left hand side of Eq. (6.33c) can be re-expressed by the aid of Eq. (3.33) and the application of chain rule as

$$\begin{aligned} \theta \frac{\partial \eta}{\partial t} &= \theta \overbrace{\frac{\partial \eta}{\partial J}}^{c_v \Gamma_0} \frac{\partial J}{\partial t} + \theta \overbrace{\frac{\partial \eta}{\partial \theta}}^{c_v} \frac{\partial \theta}{\partial t} \\ &= \theta_R c_v \Gamma_0 \frac{\partial J}{\partial t} + \theta_R c_v \left( \frac{1}{c_v} \frac{\partial \eta}{\partial t} - \Gamma_0 \frac{\partial J}{\partial t} \right) \\ &= \theta_R \frac{\partial \eta}{\partial t}. \end{aligned} \tag{6.36}$$

Linearising the expression for temperature, presented in Eq. (6.34), yields

$$\theta = \theta_R \left( \frac{\eta}{c_v} - \Gamma_0 \left(J - 1\right) \right), \tag{6.37}$$

which is utilised to reformulate the right hand side of Eq. (6.33c) in terms of the variables of interest as

$$h\frac{\partial^2\theta}{\partial X^2} = \frac{h\theta_R}{c_v}\left(\frac{\partial^2\eta}{\partial X^2} - \Gamma_0 c_v \frac{\partial^2 J}{\partial X^2}\right). \tag{6.38}$$

Substituting Eq. (6.35), Eq. (6.36) and Eq. (6.38) into the one-dimensional system of equations presented in Eq. (6.33) leads to its linearised case as

$$\rho_R\frac{\partial v}{\partial t} = \frac{\partial}{\partial X}\left(\left(\lambda + 2\mu + c_v\Gamma_0^2\theta_R\right)J - \Gamma_0\theta_R\eta - c_v\Gamma_0\theta_R(\Gamma_0 - 1)\right); \tag{6.39a}$$

$$\frac{\partial J}{\partial t} = \frac{\partial v}{\partial X}; \tag{6.39b}$$

$$\frac{\partial \eta}{\partial t} = \frac{h}{c_v}\left(\frac{\partial^2\eta}{\partial X^2} - \Gamma_0 c_v\frac{\partial^2 J}{\partial X^2}\right). \tag{6.39c}$$

---

*Remark* 15: Using Eq. (6.35)a and Eq. (6.36)a, the one-dimensional system of equations (6.33) can alternatively be expressed in a linearised form with the primary variables of $\{v, J, \theta\}$ as following

$$\rho_R\frac{\partial v}{\partial t} = \frac{\partial}{\partial X}\left(\left(\lambda + 2\mu\right)J - c_v\Gamma_0(\theta - \theta_R)\right); \tag{6.40a}$$

$$\frac{\partial J}{\partial t} = \frac{\partial v}{\partial X}; \tag{6.40b}$$

$$\frac{\partial \theta}{\partial t} = \frac{h}{c_v}\left(\frac{\partial^2\theta}{\partial X^2} - \Gamma_0\theta_R\frac{\partial v}{\partial X}\right). \tag{6.40c}$$

---

To proceed with the von Neumann stability analysis, it is first required to discretise the system of equations (6.39). To achieve this, and for simplicity, the forward Euler in time and the first order upwind scheme in space are employed which yields

$$\frac{v_i^{n+1} - v_i^n}{\Delta t} = \frac{1}{\rho_R \Delta X}\left[\left(\lambda + 2\mu + c_v\Gamma_0^2\theta_R\right)\left(J_i^n - J_{i-1}^n\right) + \Gamma_0\theta_R\left(\eta_i^n - \eta_{i-1}^n\right)\right]; \tag{6.41a}$$

$$\frac{J_i^{n+1} - J_i^n}{\Delta t} = \frac{v_i^n - v_{i-1}^n}{\Delta X}; \tag{6.41b}$$

$$\frac{\eta_i^{n+1} - \eta_i^n}{\Delta t} = \frac{h}{c_v}\left(\frac{\eta_{i+1}^n - 2\eta_i^n + \eta_{i-1}^n}{\Delta X^2} - \Gamma_0 c_v\frac{J_{i+1}^n - 2J_i^n + J_{i-1}^n}{\Delta X^2}\right). \tag{6.41c}$$

Having the discrete form of the set of equations, it is now possible to proceed with the von Neumann stability analysis. To do so, the primary variables are replaced with an arbitrary harmonic function, expressed in Eq. (6.17). As we are dealing with a system of equations, the amplitude of the harmonic function becomes a matrix, namely, the *amplification matrix* $\boldsymbol{\mathcal{G}}$. In this case, the necessary and sufficient condition for weak conditional stability is such that the

eigenvalues (or the spectral radius) of the amplification matrix have to be uniformly bounded [231]. The spectral radius can be defined as

$$\mathcal{R} = \max\{|\Lambda_1|, |\Lambda_2|, |\Lambda_3|\} \leq 1, \tag{6.42}$$

where $\Lambda_1, \Lambda_2, \Lambda_3$ are the three eigenvalues corresponding to the amplification matrix $\boldsymbol{\mathcal{G}}$. It is worthwhile noting that the weak stability is not a powerful enough criterion to be applied to systems of differential equations with variable coefficients, even though it may be sufficient for constant-coefficient problems or those with scalar variables [231].

Substituting Eq. (6.17) into the system of equations (6.41) gives

$$\left[\boldsymbol{A}_m\right]_i^{n+1} = \underbrace{\begin{bmatrix} 1 & \left(\frac{\lambda+2\mu+c_v\Gamma_0^2\theta_R}{\rho_R}\right)\frac{\Delta t}{\Delta X}f(\phi_m) & \left(\frac{-\Gamma_0\theta_R}{\rho_R}\right)\frac{\Delta t}{\Delta X}f(\phi_m) \\ \frac{\Delta t}{\Delta X}f(\phi_m) & 1 & 0 \\ 0 & (-\Gamma_0 h)\,\frac{\Delta t}{\Delta X^2}g(\phi_m) & 1+\frac{h}{c_v}\frac{\Delta t}{\Delta X^2}g(\phi_m) \end{bmatrix}}_{\boldsymbol{\mathcal{G}}} \left[\boldsymbol{A}_m\right]_i^n, \tag{6.43}$$

where $\boldsymbol{A}_m$ stands for the amplitude vector whose components correspond to each variable of interest $\{v, J, \eta\}$ and with $f(\phi_m) = \left(1 - e^{-I\phi_m}\right)$ and $g(\phi_m) = \left(e^{I\phi_m} + e^{-I\phi_m} - 2\right)$. It is possible to re-express some of the components of the amplification matrix in terms of the dimensionless parameters employed in the previous section. Hence, the further simplified amplification matrix can be defined as

$$\boldsymbol{\mathcal{G}} = \begin{bmatrix} 1 & a\,\alpha_{CFL}f(\phi_m) & \left(\frac{-\Gamma_0\theta_R}{a\rho_R}\right)\alpha_{CFL}f(\phi_m) \\ \frac{\alpha_{CFL}}{a}f(\phi_m) & 1 & 0 \\ 0 & (-\Gamma_0 c_v k)\,g(\phi_m) & 1+k\,g(\phi_m) \end{bmatrix}, \tag{6.44}$$

with $\{\alpha_{CFL}, k\}$ already defined in Eq. (6.24) and where the wave speed $a$ reads [7]

$$a = \sqrt{\frac{\lambda+2\mu+c_v\Gamma_0^2\theta_R}{\rho_R}}. \tag{6.45}$$

The eigenvalues of the obtained amplification matrix can then be evaluated using the following expression

$$|\boldsymbol{\mathcal{G}} - \Lambda\boldsymbol{I}| = \boldsymbol{0}, \tag{6.46}$$

which results in three eigenvalues and their corresponding eigenvectors. Eq. (6.46) is solved with mathematical software and its mathematical expression is not presented here for brevity.

Notice from Eq. (6.43) that the amplification matrix depends on several physical and numerical parameters, consisting of the thermo-mechanical material properties and numerical variables. Consequently, it is not trivial to extract a specific stability condition for the numerical solution

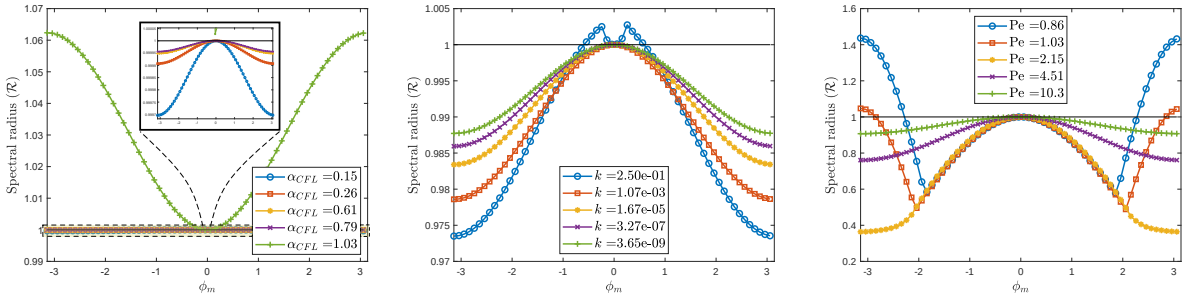


(a) (b) (c)

FIGURE 6.3: Stability analysis: Spectral radius of the amplification matrix along phase angles for different values of the dimensionless stability parameters (a) $\alpha_{CFL}$; and (b) $k$; and (c) Pe.

and, therefore, a parametric study on the stability of the solution is performed. However, the stability conditions for the linear advection equation ($0 < \alpha_{CFL} \leq 1$) and the heat equation ($0 < k \leq 0.5$) have to be essentially satisfied.

In this thesis, the dimensionless numbers $\{\text{Pe}, \alpha_{CFL}, k\}$ are considered as the parameters for stability analysis. The Peclet number indicates a comparative study between the advective and diffusive nature of the problem. Moreover, the advective and diffusive behaviours can be studied separately using the $\alpha_{CFL}$ and $k$, respectively.

Figure 6.3a shows the spectral radius distribution for different values of $\alpha_{CFL}$. As it is clear, the spectral radius is uniformly bounded except the cases where $\alpha_{CFL} \geq 1$. The distribution of the spectral radius is shown in Figure (6.3b) for different values of $k$. In this particular case of only varying $k$ whilst the mechanical material properties are fixed, the numerical solution has become unstable when $k \geq 0.25$. Otherwise, it remains stable. Figure 6.3c depicts the spectral radius distribution for different values of Peclet number. It can be observed that for Pe$< 2$, the spectral radius crosses the stability limit and that, this is compliant with the stability limit obtained for the one-dimensional linear advection-diffusion equation (see Figure 6.2c). For the larger Peclet numbers where the problem is advectively dominant, the spectral radius has remained in the stability area.

An alternative way of assessing the stability of the numerical solution is to depict the stability range of the three eigenvalues of the amplification matrix for different values of the stability parameters $\{\alpha_{CFL}, k, \text{Pe}\}$. In this case, the stability area will be a circle of radius one in order to ensure the stability condition presented in Eq. (6.20). Figure 6.4 depicts the stability area introduced by three eigenvalues of the amplification matrix for different values of $\alpha_{CFL}$. This shows the second eigenvalue ($\Lambda_2$) is the one responsible for instability since its area is larger than the stability limit (the unit radius circle). Figure 6.5 illustrates the stability ranges for three eigenvalues of the amplification matrix for different values of $k$. This time, the first eigenvalue ($\Lambda_1$) has crossed the stability limit beyond which the solution has become unstable. Figure 6.6 shows the stability area introduced by three eigenvalues of the amplification matrix for different values of the Peclet number. Although the first and second eigenvalues have shown stable behaviour, the third eigenvalue has become unstable once Pe$< 2$.

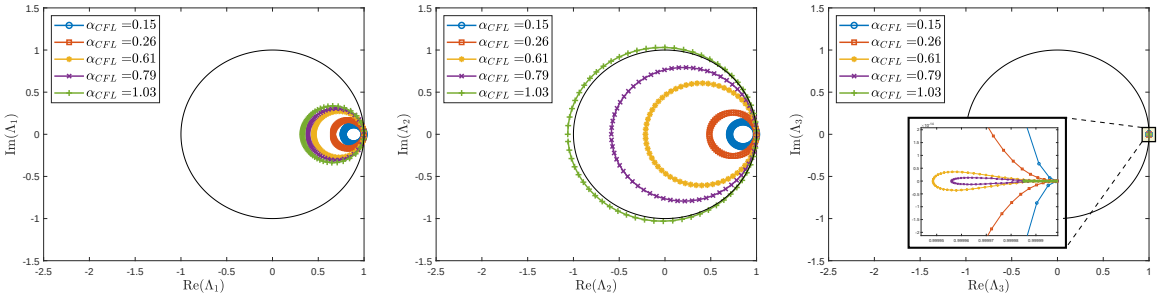


(a) (b) (c)

FIGURE 6.4: Stability range of eigenvalues of the amplification matrix for different values of $\alpha_{CFL}$.

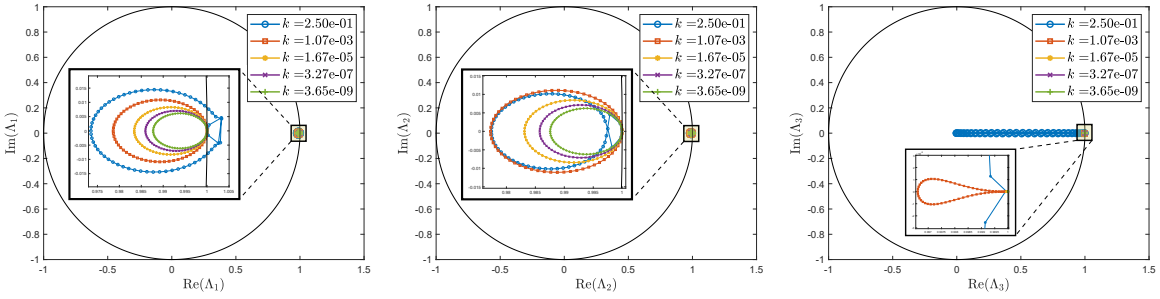


(a) (b) (c)

FIGURE 6.5: Stability range of eigenvalues of the amplification matrix for different values of $k$.

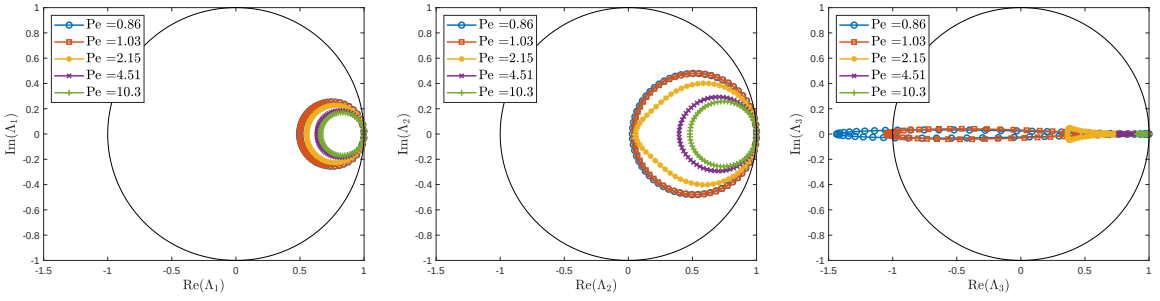


(a) (b) (c)

FIGURE 6.6: Stability range of eigenvalues of the amplification matrix for different values of the Peclet number.

## 6.6 Conclusion

In this chapter, an explicit one-step two-stage TVD Runge-Kutta time integrator is utilised in order to advance the conservative variables $\{\boldsymbol{p}, \boldsymbol{F}, \boldsymbol{H}, J, E \text{ or } \eta\}$ in time. A monolithic update of geometry is carried out only for post-processing purposes. Additionally, a consistency and von Neumann stability analysis are performed on the one-dimensional simplified case of the proposed methodology. This has illustrated the second-order accurate solution in space and time and designated an estimation on the stability limit for the presented algorithms. Finally, the complete algorithmic description of the proposed numerical methodology is presented.

# Part IV

# Numerical Results

Chapter 7

# One-dimensional problems: Fundamental studies

## 7.1 Introduction

In this chapter, a set of one-dimensional benchmark problems are introduced aimed at analysing the fundamental properties of the presented numerical algorithm. Firstly, a mesh convergence study is carried out on a one-dimensional bar using two material models, namely, a rigid conductor (Section 7.2) and linear thermo-elasticity (Section 7.3). The shock-capturing capability of the numerical scheme is then assessed. This includes investigation on severe shock problems in both elastic media (Section 7.4) and gas dynamics (Section 7.5).

In general, the total energy-based system of conservation laws presented in Eq. (2.56) can be reduced into the one-dimensional case as

$$\frac{\partial p_x}{\partial t} = \frac{\partial P_{xX}}{\partial X} + f_R; \tag{7.1a}$$

$$\frac{\partial F_{xX}}{\partial t} = \frac{1}{\rho_R}\frac{\partial p_x}{\partial X}; \tag{7.1b}$$

$$\frac{\partial E}{\partial t} = \frac{1}{\rho_R}\frac{\partial \left(P_{xX} p_x\right)}{\partial X} - \frac{\partial Q}{\partial X} + \frac{p_x}{\rho_R} f_R + s_R. \tag{7.1c}$$

Notice here that $F_{xX}$ is considered on the basis of one-dimensional strain assumption. All the one-dimensional problems in this chapter have been numerically analysed using the Vertex-Centred Finite Volume Method (VCFVM) algorithm. However, this can be considered as an equivalent one-dimensional case of the Smooth Particle Hydrodynamics algorithm, using just two neighbouring particles at upwind and downwind sides of a target particle in which the solution is approximated.

## 7.2 Rigid conductor

In this section, a rigid conductor is considered where the mechanical effects are neglected and heat will only be conducted throughout the material. In this case, Eq. (2.39) reduces to

$$\frac{\partial E}{\partial t} = -\mathrm{DIV}\left(\boldsymbol{Q}\right) + s_R. \tag{7.2}$$

Considering the linearised case of Eq. (2.38), which is, $\boldsymbol{Q} = -h\boldsymbol{\nabla}_R\theta$, with the assumption of constant conductivity coefficient ($h$) and, also, the lack of heat source term, Eq. (7.2) gives

$$\frac{\partial \theta}{\partial t} = \left(\frac{h}{c_v}\right)\left(\boldsymbol{\nabla}_R^2\theta\right), \tag{7.3}$$

which is the well-known heat conduction equation where $\boldsymbol{\nabla}_R^2$ is the Laplacian operator and $\frac{h}{c_v}$ denotes the diffusivity coefficient. The main objective of this example is to assess the spatial convergence of the proposed VCFVM methodology via the so-called *manufacturing solution* procedure. The problem consists of a unit length one-dimensional bar which is subjected to the following smooth temperature profile

$$\theta(X,t) = \theta_{\mathrm{amb}}\left[A\sin\left(\frac{\pi X}{L}\right)(t-1) + 2\right]; \quad 0 \leq X \leq L, \tag{7.4}$$

where $A = \frac{1}{t_{\mathrm{end}}}$ is a user-defined coefficient and $\theta_{\mathrm{amb}} = 293.15$ K denotes the ambient temperature, $L = 1$ m. The initial and boundary conditions are defined as

$$\theta(X, t=0) = \theta_{\mathrm{amb}}\left(-A\sin\left(\frac{\pi X}{L}\right) + 2\right); \tag{7.5}$$

$$\theta(X=0,t) = \theta(X=L,t) = 2\theta_{\mathrm{amb}}. \tag{7.6}$$

In this case, above temperature profile will be introduced into the Eq. (7.2) in order to analytically obtain its corresponding heat source term which, after some simple algebraic manipulations, yields

$$s_R(X,t) = Ac_v\theta_{\mathrm{amb}}\sin\left(\frac{\pi X}{L}\right)\left[1 + k\left(\frac{\pi}{L}\right)^2(t-1)\right]. \tag{7.7}$$

This will provide an analytical solution which can be used for comparison purposes in order to assess the spatial convergence of the numerical solution. In Figure 7.1a, the numerical solution at $t_{\mathrm{end}} = 1.5$ s is compared against the analytical solution which an extremely good agreement can be observed. The expected second order convergence rate for the temperature is also shown in Figure 7.1b.

## 7.3 Thermo-elastic bar

In this example, a one-dimensional bar is subjected to the following displacement and temperature profiles (see Figure 7.2)

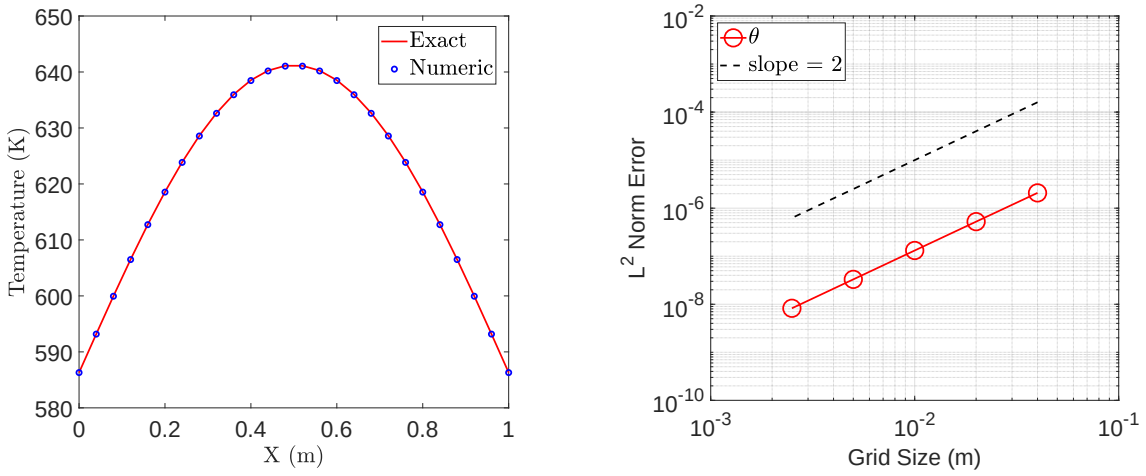


(a) (b)

FIGURE 7.1: Rigid conductor: (a) validation of the numerical solution for temperature at particular time $t = 1.5$ s and (b) $L^2$ norm convergence of temperature at particular time $t = 1.6^{-3}$ s. The material properties used are density $\rho_R = 1000$ kg/m$^3$, $h = 10$ W/m.K, $C_v = 1$ J/Kg.K and $\alpha = 2.223 \times 10^{-4}$ K$^{-1}$.

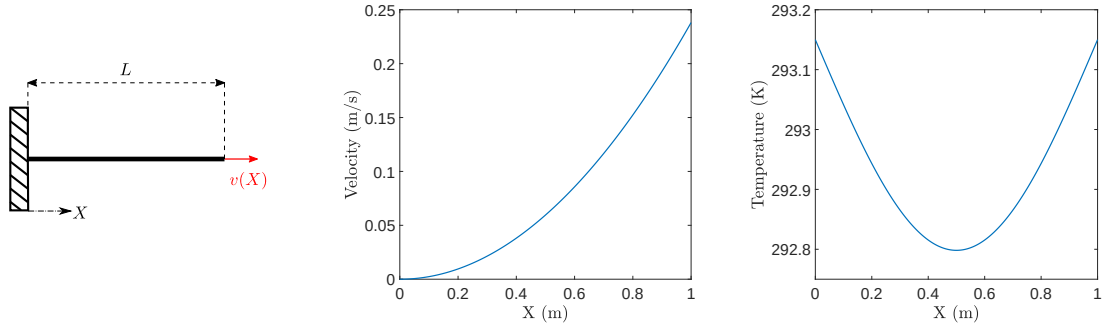


(a) (b) (c)

FIGURE 7.2: One dimensional bar: (a) Configuration; and Initial conditions for (b) displacement; and (c) temperature.

$$x(X,t) = X(\frac{A}{L}Xt + 1); \qquad 0 \leq X \leq L, \tag{7.8}$$

$$\theta(X,t) = B\,\theta_{\text{amb}}\,\sin\left(\frac{\pi X}{L}\right)(t+1) + \theta_{\text{amb}}, \tag{7.9}$$

where $\theta_{\text{amb}} = 293.15$ K denotes the ambient temperature, $L = 1$ m and $A$ and $B$ are constant coefficients, yet to be defined. The main objective of this example is to assess the spatial convergence of the proposed $\{p_x, F_{xX}, E\}$ methodology, using a linear thermo-elastic material model.

Following the manufacturing solution procedure (see Section 7.2), the linear momentum and deformation gradient can be evaluated based on Eq. (7.8) as

$$p_x = \frac{\partial x}{\partial t} = \rho_R \frac{AX^2}{L}; \tag{7.10}$$

$$F_{xX} = \frac{\partial x}{\partial X} = \frac{2AX}{L} t + 1. \tag{7.11}$$

Notice here that the one-dimensional strain assumption $F_{xX}$ is considered. Taking the one-dimensional system of equations (7.1) into account, it is now required to obtain the unknowns (source terms). To do so, we first need to obtain the general formula for evaluation of the source terms

$$f_R = \frac{\partial p_x}{\partial t} - \frac{\partial P_{xX}}{\partial X}; \tag{7.12a}$$

$$s_R = \frac{\partial E}{\partial t} - \left( \frac{\partial P_{xX} v_x}{\partial X} - \frac{\partial Q_x}{\partial X} + f_R v \right). \tag{7.12b}$$

Looking at Eq. (2.38) and Eq. (3.68), obtaining the source terms (7.12) requires the evaluation of the following derivatives

$$\frac{\partial p_x}{\partial t} = 0; \tag{7.13a}$$

$$\frac{\partial P_{xX}}{\partial X} = (\lambda + 2\mu) \frac{\partial F_{xX}}{\partial X} - C_v \Gamma_0 \frac{\partial \theta}{\partial X}; \tag{7.13b}$$

$$\frac{\partial Q_x}{\partial X} = -h \frac{\partial^2 \theta}{\partial X^2}; \tag{7.13c}$$

$$\frac{\partial E}{\partial t} = \frac{\partial \mathcal{E}}{\partial t} + \frac{\partial \left( \frac{1}{2\rho_R} p_x^2 \right)}{\partial t}. \tag{7.13d}$$

By the aid of equations (7.9), (7.10), (7.11) and (3.34a), the above derivatives can now be computed

$$\frac{\partial \theta}{\partial t} = B\theta_{\text{amb}} \sin\left( \frac{\pi X}{L} \right); \tag{7.14a}$$

$$\frac{\partial F_{xX}}{\partial t} = \frac{2AX}{L}; \tag{7.14b}$$

$$\frac{\partial F_{xX}}{\partial X} = \frac{2At}{L}; \tag{7.14c}$$

$$\frac{\partial \theta}{\partial X} = B\theta_{\text{amb}} \frac{\pi}{L} \cos\left( \frac{\pi X}{L} \right) (t+1); \tag{7.14d}$$

$$\frac{\partial^2 \theta}{\partial X^2} = -B\theta_{\text{amb}} \left( \frac{\pi}{L} \right)^2 \sin\left( \frac{\pi X}{L} \right) (t+1). \tag{7.14e}$$

Therefore, substituting the evaluated linear momentum Eq. (7.10) and the given temperature profile Eq. (7.9) into the system of equations (7.1) and with the aid of Eq. (7.14), the explicit

expressions for the body force and heat source term yield

$$f_R = -(2\mu+\lambda)\left(\frac{2At}{L}\right) + BC_v\Gamma_0\theta_{\text{amb}}\frac{\pi}{L}\cos\left(\frac{\pi X}{L}\right)(t+1); \tag{7.15a}$$

$$s_R = \theta\left(\frac{B}{\theta_R}C_v\theta_{\text{amb}}\sin\left(\frac{\pi X}{L}\right) + C_v\Gamma_0\frac{2AX}{L}\right) + Bh\theta_{\text{amb}}\left(\frac{\pi}{L}\right)^2(t+1)\sin\left(\frac{\pi X}{L}\right). \tag{7.15b}$$

This provides the required analytical solution for the spatial convergence analysis. The remaining pending task is to measure the value of constant coefficients $A$ and $B$ in such a way that the infinitesimal deformation and temperature gradient are ensured (i.e. linear thermo-elasticity). To achieve this, we can set up the value of displacement in the range of linear elasticity $\frac{x-X}{X_{\text{max}}}\big|_{X=X_{\text{max}}} = 10^{-4}$ in order to obtain the value of coefficient $A$. By replacing $x$ with the mapping profile presented in Eq. (7.8), the coefficient $A$ renders

$$A = \frac{10^{-4}}{t_{\text{end}}}, \tag{7.16}$$

where $t_{\text{end}}$ denotes the chosen final time for the simulation. The same procedure as above is employed to obtain the particular value of the coefficient $B$. That can be achieved by setting up $\frac{\theta-\theta_R}{\max(\theta_R)}\big|_{X=\frac{L}{2}} = 10^{-3}$ in order to ensure infinitesimal temperature gradient, and using Eq. (7.9) yields

$$B = \frac{10^{-3}\times\max(\theta_R)+\theta_R-\theta_{\text{amb}}}{\theta_{\text{amb}}\,(t_{\text{end}}+1)}. \tag{7.17}$$

Considering the employed final time for the convergence study as $t_{\text{end}} = 10^{-3}$ and, also, recalling Eq. (7.16) and Eq. (7.17), result in particular values of the user-defined parameters $A = 0.2381$ $\text{s}^{-1}$ and $B = -0.0012$ $\text{s}^{-1}$ for the manufactured solution.

To this end, the thermo-mechanical initial and boundary conditions are defined as

$$\text{IC:}\quad p_x(X,t=0) = \rho_R\frac{AX^2}{L}, \quad \theta(X,t=0) = \theta_{\text{amb}}\left(B\sin\left(\frac{\pi X}{L}+1\right)\right). \tag{7.18}$$

$$\begin{aligned}\text{BC:}\quad & p_x(X=0,t) = 0; \qquad p_x(X=L,t) = AL, \\ & \theta(X=0,t) = \theta_{\text{amb}}; \quad \theta(X=L,t) = \theta_{\text{amb}}.\end{aligned} \tag{7.19}$$

Figure 7.3 shows the expected second order convergence rate (e.g. $L^2$ norm error) for the conservative variables $\{v_x, F_{xX}, E\}$ and the first Piola-Kirchhoff stress tensor $P_{xX}$.

## 7.4 Blake problem

The Blake problem [107] is an example to illustrate the capability of an algorithm for capturing a shock in solid media. Although the domain is a shell of inner radius $r_i = 0.1$ m and outer radius $r_o = 1$ m (see Figure 7.4a), this problem can potentially be seen as a one-dimensional example of shock propagation (along the aperture length) through a solid continua. A constant in time boundary traction vector $\boldsymbol{t}_B = -p\boldsymbol{n}$ (with $p = 1\times10^6$ Pa) is applied to the inner surface of the shell, whereas the remaining surfaces are treated as traction free boundary conditions

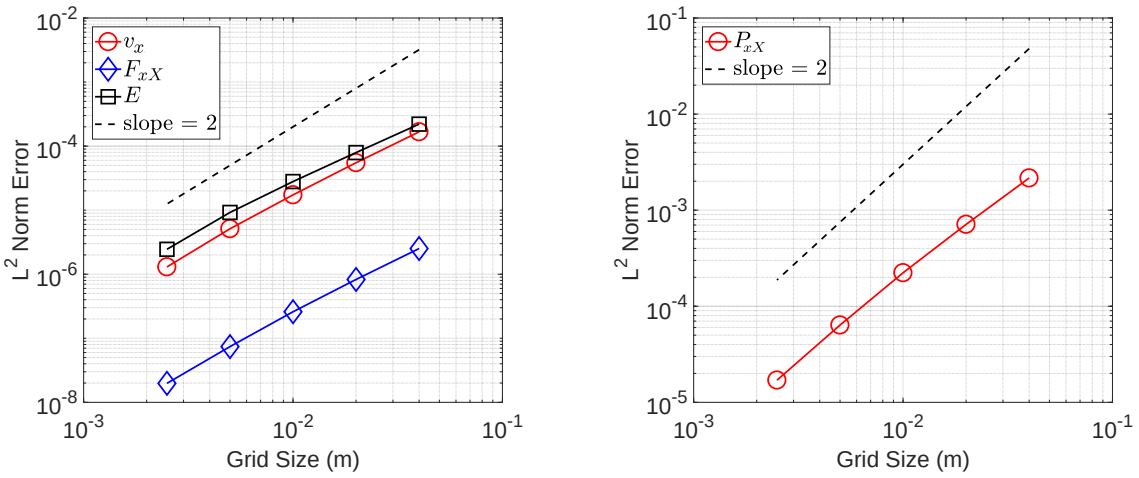


(a) (b)

FIGURE 7.3: One-dimensional bar: $L^2$ norm convergence rate for (a) velocity $v$, deformation gradient $F_{xX}$ and total energy $E$; and (b) first Piola-Kirchhoff stress $P_{xX}$ at the particular time $t = 1 \times 10^{-3}$ s. Results obtained using a neo-Hookean material model along with Mie-Grüneisen equation of state using the proposed VCFVM methodology. The material properties used are Young's modulus $E = 50.5$ KPa, density $\rho_R = 1000$ kg/m$^3$, $h = 10$ W/m.K, $C_v = 1$ J/Kg.K, $\alpha = 2.223 \times 10^{-4}$ K$^{-1}$ and $\alpha_{\text{CFL}} = 0.3$.

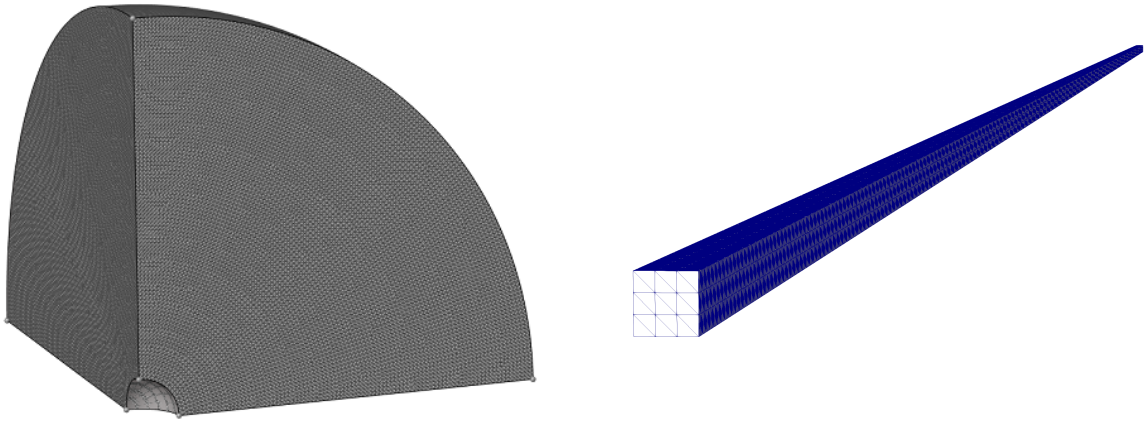

(a) (b)

FIGURE 7.4: Blake problem: (a) mesh of one-eight of a shell and (b) meshh of a needle

such that $\boldsymbol{t}_B = \boldsymbol{0}$. As reported in [107], for computational efficiency, the shell domain can be simplified to a needle of 10 aperture angle, as shown in Figure 7.4b. In this case, all the boundary faces introduced by this geometrical simplification are subjected to symmetry boundary conditions (also known as roller support). The problem is simulated using the $\{\boldsymbol{p}, \boldsymbol{F}, \boldsymbol{H}, J\}$ Total Lagrangian VCFVM scheme in conjunction with acoustic Riemann-based upwinding stabilisation and a linearised elastic neo-Hookean material model. The material properties are described as density $\rho_R = 3000$ kg/m3, Young's modulus $E = 62.5$ GPa and Poisson's ratio $\nu = 0.25$.

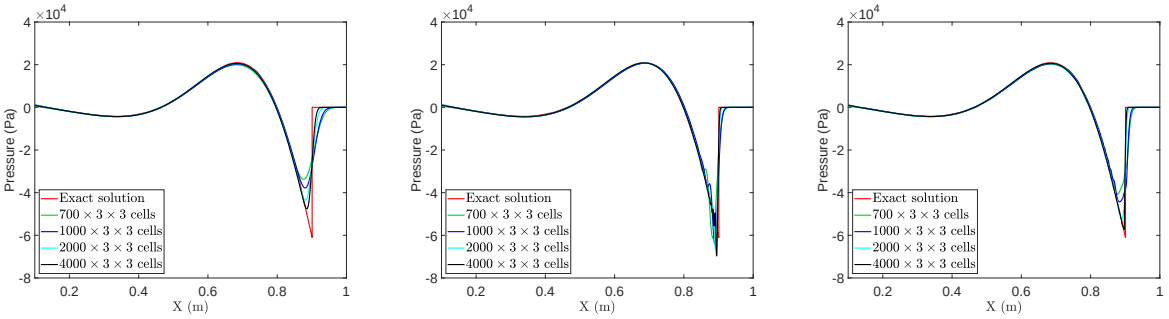


(a) (b) (c)

FIGURE 7.5: Blake problem: The spatial distribution of radial pressure at time $t = 1.6 \times 10^{-4}$ s simulated using (a) piecewise constant reconstruction, (b) piecewise linear reconstruction and (c) piecewise linear reconstruction with the Barth and Jespersen limiter. Results are obtained using the $\{\boldsymbol{p}, \boldsymbol{F}, \boldsymbol{H}, J\}$ Total Lagrangian Upwind–VCFVM scheme with a boundary traction vector $\boldsymbol{t}_B = -p\boldsymbol{n}$ (with $p = 1 \times 10^6$ Pa) constantly applied to the inner face. A neo-Hookean material is used with density $\rho_R = 3000$ kg/m3, Young's modulus $E = 62.5$ GPa, Poisson's ratio $\nu = 0.25$ and $\alpha_{\text{CFL}} = 0.3$. The domain is discretised using a linear tetrahedral mesh.

Figure 7.5 shows the spatial distribution of radial pressure at time $t = 1.6 \times 10^{-4}$ s, as compared to the analytical solution. As it can be observed, the first order VCFVM shows robust results but with considerable numerical diffusion and, then, leads to a stable yet slightly inaccurate solution (see Figure 7.5a). The second order VCFVM (using a piecewise linear reconstruction), as seen in Figure 7.5b, gives much better resolution but fails near discontinuities, where non-physical oscillations are generated. In order to control these spurious oscillations, the Barth and Jespersen limiter [209] is implemented and consequently, a great improvement is observed in Figure 7.5c.

## 7.5 Gas dynamics

In this section, three types of approximated Riemann solvers are introduced, followed by a series of shock test cases in gas dynamics. One of the main objectives is to illustrate the performance of the proposed algorithms in the vicinity of discontinuities.

### 7.5.1 Riemann solvers

Following the definition of Riemann solver in Section 4.3.2 of Chapter 4, three different types of Riemann solvers particularising to one dimensional problems are presented as follows.

### Acoustic Riemann solver

The general contact flux expressions using an acoustic Riemann solver, already presented in Eq. (4.19), can be reduced to the one-dimensional case as

$$t_x{}^C = \frac{c_p^+ c_p^-}{c_p^+ + c_p^-}\left(\frac{t_x^+}{c_p^+} + \frac{t_x^-}{c_p^-}\right) + \frac{c_p^+ c_p^-}{c_p^+ + c_p^-}\left(p_x^+ - p_x^-\right); \tag{7.20a}$$

$$p^C = \frac{c_p^+ p_x{}^+ + c_p^- p_x{}^-}{c_p^+ + c_p^-} + \frac{t_x^+ - t_x^-}{c_p^+ + c_p^-}, \tag{7.20b}$$

where $t_x = P_{xX}$ is the one-dimensional first Piola and $[\cdot]^{+,-}$ denotes the right and left sides of an interface, respectively.

### Harten-Lax-Van Leer Riemann solver

An alternative method to find the solution of a Riemann problem is the Harten-Lax-Van Leer (HLL) Riemann solver, initially introduced by [226]. Here, the structure of the solution is approximated by considering only two (shock) waves. This may result in a diffusive behaviour of the solution since the star region (see Figure 4.7) is lumped into one single region as the contact discontinuity is ignored. In this thesis, the one-dimensional case of HLL Riemann solver is only considered. An extensive discussion on the multi-dimensional HLL Riemann solver can be found at Refs. [232–234].

In this case, the contact fluxes can be obtained by application of Rankine-Hugoniot jump condition as

$$\boldsymbol{\mathcal{F}}^C_{HLL} = \begin{cases} \boldsymbol{\mathcal{F}}^- & v_x \leq S_L \\ \frac{S_R\boldsymbol{\mathcal{F}}^- - S_L\boldsymbol{\mathcal{F}}^+ + S_L S_R(\boldsymbol{\mathcal{U}}_R - \boldsymbol{\mathcal{U}}_L)}{S_R - S_L} & S_L \leq v_x \leq S_R \\ \boldsymbol{\mathcal{F}}^+ & v_x \geq S_R \end{cases} \tag{7.21}$$

where $S_L$ and $S_R$ are the speed of the left and the right waves and $v$ is the flow speed approximated as $v_x = \frac{x^+ - x^-}{t}$. In fact, there are several ways to estimate the $S_L$ and $S_R$ wave speeds [200]. For simplicity, these speeds are defined as $S_L = c_p^-$ and $S_R = c_p^+$ [235]. In fact, the Rankine-Hugoniot jump condition is applied to all conservative variables and their corresponding fluxes which is different from an acoustic Riemann solver where the jump condition only applies to the conservation of linear momentum. Using Eq. (7.21) for the system of equations (7.1), the contact fluxes can be obtained as

$$t_x{}^C = \frac{c_p^+ t_x{}^- - c_p^- t_x{}^+ - c_p^- c_p^+ \left(p_x{}^+ - p_x{}^-\right)}{c_p^+ - c_p^-}; \tag{7.22a}$$

$$p_x{}^C = \frac{c_p^+ p_x{}^- - c_p^- p_x{}^+ - c_p^- c_p^+ \left(F_{xX}^+ - F_{xX}^-\right)}{c_p^+ - c_p^-}; \tag{7.22b}$$

$$t_x{}^C p_x{}^C = \frac{c_p^+ t_x{}^- p^- - c_p^- t_x{}^+ p^+ - c_p^- c_p^+ \left(E^+ - E^-\right)}{c_p^+ - c_p^-}, \tag{7.22c}$$

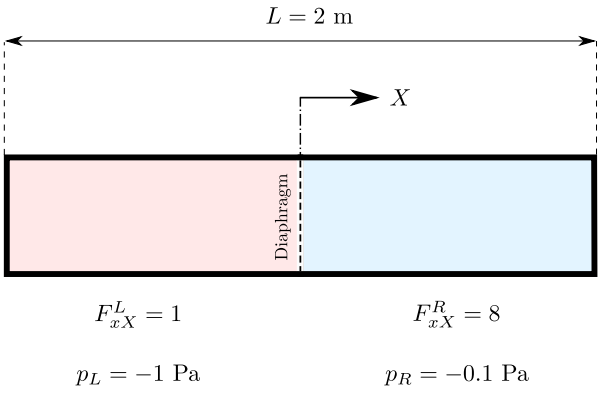


FIGURE 7.6: Sod's shock tube: Problem setup

**Rusanov Riemann solver**

Rusanov [236] proposed another very simple but effectively useful approximation for the contact fluxes as

$$\boldsymbol{\mathcal{F}}^C_{Rus} = \frac{1}{2}\left(\boldsymbol{\mathcal{F}}^- + \boldsymbol{\mathcal{F}}^+\right) - \frac{1}{2}S_{\max}\left(\boldsymbol{\mathcal{U}}^+ - \boldsymbol{\mathcal{U}}^-\right), \tag{7.23}$$

where $S_{\max}$ stands for the maximum wave speed throughout the domain and is defined as

$$S_{\max} = \max\{|c_p^-|, |c_p^+|\}. \tag{7.24}$$

The choice of $c_p$ and $c_s$ can play a crucial role in the accuracy of this approximation. In this work, and for simplicity, the wave speeds presented in Eq. (4.20) are taken into account. In the case of a one-dimensional isothermal process, the Rankine-Hugoniot jump condition can be derived for the conservation of linear momentum and as a result, the contact fluxes render

$$t^C_{Rus} = \frac{1}{2}\left(t_x^- + t_x^+\right) + \frac{1}{2}S_{\max}\left(p_x^+ - p_x^-\right); \tag{7.25a}$$

$$p^C_{Rus} = \frac{1}{2}\left(p_x^- + p_x^+\right) + \frac{1}{2S_{\max}}\left(t_x^+ - t_x^-\right). \tag{7.25b}$$

Notice that the above approximated contact fluxes (Eq. (7.25) and Eq. (7.22c)) are the simplified one-dimensional versions of Eq. (7.20) with a relatively more robust behaviour, applicable to be tested for one-dimensional examples.

### 7.5.2 Sod's shock tube

A very well-known benchmarking example in the context of gas dynamics is the Sod's shock tube, initially introduced by [237], where the behaviour of an ideal gas subjected to a discontinuous initial condition is investigated. A tube of length $L = 2$ m is separated by a diaphragm into two halves. Each half contains an ideal gas at rest with different initial states (see Figure 7.6) where a free flow boundary condition is considered.

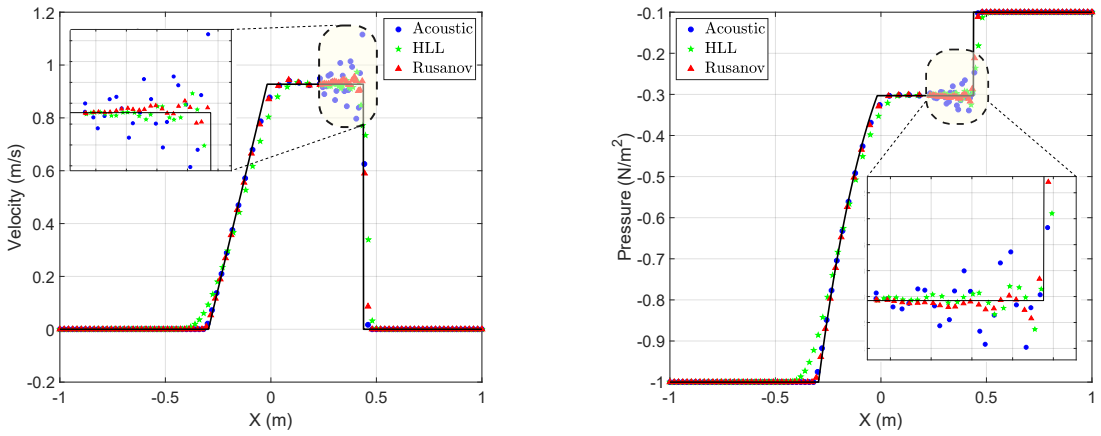


FIGURE 7.7: Sod's shock tube: Comparing the solutions obtained by the proposed approximated Riemann solvers with the analytical solution for (a) velocity and (b) pressure at $t = 0.25$ s. Results obtained for an ideal gas using the proposed VCFVM methodology with 100 elements and Barth-Jespersen limiter. The material properties used are $\rho_R = 1$ kg/m$^3$, $\Gamma_0 = 0.4$ and $\alpha_{\text{CFL}} = 0.4$.

The diaphragm is ruptured at $t = 0$ in order to let the gases get interacted and that, this triggers the generation of shock waves. An ideal gas is used with density of $\rho_R = 1$ kg/m$^3$ and Mie-Grüneisen coefficient $\Gamma_0 = 0.4$.

Figure 7.7 shows the comparison between the analytical solution [200] and the numerical solutions obtained using the three proposed approximated Riemann solvers at time $t = 0.25$ s. The wave patterns of this example is a left rarefaction, contact discontinuity at the middle (intermediate wave) and a right shock wave. In general, the Rusanov Riemann solver captured the shock waves more accurately with respect to the other two approximated Rieman solvers. The acoustic Riemann solver has shown bigger overshoots/undershoots in the vicinity of the shock wave and the HLL Riemann solver seems to be more diffusive in capturing the rarefaction. It must be mentioned that adapting other nonlinear Riemann solvers (e.g. Roe's Riemann solver) to the numerical approximation could improve the resolution of the solution in the vicinity of shocks [200]. Since the Rusanov Riemann solver shows reasonably more accurate results, the variation of velocity, Jacobian ($F_{xX}$), total energy and pressure of the ideal gas along the centerline of the tube length is shown in Figure 7.8 at time $t = 0.25$ s. It can be observed that the Rusanov Riemann solver has convincingly captured the solution in the vicinity of shock waves for all the variables of interest.

### 7.5.3 Left Woodward-Colella blast test

This example, initially introduced by [238], resembles the geometry of the Sod's shock tube but considering different initial conditions. The gases on the left and right side of the tube are initially at rest with different states ($F^L_{xX} = F^R_{xX} = 1$ and $p_L = -1000$ Pa and $p_R = -0.01$ Pa). The initial severe jump in pressure can be imposed through the total energy ($E_L = 2500$ Pa

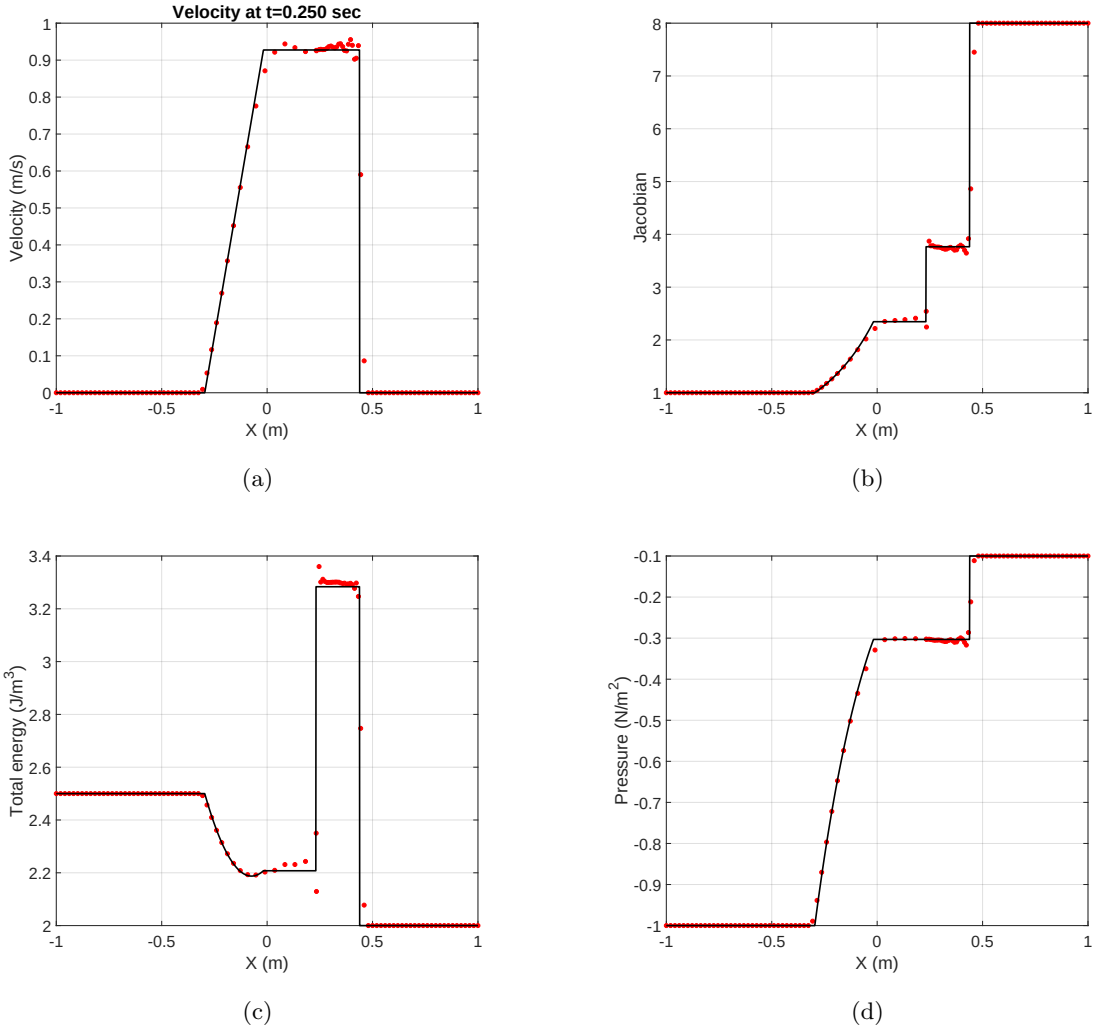


FIGURE 7.8: Sod's shock tube: Comparison between the analytical and numerical solution obtained using Rusanov Riemann solver for (a) velocity; (b) Jacobian ($F_{xX}$); (c) total energy; and (d) pressure at $t = 0.25$ s. Results obtained for an ideal gas using the proposed VCFVM methodology with 100 elements and Barth and Jespersen limiter. The material properties used are $\rho_R = 1$ kg/m$^3$, $\Gamma_0 = 0.4$ and $\alpha_{\text{CFL}} = 0.4$.

and $E_R = 0.025$ Pa). The diaphragm is ruptured at $t = 0$ allowing the interaction of the gases. An ideal gas is used with density of $\rho_R = 1$ kg/m$^3$ and Mie-Grüneisen coefficient $\Gamma_0 = 0.4$.

Figure 7.9 shows the comparison of analytical solution [200] versus the numerical solutions obtained by the proposed three approximated Riemann solvers at time $t = 0.012$ s. The similar wave patterns can be observed as the previous example of Sod's shock tube. This leads to the conclusion that the Rusanov Riemann solver has more accurately captured the shock waves against the other two approximated Riemann solvers. The acoustic Riemann solver has shown more oscillations close to the shock wave and the HLL Riemann solver remains the diffusive behaviour, particularly for the rarefaction wave. To further investigate the behaviour of Rusanov Riemann solver, the distribution of velocity, Jacobian ($F_{xX}$), total energy and

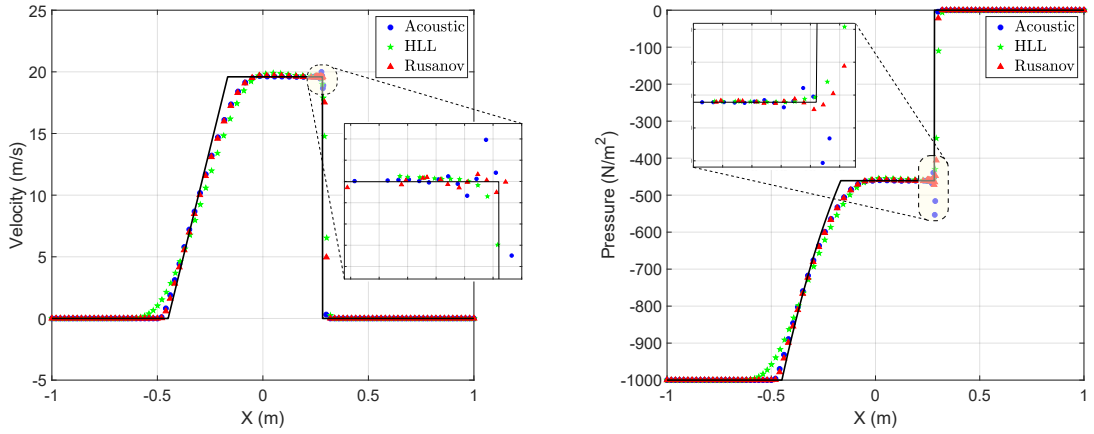


(a) (b)

FIGURE 7.9: Left Woodward-Colella blast test: Comparing the solutions obtained by the proposed approximated Riemann solvers with the analytical solution for (a) velocity and (b) pressure at $t = 0.012$ s. Results obtained for an ideal gas using the proposed VCFVM methodology with 100 elements and Barth-Jespersen limiter. The material properties used are $\rho_R = 1$ kg/m$^3$, $\Gamma_0 = 0.4$ and $\alpha_{\text{CFL}} = 0.4$.

pressure along the centerline of the tube length at time $t = 0.012$ s is depicted in Figure 7.10 in which the shock waves are well captured for all the variables of interest.

### 7.5.4 Right Woodward-Colella blast test

This example is geometrically analogous to the left Woodward-Colella blast test, but with different initial conditions, aiming at generating a different shock wave pattern. The gases on the left and right side of the tube are initially at rest with dissimilar states ($F^L_{xX} = F^R_{xX} = 1$ and $p_L = -0.01$ Pa and $p_R = -100$ Pa). The initial jump in pressure can be imposed through the total energy ($E_L = 0.025$ Pa and $E_R = 250$ Pa). The diaphragm is ruptured at $t = 0$ allowing the generation of the shock waves. An ideal gas is used with density of $\rho_R = 1$ kg/m$^3$ and Mie-Grüneisen coefficient $\Gamma_0 = 0.4$. Figure 7.11 shows the comparison of the analytical solution [200] against the numerical solutions obtained by the three proposed approximated Riemann solvers at time $t = 0.035$ s. A left shock wave and a right rarefaction wave is the wave pattern generated in this example. It can be similarly concluded that the Rusanov Riemann solver has outperformed the acoustic and HLL Riemann solvers.

Figure 7.12 shows the distribution of the velocity, Jacobian ($F_{xX}$), total energy and pressure along the centerline of the tube length at time $t = 0.035$ s where the shocks are well captured using the approximated Rusanov Riemann solver.

## 7.6 Conclusion

In this chapter, a set of one-dimensional examples are investigated with the objective of assessing the fundamental characteristics of the proposed numerical algorithm. A spatial convergence

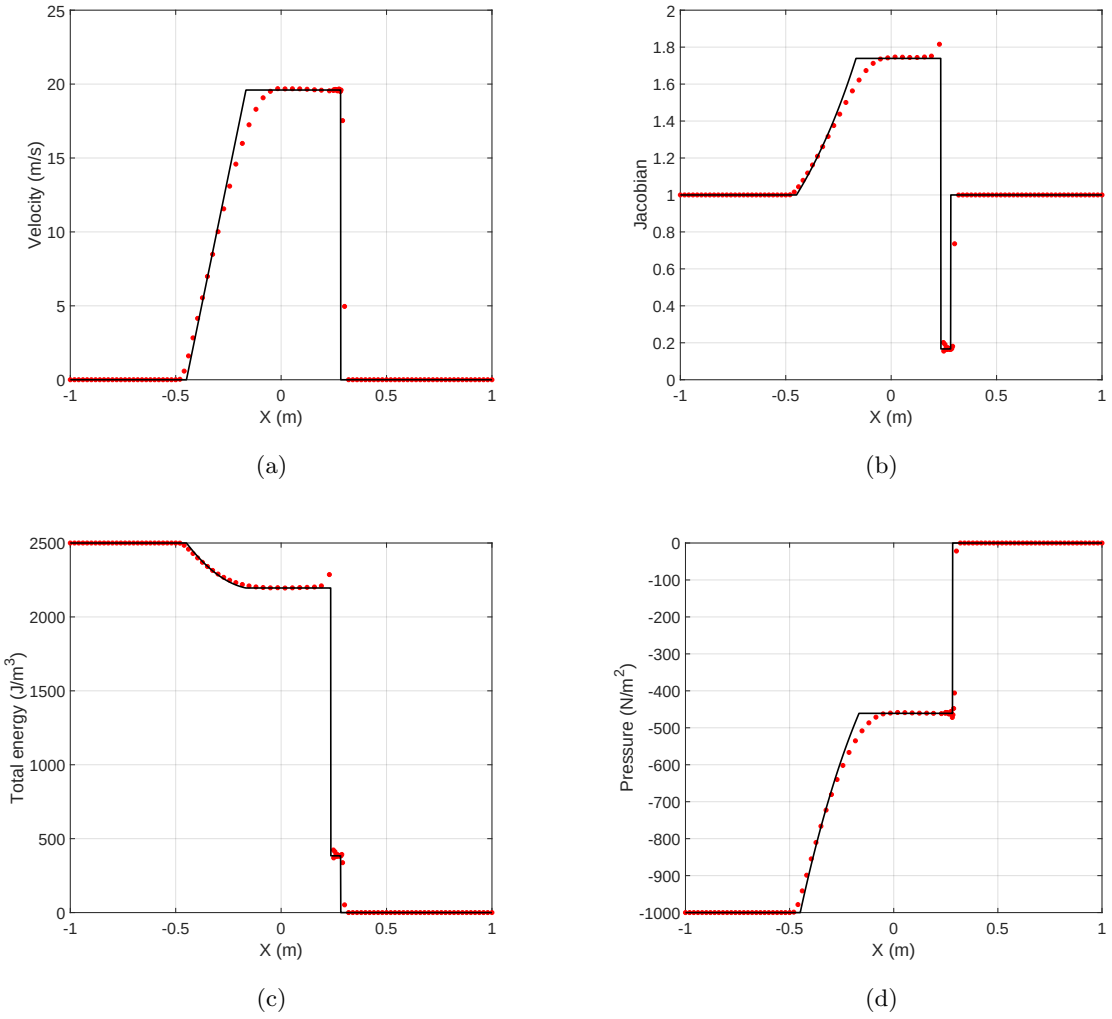


FIGURE 7.10: Left Woodward-Colella blast test: Comparison between the analytical and numerical solutions obtained using Rusanov Riemann solver for (a) velocity; (b) Jacobian ($F_{xX}$); (c) total energy; and (d) pressure at $t = 0.25$ s. Results obtained for an ideal gas using the proposed VCFVM methodology with 100 elements and Barth and Jespersen limiter. The material properties used are $\rho_R = 1$ kg/m$^3$, $\Gamma_0 = 0.4$ and $\alpha_{\text{CFL}} = 0.4$.

study is carried out in which second order accuracy for velocity, strains and stresses and the temperature is observed. In addition, the employed numerical methodology has shown excellent behaviour in the case of dealing with severe shocks, in particular case of isothermal elasticity and gas dynamics.

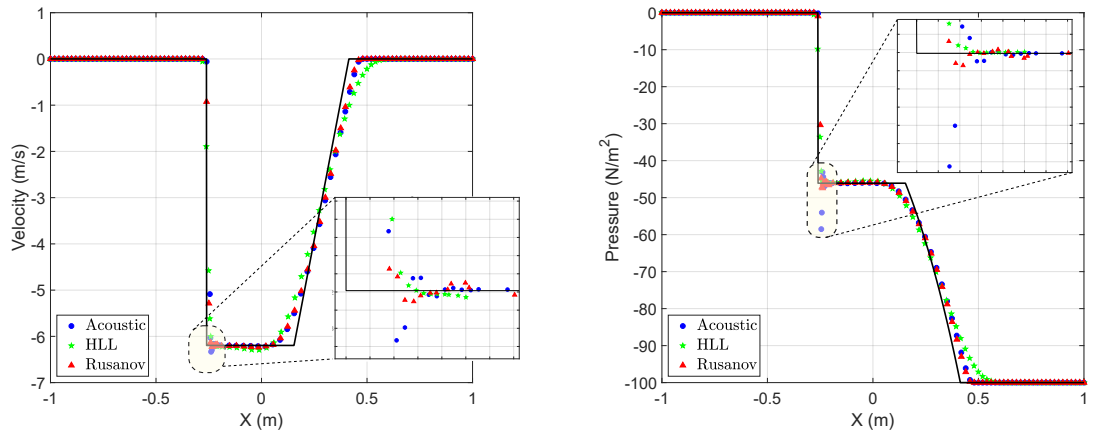


(a) (b)

FIGURE 7.11: Right Woodward-Colella blast test: Comparing the solutions obtained by the proposed approximated Riemann solvers with the analytical solution for (a) velocity and (b) pressure at $t = 0.035$ s. Results obtained for an ideal gas using the proposed VCFVM methodology with 100 elements and Barth-Jespersen limiter. The material properties used are $\rho_R = 1$ kg/m$^3$, $\Gamma_0 = 0.4$ and $\alpha_{\text{CFL}} = 0.4$.

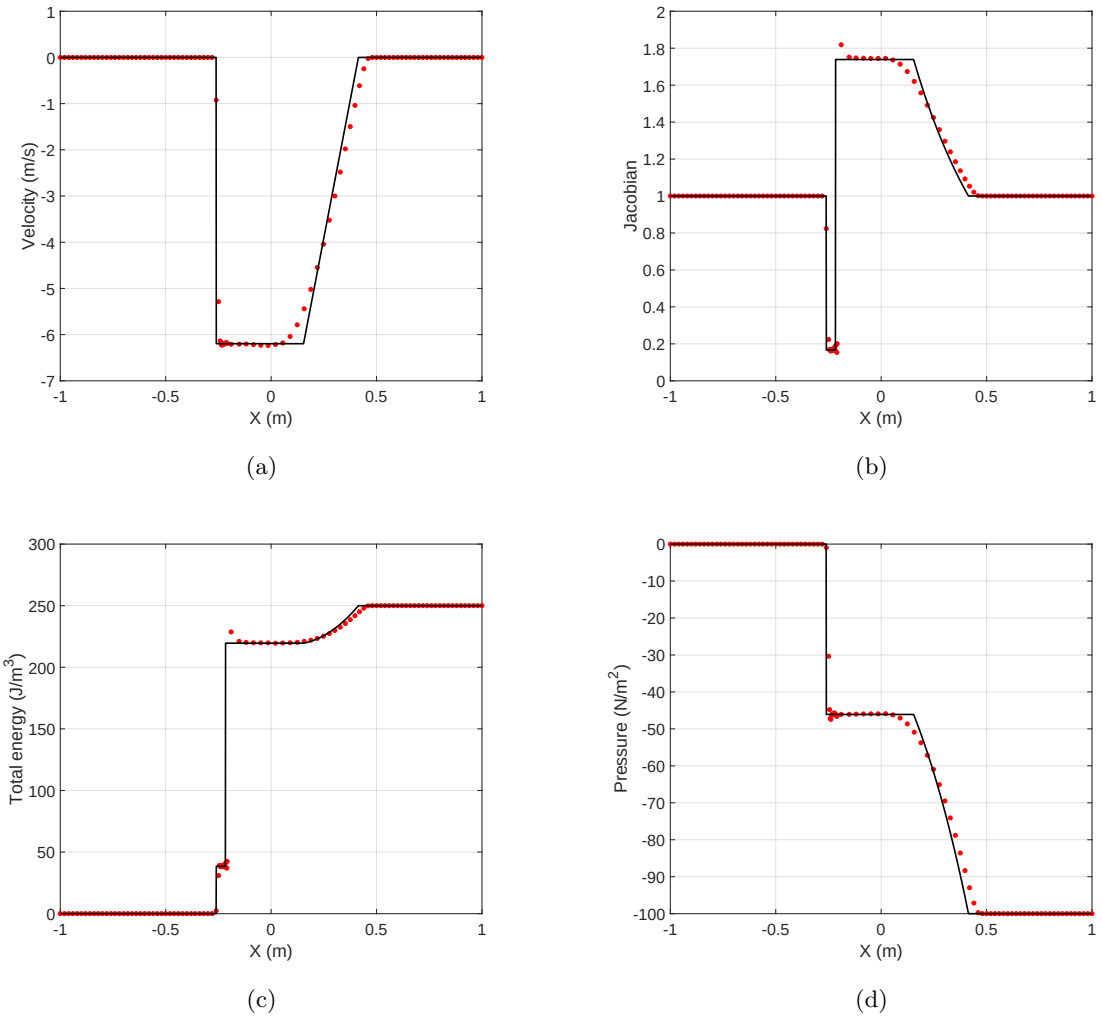


FIGURE 7.12: Right Woodward-Colella blast test: Comparison between the analytical and numerical solutions obtained using Rusanov Riemann solver for (a) velocity; (b) Jacobian ($F_{xX}$); (c) total energy; and (d) pressure at $t = 0.035$ s. Results obtained for an ideal gas using the proposed VCFVM methodology with 100 elements and Barth and Jespersen limiter. The material properties used are $\rho_R = 1$ kg/m$^3$, $\Gamma_0 = 0.4$ and $\alpha_{\text{CFL}} = 0.4$.

Chapter 8

# Multi-dimensional problems: Fundamental studies

## 8.1 Introduction

In this chapter, a set of three-dimensional problems are analysed in order to assess the fundamental properties of proposed $\{\boldsymbol{p}, \boldsymbol{F}, \boldsymbol{H}, J, \eta \text{ or } E\}$ Vertex-Centred Finite Volume method (VCFVM) and Smooth Particle Hydrodynamics (SPH) algorithms. That includes the spatial convergence of both numerical methodologies (Section 8.2), conservation properties of the field variables (Section 8.3), demonstration of the robustness of the both proposed numerical algorithms through a challenging benchmark example (Section 8.4) and, finally, investigation of the capability of the algorithms in handling incompressibility (Section 8.5).

## 8.2 Spatial convergence

### 8.2.1 Expanding cube

The main objective of this example is to show the convergence behaviour of the proposed $\{\boldsymbol{p}, \boldsymbol{\chi}, E\}$ VCFVM and SPH methodologies. A cube of unit side length (Figure 8.1) is subjected to a thermo-mechanical deformation process through the following mapping and temperature profiles

$$\begin{cases} \boldsymbol{x}(\boldsymbol{X}, t) = \frac{At}{L} (\boldsymbol{X} \cdot \boldsymbol{X}) \, \mathtt{I} + \boldsymbol{X}; \quad 0 \leq |\boldsymbol{X}| \leq L, \\ \theta(X, t) = B\theta_{amb} \sin\left(\frac{\pi X}{L}\right) (t+1) + \theta_{amb}, \end{cases} \tag{8.1}$$

where $L = 1$ m, $\theta_{amb} = 293.15$ K denotes the ambient temperature, $\mathtt{I} = [1, 1, 1]^T$ and $A = 0.2381$ s$^{-1}$ and $B = -0.0012$ s$^{-1}$ are constant coefficients, obtained in Section 7.3 in order for the particular case of linear thermo-elasticity. Taking time derivative and gradient of the

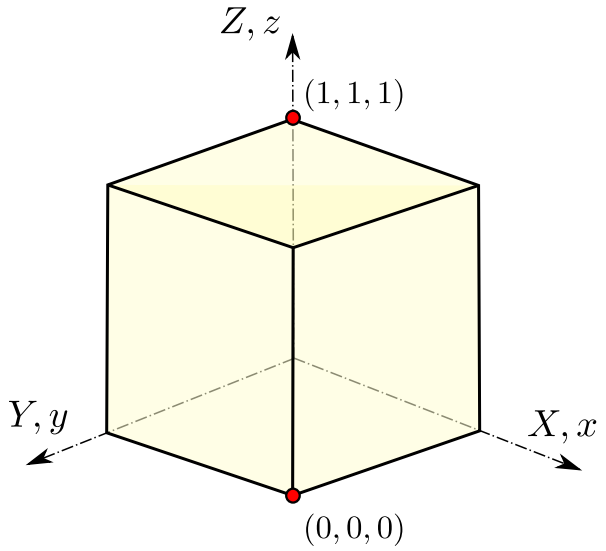


FIGURE 8.1: Expanding cube: Problem configuration.

mapping profile gives linear momentum and deformation gradient, respectively, as follows

$$\boldsymbol{p}(\boldsymbol{X},t) = \frac{\rho_R A}{L}\left(\boldsymbol{X}\cdot\boldsymbol{X}\right)\mathtt{I}; \tag{8.2}$$

$$\boldsymbol{F}(\boldsymbol{X},t) = \frac{2At}{L}\boldsymbol{\mathcal{X}} + \boldsymbol{I}, \tag{8.3}$$

where $\boldsymbol{\mathcal{X}} = \boldsymbol{X}\otimes(\boldsymbol{E}_1+\boldsymbol{E}_2+\boldsymbol{E}_3)$ and $\boldsymbol{E}_1 = [1,0,0]$, $\boldsymbol{E}_2 = [0,1,0]$, $\boldsymbol{E}_3 = [0,0,1]$. The corresponding mechanical and thermal initial conditions for linear momentum, temperature (see Figures 8.2) and deformation gradient can then be identified as follows

$$\boldsymbol{p}(\boldsymbol{X},t=0) = \frac{\rho_R A}{L}\left(\boldsymbol{X}\cdot\boldsymbol{X}\right)\mathtt{I}; \tag{8.4a}$$

$$\boldsymbol{F}(\boldsymbol{X},t=0) = \boldsymbol{I}; \tag{8.4b}$$

$$\theta(\boldsymbol{X},t=0) = \theta_{amb}\left(B\sin\left(\frac{\pi X}{L}\right)+1\right). \tag{8.4c}$$

Symmetric mechanical boundary conditions corresponding to the given mapping at faces $X=0$, $Y=0$ and $Z=0$ and free boundary conditions at faces $X=1$, $Y=1$ and $Z=1$ are taken into account. The thermal boundary conditions will also be Dirichlet type at faces $X=0$ and $X=1$ as $\theta=\theta_{amb}$ and free boundary (zero-flux) for the rest of the faces.

Recalling Eq. (2.10) and Eq. (2.46), the expressions for computing body force $f_R$ and heat source term $s_R$ are as follows

$$\boldsymbol{f_R} = \frac{\partial \boldsymbol{p}}{\partial t} - \mathrm{DIV}(\boldsymbol{P}); \tag{8.5}$$

$$s_R = \theta\dot{\eta} + \mathrm{DIV}\left(\boldsymbol{Q}\right). \tag{8.6}$$

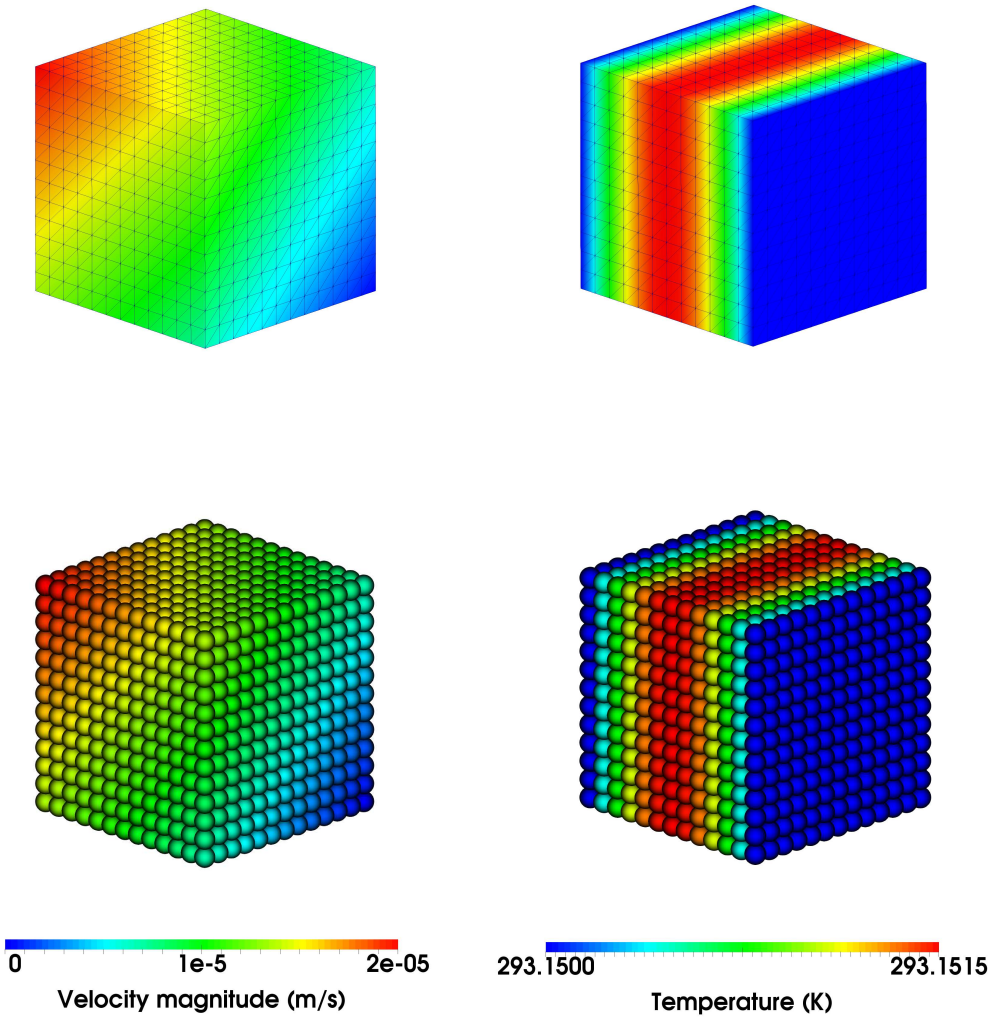


FIGURE 8.2: Expanding cube: Initial conditions.

Looking in Equations (8.5) and (8.6), and recalling the expressions for the linearised first Piola Eq. (3.69) and the linearised entropy Eq. (3.70), it is essential to compute the derivatives presented in Table 8.1 in order to achieve explicit expressions for the source terms. Therefore, substituting the given linear momentum and temperature profile to the set of $\{\boldsymbol{p}, \boldsymbol{F}, \boldsymbol{H}, J, E\}$ equations and also with the aid of Equations presented in Table (8.1), the body force and heat

TABLE 8.1: Manufacturing solution: Required derivatives to obtain the source terms

| Variable | Space derivatives | Time derivatives |
|---|---|---|
| $\boldsymbol{p}$ | $\boldsymbol{\nabla}_0 \boldsymbol{p} = \frac{2A\rho_R}{L}\boldsymbol{\mathcal{X}}$ | $\frac{\partial \boldsymbol{p}}{\partial t} = \boldsymbol{0}$ |
| $\boldsymbol{F}$ | $\mathrm{DIV}\boldsymbol{F} = \frac{2At}{L}\mathtt{I}$ | $\frac{\partial \boldsymbol{F}}{\partial t} = \frac{2A}{L}\boldsymbol{\mathcal{X}}$ |
| $\theta$ | $\mathrm{DIV}(\theta \boldsymbol{I}) = \left[B\theta_{amb}(t+1)\frac{\pi}{L}cos\left(\frac{\pi X}{L}\right)\right]\boldsymbol{E}_1$ | $\frac{\partial \theta}{\partial t} = B\theta_{amb}\sin\left(\frac{\pi X}{L}\right)$ |

source term yields

$$\boldsymbol{f_R} = -(2\mu+\lambda)\left(\frac{2At}{L}\right)\mathtt{I} + \left[BC_v\Gamma_0\theta_{amb}\frac{\pi}{L}cos\left(\frac{\pi X}{L}\right)(t+1)\right]\boldsymbol{E}_1; \tag{8.7}$$

$$s_R = \underbrace{\theta\left(\frac{B}{\theta_R}C_v\theta_{amb}\sin\left(\frac{\pi X}{L}\right) + \frac{2AC_v\Gamma_0}{L}(X+Y+Z)\right)}_{\dot{\eta}} + \tag{8.8}$$

$$\underbrace{Bh\theta_{amb}\left(\frac{\pi}{L}\right)^2(t+1)\sin\left(\frac{\pi X}{L}\right)}_{\mathrm{DIV}\boldsymbol{Q}},$$

where $\theta$ is defined in Equation (8.1b). Figure 8.3 depicts the expected second order convergence pattern ($L^2$ norm error) for the components of the linear momentum, diagonal components of the first Piola-Kirchhoff stress tensor and also temperature. It is interesting to note that the SPH methodology requires finer grid size (the characteristic length defining the particle spacing) in comparison with the VCFVM. This is expected as we know the SPH algorithm is prone to more diffusive behaviour, depending on the kernel approximation and its smoothing length. However, the VCFVM algorithm provides a sufficient number of neighbours for a control volume in which any field variable can be properly approximated. Additionally, a slightly less accurate solution (with the same slope but a higher translation error) can be observed for the SPH methodology which, again, stems from its diffusive behaviour.

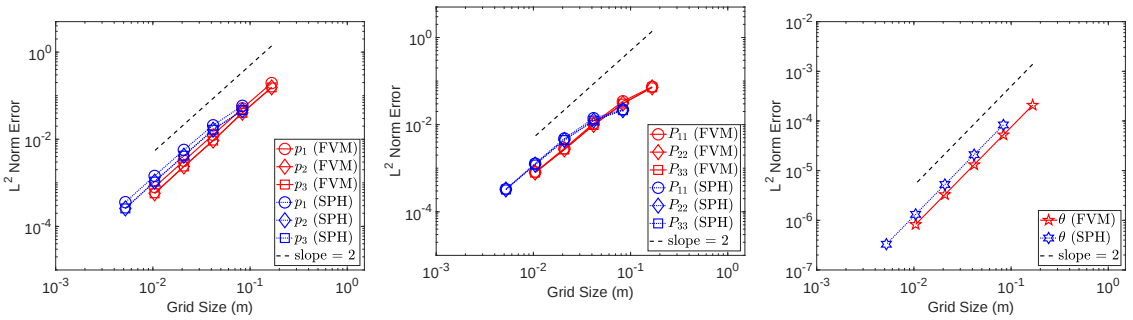


(a) Linear momentum (b) First Piola-Kirchhoff stress tensor (c) Temperature

FIGURE 8.3: Expanding cube: $L^2$ norm convergence of (a) Linear momentum; (b) first Piola-Kirchhoff stress tensor components; and (c) Temperature at a particular time $t = 0.001$ s. Results obtained using a neo-Hookean constitutive model along with Mie-Grüneisen equation of state using the proposed total energy-based SPH methodology. The material properties used are Young's modulus $E = 50.05$ KPa, density $\rho_R = 1000$ kg/m$^3$, thermal conductivity $h = 10$ W/m.K, Specific heat capacity $C_v = 1$ J/Kg.K, thermal expansion coefficient $\alpha = 2.223 \times 10^{-4}$ K$^{-1}$ and $\alpha_{\text{CFL}} = 0.3$.

## 8.3 Conservation

### 8.3.1 L-shaped block

The motion of a L-shaped block (Figure 8.4) is investigated initially introduced by [78] and, then, studied by [3, 6, 7, 118, 239, 240], subjected to time-dependent forces (mechanical Neumann boundary condition) on two of its sides and is then left free flying in space

$$\boldsymbol{F}_1(t) = -\boldsymbol{F}_2(t) = (150, 300, 450)^T\, p(t); \qquad p(t) = \begin{cases} t & 0 \le t < 2.5 \\ 5 - t & 2.5 \le t < 5 \\ 0 & t \ge 5 \end{cases},$$

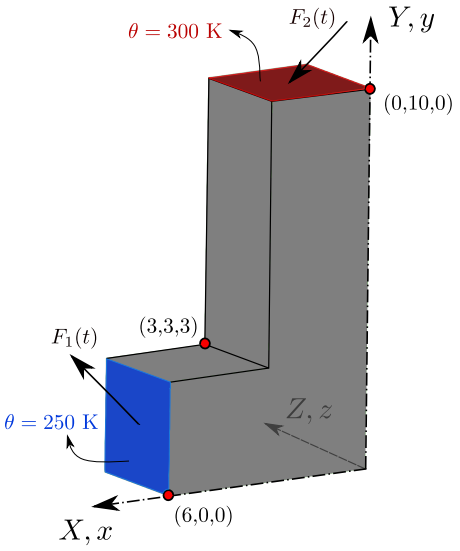


FIGURE 8.4: L-shaped block: Problem setup

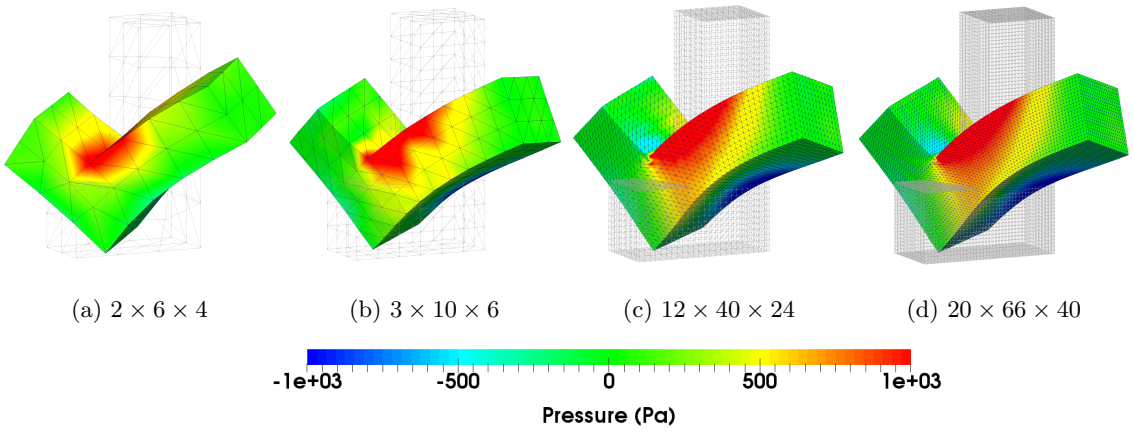


(a) $2 \times 6 \times 4$ (b) $3 \times 10 \times 6$ (c) $12 \times 40 \times 24$ (d) $20 \times 66 \times 40$

(e)

FIGURE 8.5: L-shaped block: mesh refinement of deformed states with pressure contour plots at time $t = 7.7$ s for four different mesh sizes (a) $h = 1.67$ m; (b) $h = 1$ m; (c) $h = 0.25$ m and (d) $h = 0.15$ m. Results obtained using a neo-Hookean constitutive model along with Mie-Grüneisen equation of state using the proposed total energy-based VCFVM methodology. The material properties used are Young's modulus $E = 50.05$ KPa, density $\rho_R = 1000$ kg/m$^3$, Poisson's ratio $\nu = 0.3$, thermal conductivity $h = 10$ W/m.K, Specific heat capacity $C_v = 1$ J/Kg.K, thermal expansion coefficient $\alpha = 2.223 \times 10^{-4}$ K$^{-1}$ and $\alpha_{\text{CFL}} = 0.3$.

while the block is thermally insulated from the environment. A thermo-elastic neo-Hookean material model along with Mie-Grüneisen equation of state is employed with Young's modulus $E = 50.05$ KPa, density $\rho_R = 1000$ Kg/m$^3$, Poisson's ratio $\nu = 0.3$, thermal conductivity $h = 10$ W/m.K, specific heat capacity $C_v = 1$ J/Kg.K and thermal expansion coefficient $\alpha = 2.223 \times 10^{-4}$ K$^{-1}$ where the block has an initial homogeneous temperature distribution $\theta_R = 293.15$ K. The main objective of this example is to computationally demonstrate the long term preservation of linear momentum, angular momentum and global total energy.

A mesh refinement study for the block is carried out where pressure contour plots are shown in Figure 8.5 at time $t = 7.7$ s. In addition, displacement and velocity evolution at the material position $\boldsymbol{X} = [0, 10, 0]^T$ are plotted for three different meshes in Figure 8.6.

In order to benchmark the numerical solution, Figure 8.7 depicts a comparison between the proposed total energy-based VCFVM and SPH methodologies. The temperature and pressure distributions are presented at the physical time of $t = 11$ s and a very good agreement can be observed between the results. Figures 8.8a and 8.8c illustrate the linear momentum and global total energy preservations. The latter proves the satisfaction of first law of thermodynamics as the total energy grows due to the implication of the external forces (tractions) and, then, remains constant once the tractions are released. The evolution of the total kinetic energy and the total internal energy are also depicted. The sum is conserved, but there is an irreversible transfer from the first to the second because of conduction (which is dissipative). The average value (around which the quantities fluctuate) decrease for the total kinetic energy and increase for the total internal energy, and the latter corresponds to an increase of the (spatial) average temperature. In this case, since we have a free-flying structure, the long-term solution is a block in rigid body motion with a uniform temperature (higher than the initial one), so the kinetic

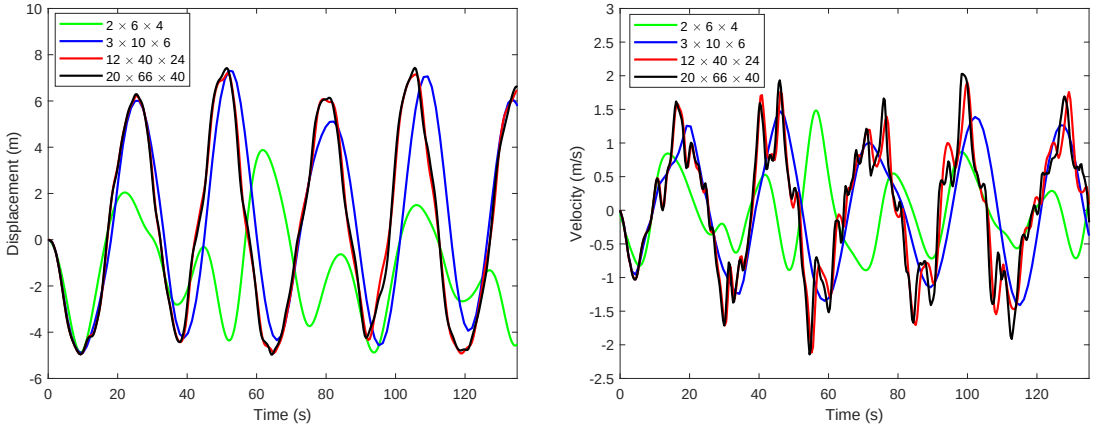


(a) Z-Displacement evolution

(b) Z-Velocity evolution

FIGURE 8.6: L-shaped block: time evolution of (a) horizontal displacement $u_z$ and (b) horizontal velocity $v_z$ at material point $\boldsymbol{X} = [0, 10, 0]^T$. Results obtained using a neo-Hookean constitutive model along with Mie-Grüneisen equation of state using the proposed total energy-based VCFVM methodology. The material properties used are Young's modulus $E = 50.05$ KPa, density $\rho_R = 1000$ kg/m$^3$, Poisson's ratio $\nu = 0.3$, thermal conductivity $h = 10$ W/m.K, Specific heat capacity $C_v = 1$ J/Kg.K, thermal expansion coefficient $\alpha = 2.223 \times 10^{-4}$ K$^{-1}$ and $\alpha_{\text{CFL}} = 0.3$.

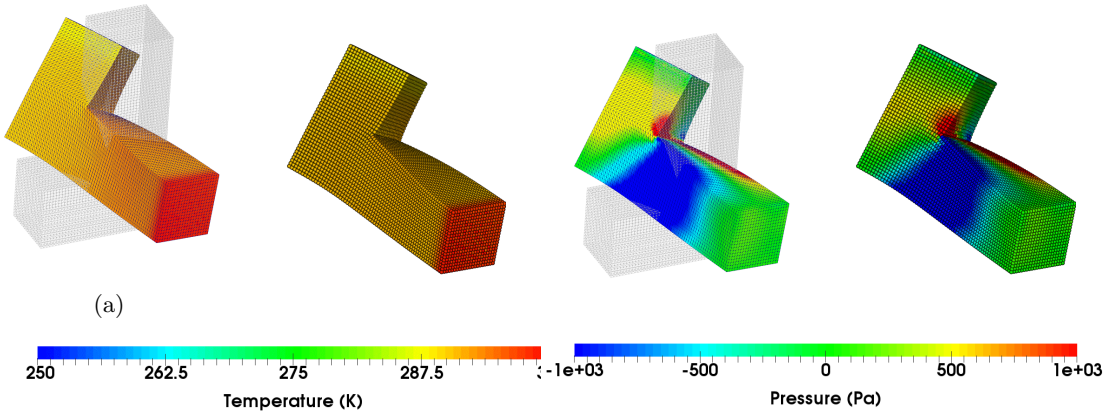


(a)

FIGURE 8.7: L-shaped block: Comparison of deformed shape plotted with temperature and pressure distributions using the total energy-based VCFVM and SPH methodologies at time $t = 11$ s. Results obtained using a neo-Hookean constitutive model along with Mie-Grüneisen equation of state with material properties Young's modulus $E = 50.05$ KPa, density $\rho_R = 1000$ kg/m$^3$, Poisson's ratio $\nu = 0.3$, thermal conductivity $h = 10$ W/m.K, specific heat capacity $C_v = 1$ J/Kg.K, thermal expansion coefficient $\alpha = 2.223 \times 10^{-4}$ K$^{-1}$ and $\alpha_{\text{CFL}} = 0.3$.

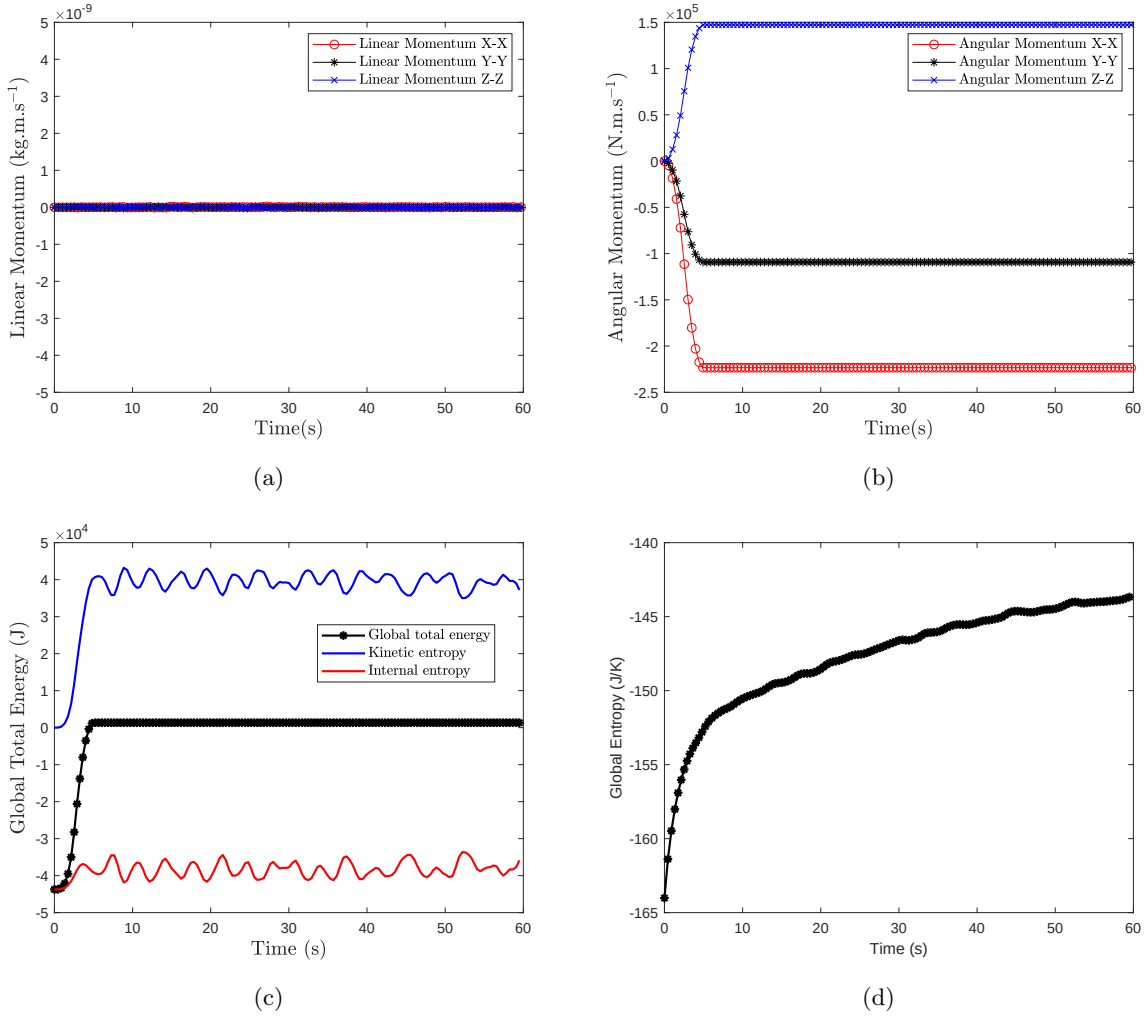


FIGURE 8.8: L-shaped block: Time evolution of (a) linear momentum; (b) angular momentum; (c) global total energy; and (d) global entropy. Results obtained using a neo-Hookean constitutive model along with Mie-Grüneisen equation of state using the proposed total energy-based VCFVM methodology. The material properties used are Young's modulus $E = 50.05$ KPa, density $\rho_R = 1000$ kg/m$^3$, Poisson's ratio $\nu = 0.3$, thermal conductivity $h = 10$ W/m.K, specific heat capacity $C_v = 1$ J/Kg.K, thermal expansion coefficient $\alpha = 2.223 \times 10^{-4}$ K$^{-1}$ and $\alpha_{\text{CFL}} = 0.3$.

energy may not tend towards zero but a positive constant value. In addition, the time evolution of angular momentum is shown in Figure 8.8b where it preserved once the external forces are released. Figure 8.8d depicts the evolution of global entropy which is growing positively all the time as a result of increasing temperature within the insulated free-flying structure. A sequence of the deformed states are shown in Figure 8.9 where a very smooth temperature and pressure distributions can be observed. In fact, the temperature field shows how the heat is conducting through the insulated body as results of the applied initial temperature gradient.

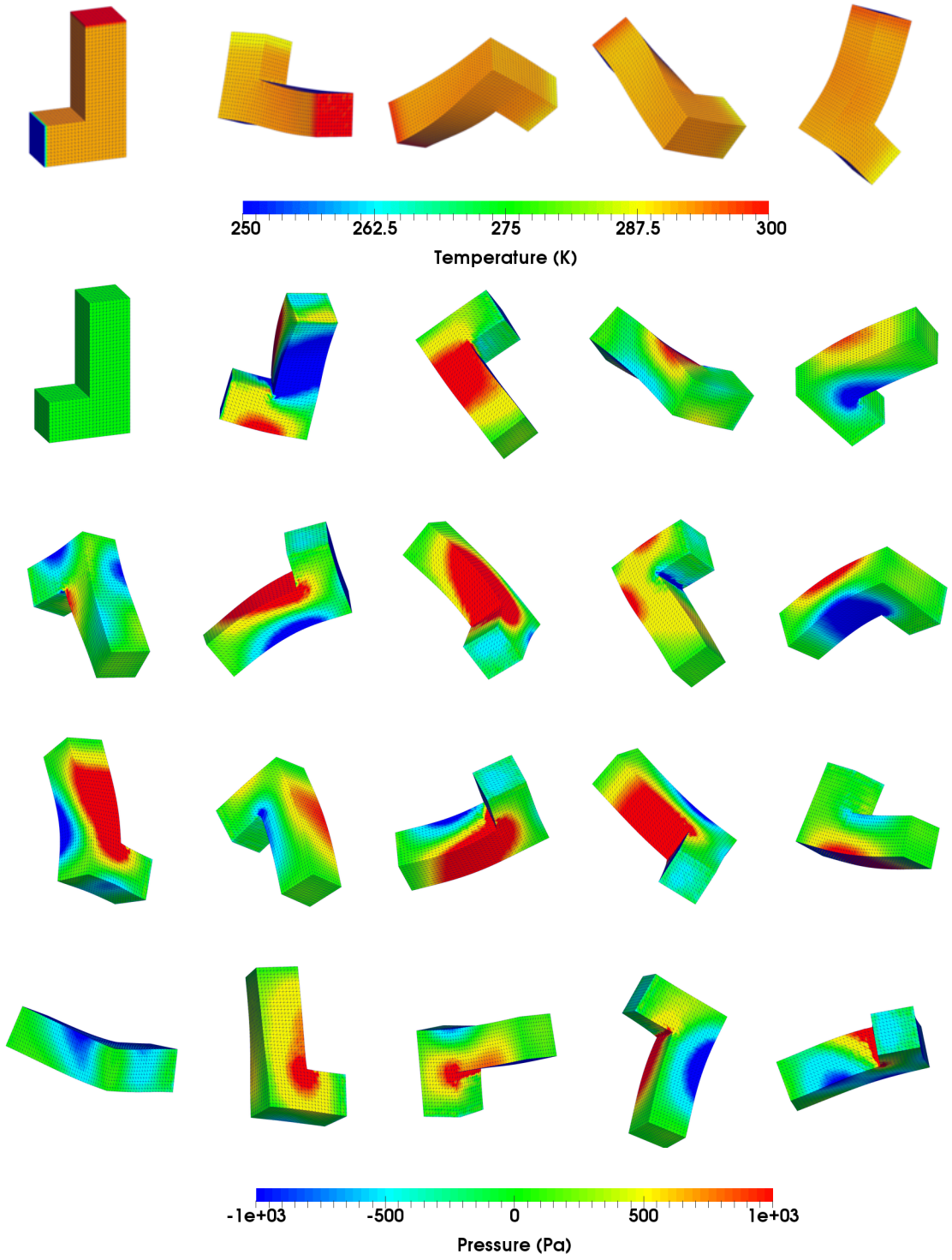


FIGURE 8.9: L-shaped block: A sequence of deformed configuration with temperature and pressure distributions at times $t = 10 \times \{0, 1, 2, 2.5, 3\}$ s (left to right) and $t = 2 \times \{0, 1, 2, 3, ..., 19\}$ s (left to right-top to bottom), respectively. Results obtained using a neo-Hookean constitutive model along with Mie-Grüneisen equation of state using the proposed total energy-based VCFVM methodology. The material properties used are Young's modulus $E = 50.05$ KPa, density $\rho_R = 1000$ kg/m$^3$, Poisson's ratio $\nu = 0.3$, thermal conductivity $h = 10$ W/m.K, specific heat capacity $C_v = 1$ J/Kg.K, thermal expansion coefficient $\alpha = 2.223 \times 10^{-4}$ K$^{-1}$ and $\alpha_{\text{CFL}} = 0.3$.

### 8.3.2 Rotating Disk

This example presents the rotation of a free-flying disk (no mechanical Dirichlet or Neumann boundary conditions) shown in Figure 8.10, which is initialised by the following velocity field

$$v_R(\boldsymbol{X}) = \boldsymbol{\omega}_R \times \boldsymbol{X}, \quad \text{with} \quad \boldsymbol{\omega}_R = [1,1,1]^T. \tag{8.9}$$

The disk is thermally insulated from the environment except for a quarter of its lateral surface (see Figure 8.10) in which a thermal Neumann boundary condition (sinusoidal heat flux $\boldsymbol{Q}$) is imposed as

$$Q = \frac{2000}{A_0} f(t); \qquad f(t) = \begin{cases} \sin\left(\frac{\pi}{2}t\right) & t \leq 4s \\ 0 & t > 4s \end{cases}, \tag{8.10}$$

with $A_0$ considered as the area where the heat flux is applied. A thermo-elastic neo-Hookean material model along with Mie-Grüneisen equation of state is employed with Young's modulus $E = 1474$ Pa, density $\rho_R = 10$ Kg/m$^3$, Poisson's ratio $\nu = 0.478$, thermal conductivity $h = 10$ W/m.K, specific heat capacity $C_v = 10$ J/Kg.K and thermal expansion coefficient $\alpha = 2.223 \times 10^{-4}$ K$^{-1}$ where the disk has an initial homogeneous temperature distribution $\theta_R = 308.15$ K. The main objective of this example is to computationally demonstrate the satisfaction of the first law of thermodynamics along with preservation of conservative variables.

Figure 8.11 illustrates a particle refinement for the disk with pressure contour plots at time $t = 1.35$ s. It is evident how the pressure resolution is enhanced through the particle refinements. Figure 8.12 shows the comparison between the total energy-based and the entropy-based formulations using the proposed SPH methodology for three different particle refinements. The time evolution of the vertical velocity $\boldsymbol{v}_Z$ and temperature at the material point $\boldsymbol{X} = [2,4,0]^T$

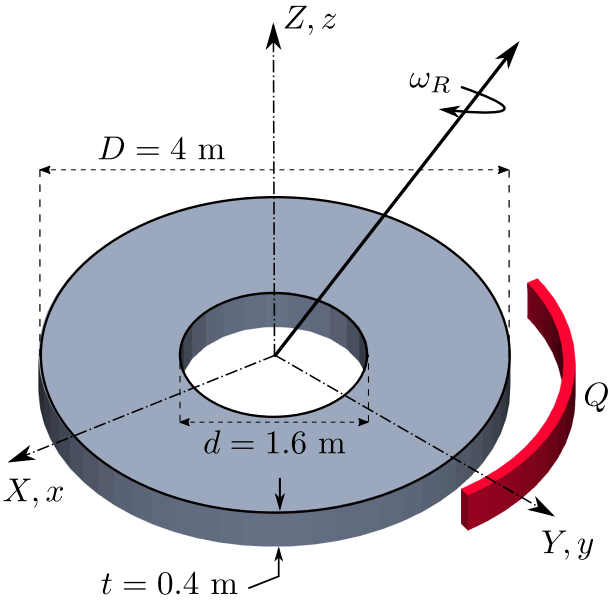


FIGURE 8.10: Rotating disk: Problem setup

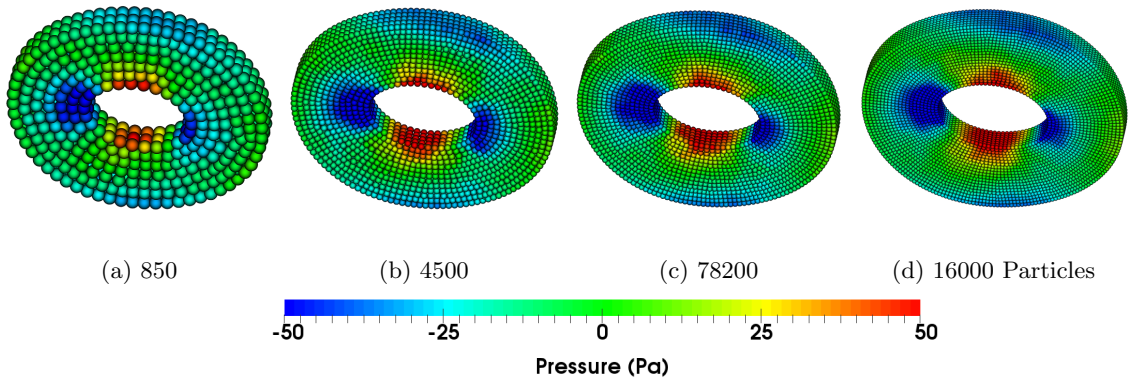


(a) 850 (b) 4500 (c) 78200 (d) 16000 Particles

FIGURE 8.11: Rotating disk: Particle refinement of deformed states with pressure contour plots at time $t = 1.35$ s for four different particle spacing (a) $h = 0.12$ m; (b) $h = 0.07$ m; (c) $h = 0.06$ m and (d) $h = 0.05$ m. Results obtained using a nearly incompressible thermo-elastic neo-Hookean constitutive model along with Mie-Grüneisen equation of state using the proposed entropy-based SPH methodology. The material properties used are Young's modulus $E = 1474$ Pa, density $\rho_R = 10$ kg/m$^3$, Poisson's ratio $\nu = 0.478$, thermal conductivity $h = 10$ W/m.K, specific heat capacity $C_v = 10$ J/Kg.K, thermal expansion coefficient $\alpha = 2.223 \times 10^{-4}$ K$^{-1}$ and $\alpha_{\text{CFL}} = 0.3$.

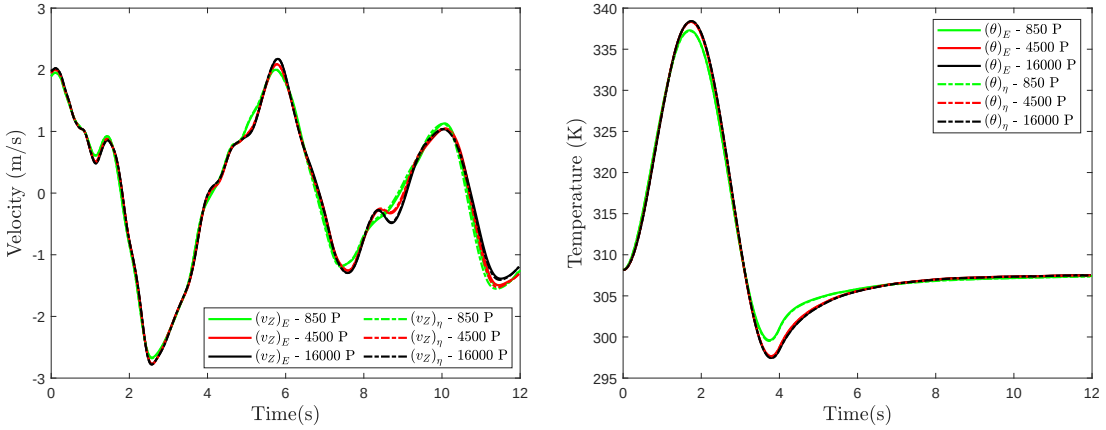


(a) Z-Velocity evolution (b) Temperature evolution

FIGURE 8.12: Rotating disk: Time evolution of the components of (a) vertical velocity $v_Z$ and (b) temperature at material point $\boldsymbol{X} = [2, 4, 0]^T$ m. Results obtained using the total energy-based and entropy-based system of equations considering a nearly incompressible thermo-elastic neo-Hookean constitutive model along with Mie-Grüneisen equation of state discretised by the proposed SPH methodology. The material properties used are Young's modulus $E = 1474$ Pa, density $\rho_R = 10$ kg/m$^3$, Poisson's ratio $\nu = 0.478$, thermal conductivity $h = 10$ W/m.K, specific heat capacity $C_v = 10$ J/Kg.K, thermal expansion coefficient $\alpha = 2.223 \times 10^{-4}$ K$^{-1}$ and $\alpha_{\text{CFL}} = 0.3$.

m is presented as a very good agreement can be observed between the obtained results. Figure 8.13 compares the solution of the proposed entropy-based SPH and VCFVM methodologies. An extremely good agreement can be observed between the results in terms of deformation and pressure and temperature distributions.

Figures 8.14a shows how the components of linear momentum are preserved as expected, up to zero machine accuracy. The evolution of the components of angular momentum is also depicted in Figure 8.14b where the initial values are conserved. Figure 8.14c presents the evolution of

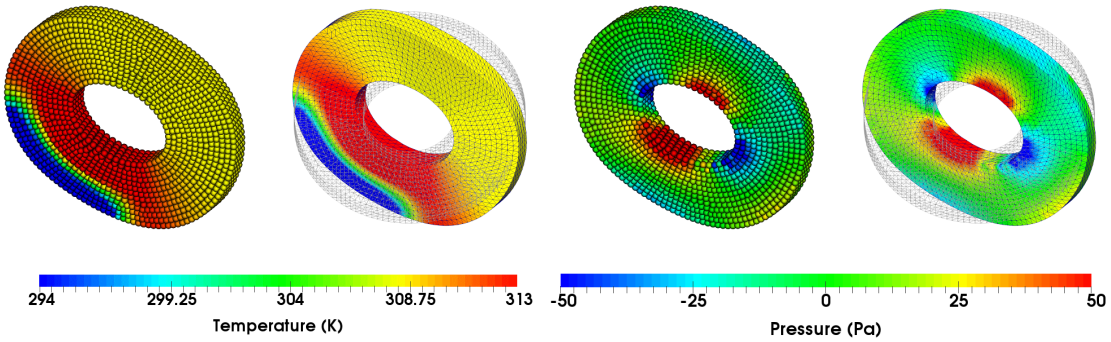


FIGURE 8.13: Rotating disk: Comparison of deformed shapes plotted with pressure and temperature distributions using the entropy-based SPH and VCFVM methodologies at time $t = 4$ s. Results obtained using a nearly incompressible thermo-elastic neo-Hookean constitutive model along with Mie-Grüneisen equation of state with material properties Young's modulus $E = 1474$ Pa, density $\rho_R = 10$ kg/m$^3$, Poisson's ratio $\nu = 0.478$, thermal conductivity $h = 10$ W/m.K, specific heat capacity $C_v = 10$ J/Kg.K, thermal expansion coefficient $\alpha = 2.223 \times 10^{-4}$ K$^{-1}$ and $\alpha_{\text{CFL}} = 0.3$.

the global total energy. It has initially increased and, then, decreased due to the implication of the employed sinusoidal heat flux. This is expected as the disk is only exchanging heat through a quarter of its boundary in which the heat flux is imposed and the rest of the body is insulated. Therefore, the total energy has got the trend of the sinusoidal heat flux and, then, remained constant once the boundary heat flux is removed. Additionally, the evolution of total kinetic energy and total internal energy are shown once the total energy is conserved. The fluctuations, as a result of disk's vibration, of the total kinetic energy and the total internal energy are gradually damped due to the diffusive nature of heat conduction. The (very) long-term solution is expected to be a disk with a unified temperature, slightly higher than the reference temperature. This is due to the relatively small generated heat by the deformation which remains in the insulated body and also, the particular imposed heat flux to the disk. Figure 8.14d shows the time evolution of global entropy which has initially followed the trend of the imposed heat flux and, then, gradually increased, once the heat flux is removed. This can be seen as the satisfaction of the second law of thermodynamics.

A sequence of deformed configurations are depicted in Figure 8.15 with very smooth pressure and temperature distributions. The implication of the imposed sinusoidal heat flux can clearly be observed through the evolution of temperature. The final state of the deformation demonstrates the nearly uniform temperature distribution with a value slightly higher than the reference temperature. Moreover, the pressure distribution pattern illustrates the contraction and expansion of the inner circle in the middle of the disk during the deformation process.

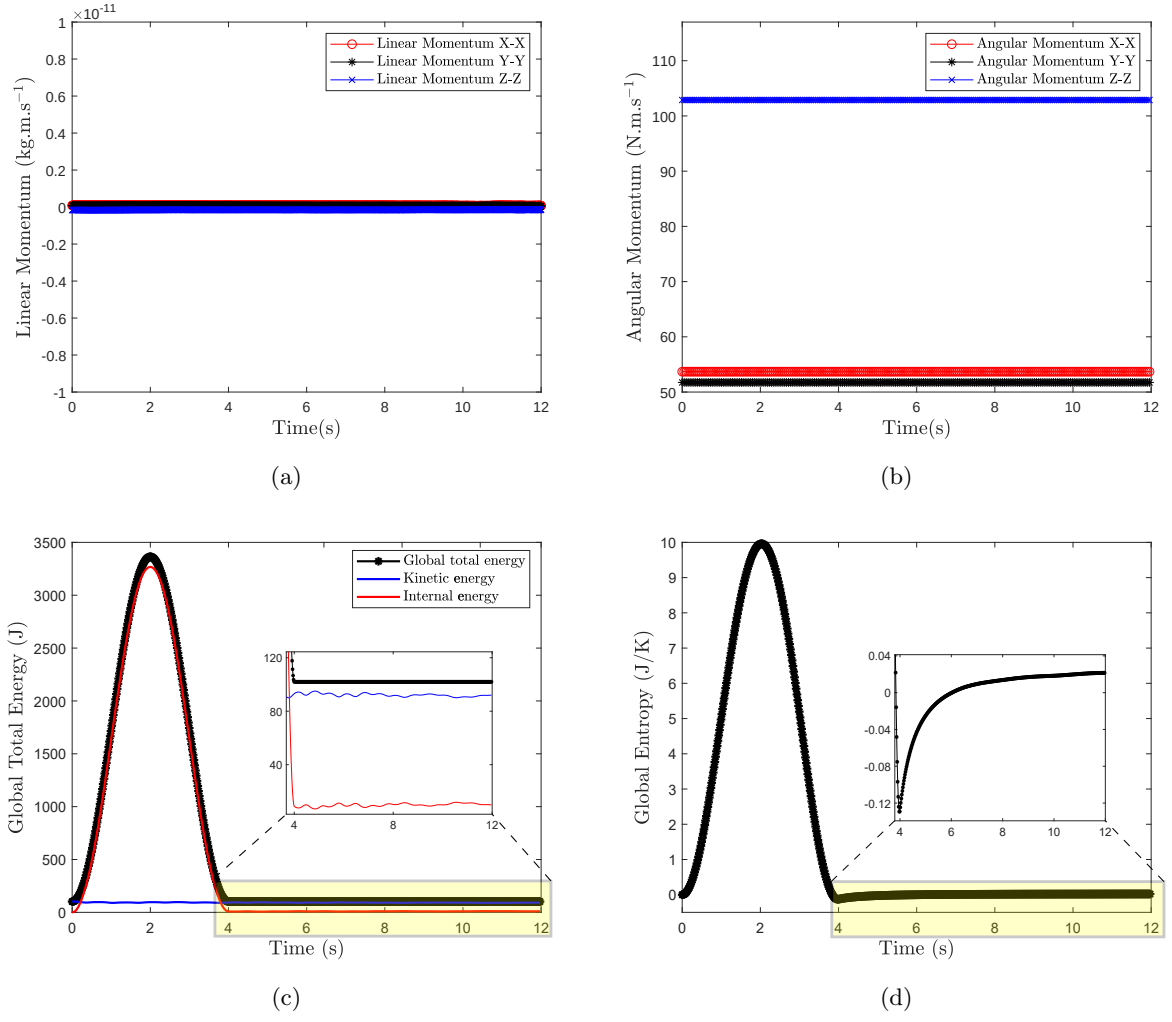


FIGURE 8.14: Rotating disk: Time evolution of the components of (a) linear momentum; (b) angular momentum; (c) global total energy; and (d) global entropy. Results obtained using a nearly incompressible thermo-elastic neo-Hookean constitutive model along with Mie-Grüneisen equation of state using the proposed entropy-based SPH methodology. The material properties used are Young's modulus $E = 1474$ Pa, density $\rho_R = 10$ kg/m$^3$, Poisson's ratio $\nu = 0.478$, thermal conductivity $h = 10$ W/m.K, specific heat capacity $C_v = 10$ J/Kg.K, thermal expansion coefficient $\alpha = 2.223 \times 10^{-4}$ K$^{-1}$ and $\alpha_{\text{CFL}} = 0.3$.

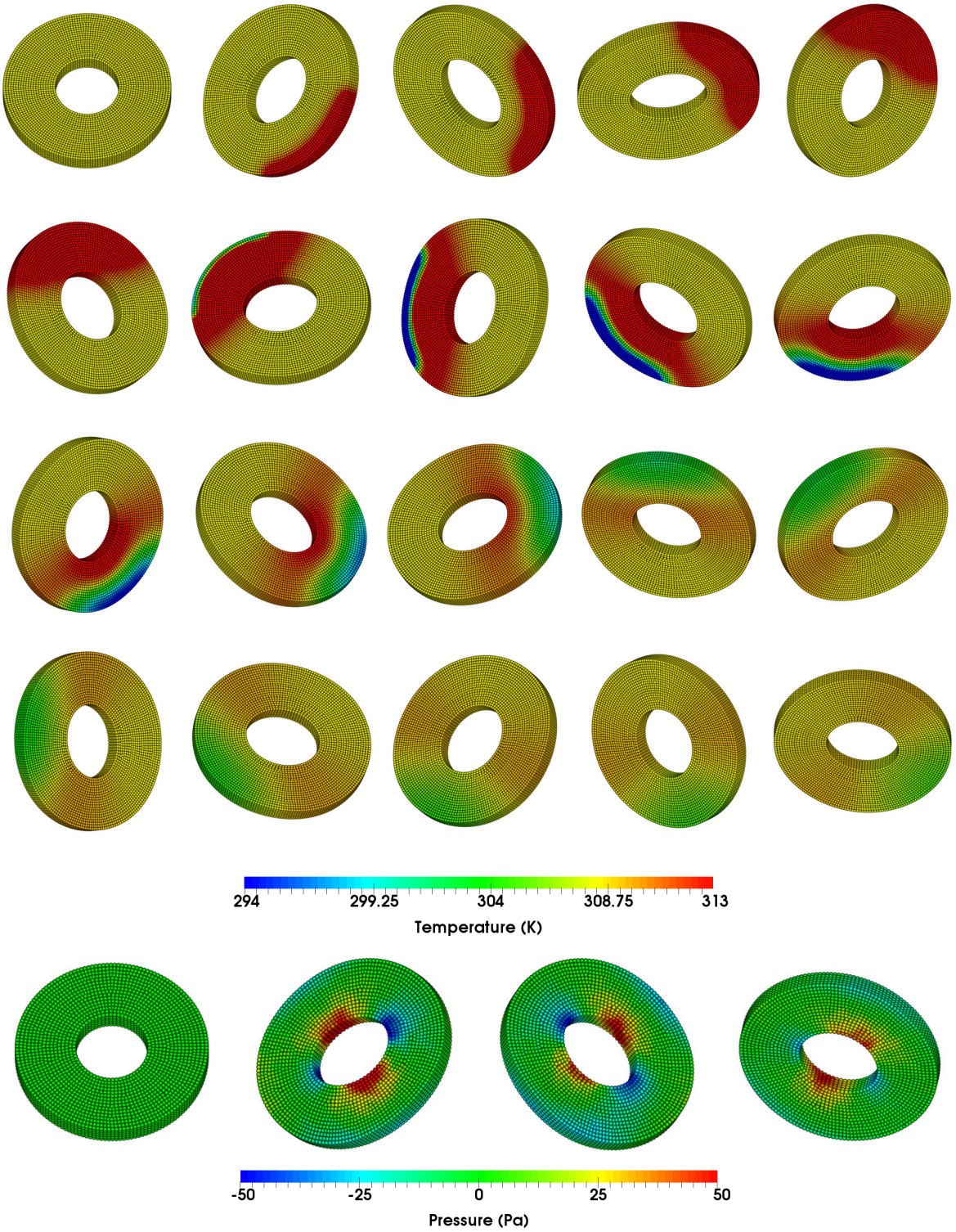


FIGURE 8.15: Rotating disk: A sequence of deformed configurations with temperature and pressure distributions at time $t = 0.5 \times \{0, 1, 2, 3, ..., 19\}$ s (left to right-top to bottom) and $t = 3.3 \times \{0, 1, 2, 3\}$ s (left to right), respectively. Results obtained using a nearly incompressible thermo-elastic neo-Hookean constitutive model along with Mie-Grüneisen equation of state using the proposed entropy-based SPH methodology. The material properties used are Young's modulus $E = 1474$ Pa, density $\rho_R = 10$ kg/m$^3$, Poisson's ratio $\nu = 0.478$, thermal conductivity $h = 10$ W/m.K, specific heat capacity $C_v = 10$ J/Kg.K, thermal expansion coefficient $\alpha = 2.223 \times 10^{-4}$ K$^{-1}$ and $\alpha_{\text{CFL}} = 0.3$.

## 8.4 Robustness

### 8.4.1 Nearly incompressible twisting column: Isothermal elasticity

A challenging benchmark test, already explored in References [4, 6, 7, 16, 18, 22, 118], is presented aimed at examining the applicability and robustness of the proposed SPH and VCFVM algorithms in an isothermal process. A column with a unit square cross section is twisted, initialising with a sinusoidal angular velocity field relative to the column's origin expressed as $\boldsymbol{\omega}_0 = [0, 0, \Omega \sin(\pi Z/2L)]^T$, where $\Omega = 105$ rad/s and $L = 6$ m is the length of the column (see Figure 8.16). An isothermal nearly incompressible neo-Hookean material is considered with Young's modulus $E = 1.7 \times 10^7$ Pa, density $\rho_0 = 1.1 \times 10^3$ kg/m$^3$ and Poisson's ratio $\nu = 0.45$.

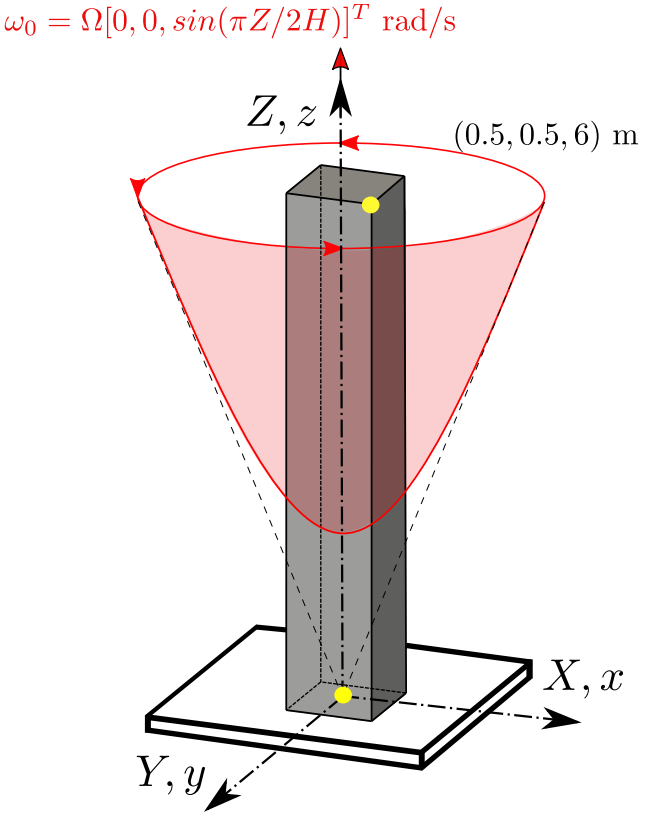


FIGURE 8.16: Twisting column: Problem setup

Figure 8.17 illustrates a mesh/particle refinement for the column. A very smooth pressure distribution can be observed for the deformed state of the column at time $t = 0.1$ s. The resolution of the solution is clearly enhanced through the refinement process. It is also interesting to note that the optical convergence of both VCFVM and SPH numerical methodologies are evident in such a way that both obtained deformation and pressure resolutions are practically identical, from the very coarse to the very fine solutions. Figure 8.18 monitors the evolution of the horizontal displacement and horizontal velocity components at the material position $\boldsymbol{X} = [0.5, 0.5, 6]^T$ m. The main purpose of this plot is to illustrate how the numerical methodologies preserve perfect axial rotation without introducing out-of-axis characteristics, both within zero machine accuracy.

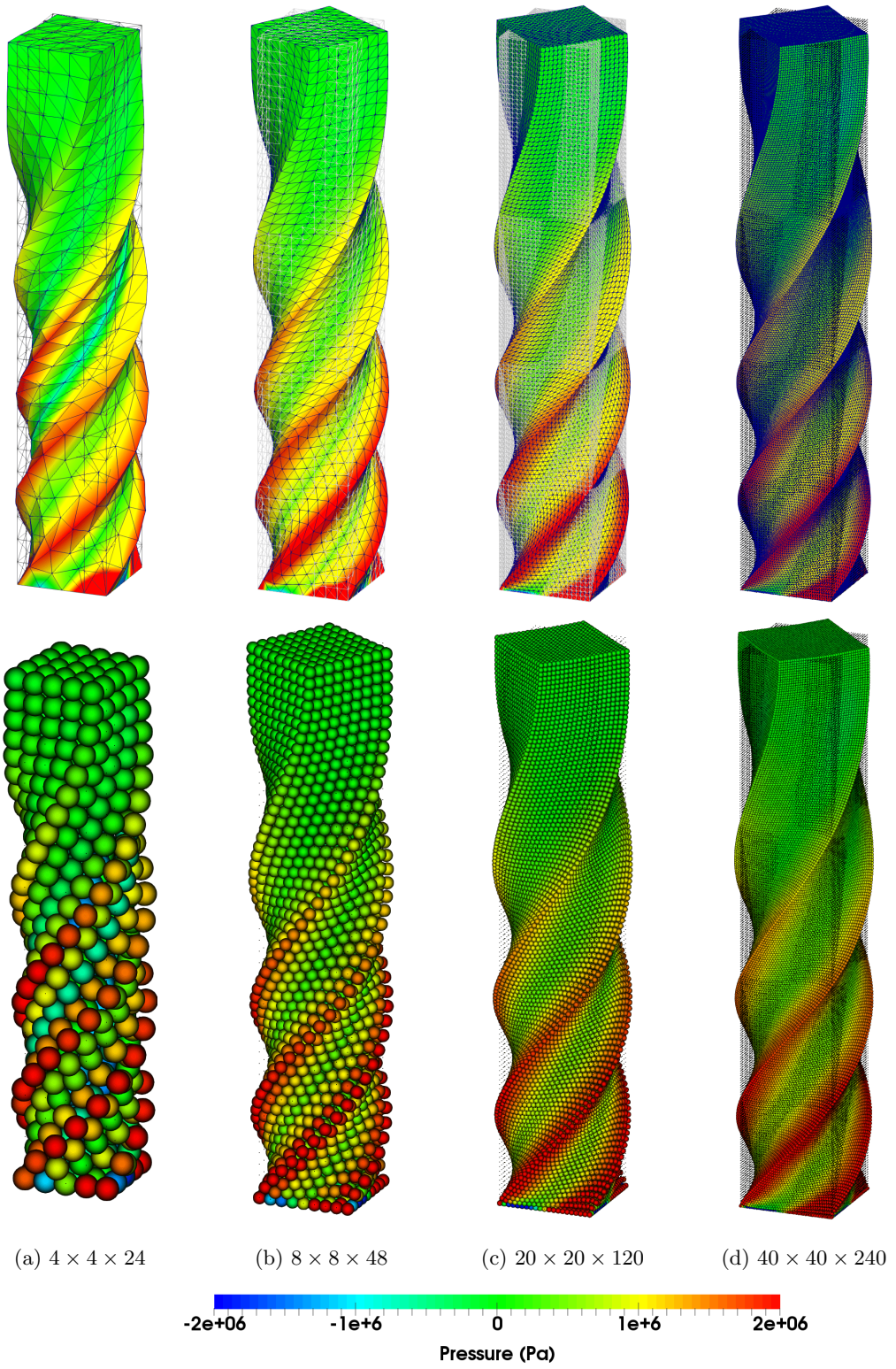


(a) $4 \times 4 \times 24$ (b) $8 \times 8 \times 48$ (c) $20 \times 20 \times 120$ (d) $40 \times 40 \times 240$

FIGURE 8.17: Twisting column: Mesh/Particle refinement of the deformed state with pressure contour plots at time $t = 0.1$ s for four different mesh/particle spacing (a) $h = 0.24$ m; (b) $h = 0.125$ m; (c) $h = 0.05$ m and (d) $h = 0.025$ m. Results obtained using an isothermal nearly incompressible neo-Hookean constitutive model using the proposed VCFVM and SPH methodologies. The material properties used are Young's modulus $E = 1.7 \times 10^7$ Pa, density $\rho_R = 1100$ kg/m$^3$, Poisson's ratio $\nu = 0.45$ and $\alpha_{\text{CFL}} = 0.3$.

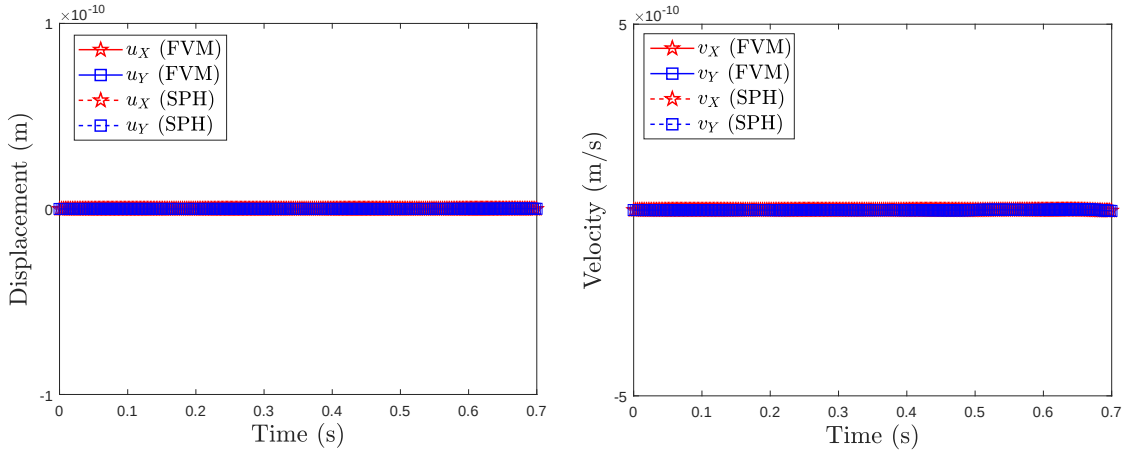


(a) Horizontal displacement

(b) Horizontal velocity

FIGURE 8.18: Twisting column: Time evolution of the components of (a) horizontal displacement $u_Z$ and (b) horizontal velocity $v_Z$ at material point $\boldsymbol{X} = [0.5, 0.5, 6]^T$ m. Results obtained using the VCFVM and SPH methodologies considering an isothermal nearly incompressible neo-Hookean constitutive model with Young's modulus $E = 1.7 \times 10^7$ Pa, density $\rho_R = 1100$ kg/m$^3$, Poisson's ratio $\nu = 0.45$ and $\alpha_{\text{CFL}} = 0.3$.

For benchmarking purposes, the mixed-based $\{\boldsymbol{p}, \boldsymbol{F}, \boldsymbol{H}, J\}$ Upwind-VCFVM and Upwind-SPH schemes are compared with Jameson-Schmidt-Turkel (JST)-VCFVM [16], JST-SPH [4], Streamline Upwind Petrov Galerkin (SUPG)-SPH [5], Petrov Galerkin (PG)-FEM [23] and Constrained-TOUCH [6] (see Figure 8.19). Remarkably, the results obtained using different methodologies are in an extremely good agreement in terms of deformation and pressure field.

To make the twisting column problem significantly more challenging, we increased the initial angular velocity now to $\Omega = 180$ rad/s. Figure 8.20 shows the time evolution of displacement and velocity of the material position $\boldsymbol{X} = [0.5, 0.5, 6]$ for three different mesh/particle refinements using VCFVM and SPH schemes.

It is interesting to note that the mesh refinement for the VCFVM scheme converges from the lower bound limit whilst the particle refinement for the SPH scheme converges from the upper bound limit. The optimal convergence of the solution for both numerical schemes can be observed. It is essential to note that the SPH results have shown a more diffusive behaviour than the VCFVM, as it is expected.

Figure 8.21 depicts the deformed states of the column using both VCFVM and SPH methodologies in which a very smooth pressure distribution can be observed. It is interesting how the deformation of the highly twisted column is similarly well captured for both VCFVM and SPH schemes.

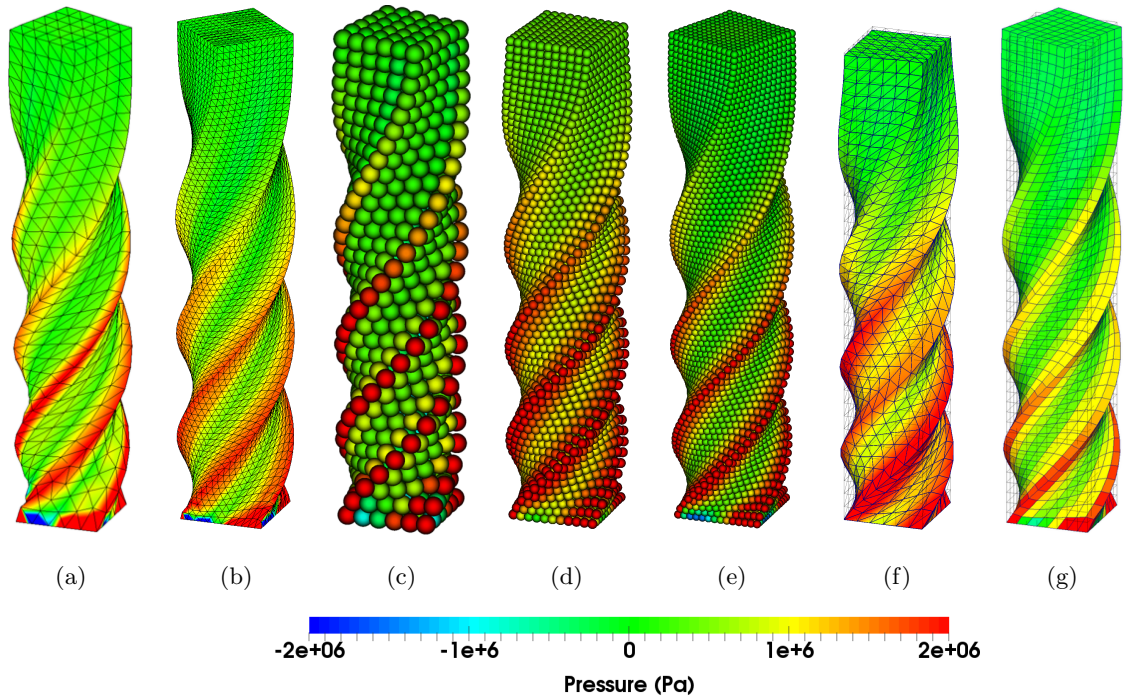


FIGURE 8.19: Twisting column: Comparison of the deformed shaped plotted with pressure field at time $t = 0.1$ s using different numerical methodologies (a) Upwind-VCFVM; (b) JST-VCFVM [16]; (c) Upwind-SPH; (d) JST-SPH ($\varepsilon_{\boldsymbol{p}}^{(2)} = 0$ and $\varepsilon_{\boldsymbol{p}}^{(4)} = \frac{1}{8}$) [4]; (e) SUPG-SPH-H1 ($\tau_{\boldsymbol{F}} = \Delta t$, $\xi_{\boldsymbol{F}} = 0.2$, $\tau_{\boldsymbol{p}} = 0.1\Delta t$) [5]; (f) PG-FEM [23]; and (g) Constrained-TOUCH [6]. Results obtained using an isothermal nearly incompressible neo-Hookean constitutive model using the proposed VCFVM and SPH methodologies. The material properties used are Young's modulus $E = 1.7 \times 10^7$ Pa, density $\rho_R = 1100$ kg/m$^3$, Poisson's ratio $\nu = 0.45$ and $\alpha_{\text{CFL}} = 0.3$.

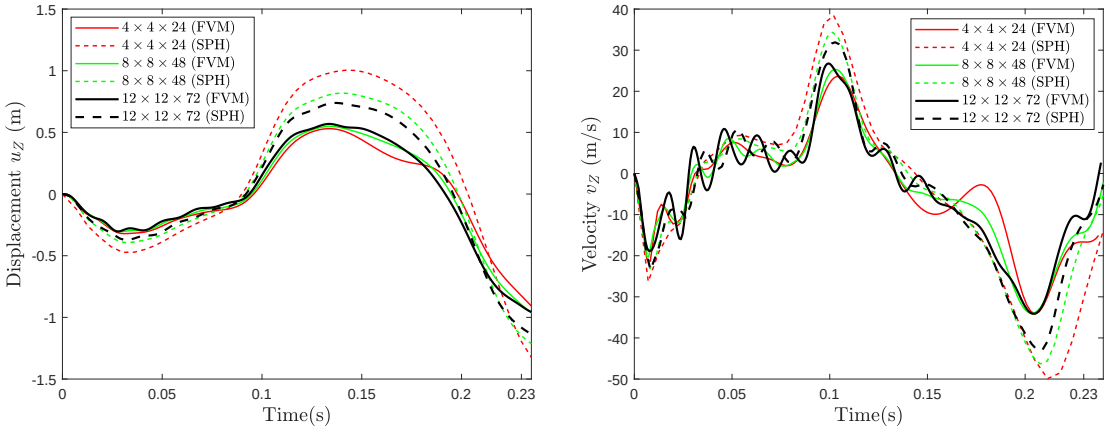


(a) Horizontal displacement

(b) Horizontal velocity

FIGURE 8.20: Twisting column: Time evolution of the components of (a) vertical displacement $u_Z$ and (b) vertical velocity $v_Z$ at material point $\boldsymbol{X} = [0.5, 0.5, 6]^T$ m. Results obtained using three different mesh/particle refinements of $4 \times 4 \times 24$, $8 \times 8 \times 48$ and $12 \times 12 \times 72$ with an increased angular velocity expressed as $\boldsymbol{\omega}_0 = [0, 0, \Omega \sin(\pi Z/2L)]^T$, where $\Omega = 180$ rad/s. An isothermal nearly incompressible neo-Hookean constitutive model is considered with Young's modulus $E = 1.7 \times 10^7$ Pa, density $\rho_R = 1100$ kg/m$^3$, Poisson's ratio $\nu = 0.45$ and $\alpha_{\text{CFL}} = 0.3$.

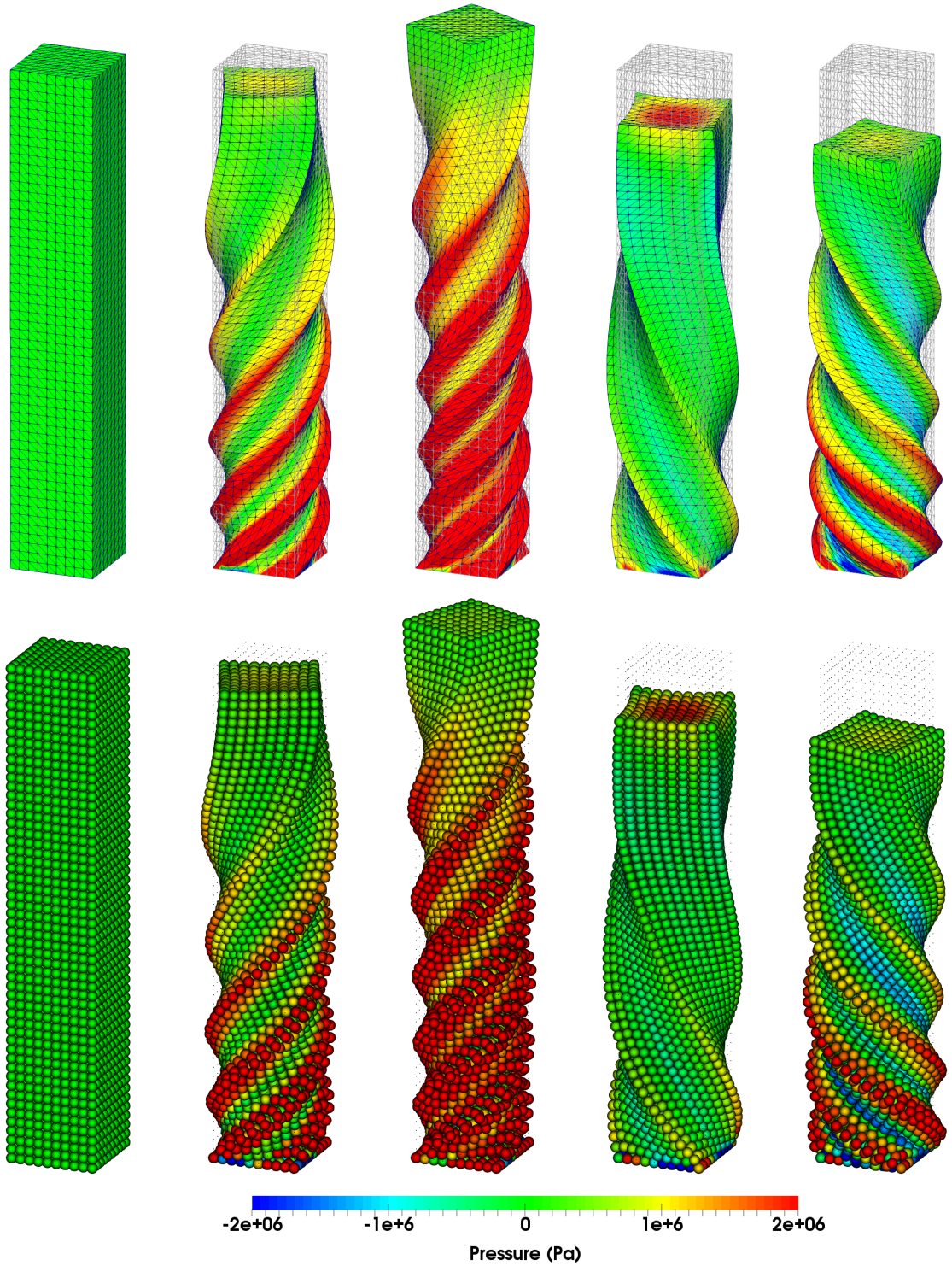


FIGURE 8.21: Twisting column: Evolution of the deformed states with pressure contour plots for (a) Upwind-VCFVM scheme on the top row ; and (b) Upwind-SPH scheme on the bottom row. Results obtained using an increased angular velocity expressed as $\boldsymbol{\omega}_0 = [0, 0, \Omega \sin(\pi Z/2L)]^T$ with $\Omega = 180$ rad/s considering an isothermal nearly incompressible neo-Hookean constitutive model. The material properties are Young's modulus $E = 1.7 \times 10^7$ Pa, density $\rho_R = 1100$ kg/m$^3$, Poisson's ratio $\nu = 0.45$ and $\alpha_{\text{CFL}} = 0.3$.

### 8.4.2 Nearly incompressible twisting cylinder: Entropic elasticity

In this section, we made the twisting column example more challenging by changing the geometry from a column to a hollow cylinder (see Figure 8.22). The main objective of this example is

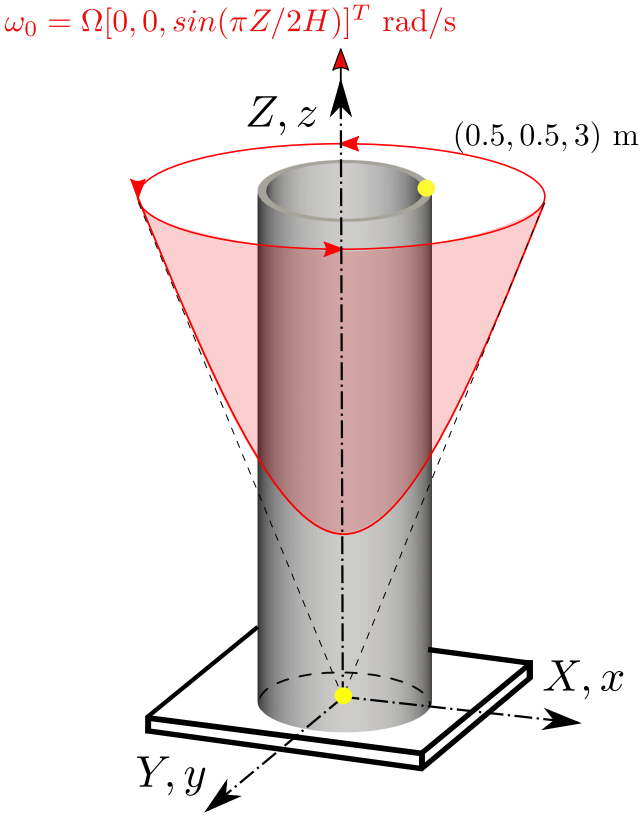


FIGURE 8.22: Twisting cylinder: Problem setup

to assess the robustness of the proposed VCFVM and SPH algorithms in the case of a thermo-mechanical problem, entropic elasticity in particular. The cylinder is initially twisted with the same angular velocity used for the twisting column example (presented in Section 8.4.1) where $\Omega = 180$ rad/s is considered. The insulated structure is clamped at the bottom and the rest of the cylinder moves freely. A nearly incompressible entropic-elastic neo-Hookean material model is employed with the material properties Young's modulus $E = 1.7 \times 10^7$ Pa, density $\rho_0 = 1.1 \times 10^3$ kg/m$^3$, Poisson's ratio $\nu = 0.45$, thermal conductivity $h = 0.2$ W/m.K, specific heat capacity $C_v = 100$ J/Kg.K and thermal expansion coefficient $\alpha = 2.223 \times 10^{-4}$ K$^{-1}$ where the hollow cylinder has an initial homogeneous temperature distribution $\theta_R = 293.15$ K.

For benchmarking purposes, the solution of the mixed-based $\{\boldsymbol{p}, \boldsymbol{F}, \boldsymbol{H}, J, E\}$ Upwind-VCFVM and Upwind-SPH are compared together in Figure 8.23. It is remarkable to observe that the obtained results are in an extremely good agreement in terms of temperature and pressure fields. Additionally, the complex deformation of the cylindrical structure is analogously well captured by both algorithms. Figure 8.24 shows the time evolution of the components of displacement and velocity and also diagonal components of the first Piola-Kirchhoff stress tensor at the material position $\boldsymbol{X} = [-0.45, 0, 3]$ for three different mesh/particle refinements using the VCFVM schemes.

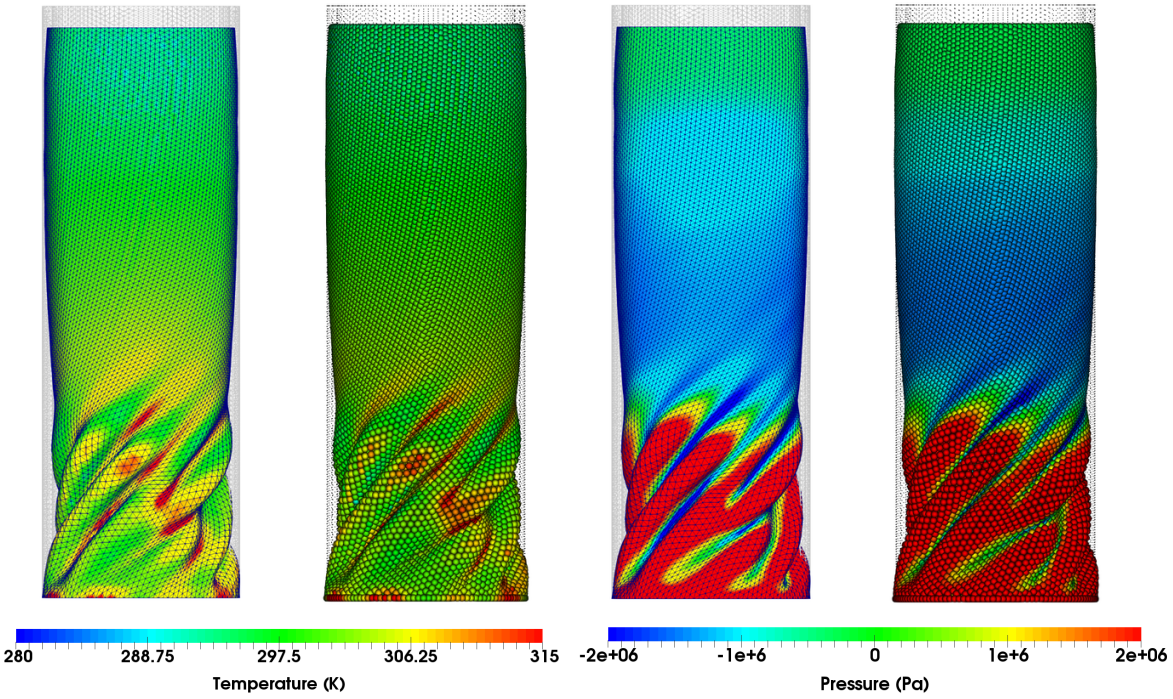


FIGURE 8.23: Twisting cylinder: Comparison of deformed shapes plotted with pressure and temperature distributions using the total energy-based SPH and VCFVM methodologies at time $t = 0.022$ s. Results obtained using a nearly incompressible entropic-elastic neo-Hookean constitutive model with material properties Young's modulus $E = 1.7 \times 10^7$ Pa, density $\rho_0 = 1.1 \times 10^3$ kg/m$^3$, Poisson's ratio $\nu = 0.45$, thermal conductivity $h = 0.2$ W/m.K, specific heat capacity $C_v = 100$ J/Kg.K, thermal expansion coefficient $\alpha = 2.223 \times 10^{-4}$ K$^{-1}$ and $\alpha_{\text{CFL}} = 0.3$.

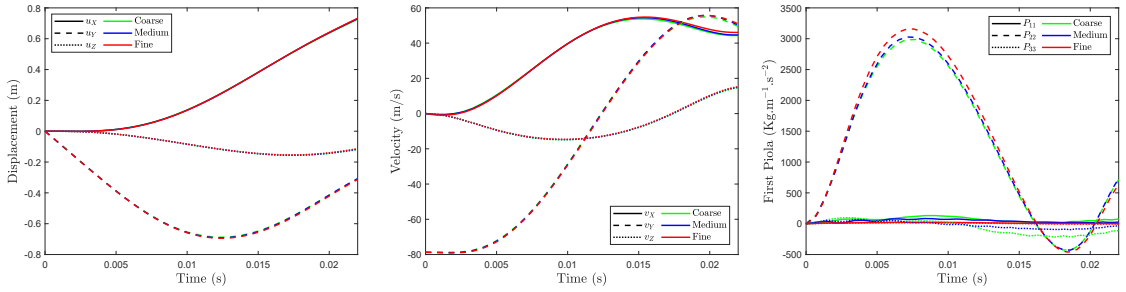


(a) (b) (c)

FIGURE 8.24: Twisting cylinder: Time evolution of the components of displacement $\boldsymbol{u}$; (b) velocity $\boldsymbol{v}$; and and first Piola-Kirchhoff stress $\boldsymbol{P}$ at material point $\boldsymbol{X} = [-0.45, 0, 3]^T$ m. Results obtained using three different mesh/particle refinements of 1910, 11300 and 44200 cells/particles with an angular velocity expressed as $\boldsymbol{\omega}_0 = [0, 0, \Omega \sin(\pi Z/2L)]^T$, where $\Omega = 180$ rad/s. A nearly incompressible entropic-elastic neo-Hookean constitutive model with material properties Young's modulus $E = 1.7 \times 10^7$ Pa, density $\rho_0 = 1.1 \times 10^3$ kg/m$^3$, Poisson's ratio $\nu = 0.45$, thermal conductivity $h = 0.2$ W/m.K, specific heat capacity $C_v = 100$ J/Kg.K, thermal expansion coefficient $\alpha = 2.223 \times 10^{-4}$ K$^{-1}$ and $\alpha_{\text{CFL}} = 0.3$.

The convergence of the solution through the refined computational domains is evident for the evolution of displacement, velocity and the diagonal components of the first Piola stress tensor. It must be noted that the solution with the coarse mesh is interestingly very much close to solution with the fine mesh. This shows the capability of the proposed algorithms as it can capture the solution of complex problems in a computationally efficient manner.

Figure 8.25 depicts the deformed states of the hollow cylinder using the VCFVM methodology. The particular cylindrical shape of the structure results in an initial expansion which is due to the high value of the initial angular momentum. The expansion is also related to the thermal expansion coefficient ($\alpha$) in such a way that the extremely large deformation of the cylinder generates heat and, therefore, that increases the temperature of the insulated cylinder. Evolving in time, the cylinder starts to form some wrinkles at the bottom in which a very smooth pressure and temperature distributions can be observed.

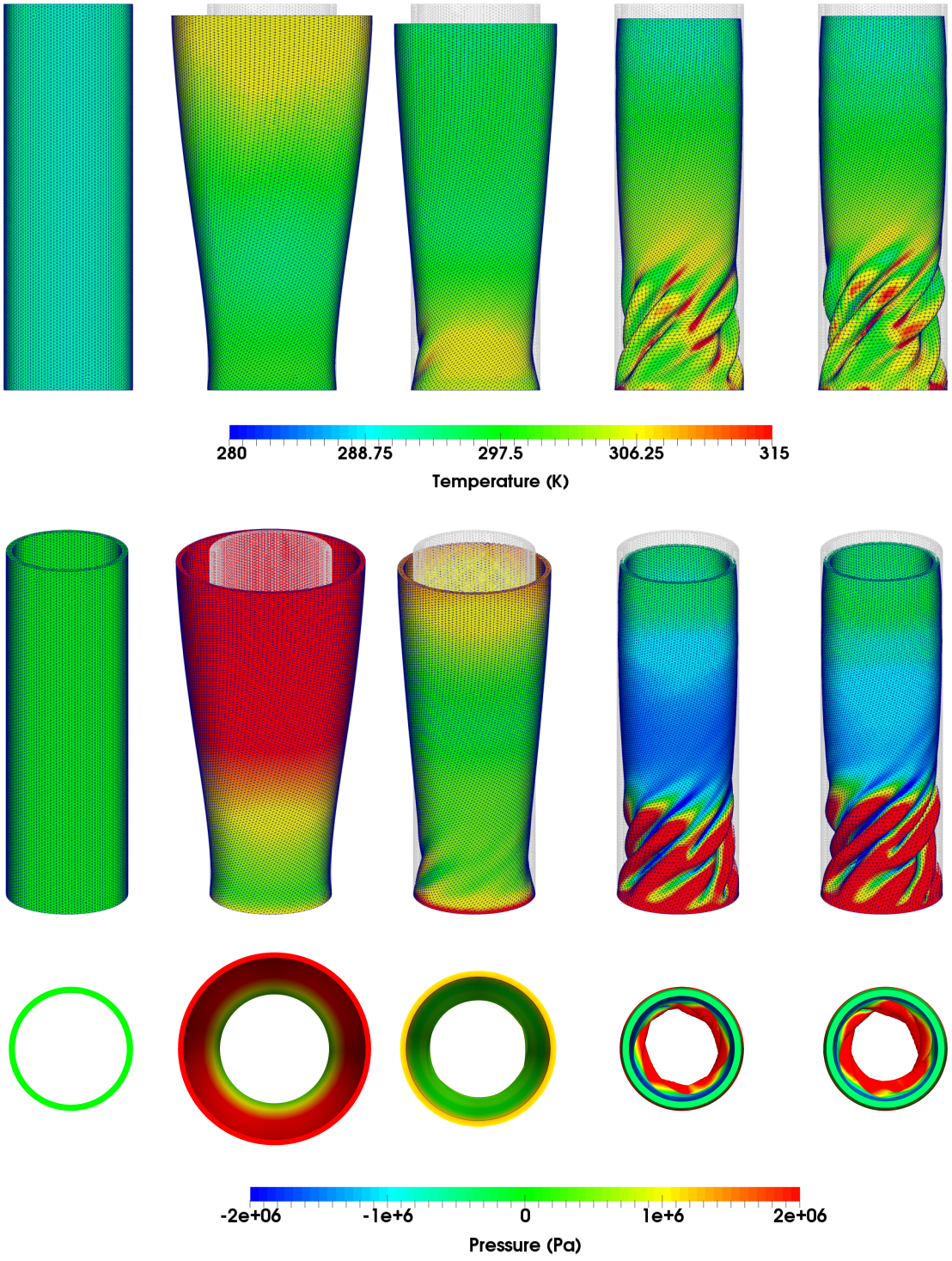


FIGURE 8.25: Twisting cylinder: A sequence of deformed configuration with temperature distribution (side view) and pressure distribution (isometric and top view) at times $t = \{0, 0.01, 0.017, 0.022, 0.023\}$ s (left to right). Results obtained using three different mesh/particle refinements of 1910, 11300 and 44200 cells/particles with an angular velocity expressed as $\boldsymbol{\omega}_0 = [0, 0, \Omega \sin(\pi Z/2L)]^T$, where $\Omega = 180$ rad/s. A nearly incompressible entropic-elastic neo-Hookean constitutive model with material properties Young's modulus $E = 1.7 \times 10^7$ Pa, density $\rho_0 = 1.1 \times 10^3$ kg/m$^3$, Poisson's ratio $\nu = 0.45$, thermal conductivity $h = 0.2$ W/m.K, specific heat capacity $C_v = 100$ J/Kg.K, thermal expansion coefficient $\alpha = 2.223 \times 10^{-4}$ K$^{-1}$ and $\alpha_{\text{CFL}} = 0.3$.

## 8.5 Extension to incompressibility

### 8.5.1 Punch test

A perforated cylinder is initially punched on the middle-top face with a linear velocity field expressed as $\boldsymbol{v}_0 = -10[0, 0, Z/H]^T$ m/s where $H = 1$ m (see Figure 8.26). A symmetric

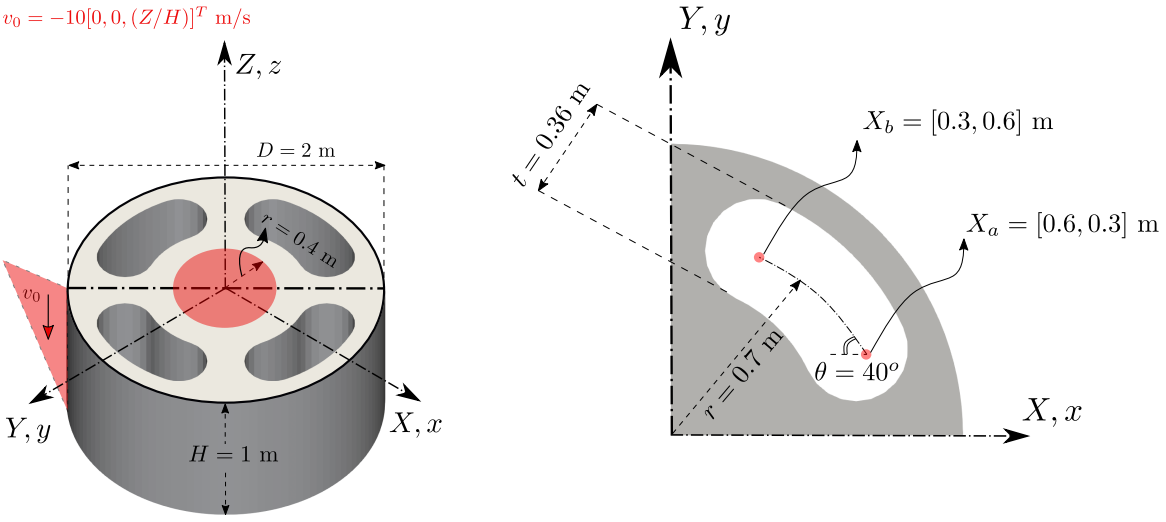


(a) (b)

FIGURE 8.26: Punch test: (a) Initial configuration; and (b) Planar $1/4^{\text{th}}$ geometry

mechanical boundary condition (i.e. roller support) is set on the bottom of the cylinder whilst the rest of boundaries are subjected to a free movement. The cylinder is also thermally insulated from the environment. The main objective of this example is to show the capability of the proposed VCFVM and SPH algorithms in alleviating spurious pressure modes in the case of nearly incompressible scenarios. A nearly incompressible thermo-elastic neo-Hookean material model along with Mie-Grüneisen equation of state is employed with the material properties Young's modulus $E = 50.05$ KPa, density $\rho_R = 1000$ Kg/m$^3$, Poisson's ratio $\nu = 0.499$, thermal conductivity $h = 10$ W/m.K, specific heat capacity $C_v = 1$ J/Kg.K and thermal expansion coefficient $\alpha = 2.223 \times 10^{-4}$ K$^{-1}$ where the cylinder has an initial homogeneous temperature distribution $\theta_R = 293.15$ K.

Looking at Figure 8.27, it is evident that the $\{\boldsymbol{p}, \boldsymbol{F}\}$ Upwind-SPH methodology suffers from spurious temperature/pressure modes. The numerical oscillations, however, is alleviated using the $\{\boldsymbol{p}, \boldsymbol{F}, \boldsymbol{H}, J\}$ Upwind-SPH algorithm in which very smooth temperature and pressure fields can be observed. In fact, the additional conservation laws $\{\boldsymbol{H}, J\}$ provide more flexibility into the algorithm such that we can avoid some numerical deficiencies. In particular, the $J$ equation is useful in the case of incompressible materials in order to avoid spurious pressure oscillations. Moreover, $\boldsymbol{H}$ equation could be helpful to suppress bending locking. Figure 8.28 depicts a comparison between the proposed total energy-based SPH methodology with the in-house mixed-based Vertex-Centred Finite Volume Method (VCFVM) in terms of pressure and temperature distributions as a good agreement can be observed between the results.

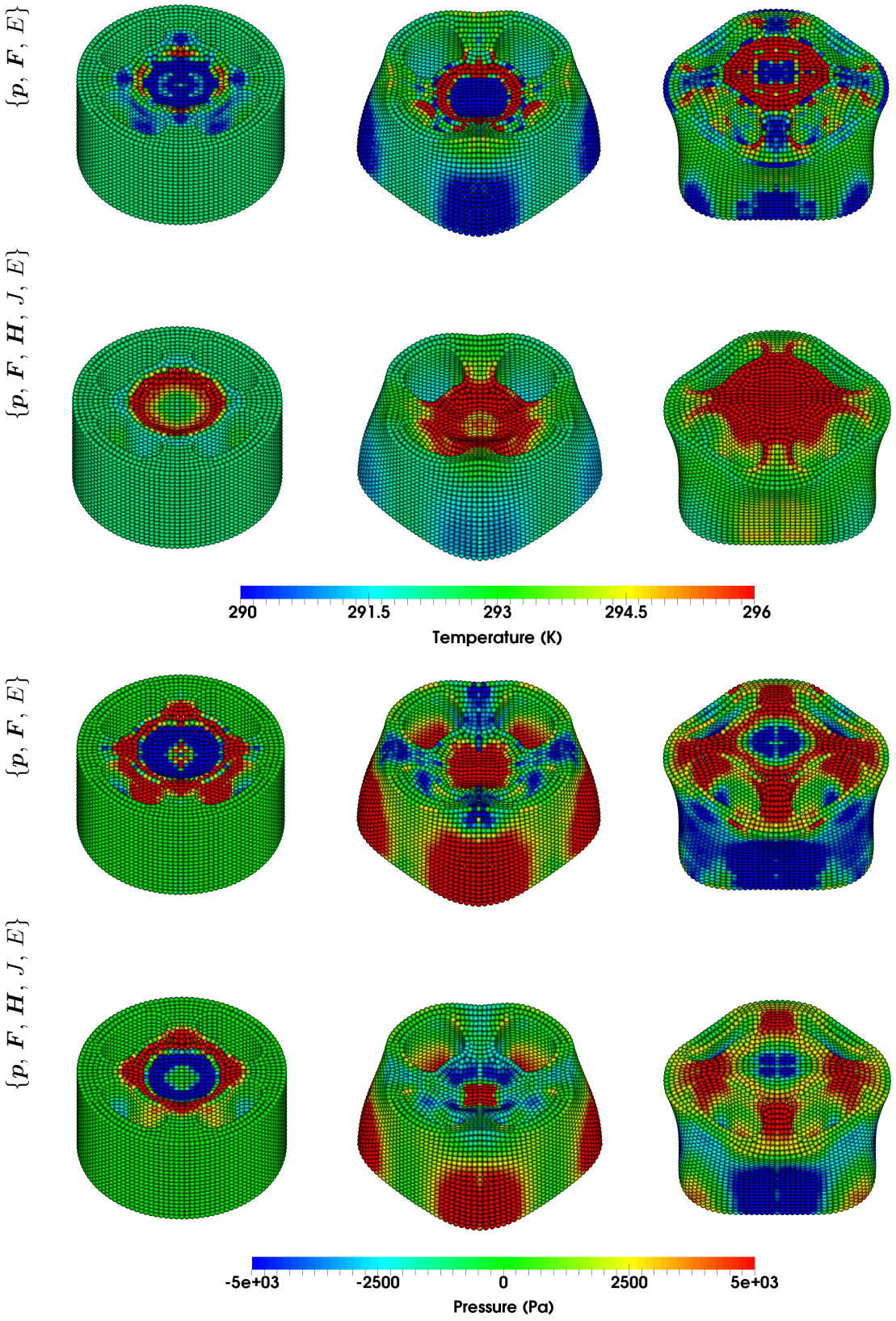


FIGURE 8.27: Punch test: A sequence of deformed configuration with temperature and pressure distributions using the mixed-based $\{\boldsymbol{p}, \boldsymbol{F}, E\}$ and $\{\boldsymbol{p}, \boldsymbol{F}, \boldsymbol{H}, J, E\}$ total energy-based Upwind-SPH methodology. Results obtained using a nearly incompressible thermo-elastic neo-Hookean constitutive model along with Mie-Grüneisen equation of state. The material properties used are Young's modulus $E = 50.05$ KPa, density $\rho_R = 1000$ kg/m$^3$, Poisson's ratio $\nu = 0.499$, thermal conductivity $h = 10$ W/m.K, specific heat capacity $C_v = 1$ J/Kg.K, thermal expansion coefficient $\alpha = 2.223\times10^{-4}$ K$^{-1}$ and $\alpha_{\text{CFL}} = 0.3$.

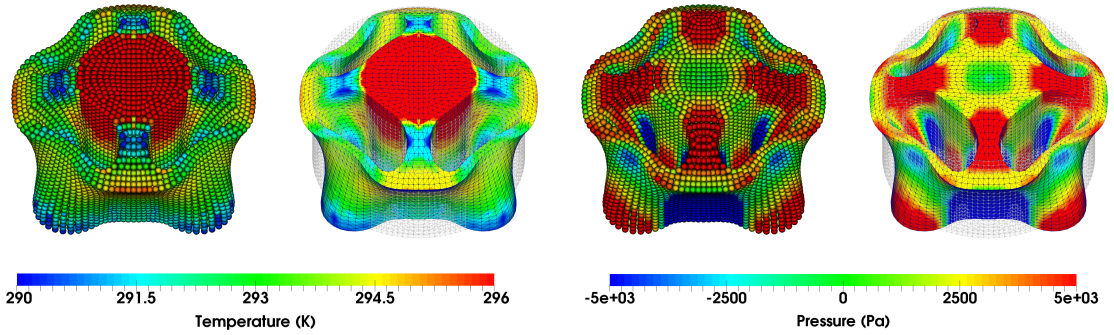


FIGURE 8.28: Punch test: Comparison of deformed shapes plotted with pressure and temperature distributions using the total energy-based SPH and VCFVM methodologies at time $t = 0.38$ s. Results are obtained using a nearly incompressible thermo-elastic neo-Hookean constitutive model along with Mie-Grüneisen equation of state. The material properties used are Young's modulus $E = 50.05$ KPa, density $\rho_R = 1000$ kg/m$^3$, Poisson's ratio $\nu = 0.499$, thermal conductivity $h = 10$ W/m.K, specific heat capacity $C_v = 1$ J/Kg.K, thermal expansion coefficient $\alpha = 2.223 \times 10^{-4}$ K$^{-1}$ and $\alpha_{\text{CFL}} = 0.3$.

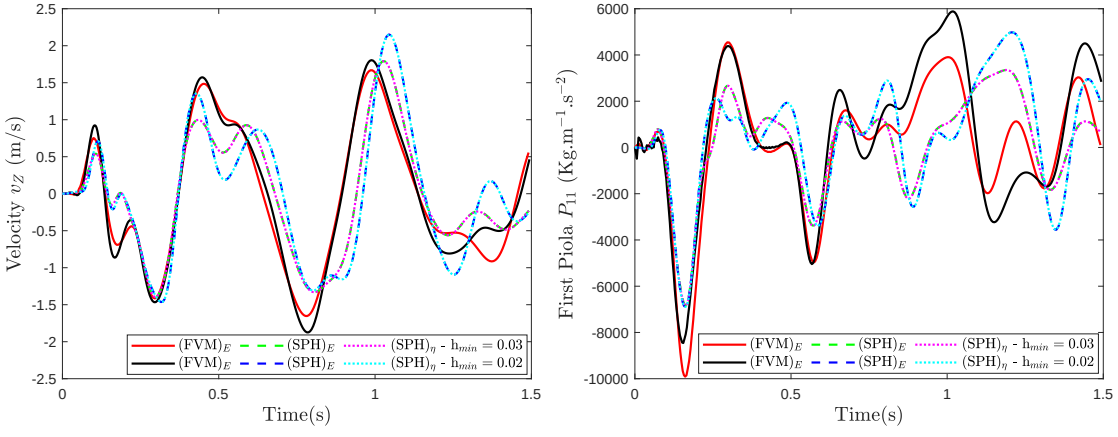


(a) Z-Velocity (b) First Piola-Kirchhoff component $P_{11}$

FIGURE 8.29: Punch test: Time evolution of the components of (a) vertical velocity $v_Z$ and (b) Component of first Piola-Kirchhoff stress tensor $P_{11}$ at material point $\boldsymbol{X} = [0, 1, 1]^T$ m. The total energy-based VCFVM, the total energy-based SPH and entropy-based SPH algorithms are compared. A nearly incompressible thermo-elastic neo-Hookean constitutive model is considered along with Mie-Grüneisen equation of state with Young's modulus $E = 50.05$ KPa, density $\rho_R = 1000$ kg/m$^3$, Poisson's ratio $\nu = 0.499$, thermal conductivity $h = 10$ W/m.K, specific heat capacity $C_v = 1$ J/Kg.K, thermal expansion coefficient $\alpha = 2.223 \times 10^{-4}$ K$^{-1}$ and $\alpha_{\text{CFL}} = 0.3$.

The time evolution of vertical velocity $v_Z$ and the first component of the first Piola-Kirchhoff stress tensor $P_{11}$ is depicted for two different mesh/particle refinements in Figure 8.29 using three approaches consisting of the total energy-based VCFVM, the total energy-based SPH and the entropy-based SPH schemes. A perfect agreement can be observed between the total energy-based and the entropy-based SPH methodologies for velocity and stress component. Moreover, the diffusive behaviour of the SPH scheme, as expected, is evident with respect to the VCFVM algorithm through the spatial convergence of the solution. A sequence of the deformed states of the cylinder with very smooth temperature and pressure distributions are shown in Figure 8.30.

### 8.5.2 Incompressible twisting column

The main objective of this example is to assess the robustness of the proposed Artificial Compressibility (AC) algorithms in the case of dealing with nearly/truly incompressible scenarios. To achieve this, the challenging twisting column example is studied with the same problem setup defined in Section 8.4.1.

Figure 8.31 depicts the qualitative comparison between the explicit Upwind-SPH scheme and the SPH-AC algorithm (presented in Section 5.6.2). A larger numerical dissipation can be observed introduced by the artificial compressibility algorithm due to the use of the (conservative) Laplacian viscosity term described in Eq. (5.70). Moreover, as illustrated in Figure 8.31, the column's top view entails that the methodology preserves perfect axial rotation without introducing out-of-plane characteristics. A progressive mesh/particle refinement study is carried out and shown in Figure 8.32. It is remarkable that the deformation pattern predicted with a coarse discretisation agrees extremely well with the refined solution. The resolution of the pressure field is evidently enhanced by refining the discretisation.

Figure 8.33 and 8.34 show the effects of adding pseudo viscosity term to the both VCFVM and SPH artificial compressibility approaches, with the primary objective of speeding up the iterative process of the algorithm. In fact, using the viscosity term dramatically reduces the number of iterations required for convergence within the pseudo time integration when solving truly incompressible solids. The $L^2$ norm convergence of pressure has shown for each value of Poisson's ratio for the particular value of artificial viscosity $\alpha_{\mathcal{D}} = 0.2$. In addition, comparing Figure 8.33 with Figure 8.34 entails that the VCFVM-AC algorithm is converging to the solution with less number of iterations rather than the SPH-AC scheme. This leads to the conclusion that the VCFVM-AC algorithms have a better resolution than SPH-AC as it might be due to the diffusive nature of the SPH method.

## 8.6 Conclusion

In this chapter, the fundamental properties of the proposed $\{\boldsymbol{p}, \boldsymbol{F}, \boldsymbol{H}, J, \eta \text{ or } E\}$ VCFVM and SPH algorithms are assessed through several three-dimensional benchmarking examples. The numerical algorithms have shown second order accuracy in space for velocity, stresses and temperature. The conservation property of the numerical methodologies is also demonstrated. To

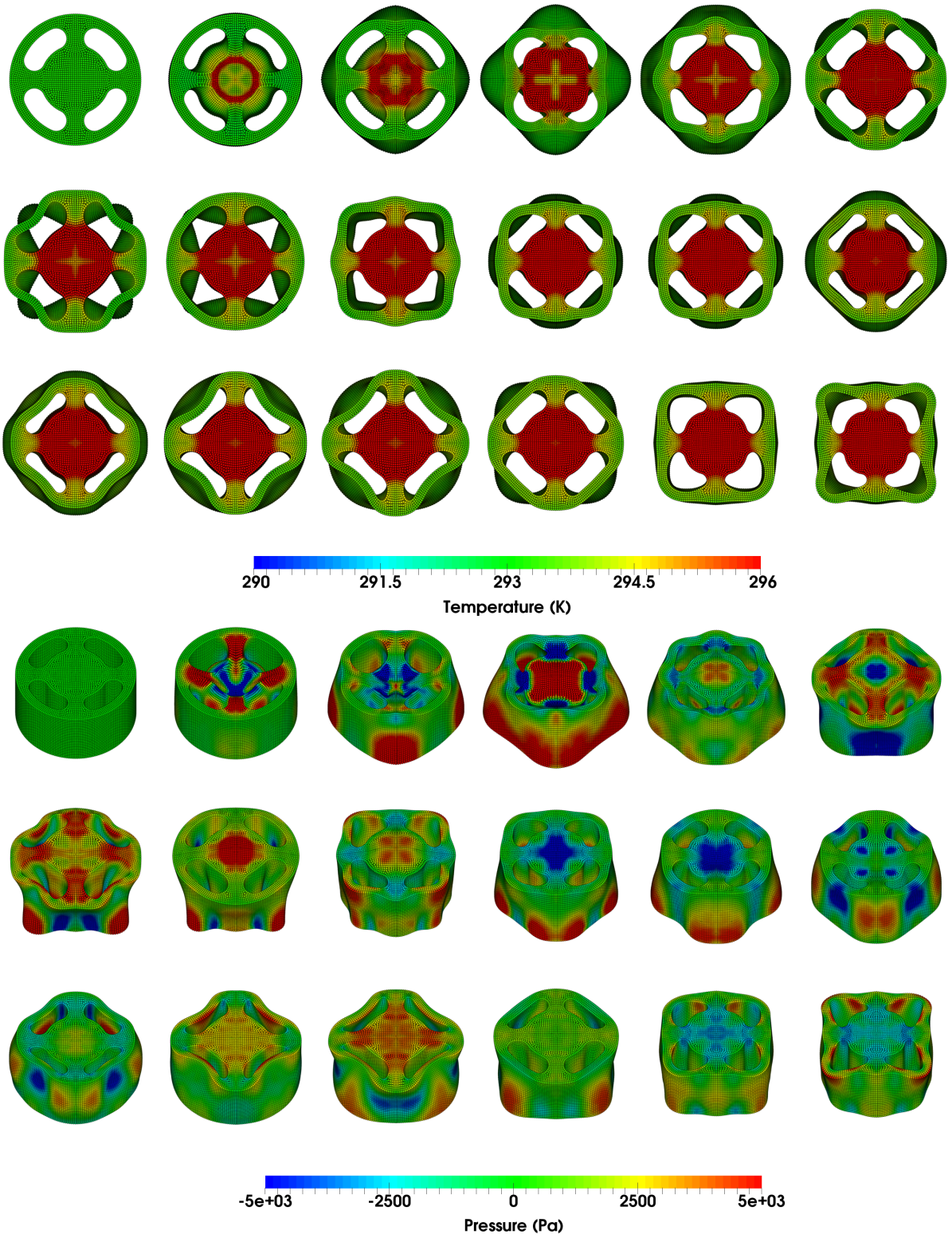


FIGURE 8.30: Punch test: A sequence of deformed configurations with temperature (top view) and pressure (isometric view) distributions at time $t = 0.07 \times \{0, 1, 2, 3, ..., 17\}$ s (left to right-top to bottom), respectively. Results obtained using a nearly incompressible thermo-elastic neo-Hookean constitutive model along with Mie-Grüneisen equation of state using the proposed total energy-based SPH methodology. The material properties used are Young's modulus $E = 50.05$ KPa, density $\rho_R = 1000$ kg/m$^3$, Poisson's ratio $\nu = 0.499$, thermal conductivity $h = 10$ W/m.K, specific heat capacity $C_v = 1$ J/Kg.K, thermal expansion coefficient $\alpha = 2.223 \times 10^{-4}$ K$^{-1}$ and $\alpha_{\text{CFL}} = 0.3$.

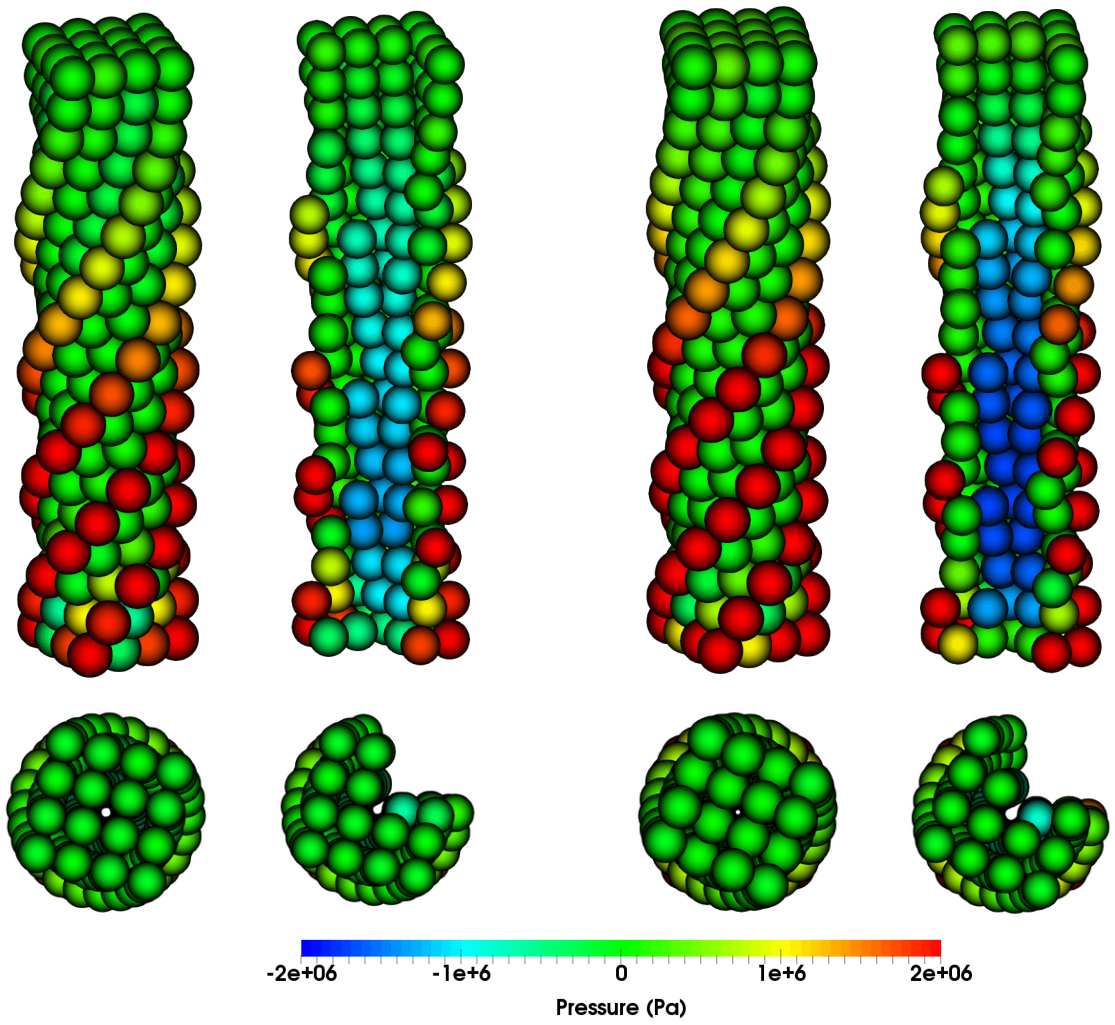


FIGURE 8.31: Twisting column: A comparison between $\{\boldsymbol{p},\ \boldsymbol{F},\ \boldsymbol{H}, p\}$ artificial compressibility approach (left column) and Explicit $\{\boldsymbol{p},\ \boldsymbol{F}, \boldsymbol{H}, J\}$ Upwind-SPH (right column), with isometric view (top row) and top view (bottom row), at time $t = 0.1$ s. Results obtained with an angular velocity field $\boldsymbol{\omega}_0 = [0, 0, \Omega \sin(\pi Z/2L)]$ where $\Omega = 105$ rad/s and $L = 6$ m. A nearly incompressible neo-Hookean constitutive model is employed with Young's modulus $E = 1.7 \times 10^7$ Pa, density $\rho_0 = 1.1 \times 10^3$ kg/m$^3$, Poisson's ratio $\nu = 0.4999$ and $\alpha_{\text{CFL}} = 0.3$.

this end, the robustness of the numerical schemes has been examined through some challenging examples in which extremely good behaviour is observed, even in the limiting case of nearly and truly incompressibility.

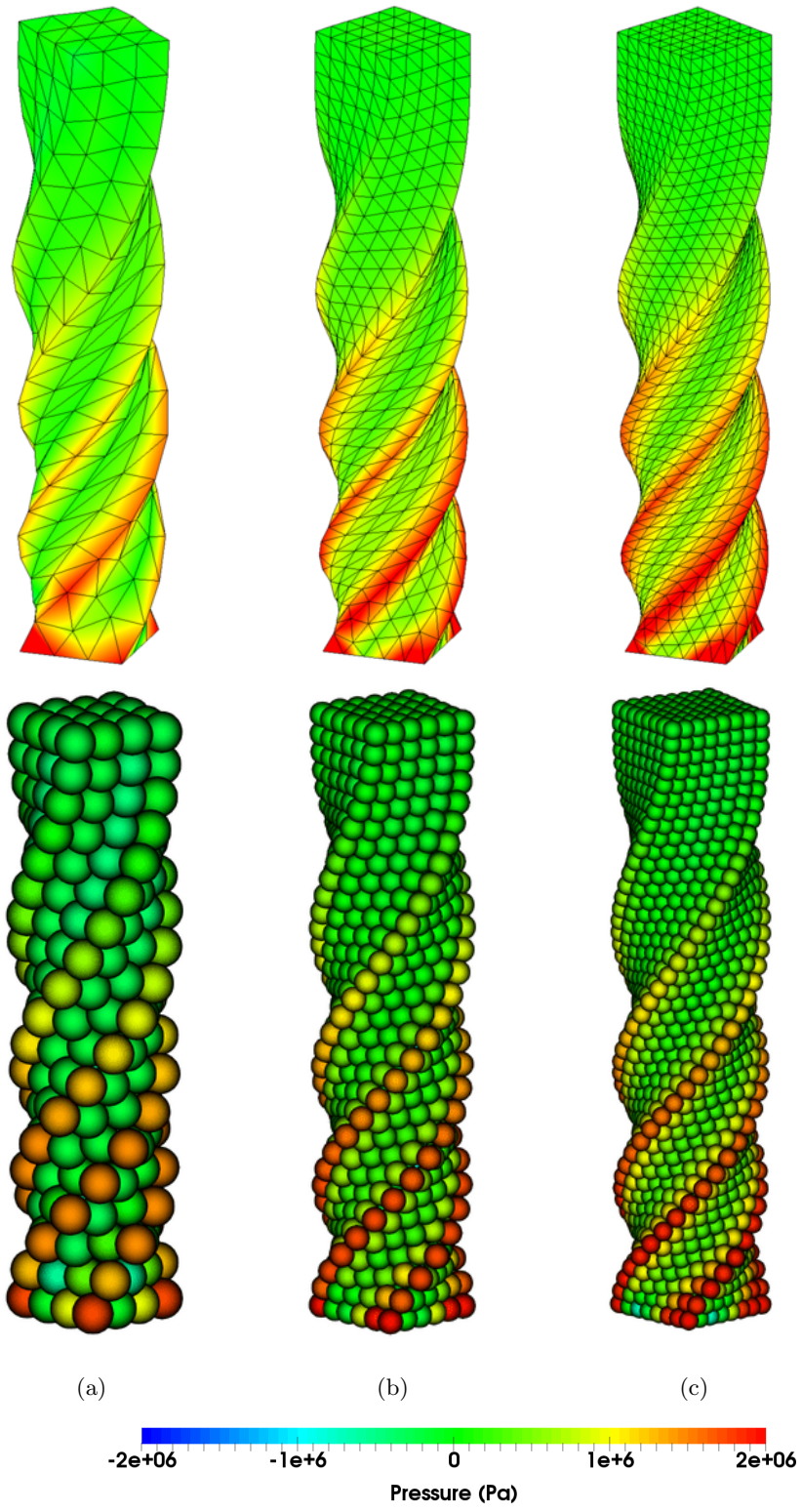


FIGURE 8.32: Twisting column: A sequence of mesh/particle refinement using the mixed-based $\{\boldsymbol{p}, \boldsymbol{F}, \boldsymbol{H}, p\}$ VCFVM and SPH artificial compressibility algorithms at time step $t = 0.1$s: (a) $4 \times 4 \times 24$, (b) $6 \times 6 \times 36$, and (c) $8 \times 8 \times 48$ cells/particles. Results obtained with an angular velocity field $\boldsymbol{\omega}_0 = [0, 0, \Omega \sin(\pi Z/2L)]$ where $\Omega = 105$ rad/s and $L = 6$ m. A truly incompressible neo-Hookean constitutive model is employed with Young's modulus $E = 1.7 \times 10^7$ Pa, density $\rho_0 = 1.1 \times 10^3$ kg/m$^3$, Poisson's ratio $\nu = 0.5$ and $\alpha_{\text{CFL}} = 0.3$.

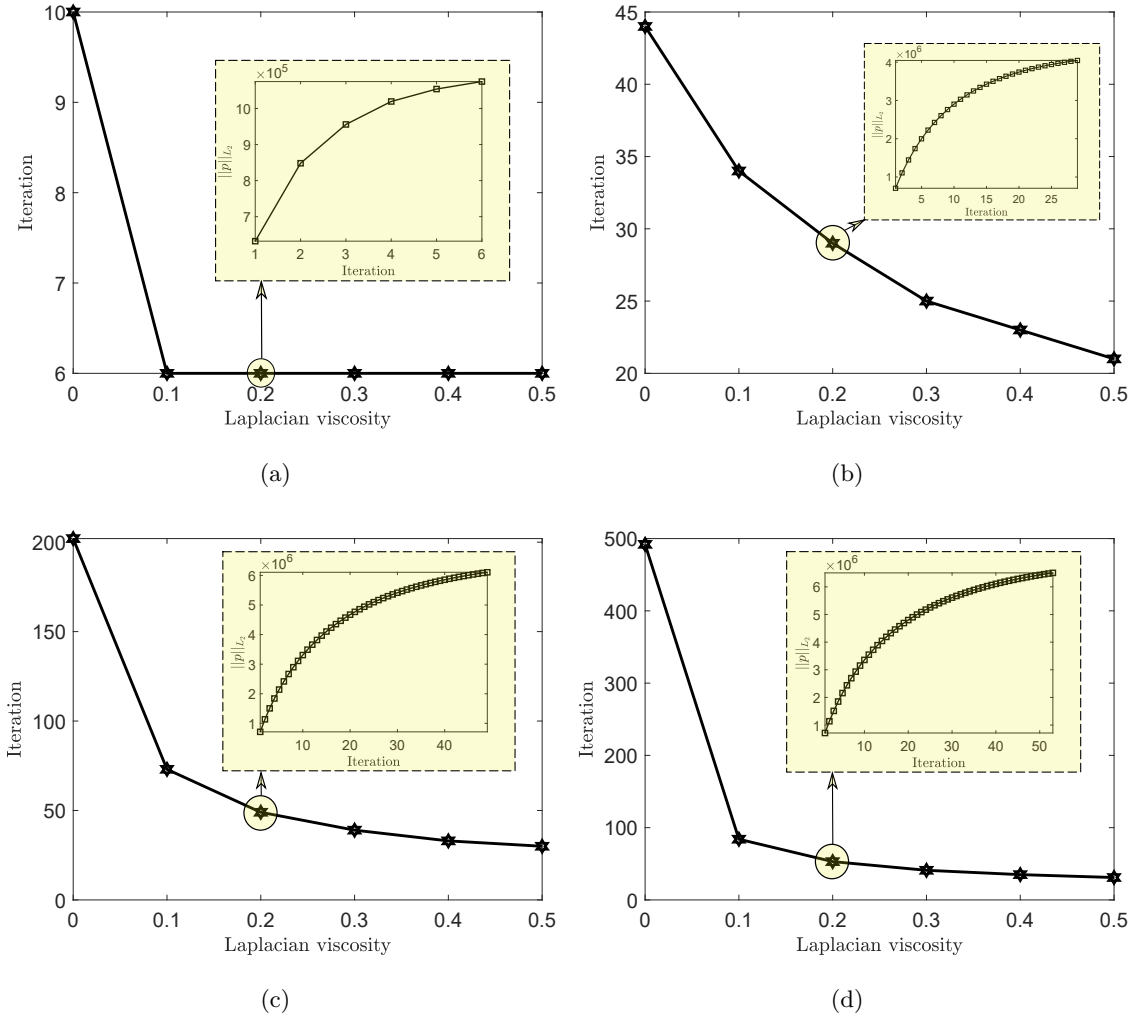


FIGURE 8.33: Twisting column: The effect of incorporating Laplacian viscosity (Eq. (5.70)) to the VCFVM artificial compressibility approach in different scenarios: (a) $\nu = 0.499$, (b) $\nu = 0.4999$, (c) $\nu = 0.49999$ and (d) $\nu = 0.5$. Results obtained for the first step of Runge-Kutta time integrator with an angular velocity field $\boldsymbol{\omega}_0 = [0, 0, \Omega \sin(\pi Z/2L)]$ where $\Omega = 105$ rad/s and $L = 6$ m. A neo-Hookean constitutive model is employed with Young's modulus $E = 1.7 \times 10^7$ Pa, density $\rho_0 = 1.1 \times 10^3$ kg/m$^3$ and $\alpha_{\text{CFL}} = 0.3$.

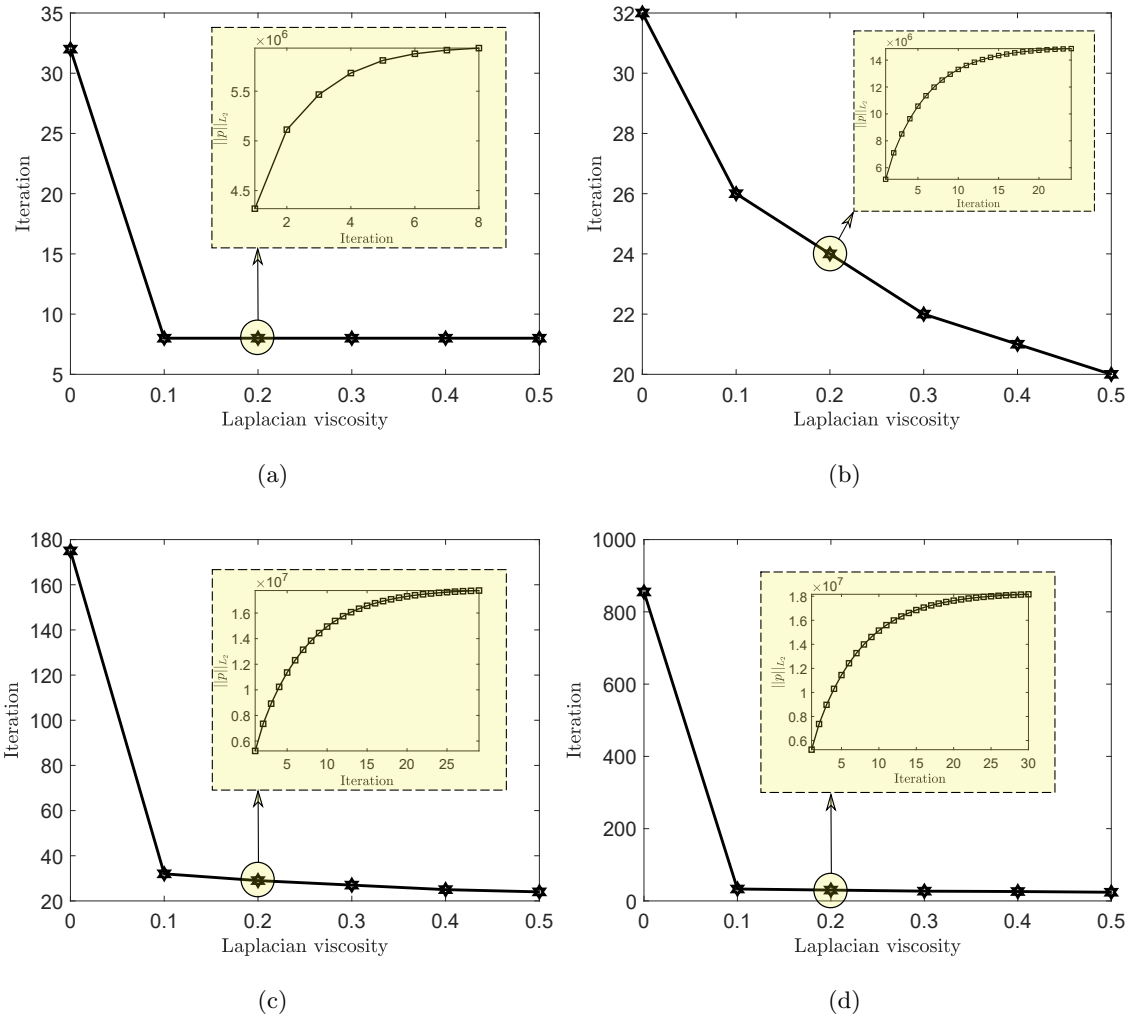


FIGURE 8.34: Twisting column: The effect of incorporating Laplacian viscosity (Eq. (5.70)) to the SPH artificial compressibility approach in different scenarios: (a) $\nu = 0.499$, (b) $\nu = 0.4999$, (c) $\nu = 0.49999$ and (d) $\nu = 0.5$. Results obtained for the first step of Runge-Kutta time integrator with an angular velocity field $\boldsymbol{\omega}_0 = [0, 0, \Omega \sin(\pi Z/2L)]$ where $\Omega = 105$ rad/s and $L = 6$ m. A neo-Hookean constitutive model is employed with Young's modulus $E = 1.7 \times 10^7$ Pa, density $\rho_0 = 1.1 \times 10^3$ kg/m$^3$ and $\alpha_{\text{CFL}} = 0.3$.

Chapter 9

# Multi-dimensional problems: Applications

## 9.1 Introduction

The aim of this chapter is to prove the applicability and robustness of the both proposed $\{\boldsymbol{p}, \boldsymbol{F}, \boldsymbol{H}, J, \eta \text{ or } E\}$ Vertex-Centred Finite Volume method (VCFVM) and Smooth particle hydrodynamics (SPH) algorithms. To achieve this, a set of challenging practical examples with either complex geometries or deformations are assessed. The chapter is divided into two categorises as of isothermal process (Section 9.2) and irreversible process (Section 9.2) under which different practical examples are presented and discussed.

## 9.2 Isothermal process

### 9.2.1 Impact

This example is initially introduced by Taylor [241] aimed at determining the dynamic yield stress of materials. It is then studied in many references as a benchmark example [6, 16, 17, 118, 239]. A circular copper bar of initial length $L = 0.0324$ m and of initial radius $r = 0.0032$ m impacts against a rigid frictionless wall with a dropping velocity of $v_0 = 227$ m/s (see Figure 9.1). The aim of this classical benchmark example is to assess the performance of the proposed VCFVM and SPH algorithms in capturing large elastic-plastic deformations and show its applicability in impact scenarios with application to metal forming [14]. A von Mises hyperelastic-plastic material with isotropic hardening is employed with the material parameters Young's modulus $E = 117$ GPa, density $\rho_0 = 8.930 \times 10^3$ kg/m$^3$, Poisson's ratio $\nu = 0.35$, yield stress $\bar{\tau}_y^0 = 0.4$ GPa and hardening modulus $H = 0.1$ GPa.

Figure 9.2 shows both plastic strain and pressure fields together at time $t = 80\,\mu$s where extremely smooth pressure and plastic strain distributions can be observed. In addition, a very good agreement between the VCFVM and SPH results can be observed. It is worth noting that the solutions obtained on the basis of the standard linear 4-noded tetrahedral element (being

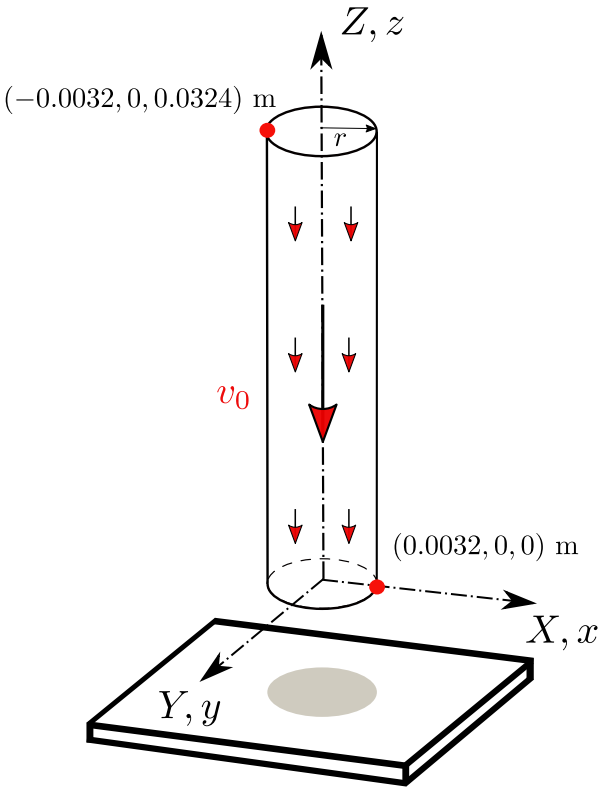


FIGURE 9.1: Taylor impact: Problem setup.

widely used in commercial packages) typically suffer from volumetric locking and spurious pressure oscillations [42, 44] and the proposed algorithms evidently rectify these issues.

Figure 9.3 depicts the time evolution of X coordinate at the material point $\boldsymbol{X} = [0.0032, 0, 0]^T$ at the bottom of the copper bar. The VCFVM and SPH results are compared for three different mesh/particle refinements (800, 1880 and 3200 cells/particles). It is interesting how the SPH methodology is converging to the reference solution from the upper bound limit whereas the VCFVM results are converging from the lower bound limit. The numerical solutions are both eventually converged close to the reference solution, thanks to the refinement. The deformed states of the copper bar with pressure and plastic strain distributions are depicted at time $t = \{20, 40\}\mu$s obtained by the VCFVM scheme and at times $t = \{30, 60\}\mu$s using the SPH algorithm.

For verification purposes, the final radius of the copper bar at time $t = 80\mu$s, where the problem reaches a steady-state solution, predicted by VCFVM and SPH algorithms is shown in Table 9.1. The obtained solutions are benchmarked against other published results using different numerical schemes [17, 42, 118].

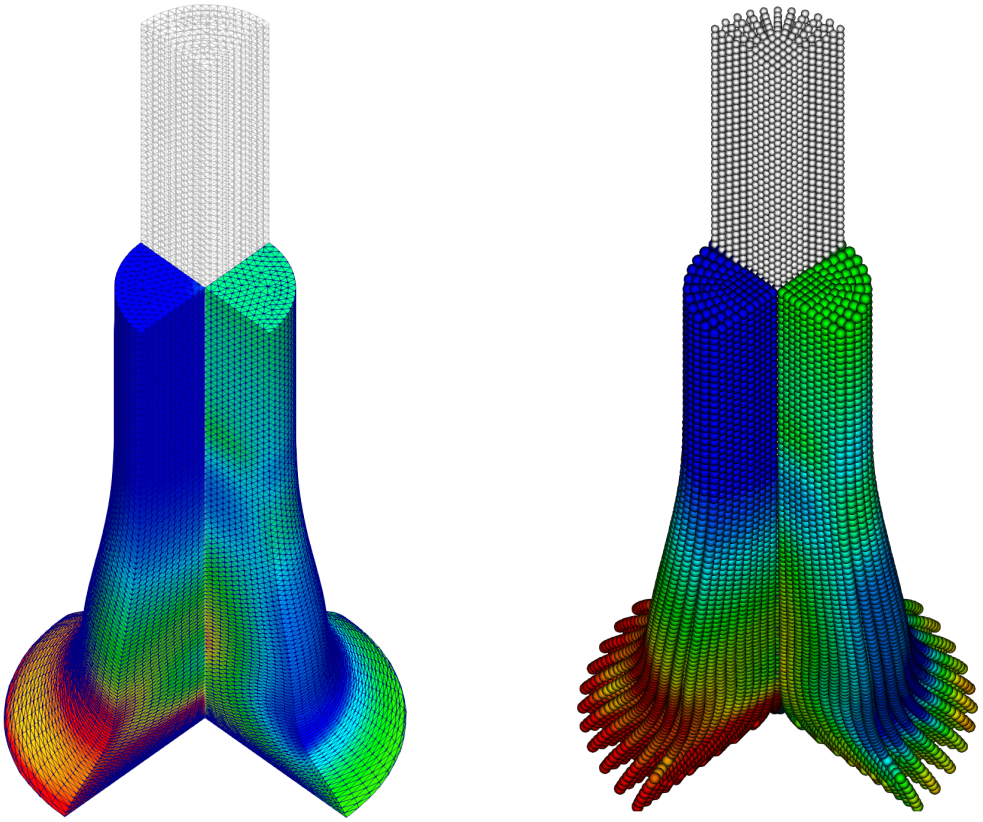

(a) (b)

FIGURE 9.2: Taylor impact: The deformed state of the copper bar at $t = 80\,\mu$s with plastic strain field in the left quarter and pressure distribution in the right quarter of the domain. Results obtained using the proposed VCFVM and SPH algorithms with an initial velocity of $\boldsymbol{v}_0 = (0, 0, -227)^T$ m/s. A hyperelastic-plastic constitutive model is employed with Young's modulus $E = 117$ GPa, density $\rho_0 = 8930$ kg/m$^3$, Poisson's ratio $\nu = 0.35$, yield stress $\bar{\tau}_y^0 = 0.4$ GPa, hardening modulus $H = 0.1$ GPa and $\alpha_{\text{CFL}} = 0.3$.

TABLE 9.1: Final radii of copper bar at $t = 80\,\mu$s. Results obtained using the proposed VCFVM and SPH algorithms, benchmarked against other published methodologies.

| Method | Final radius (cm) |
|---|---|
| Standard 4-Noded Tetrahedra [42] | 0.555 |
| Under-integrated 8-Noded Hexahedra [42] | 0.695 |
| Average Nodal Pressure 4-Noded Tetrahedra [42] | 0.699 |
| Jameson-Schmidt-Turkel Vertex Centred FVM [118] | 0.698 |
| Petrov-Galerkin FEM [17] | 0.700 |
| Upwind Cell Centred FVM [6] | 0.700 |
| **Upwind-SPH mesh-free method** | 0.711 |
| **Upwind-VCFVM method** | 0.711 |

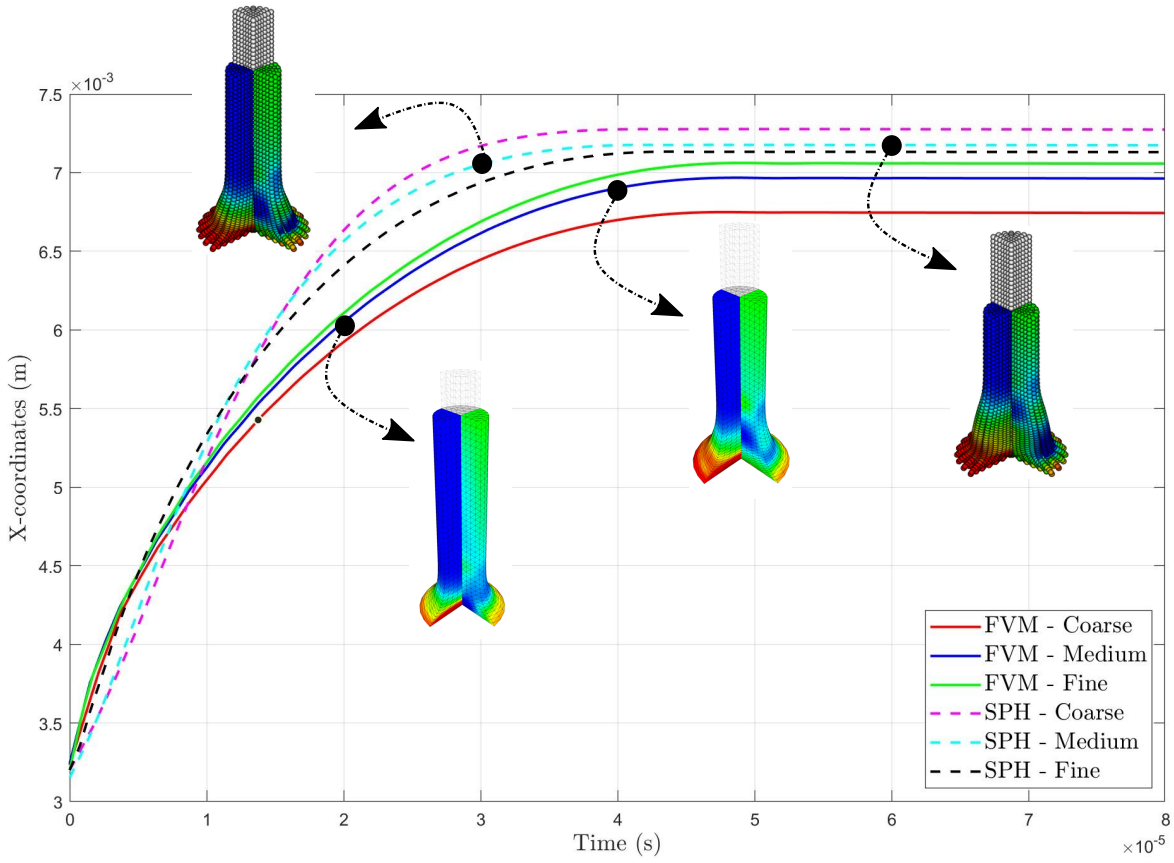


FIGURE 9.3: Taylor impact: Time evolution of X coordinate at the material point $\boldsymbol{X} = [0.0032, 0, 0]^T$ with three mesh/particle refinements (800, 1880 and 3200 cells/particles). Results obtained using the proposed VCFVM and SPH algorithms with an initial velocity of $\boldsymbol{v}_0 = (0, -227, 0)^T$ m/s. A hyperelastic-plastic constitutive model is employed with Young's modulus $E = 117$ GPa, density $\rho_0 = 8930$ kg/m$^3$, Poisson's ratio $\nu = 0.35$, yield stress $\bar{\tau}_y^0 = 0.4$ GPa, hardening modulus $H = 0.1$ GPa and $\alpha_{\text{CFL}} = 0.3$.

### 9.2.2 Stent-like structure

This example represents the expansion of a stent-like structure aimed at demonstrating the robustness of the proposed VCFVM algorithm on rather complex geometry (see Figure 9.4). The (coronary artery) medical stent is widely used in biomedical applications aiming at keeping a vessel or passageway open. The structure has an initial outer diameter of $d = 10$ mm, a thickness of $T = 0.1$ mm and a total length of $L = 20$ mm. The dimension of one of the repeated geometrical pattern is depicted in Figure 9.4b. In this case, the expansion of the stent-like structure is studied by applying constant traction of $t_B = 10$ KPa directed outward perpendicular on the interior of the cylindrical structure. For computational purposes and due to the presence of three symmetry planes, only one-eighth of the problem is solved with appropriate boundary conditions.

Figure 9.5 illustrates the deformed state of the expanded stent-like structure at time $t = 3.4 \times 10^{-4}$ s. The overall view of the deformation consists of two zoom sections in order to better visualise the regions with sharp gradients. A very smooth pressure distribution can be observed throughout the structure, and, at the sharp edges in particular. The front view shows how much the stent-like structure is expanded relative to the reference state. The contraction of the structure, however, is clear by looking at the top view.

It is evident that the proposed VCFVM algorithm produced reliable results without exhibiting any zero-energy mode, locking or spurious pressure modes. It is also capable of capturing highly nonlinear structural deformations. This can open up some interesting possibilities to numerically simulate biomedical applications [242], in which this consideration is very relevant.

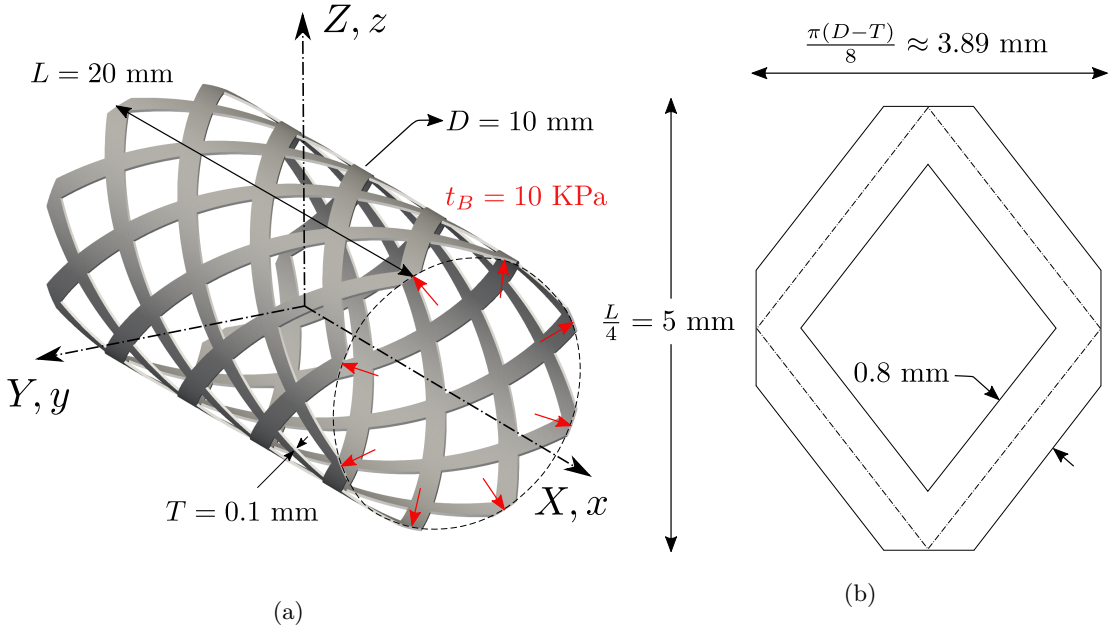


FIGURE 9.4: Stent-like structure: (a) Problem setup; and (b) Planar 1/32$^{\text{th}}$ geometry

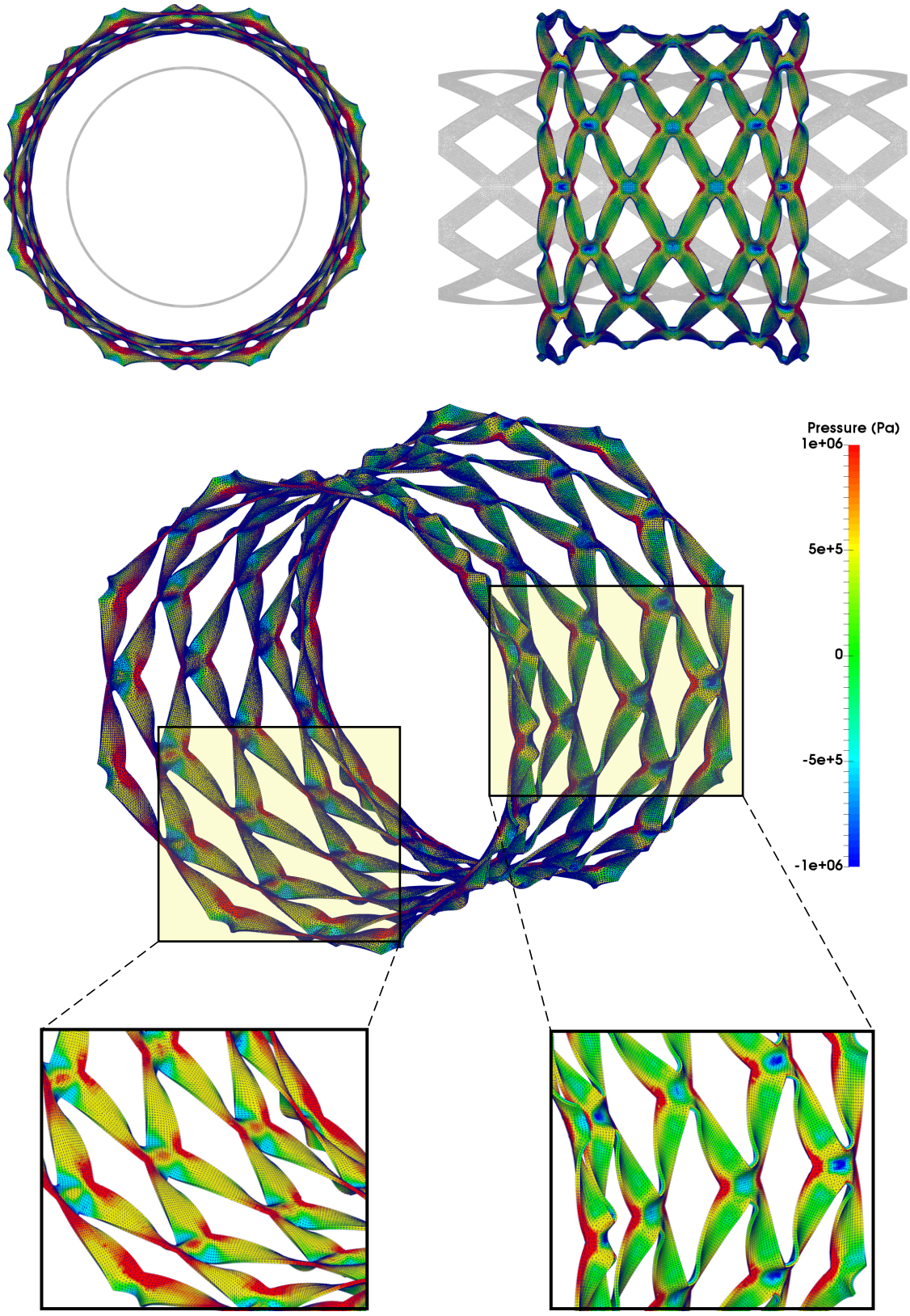


FIGURE 9.5: Stent-like structure: Snapshot of the deformed state with pressure field at $t = 3.4 \times 10^{-4}$ s. A Front view (top row - left), top view (top row - right) and an Isometric view (middle) with two highlighted regions of the structure are presented. Results obtained using the proposed VCFVM algorithm with a constant traction of $t_B = 10$ KPa directed outward perpendicular on the interior of the cylindrical structure. A neo-Hookean material model is employed with Young's modulus $E = 1.7 \times 10^7$ Pa, density $\rho_0 = 1100$ kg/m$^3$, Poisson's ratio $\nu = 0.45$ and $\alpha_{\text{CFL}} = 0.3$.

## 9.3 Irreversible process

### 9.3.1 Deep drawing

A very thin plate is considered for deep drawing process in which a sheet metal undergoes a shape transformation process with material retention. Figure 9.6a shows the problem setup

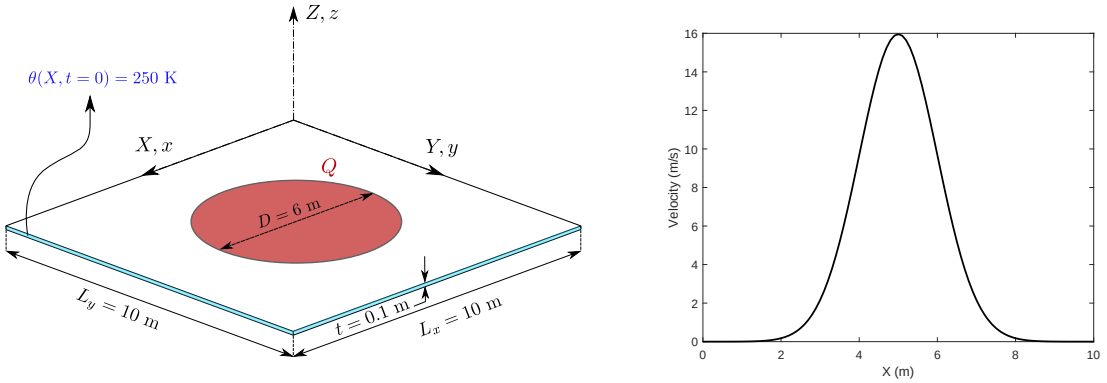


(a) (b)

FIGURE 9.6: Thin plate: (a) Initial configuration; and (b) Velocity profile

where the plate is initialised with the following velocity profile

$$\boldsymbol{v} = [0, 0, v_Z]; \quad v_Z = \sqrt{\frac{\pi}{2}} v_0 \left( \exp\left( -\frac{(X-5)^2}{2} \right) + \exp\left( -\frac{(Y-5)^2}{2} \right) \right), \tag{9.1}$$

with $v0 = 20$ m/s. In addition, the thin faces around the plate are also initialised with a temperature of 250 K (see Figure 9.6b). A sinusoidal heat flux is imposed on the middle of the plate as

$$Q_B = \frac{10000}{A_0} \sin\left( \frac{\pi}{2} t \right), \tag{9.2}$$

with $A_0$ considered as the area where the thermal Neumann boundary condition ($Q$) is applied. Homogeneous distribution of initial temperature of $\theta_R = 293.15$ K throughout the plate is considered with free mechanical boundary conditions. A thermo-elastic neo-Hookean material model along with Mie-Grüneisen equation of state is employed with Young's modulus $E = 50.05$ KPa, density $\rho_R = 1000$ Kg/m$^3$, Poisson's ratio $\nu = 0.3$, thermal conductivity $h = 10$ W/m.K, specific heat capacity $C_v = 1$ J/Kg.K and thermal expansion coefficient $\alpha = 2.223 \times 10^{-4}$ K$^{-1}$. The main objective of this example is to show the robustness of the proposed VCFVM methodology in terms of handling a challenging and practical thermo-mechanical example.

Figure 9.7 depicts a sequence of the deformed states of the thin plate with temperature and pressure distributions. It is interesting to note that the plate is eventually reformed into a state with very sharp edges in which the deformation is well captured and very smooth pressure and temperature fields can be observed.

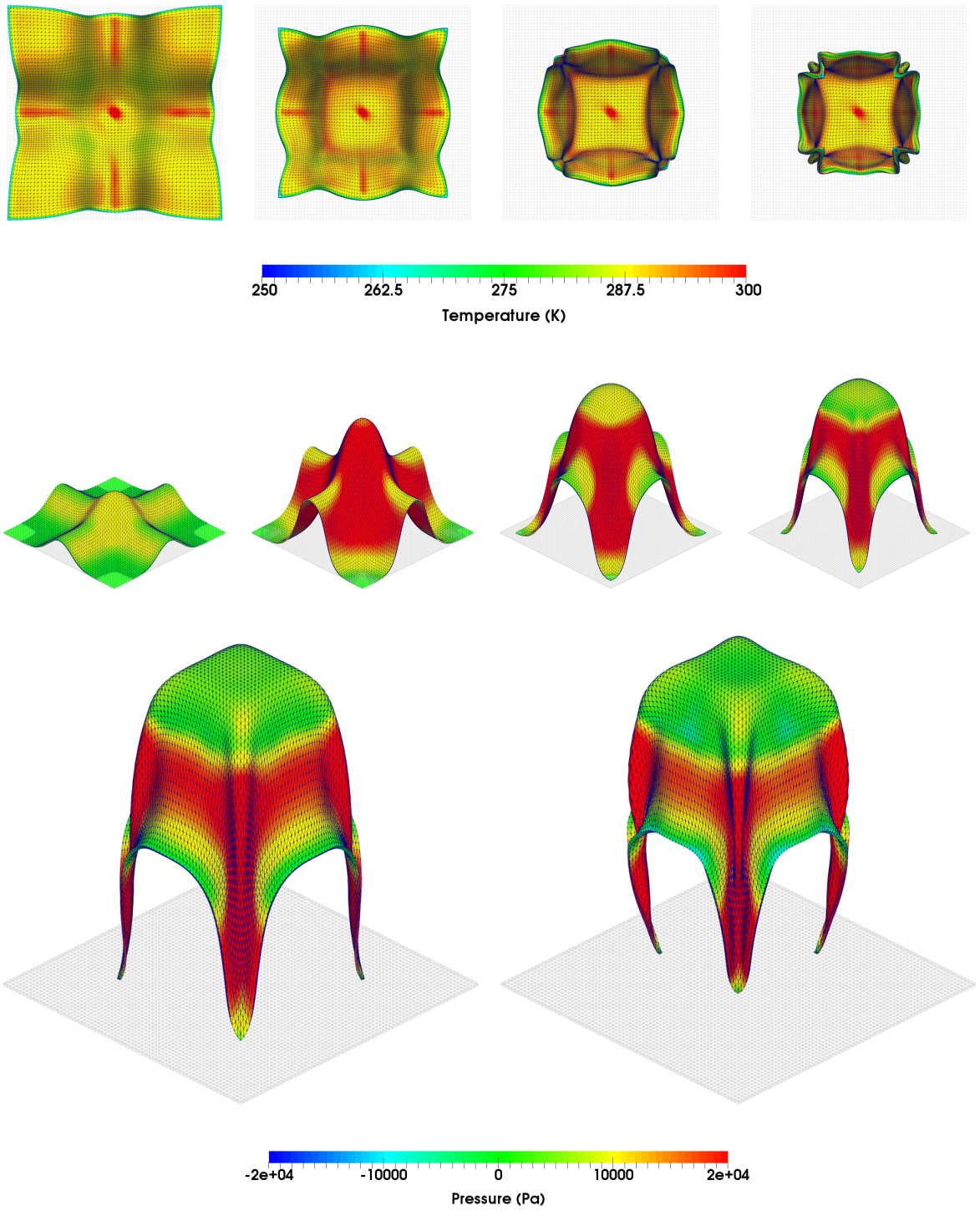


FIGURE 9.7: Thin plate: A sequence of deformed configurations with temperature field on the top row at $t = \{0.45, 0.76, 0.90, 0.98\}$ s and isometric view with pressure distribution on the bottom rows at $t = \{0.10, 0.16, 0.21, 0.32, 0.41, 0.59, 0.70, 0.81, 0.90, 0.98\}$ s. Results obtained using a nearly incompressible thermo-elastic neo-Hookean constitutive model along with Mie-Grüneisen equation of state using the proposed VCFVM methodology. The material properties used are Young's modulus $E = 50.05$ KPa, density $\rho_R = 1000$ kg/m$^3$, Poisson's ratio $\nu = 0.45$, thermal conductivity $h = 10$ W/m.K Specific heat capacity $C_v = 1$ J/Kg.K, thermal expansion coefficient $\alpha = 2.223 \times 10^{-4}$ K$^{-1}$ and $\alpha_{\text{CFL}} = 0.3$.

### 9.3.2 Ball joint

Spherical structures are utilised in many industrial applications such as ball joints for bearing and casters, ball valves, pressure tanks and ball in toy industry. In fact, these structures helps to minimise the material consumption as a sphere provides the smallest surface area for a given volume. Here a thin spherical ball is considered which is perforated in an unsymmetrical manner in order to provide a rather more complex geometry. The ball is punched on its top surface with a velocity field of $\boldsymbol{v} = [0, 0, 1.5]^T$ m/s. The geometry and problem setup are shown in Figure 9.8. This example aimed at demonstrating the robustness of the proposed SPH algorithm with respect to massive deformation of a rather complex geometry. A free (mechanical) boundary condition is considered for the ball while it is thermally subjected to a heat flux $Q_B = 1000/A$ where $A$ denotes the surface in which the heat flux is imposed. An entropic-elastic constitutive model is used with material properties Young's modulus $E = 1.7 \times 10^7$ Pa, density $\rho_R = 1100$ kg/m$^3$, Poisson's ratio $\nu = 0.3$, thermal conductivity $h = 0.2$ W/m.K, specific heat capacity $C_v = 1000$ J/Kg.K and thermal expansion coefficient $\alpha = 2.223 \times 10^{-4}$ K$^{-1}$ with the initial homogeneous temperature distribution of $\theta_R = 293.15$ K.

Figure 9.9 shows the deformed state of the ball at time $t = 0.42$ s. The extremely large deformation of the ball is evident where the pressure distribution is shown to be very smooth, particularly close to the sharp edges of the holes. In addition, different viewpoints of the deformed configuration is depicted with a very smooth temperature distribution. It is worth to mention that the small temperature gradient of the entropic-elastic material is expected considering its material properties with a large specific heat capacity and a small heat conduction coefficient (which results in a very small temperature gradient).

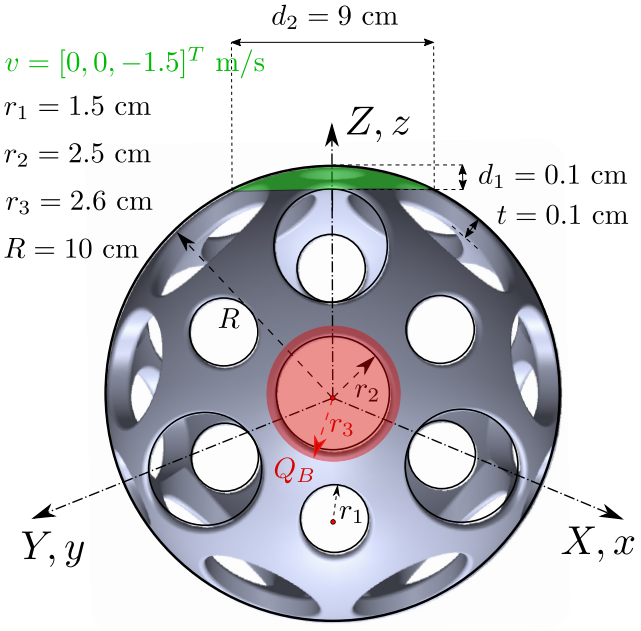


FIGURE 9.8: Spherical ball: Problem setup

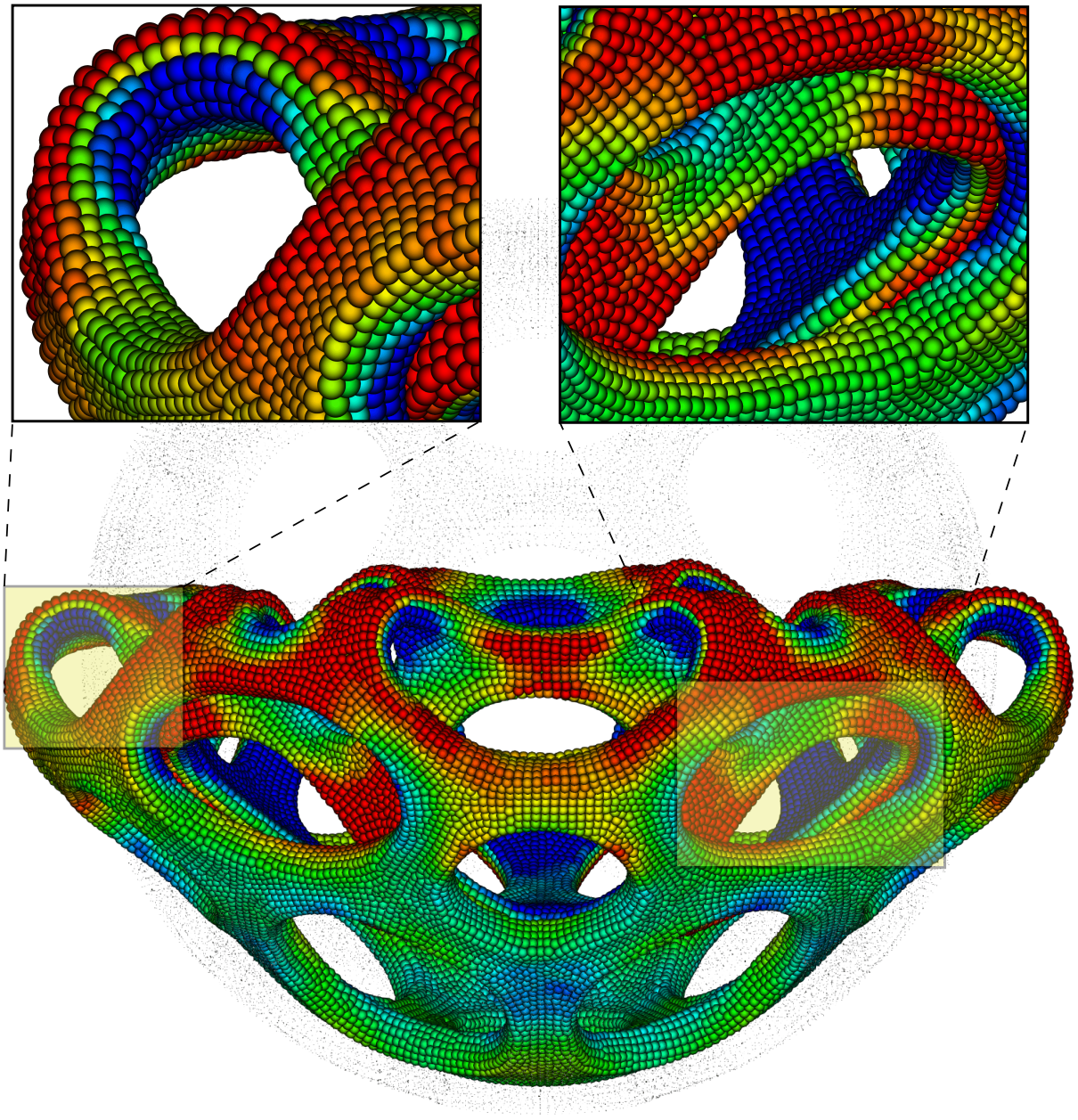

FIGURE 9.9: Spherical ball: The deformed state along with pressure distribution at time $t = 0.042$ s. Results obtained using a nearly incompressible entropic-elastic neo-Hookean constitutive model using the proposed SPH methodology. The material properties used are Young's modulus $E = 1.7 \times 10^7$ Pa, density $\rho_R = 1100$ kg/m$^3$, Poisson's ratio $\nu = 0.3$, thermal conductivity $h = 0.2$ W/m.K, specific heat capacity $C_v = 1000$ W/Kg.K, thermal expansion coefficient $\alpha = 2.223 \times 10^{-4}$ and $\alpha_{\text{CFL}} = 0.3$.

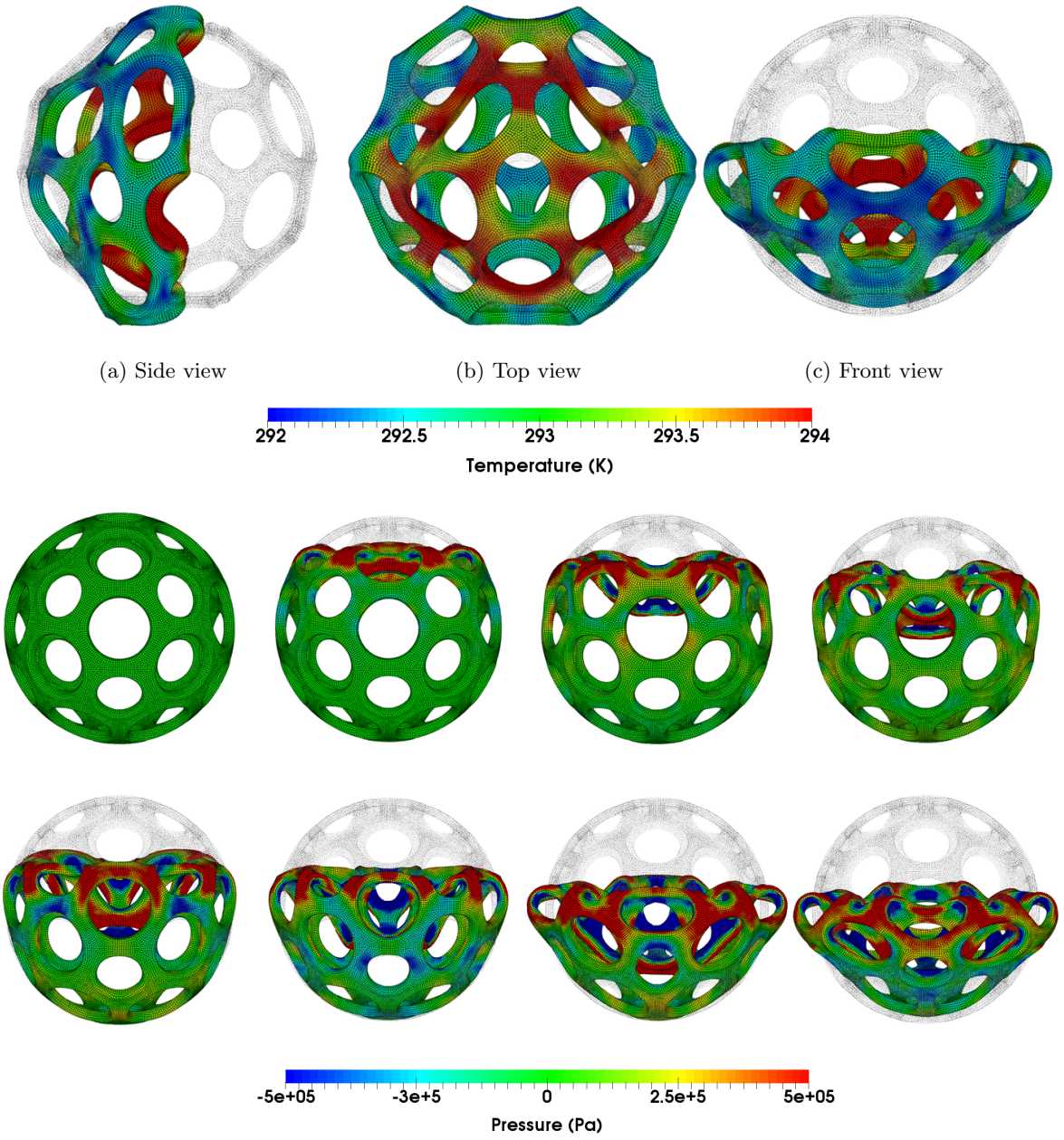


(a) Side view (b) Top view (c) Front view

FIGURE 9.10: Spherical ball: A sequence of deformed configurations with temperature and pressure distributions at time $t = 0.042$ s and $t = 0.01 \times \{0, 1, 2, 3, 4, 4.2\}$ s (left to right-top to bottom), respectively. Results obtained using a nearly incompressible entropic-elastic neo-Hookean constitutive model using the proposed SPH methodology. The material properties used are Young's modulus $E = 1.7 \times 10^7$ Pa, density $\rho_R = 1100$ kg/m$^3$, Poisson's ratio $\nu = 0.3$, thermal conductivity $h = 0.2$ W/m.K specific heat capacity $C_v = 1000$ J/Kg.K, thermal expansion coefficient $\alpha = 2.223 \times 10^{-4}$ K$^{-1}$ and $\alpha_{\text{CFL}} = 0.3$.

### 9.3.3 Pipe expansion joint

This example is representative of a rubber expansion joint which is usually used in pipe systems in order to absorb temperature-induced expansions and withstand the internal pressure of the pipes. Moreover, it has the functionality to absorb noises, vibrations and/or deformations. The representative geometry is a very thin truncated sphere (see Figure 9.11) subjected to a free expansion and the body is adiabatically insulated. A constant traction is applied on the physical boundary within the sphere as $t_B = 500$ N/m$^2$ (as shown in Figure 9.11b). The aim of this example is to demonstrate the capability of the proposed VCFVM algorithm in capturing extreme deformations in nearly incompressible scenarios in which numerical difficulties such as locking or spurious pressure oscillations are effectively alleviated. A neo-Hookean material model along with Mie-Grüneisen equation of state is employed with Young's modulus $E = 50.05$ KPa, density $\rho_R = 1000$ Kg/m$^3$, Poisson's ratio $\nu = 0.499$, thermal conductivity $h = 10$ W/m.K, specific heat capacity $C_v = 1$ J/Kg.K and thermal expansion coefficient $\alpha = 2.223 \times 10^{-4}$ K$^{-1}$ where the body has a homogeneous distribution of initial temperature $\theta_R = 293.15$ K.

Figure 9.12 shows the side-view evolution of the spherical structure which its extreme deformation is well captured along with very smooth pressure distribution. For a better vision of the deformed states, the sphere is clipped into half and the evolution of temperature field is shown in Figure 9.13 in which a very smooth temperature distribution can be observed. It is worthy to note that the coupling effect, and so the heat generated by the deformation, is just taking place through the volumetric part of the stresses. Consequently, an extremely small temperature gradient is expectable in this case as the near incompressibility feature of the material leads to a very small coupling term.

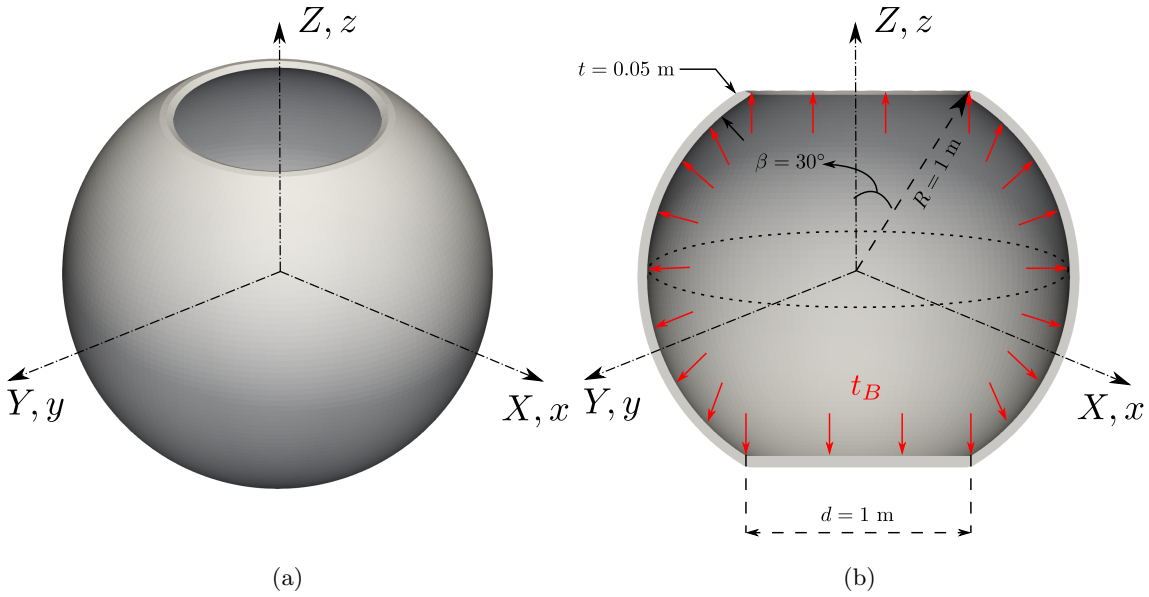


FIGURE 9.11: Expansion joint: (a) Initial configuration; and (b) Problem setup

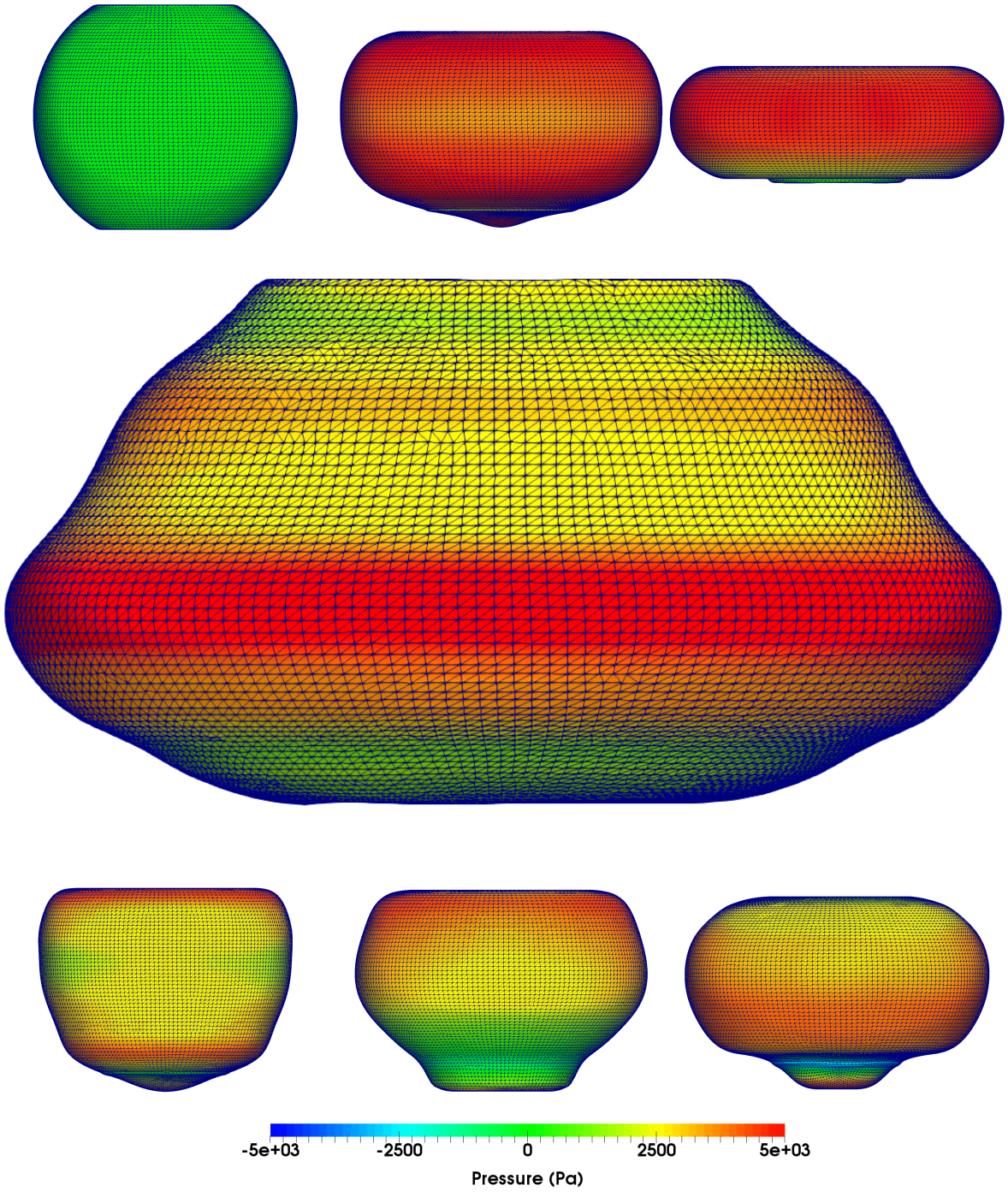


FIGURE 9.12: Expansion joint: A sequence of deformed configurations along with pressure field at $t = \{0, 0.31, 0.55, 1.42, 1.78, 1.93, 2.04\}$ s (left to right - top to bottom). Results obtained using a nearly incompressible thermo-elastic neo-Hookean constitutive model along with Mie-Grüneisen equation of state using the proposed vertex-centred FVM methodology. The material properties used are Young's modulus $E = 50.05$ KPa, density $\rho_R = 1000$ kg/m$^3$, Poisson's ratio $\nu = 0.499$, thermal conductivity $h = 10$ W/m.K, Specific heat capacity $C_v = 1$ J/Kg.K, thermal expansion coefficient $\alpha = 2.223 \times 10^{-4}$ K$^{-1}$ and $\alpha_{\text{CFL}} = 0.31$.

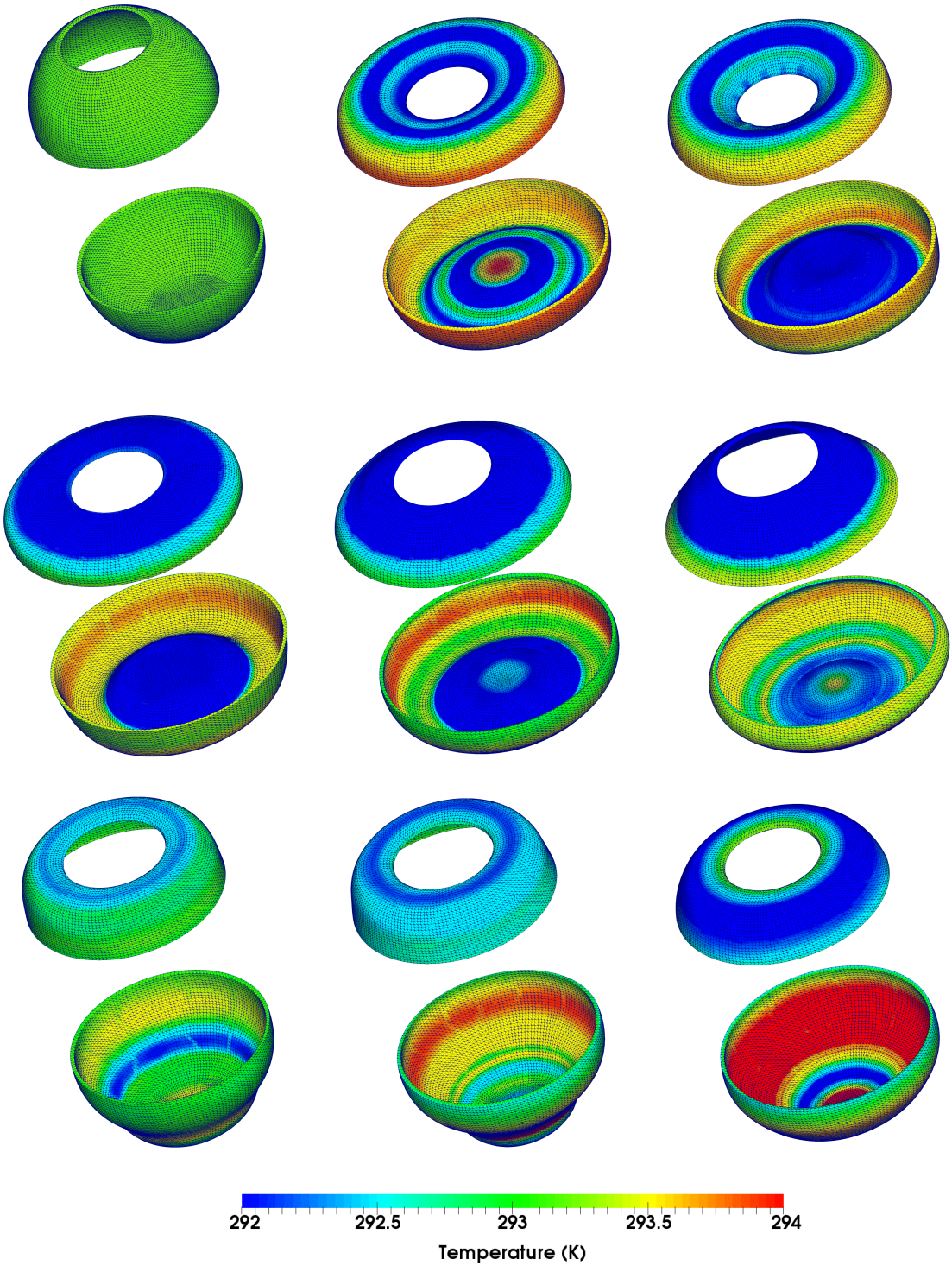


FIGURE 9.13: Expansion joint: A sequence of deformed configurations with temperature distributions at $t = \{0, 0.66, 0.74, 1.20, 1.28, 1.37, 1.83, 1.88, 1.98\}$ s (left to right - top to bottom). Results obtained using a nearly incompressible thermo-elastic neo-Hookean constitutive model along with Mie-Grüneisen equation of state using the proposed vertex-centred FVM methodology. The material properties used are Young's modulus $E = 50.05$ KPa, density $\rho_R = 1000$ kg/m$^3$, Poisson's ratio $\nu = 0.499$, thermal conductivity $h = 10$ W/m.K, Specific heat capacity $C_F = 1$ J/Kg.K, thermal expansion coefficient $\alpha = 2.223 \times 10^{-4}$ K$^{-1}$ and $\alpha_{\text{CFL}} = 0.31$.

### 9.3.4 Soft robotic

This example studies the deformation of a gripper-like structure (see Figure 9.14) widely used in (soft) robotic applications. The gripper has four geometrically symmetric arms with $L = 0.4$ m which are connected to a hollow cylindrical shape with a radius of $R = 0.1$ m. The central interior of the cylinder has a constant temperature of $\theta = 280$ K (thermal Dirichlet boundary condition) while the rest of the domain is thermally insulated. The end faces of the arms (at XY plane) are also subjected to a constant tractions $t_B = 1000$ N/m$^2$ where the temperature is initially set to be $\theta = 300$ K. The main objective of this example is to show the robustness of the proposed SPH algorithm in bending dominated scenarios where mechanical and thermal boundary conditions are imposed to the problem. A thermo-elastic neo-Hookean material model along with Mie-Grüneisen equation of state is employed using the entropy-based SPH methodology. The material properties used are Young's modulus $E = 50.05$ KPa, density $\rho_R = 1000$ Kg/m$^3$, Poisson's ratio $\nu = 0.45$, thermal conductivity $h = 10$ W/m.K, specific heat capacity $C_v = 1$ J/Kg.K and thermal expansion coefficient $\alpha = 2.223 \times 10^{-4}$ K$^{-1}$ where the gripper has an initial homogeneous temperature distribution $\theta_R = 293.15$ K.

Figure 9.15 shows the overall states of deformation in three different viewpoints with very smooth pressure and temperature distributions. In fact, heat conduction has occurred through the four arms as a result of temperature gradient which origins from the difference in temperature between the reference temperature and the thermal Dirichlet boundary condition imposed at the hollow cylindrical shape of gripper's centre. In addition, the bending deformation, due to the imposed Neumann boundary condition (tractions), leads to a heat generation in the arms and that, this affects the heat conduction process.

Looking at the pressure distribution in Front view of the gripper, the areas with the most contractions and extensions are evident. For instance, the bottom of the hollow cylinder at the

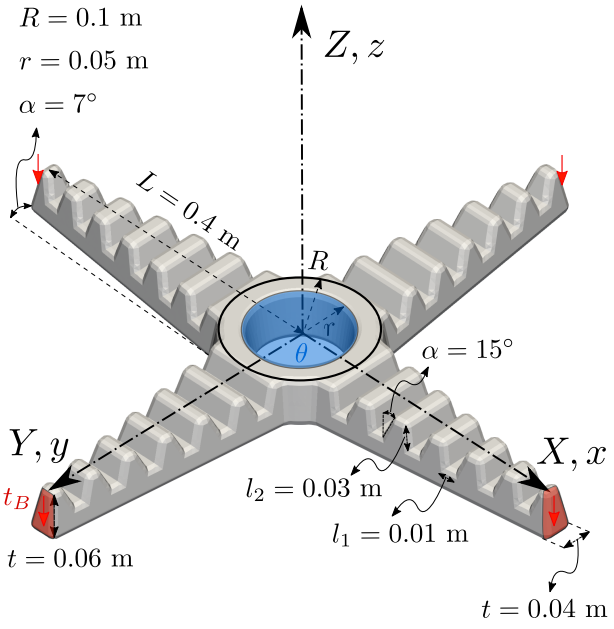


FIGURE 9.14: Gripper: Problem setup

gripper's centre is contracted and consequently, yielded an increase in temperature. This can be clearly seen in Bottom view with temperature distribution. Moreover, notice the decrease in temperature at the hollow centre of the gripper (at Isometric view with temperature distribution) which is a result of its extension. This is illustrated in the top view with pressure distribution.

## 9.4 Conclusion

In this chapter, the capability of the $\{\boldsymbol{p}, \boldsymbol{F}, \boldsymbol{H}, J, \eta \text{ or } E\}$ VCFVM and SPH algorithms are assessed through several numerical examples with relatively complex geometries. These challenging examples can also be seen as some conceivable industrial applications. The numerical algorithms have shown excellent behaviour on capturing extremely large deformations in conjunction with smooth distribution of the variable fields (e.g. pressure and temperature).

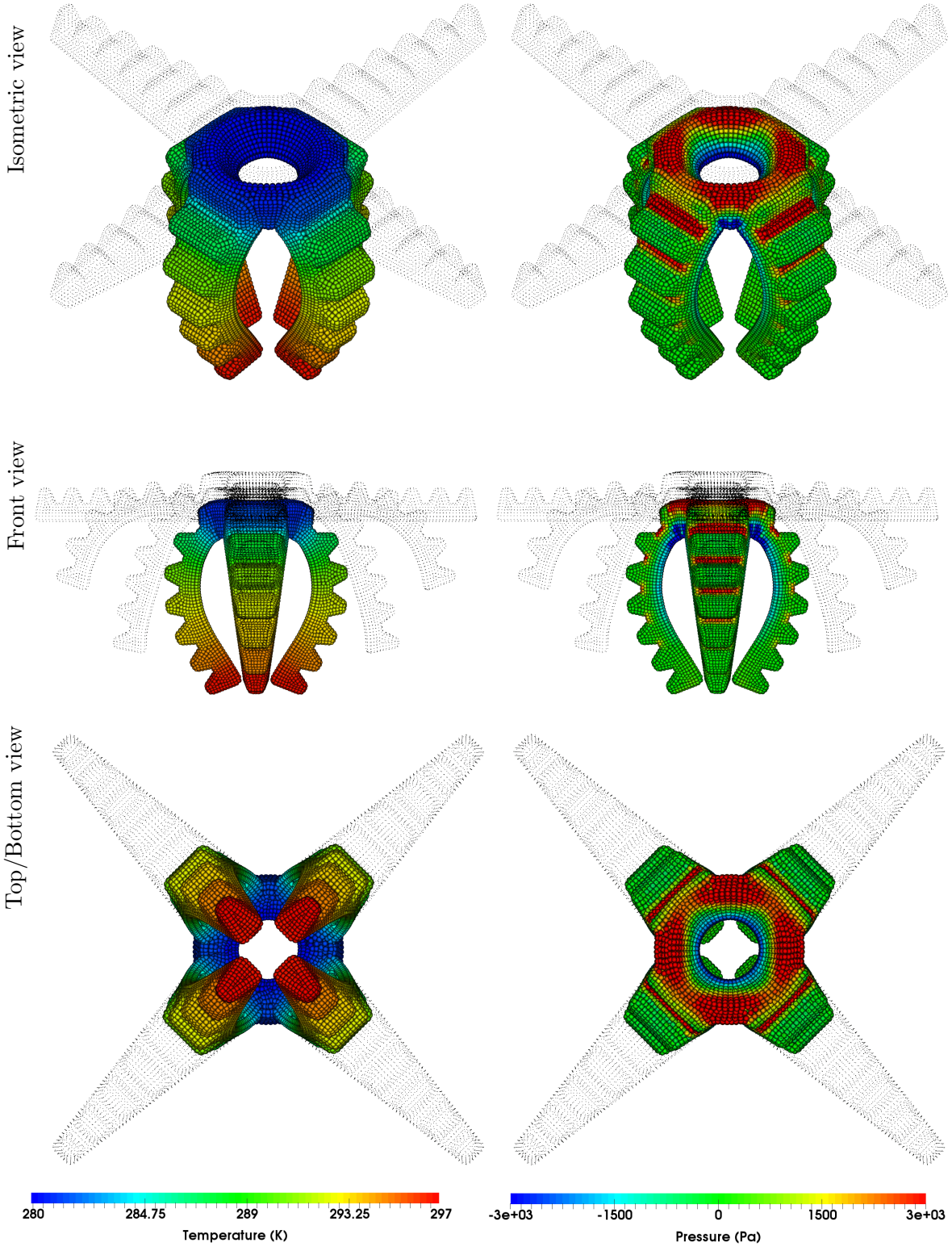


FIGURE 9.15: Gripper: A sequence of deformed configurations with temperature and pressure distributions at $t = 0.47$ s. Results obtained using a nearly incompressible thermo-elastic neo-Hookean constitutive model along with Mie-Grüneisen equation of state using the proposed SPH methodology. The material properties used are Young's modulus $E = 50.05$ KPa, density $\rho_R = 1000$ kg/m$^3$, Poisson's ratio $\nu = 0.45$, thermal conductivity $h = 10$ W/m.K, specific heat capacity $C_v = 1$ J/Kg.K, thermal expansion coefficient $\alpha = 2.223 \times 10^{-4}$ K$^{-1}$ and $\alpha_{\text{CFL}} = 0.3$.

# Part V

# Conclusion and future outlook

# Chapter 10

# Concluding remarks

## 10.1 Summary

This work has been devoted to study and analyse the behaviour of nonlinear solid materials undergoing large deformations with the focus on fast transient applications. Following the works of Aguirre *et al.* [7] and Lee *et al.* [4, 5], a mixed system of first order conservation laws [3, 6, 7, 16–18, 22, 23, 118] is first presented in order to explore some limiting scenarios in the isothermal case, such as the consideration of near and true incompressibility. Specifically, the Total Lagrangian system of hyperbolic equations is expressed in terms of the linear momentum $\boldsymbol{p}$ and the minors of the deformation, namely, the deformation gradient $\boldsymbol{F}$, its co-factor $\boldsymbol{H}$ and its Jacobian $J$. One of the main contributions of this work is to extend the above mixed-based set of equations to the case of thermo-elasticity to account for irreversible processes. This is achieved by the introduction of an additional conservation law for the total energy (also known as the first law of thermodynamics) to the set of physical laws presented above. Typically, the first law of thermodynamics is written in terms of total energy, similar to that of Euler equations used in CFD. In this work, and for completeness, we also re-write the first law in terms of entropy variable. For closure of the system, appropriate constitutive models derived on the basis of polyconvex energy functions are presented. This guarantees the existence of real wave speeds (and hence, material stability) for the entire range of deformation and temperature. For instance, in the context of thermo-elasticity, new convex thermo-mechanical models (in this case, Mie-Grüneisen equation of state and modified entropic elasticity) are presented.

From the spatial discretisation viewpoint, two distinct and competitive numerical methodologies are utilised, namely, a mesh-based Vertex-Centred Finite Volume Method (VCFVM) and a meshless Smooth Particle Hydrodynamics (SPH). Taking advantage of the new conservation law formulation, well established stabilisation algorithms are then explored.

Naturally, discontinuity of the conservation variables across (dual) control volume interfaces or between any pair of particles leads to a Riemann problem, whose approximate solution derived by means of an acoustic Riemann solver. For this reason, artificial user-defined stabilisation parameters typically used in the classical SPH formalism can be avoided. Both spatial discretisations are accompanied by a linear reconstruction procedure to ensure second-order of

accuracy in space. In addition, Barth and Jespersen slope limiter is applied in order to avoid spurious numerical oscillations in the vicinity of sharp gradients. The overall VCFVM and SPH algorithms are shown to satisfy the discrete version of entropy dissipation law via the Coleman-Noll procedure.

In order to monotonically update the semi-discrete second-order system of equations and geometry in time, a second-order explicit one-step two-stage Total Variation Diminishing (TVD) Runge-Kutta time integrator is utilised.

In terms of computer implementation, the in-house $\{\boldsymbol{p}, \boldsymbol{F}, \boldsymbol{H}, J\}$ Upwind-SPH algorithm has been used [22]. The novel $\{\boldsymbol{p}, \boldsymbol{F}, \boldsymbol{H}, J, \eta \text{ or } E\}$ VCFVM solver, artificial compressibility algorithm and the edge-based $\{\boldsymbol{p}, \boldsymbol{F}, \boldsymbol{H}, J, \eta \text{ or } E\}$ SPH methodology are implemented from scratch in *MatLab*. In order to speed up the computation time, the numerical examples are compiled using the Application Program Interface (API) of the *MatLab* and C++ reference library.

The key contributions and novelties of this thesis are:

▷ **Continuum level**

- Introduction of a general mixed-based set $\{\boldsymbol{p}, \boldsymbol{F}, \boldsymbol{H}, J, \eta \text{ or } E\}$ of first order conservation laws in Total Lagrangian description for large strain (isothermal and/or thermo-elastic) solid dynamics.
- Derivation of advanced polyconvex (mechanical and thermo-mechanical) constitutive models.
- Introduction of a unified computational framework that can be generalised to a myriad of discretisation techniques.

▷ **Discrete level**

- Derivation and implementation of two distinct numerical methodologies for spatial discretisation, namely, the mesh-based Vertex-Centred Finite Volume Method (VCFVM) and the meshless Smooth Particle Hydrodynamics (SPH).
- The implementation of a tailor-made artificial compressibility and an angular momentum preservation algorithms suitably adapted to both VCFVM and SPH numerical schemes.
- Derivation of a Riemann-based upwinding stabilisation for the both VCFVM and SPH algorithms in Total Lagrangian framework. Notice that the nature of this type of stabilisation does not require the selection of any user-defined artificial stabilisation parameter.
- The satisfaction of local entropy production at the discrete level via a Coleman-Noll procedure for both developed VCFVM and SPH techniques.
- An edge-based implementation is carried out for the SPH method, not only reducing its computational cost but also bridging the gap with the VCFVM implementation.
- Study of the consistency and stability of the schemes for some simplified linearised cases.

## 10.2 Future outlook

The following suggestions and possibilities can be considered for the continuation of this work in future

- ***Nonlinear Riemann solver for solids:***

  In this work, the numerical fluxes are approximated on the basis of an acoustic Riemann solver. This can be further improved by adopting a more accurate (nonlinear) Riemann solver (i.e. Roe's Riemann solver) accounting for severe shocks and interactions between several materials.

- ***Constitutive models:***

  The library of the constitutive models employed in this work can be extended by including mechanical and thermo-mechanical material models such as visco-elasticity [25], visco-plasticity [26], thermo-visco-elasticity [85] and thermo-plasticity [169]. In addition, a time-dependent equation of state can be considered which involves the time needed for acceleration of the heat flow. In this case, the so-called relaxation time is introduced to account for the time-lag needed to establish a steady-state heat conduction [75]. This requires the theory of the generalised thermo-elasticity and a different representation of the discretised system of equations [75, 76].

- ***Fluid-Structure Interaction:***

  The promising presented framework can be extended to the case of tackling multi-physics applications such as Fluid-Structure Interaction (FSI) where a deformable structure interacting with an internal or surrounding fluid flow. Consideration of FSI is essential in the design of many engineering applications (e.g. aircraft, engines, bridges, etc) and to account for biomedical problems (e.g. aneurysms). In this case, an alternative Arbitrary Lagrangian-Eulerian (ALE) description of motion can be used [243, 244].

- ***Application in mechanobiology:***

  Nowadays, the applicability of the computational mechanics is very well accepted in the field of biomechanics as it is applied from the small scale of the molecular simulations up to the cardiovascular and musculoskeletal systems. As an example, the arterial wall exhibit a thermo-elastic behaviour similar to that of rubber [245]. Therefore, the current developed work has great potential to be applied in those type of applications.

- ***Computational efficiency:*** Although the implementation of the presented numerical algorithms are efficiently carried out in Matlab, they can be further computationally enhanced by using more basic computer programming languages (i.e. C or C++) in order to be potentially re-developed in open-source software (e.g. OpenFOAM). This, in conjunction with parallelisation of the numerical algorithm, can potentially lead to the capability of tackling real-life engineering problems.

- ***Dynamic fracture:*** An interesting application can be dynamic fracture where the role of material inertia in fracture phenomena becomes significant. In this case, the crack

initiation/propagation and, also, the transient driving forces acting on the crack can be accurately captured and determined by means of Riemann solver in the contact between cells/particles. Using SPH algorithm, it would be also interesting to utilise a variable smoothing length. This way, an anisotropic compact support can be introduce for the kernel interpolation function in order to approximate the solution in the region of interest in a more efficient manner.

# Part VI

# Appendices

Appendix A

# Mathematical preliminaries

The objective of this section is to introduce some basic mathematical concepts and notation used throughout this thesis.

## A.1 Scalar, vector and tensor

A scalar can be considered as an element of a field with a magnitude which is used to define a vector space [14, 28].

Vectors are quantities with a magnitude and a direction and can be mathematically presented as [14]

$$\boldsymbol{a} = \sum_{I=1}^{3} a_I \boldsymbol{E}_I. \tag{A.1}$$

where $a_I$ are the three components of the vector and $\{\boldsymbol{E}_1, \boldsymbol{E}_2, \boldsymbol{E}_3\}$ is the set of vectors that form an orthonormal basis (i.e. Cartesian coordinate).

A tensor can be defined as an algebraic object that describes a linear transformation (mapping) from one algebraic object to another [14]. A tensor can take different forms on the basis of its order. For instance, the second-order tensor $\boldsymbol{A}$ is a linear mapping that associates a given vector $\boldsymbol{a}$ to vector $\boldsymbol{b}$ as

$$\boldsymbol{a} = \boldsymbol{A}\boldsymbol{b}. \tag{A.2}$$

and it can be mathematically represented as

$$\boldsymbol{A} = \sum_{I,J=1}^{3} A_{IJ} \boldsymbol{E}_I \otimes \boldsymbol{E}_J. \tag{A.3}$$

with $\boldsymbol{E}_{I,J}$ considered as the unit normal vector and $\{I, J = 1, 2, 3\}$. A simple mathematical example of a second-order tensor is the identity tensor which maps a vector onto itself as

$$\boldsymbol{a} = \boldsymbol{I}\boldsymbol{a}. \tag{A.4}$$

To give a physical example of a second-order tensor, the Cauchy stress tensor $\boldsymbol{\sigma}$ that takes a unit normal vector $\boldsymbol{n}$ of a plane and map (transform) the stress into a force (traction) $\boldsymbol{t}$ on that plane

$$\boldsymbol{t} = \boldsymbol{\sigma}\boldsymbol{n}. \tag{A.5}$$

It is worthwhile noting that a zeroth-order tensor is a scalar and a first-order tensor is a vector.

## A.2 Mathematical operators

### A.2.1 Multiplications

The dyadic or tensor product of two given vectors ($\boldsymbol{a}$ and $\boldsymbol{b}$) yield a second-order tensor ($\boldsymbol{A}$) and mathematically is defined as [14]

$$\boldsymbol{A} = \left(\sum_{I=1}^{3} a_I \boldsymbol{E}_I\right) \otimes \left(\sum_{J=1}^{3} b_J \boldsymbol{E}_J\right) = \sum_{I,J=1}^{3} \underbrace{a_I b_J}_{A_{IJ}} (\boldsymbol{E}_I \otimes \boldsymbol{E}_I)\,. \tag{A.6}$$

The scalar or dot product of two given vectors ($\boldsymbol{a}$ and $\boldsymbol{b}$) will result in a scalar and can be mathematically presented as

$$\boldsymbol{a} \cdot \boldsymbol{b} = \left(\sum_{I=1}^{3} a_I \boldsymbol{E}_I\right) \cdot \left(\sum_{J=1}^{3} b_J \boldsymbol{E}_J\right) \tag{A.7}$$

$$= \sum_{I,J=1}^{3} a_I b_J \underbrace{(\boldsymbol{E}_I \cdot \boldsymbol{E}_J)}_{\delta_{IJ}} = a_1 b_1 + a_2 b_2 + a_3 b_3. \tag{A.8}$$

with $\delta_{IJ}$ as the Kronecker delta defined as

$$\delta_{IJ} = \begin{cases} 1 & \text{if } I = J, \\ 0 & \text{if } I \neq J. \end{cases} \tag{A.9}$$

Similar to the dot product of two vectors, the double product or double contraction of two given tensors ($\boldsymbol{A}$ and $\boldsymbol{B}$) gives a scalar and reads

$$\boldsymbol{A} : \boldsymbol{B} = \left(\sum_{I,J=1}^{3} A_{IJ} \boldsymbol{E}_I \otimes \boldsymbol{E}_J\right) : \left(\sum_{M,N=1}^{3} B_{MN} \boldsymbol{E}_M \otimes \boldsymbol{E}_N\right) \tag{A.10}$$

$$= \sum_{I,J=1}^{3} \sum_{M,N=1}^{3} A_{IJ} B_{MN} \delta_{IJ} \delta_{MN} = \sum_{I,J=1}^{3} A_{IJ} B_{IJ}. \tag{A.11}$$

The cross product of two vectors ($\boldsymbol{a}$ and $\boldsymbol{b}$) renders a vector and introduced as

$$\boldsymbol{a}\times\boldsymbol{b}=\sum_{I=1}^{3}\sum_{J=1}^{3}\sum_{K=1}^{3}\epsilon_{IJK}\boldsymbol{E}_I a_J b_K=\begin{vmatrix}\boldsymbol{E}_1 & \boldsymbol{E}_2 & \boldsymbol{E}_3\\ a_1 & a_2 & a_3\\ b_1 & b_2 & b_3\end{vmatrix}. \tag{A.12}$$

with $\epsilon_{IJK}$ as the permutation (Levi-Civita) symbol defined as [28]

$$\epsilon_{IJK}=\boldsymbol{E}_I\cdot(\boldsymbol{E}_J\times\boldsymbol{E}_K), \tag{A.13}$$

where

$$\begin{cases}\epsilon_{IJK} &= 1 \qquad \text{if } I,J,K=1,2,3 \text{ (cyclic order)}\\ \epsilon_{IJK} &= 0 \qquad \text{if } I=J \text{ or } J=K \text{ or } I=K\\ \epsilon_{IJK} &= -1 \qquad \text{if } I,J,K=1,3,2 \text{ (anti cyclic order)}\end{cases} \tag{A.14}$$

### A.2.2 Gradient, divergence and curl

The material gradient operator of a quantity is defined as [14]

$$\text{GRAD}\,([\bullet])=\boldsymbol{\nabla}_R\,([\bullet])=\frac{\partial[\bullet]}{\partial X_I}\otimes\boldsymbol{E}_I. \tag{A.15}$$

where $I=\{1,2,3\}$, $([\bullet])$ as representative of a tensor with order $\{0,1,2,3,..\}$ and $\boldsymbol{\nabla}_R$ is the material differential operator. By consideration of the tensor product feature, it is evident that the gradient operator increases the order of a tensor by one order of magnitude.

The material divergence operator of a quantity can be expressed as [14]

$$\text{DIV}\cdot([\bullet])=\boldsymbol{\nabla}_R\cdot([\bullet])=\frac{\partial[\bullet]}{\partial X_I}\cdot\boldsymbol{E}_I. \tag{A.16}$$

This shows the divergence operator decrease the order of a tensor by one order of magnitude.

The curl of a second-order tensor is defined as

$$\text{CURL}\times([\bullet])=\boldsymbol{\nabla}_R\times([\bullet])=\epsilon_{IJK}\frac{\partial[\bullet]_{iK}}{\partial X_J}. \tag{A.17}$$

where $\epsilon_{IJK}$ is introduced at Eq. (A.14).

### A.2.3 Tensor cross product

The tensor cross product between two second-order tensors ($\boldsymbol{A}$ and $\boldsymbol{B}$) can be defined as follows [3, 185]

$$[\boldsymbol{A}\times\boldsymbol{B}] = \begin{bmatrix} [\boldsymbol{A}\times\boldsymbol{B}]_{xX} & [\boldsymbol{A}\times\boldsymbol{B}]_{xY} & [\boldsymbol{A}\times\boldsymbol{B}]_{xZ} \\ [\boldsymbol{A}\times\boldsymbol{B}]_{yX} & [\boldsymbol{A}\times\boldsymbol{B}]_{yY} & [\boldsymbol{A}\times\boldsymbol{B}]_{yZ} \\ [\boldsymbol{A}\times\boldsymbol{B}]_{zX} & [\boldsymbol{A}\times\boldsymbol{B}]_{zY} & [\boldsymbol{A}\times\boldsymbol{B}]_{zZ} \end{bmatrix} \tag{A.18}$$

where the resultant tensor components are defined as

$$\begin{aligned}
[\boldsymbol{A}\times\boldsymbol{B}]_{xX} &= A_{yY}B_{zZ} - A_{yZ}B_{zY} + A_{zZ}B_{yY} - A_{zY}B_{yZ} \\
[\boldsymbol{A}\times\boldsymbol{B}]_{xY} &= A_{yZ}B_{zX} - A_{yX}B_{zZ} + A_{zX}B_{yZ} - A_{zZ}B_{yX} \\
[\boldsymbol{A}\times\boldsymbol{B}]_{xZ} &= A_{yX}B_{zY} - A_{yY}B_{zX} + A_{zY}B_{yX} - A_{zX}B_{yY} \\
[\boldsymbol{A}\times\boldsymbol{B}]_{yX} &= A_{xZ}B_{zY} - A_{xY}B_{zZ} + A_{zY}B_{xZ} - A_{zZ}B_{xY} \\
[\boldsymbol{A}\times\boldsymbol{B}]_{yY} &= A_{zZ}B_{xX} - A_{zX}B_{xZ} + A_{xX}B_{zZ} - A_{xZ}B_{zX} \\
[\boldsymbol{A}\times\boldsymbol{B}]_{yZ} &= A_{zX}B_{xY} - A_{zY}B_{xX} + A_{xY}B_{zX} - A_{xX}B_{zY} \\
[\boldsymbol{A}\times\boldsymbol{B}]_{zX} &= A_{xY}B_{yZ} - A_{xZ}B_{yY} + A_{yZ}B_{xY} - A_{yY}B_{xZ} \\
[\boldsymbol{A}\times\boldsymbol{B}]_{zY} &= A_{xZ}B_{yX} - A_{xX}B_{yZ} + A_{yX}B_{xZ} - A_{yZ}B_{xX} \\
[\boldsymbol{A}\times\boldsymbol{B}]_{zZ} &= A_{xX}B_{yY} - A_{xY}B_{yX} + A_{yY}B_{xX} - A_{yX}B_{xY}
\end{aligned} \tag{A.19}$$

with $\boldsymbol{U}$ and $\boldsymbol{u}$ representing material and spatial vectors, respectively. In addition, the tensor cross product between a second-order tensor ($\boldsymbol{A}$) and a spatial or material vector ($\boldsymbol{u}$ or $\boldsymbol{U}$) can be defined as

$$[\boldsymbol{u}\times\boldsymbol{A}] = \begin{bmatrix} u_yA_{zX} - u_zA_{yX} & u_yA_{zY} - u_zA_{yY} & u_yA_{zZ} - u_zA_{yZ} \\ u_zA_{xX} - u_xA_{zX} & u_zA_{xY} - u_xA_{zY} & u_zA_{xZ} - u_xA_{zZ} \\ u_xA_{yX} - u_yA_{xX} & u_xA_{yY} - u_yA_{xY} & u_xA_{yZ} - u_yA_{xZ} \end{bmatrix} \tag{A.20a}$$

(A.20b)

$$[\boldsymbol{A}\times\boldsymbol{U}] = \begin{bmatrix} A_{xY}U_Z - A_{xZ}U_Y & A_{xZ}U_X - A_{xX}U_Z & A_{xX}U_Y - A_{xY}U_X \\ A_{yY}U_Z - A_{yZ}U_Y & A_{yZ}U_X - A_{yX}U_Z & A_{yX}U_Y - A_{yY}U_X \\ A_{zY}U_Z - A_{zZ}U_Y & A_{zZ}U_X - A_{zX}U_Z & A_{zX}U_Y - A_{zY}U_X \end{bmatrix} \tag{A.20c}$$

The following properties are satisfied using the presented tensor cross product

$$\boldsymbol{I} \times \boldsymbol{I} = 2\boldsymbol{I} \tag{A.21}$$

$$\boldsymbol{A} \times \boldsymbol{I} = (\mathrm{tr}\boldsymbol{A})\, \boldsymbol{I} - \boldsymbol{A}^T \tag{A.22}$$

$$\mathrm{Cof}\boldsymbol{A} = \frac{1}{2}\boldsymbol{A} \times \boldsymbol{A} \tag{A.23}$$

$$(\boldsymbol{A} \times \boldsymbol{A}) : \boldsymbol{A} = 6\ \det\boldsymbol{A} \tag{A.24}$$

$$\boldsymbol{A} \times \boldsymbol{B} = \boldsymbol{B} \times \boldsymbol{A} \tag{A.25}$$

$$\boldsymbol{A} \times \boldsymbol{B} = \boldsymbol{A}^T \times \boldsymbol{B}^T \tag{A.26}$$

$$S\,(\boldsymbol{A} \times \boldsymbol{B}) = (S\boldsymbol{A}) \times \boldsymbol{B} = \boldsymbol{A} \times (S\boldsymbol{B}) \tag{A.27}$$

$$\boldsymbol{A} \times (\boldsymbol{B} + \boldsymbol{C}) = \boldsymbol{A} \times \boldsymbol{B} + \boldsymbol{A} \times \boldsymbol{C} \tag{A.28}$$

$$(\boldsymbol{A}\boldsymbol{C}) \times (\boldsymbol{B}\boldsymbol{C}) = (\boldsymbol{A} \times \boldsymbol{B})\,(\mathrm{Cof}\boldsymbol{C}) \tag{A.29}$$

$$\boldsymbol{A} \times (\boldsymbol{v} \otimes \boldsymbol{V}) = -\boldsymbol{v} \times \boldsymbol{A} \times \boldsymbol{V} \tag{A.30}$$

$$\boldsymbol{v} \times (\boldsymbol{A} \times \boldsymbol{V}) = (\boldsymbol{v} \times \boldsymbol{A}) \times \boldsymbol{V} = \boldsymbol{v} \times \boldsymbol{A} \times \boldsymbol{V} \tag{A.31}$$

$$(\boldsymbol{A} \times \boldsymbol{B}) : \boldsymbol{C} = (\boldsymbol{B} \times \boldsymbol{C}) : \boldsymbol{A} + (\boldsymbol{A} \times \boldsymbol{C}) : \boldsymbol{B} \tag{A.32}$$

$$(\boldsymbol{v} \otimes \boldsymbol{V}) \times (\boldsymbol{u} \otimes \boldsymbol{U}) = (\boldsymbol{v} \times \boldsymbol{u}) \otimes (\boldsymbol{V} \times \boldsymbol{U}) \tag{A.33}$$

$$(\boldsymbol{A} \times \boldsymbol{B})\,(\boldsymbol{V} \times \boldsymbol{U}) = (\boldsymbol{A}\boldsymbol{V}) \times (\boldsymbol{B}\boldsymbol{U}) + (\boldsymbol{B}\boldsymbol{V}) \times (\boldsymbol{A}\boldsymbol{U}) \tag{A.34}$$

Appendix B

# Riemann solver: Physical boundaries

The aim of this section is to introduce interface contact fluxes at the physical boundaries using a Riemann-based approach. This can be achieved by providing appropriate values in Eq. (4.19), depending on the type of boundary condition (see Figure B.1).

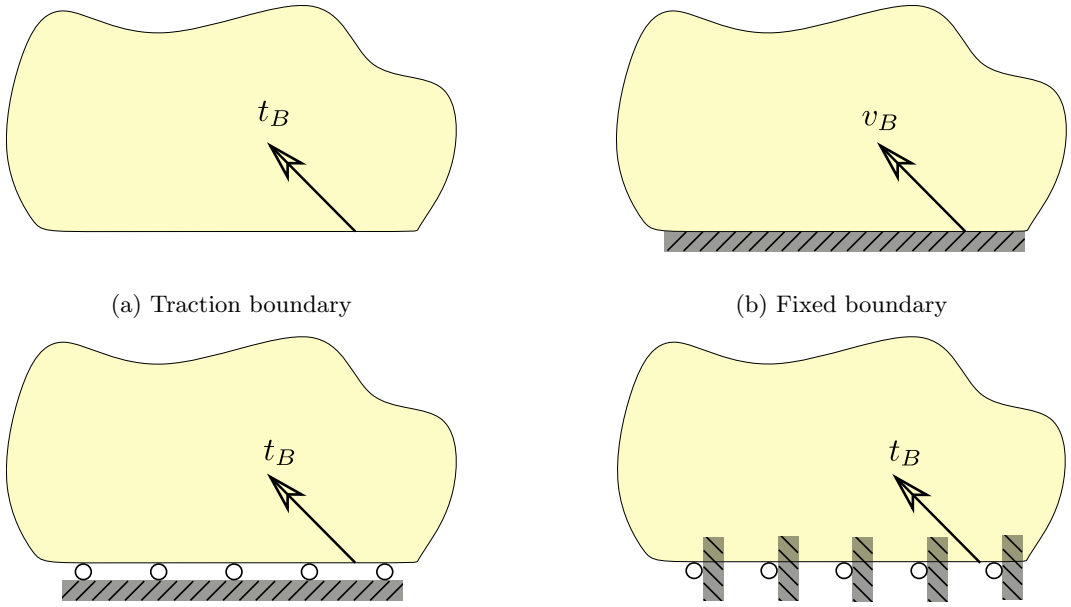


(a) Traction boundary

(b) Fixed boundary

(c) Symmetric boundary

(d) Skew-symmetric boundary

Figure B.1: Schematic representation of (a) traction; (b) fixed (clamped); (c) symmetric (tangentially sliding); and (d) skew-symmetric (normally sliding) boundary conditions

## B.1 Traction boundary

In the case of traction (Neumann) boundary condition, depicted in Figure B.1a, the wave speeds and traction in the outer domain read

$$\boldsymbol{t}^{+} = \boldsymbol{t}_B; \qquad c_p^{+} = c_s^{+} = 0, \tag{B.1}$$

with $\boldsymbol{t}_B$ as the applied force on the physical boundary. Replacing these values into Eq. (4.19) yields

$$\begin{aligned} \boldsymbol{p}^C &= \boldsymbol{p}^{-} + \boldsymbol{S}^{\boldsymbol{t}} \left(\boldsymbol{t}_B - \boldsymbol{t}^{-}\right); \\ \boldsymbol{t}^C &= \boldsymbol{t}_B. \end{aligned} \tag{B.2}$$

Notice that for a free boundary condition $\boldsymbol{t}_B = \boldsymbol{0}$.

## B.2 Fixed boundary

Considering a fixed (clamped) boundary condition, depicted in Figure B.1b, no deformation (e.g. displacement) is allowed in any direction and, therefore,

$$\boldsymbol{p}^{+} = \boldsymbol{p}_B = \boldsymbol{0}; \qquad c_p^{+} = c_s^{+} \approx \infty, \tag{B.3}$$

Substituting these values into Eq. (4.19) renders

$$\begin{aligned} \boldsymbol{p}^C &= \boldsymbol{p}_B; \\ \boldsymbol{t}^C &= \boldsymbol{t}^{-} + \boldsymbol{S}^{\boldsymbol{p}} \left(\boldsymbol{p}_B - \boldsymbol{p}^{-}\right). \end{aligned} \tag{B.4}$$

## B.3 Symmetric boundary

Figure B.1c shows a symmetric, also known as roller, boundary condition where the normal displacement is prevented (zero normal velocity). This leads to

$$\boldsymbol{p}_n^{+} = \boldsymbol{0}; \qquad c_p^{+} \approx \infty; \qquad c_s^{+} = 0. \tag{B.5}$$

By the aid of Eq. (4.19) and using the above values, the contact fluxes read

$$\begin{aligned} \boldsymbol{p}^C &= (\boldsymbol{I} - \boldsymbol{n} \otimes \boldsymbol{n}) \left[\boldsymbol{p}^{-} + \frac{1}{c_s^{-}} (\boldsymbol{t}_B - \boldsymbol{t}^{-})\right]; \\ \boldsymbol{t}^C &= (\boldsymbol{n} \otimes \boldsymbol{n}) \left[\boldsymbol{t}^{-} - c_p^{-} \boldsymbol{p}^{-}\right] + (\boldsymbol{I} - \boldsymbol{n} \otimes \boldsymbol{n}) \boldsymbol{t}_B. \end{aligned} \tag{B.6}$$

## B.4 Skew-symmetric boundary

The tangential displacement is restricted in a skew-symmetric boundary condition, shown in Figure B.1d, and consequently,

$$\boldsymbol{p}_t^+ = \mathbf{0}; \qquad c_p^+ = 0; \qquad c_s^+ \approx \infty. \tag{B.7}$$

Using these values reduce Eq. (4.19) into

$$\begin{aligned} \boldsymbol{p}^C &= (\boldsymbol{n} \otimes \boldsymbol{n}) \left[ \boldsymbol{p}^- + \frac{1}{c_s^-} (\boldsymbol{t}_B - \boldsymbol{t}^-) \right]; \\ \boldsymbol{t}^C &= (\boldsymbol{n} \otimes \boldsymbol{n}) \boldsymbol{t}_B + (\boldsymbol{I} - \boldsymbol{n} \otimes \boldsymbol{n}) \left[ \boldsymbol{t}^- - c_p^- \boldsymbol{p}^- \right]. \end{aligned} \tag{B.8}$$

Appendix C

# VCFVM ARTIFICIAL COMPRESSIBILITY ALGORITHM

Following the VCFVM discretisation procedure presented in Section 4.3, and the artificial compressibility algorithm introduced in Section 5.6, the predictor step of the mixed-based system $\{\boldsymbol{p}, \boldsymbol{F}, \boldsymbol{H}, p\}$ reads

$$\Omega_R^a \left[\frac{\boldsymbol{p}_a^{\text{int}} - \boldsymbol{p}_a^n}{\Delta t}\right] = \sum_{b\in\Lambda_a} \boldsymbol{P}^{\text{Ave},n} \boldsymbol{C}_{ab} + \sum_{\gamma\in\Gamma_a^B} \boldsymbol{t}_a^{\gamma,n} \|\boldsymbol{C}^\gamma\| + \Omega_R^a \boldsymbol{f}_R^{a,n} + \boldsymbol{\mathcal{D}}(\boldsymbol{p}_a^n); \tag{C.1a}$$

$$\Omega_R^a \left[\frac{\boldsymbol{F}_a^{n+1} - \boldsymbol{F}_a^n}{\Delta t}\right] = \sum_{b\in\Lambda_a} \frac{1}{\rho_R} \boldsymbol{p}^{\text{Ave},n} \otimes \boldsymbol{C}_{ab} + \sum_{\gamma\in\Gamma_a^B} \frac{1}{\rho_R} \boldsymbol{p}_a^{\gamma,n} \otimes \boldsymbol{C}^\gamma; \tag{C.1b}$$

$$\Omega_R^a \left[\frac{\boldsymbol{H}_a^{n+1} - \boldsymbol{H}_a^n}{\Delta t}\right] = \boldsymbol{F}_a^n \times \left( \sum_{b\in\Lambda_a} \frac{1}{\rho_R} \boldsymbol{p}^{\text{Ave},n} \otimes \boldsymbol{C}_{ab} + \sum_{\gamma\in\Gamma_a^B} \frac{1}{\rho_R} \boldsymbol{p}_a^{\gamma,n} \otimes \boldsymbol{C}^\gamma \right); \tag{C.1c}$$

$$\Omega_R^a \left[\frac{p_a^{\text{int}} - p_a^n}{\tilde{\kappa}\Delta t}\right] = \boldsymbol{H}_a^n : \left( \sum_{b\in\Lambda_a} \frac{1}{\rho_R} \boldsymbol{p}^{\text{Ave},n} \otimes \boldsymbol{C}_{ab} + \sum_{\gamma\in\Gamma_a^B} \frac{1}{\rho_R} \boldsymbol{p}_a^{\gamma,n} \otimes \boldsymbol{C}^\gamma \right) + \mathcal{D}(J_a^n). \tag{C.1d}$$

where $\{\boldsymbol{\mathcal{D}}(\boldsymbol{p}_a), \mathcal{D}(J_a)\}$ are the upwinding stabilisation terms, already defined in Section 4.3.2. In addition, the corrector step of the discrete system $\{\boldsymbol{p}, \boldsymbol{F}, \boldsymbol{H}, p\}$ renders

$$\Omega_R^a \frac{d\boldsymbol{p}_a}{d\tau} = \frac{1}{2} \sum_{b\in\Lambda_a} \left[ \left(p_b^{n+1} - p_b^n\right) \boldsymbol{H}_b^n \right] \boldsymbol{C}_{ab} - \Omega_R^a \frac{\left(\boldsymbol{p}_a^{n+1} - \boldsymbol{p}_a^{\text{int}}\right)}{\Delta t}; \tag{C.2a}$$

$$\frac{\Omega_R^a}{\gamma} \frac{dp_a}{d\tau} = \frac{\Omega_R^a}{\tilde{\kappa}} \frac{p_a^{\text{int}} - p_a^n}{\Delta t} - \frac{\Omega_R^a}{\kappa} \frac{\left(p_a^{n+1} - p_a^n\right)}{\Delta t} + \frac{1}{2} \boldsymbol{H}_a^n : \sum_{b\in\Lambda_a^b} \left( \frac{\boldsymbol{p}_b^{n+1}}{\rho_R} - \frac{\boldsymbol{p}_b^n}{\rho_R} \right) \otimes \boldsymbol{C}_{ab}. \tag{C.2b}$$

At each time step $\Delta t$, above system (C.2) is iteratively solved for the linear momentum and pressure within the pseudo time integration in order to obtain convergence to a pseudo steady state (e.g. $\frac{d\boldsymbol{p}_a}{d\tau} \approx \boldsymbol{0}$ and $\frac{dp_a}{d\tau} \approx 0$).

**Iteration speed-up procedure**

An additional Laplacian (or harmonic) dissipative operator can be incorporated to equation (C.2b), aimed at accelerating the speed of convergence within the iterative process of the correction step as

$$\frac{\Omega_R^a}{\gamma}\frac{dp_a}{d\tau} = \frac{\Omega_R^a}{\tilde{\kappa}}\frac{p_a^{\text{int}} - p_a^n}{\Delta t} - \frac{\Omega_R^a}{\kappa}\frac{\left(p_a^{n+1} - p_a^n\right)}{\Delta t} + \frac{1}{2}\boldsymbol{H}_a^n : \sum_{b\in\Lambda_a^b}\left(\frac{\boldsymbol{p}_b^{n+1}}{\rho_R} - \frac{\boldsymbol{p}_b^n}{\rho_R}\right)\otimes\boldsymbol{C}_{ab} + \mathcal{D}_{\text{PSE}}(p_a). \tag{C.3}$$

where the discrete Laplacian viscosity operator is defined as

$$\mathcal{D}_{\text{PSE}}(p_a) := \alpha_{\mathcal{D}}\frac{c_s^2\Delta t}{\mu}\sum_{b\in\Lambda_a}\left[\frac{p_b - p_a}{\|\boldsymbol{X}_b - \boldsymbol{X}_a\|}\boldsymbol{N}_{ab}\right]\cdot\boldsymbol{C}_{ab}, \tag{C.4}$$

Here $\alpha_{\mathcal{D}}$ is a dimensionless user-defined parameter in the range of $[0, 1]$. Above dissipative operator automatically ensures fulfillment of the global conservation requirement, that is $\sum_a \Omega_R^a \mathcal{D}_{\text{PSE}}(p_a) = 0$. It is also worth recalling that the viscosity operator $\mathcal{D}_{\text{PSE}}(p_a)$ is added to Eq. (C.3) with the only purpose of accelerating the speed of convergence within the pseudo-time integration process in correction step. This is in clear contrast to the upwinding stabilisation terms $\{\boldsymbol{\mathcal{D}}(\boldsymbol{p}_a), \mathcal{D}(J_a)\}$ introduced in the predictor step Eq. (C.1), necessary to guarantee the robustness (ovreall stability) of the algorithm.

Appendix D

# Discrete angular momentum preserving algorithm

It is mentioned earlier in Chapter 6 that the proposed numerical algorithms do not necessarily ensure the conservation of angular momentum of the system. This is due to the fact that the minors of the deformation gradient tensor, namely, $\{\boldsymbol{F}, \boldsymbol{H}, J\}$, are no longer computed on the basis of the material gradient of a current geometry (e.g. $\boldsymbol{F} \neq \boldsymbol{F}_{\boldsymbol{x}} := \boldsymbol{\nabla}_0 \boldsymbol{x}$, $\boldsymbol{H} \neq \boldsymbol{H}_{\boldsymbol{x}} := \frac{1}{2}\boldsymbol{F}_{\boldsymbol{x}} \times \boldsymbol{F}_{\boldsymbol{x}}$, $J \neq J_{\boldsymbol{x}} := \frac{1}{6}\boldsymbol{F}_{\boldsymbol{x}} : (\boldsymbol{F}_{\boldsymbol{x}} \times \boldsymbol{F}_{\boldsymbol{x}})$) [3].

To rectify this, and taking inspiration from the work of [6], this section is aimed at presenting a global least-square angular momentum projection procedure. Specifically, the local internal nodal force $\boldsymbol{T}_a$, presented in Eq. (D.1) and, is modified (in a least-square sense) in order to conserve the total angular momentum, whilst still ensuring the global preservation of linear momentum. The internal force for the VCFVM scheme can be expressed as

$$\boldsymbol{T}_a = \sum_{b \in \Lambda_a} \boldsymbol{t}^C \|\boldsymbol{C}_{ab}\|. \tag{D.1}$$

Moreover, the internal forces for the SPH scheme are already presented in Eq. (5.31c). Sufficient conditions for the global preservation of the discrete linear and angular momentum within a time step are enforced at each stage of the one-step two-stage Runge–Kutta time integrator (6.1-6.3) described as

$$\sum_a \Omega_R^a \boldsymbol{T}_a^{\mathcal{X}} = \boldsymbol{0}; \qquad \sum_a \Omega_R^a \mathscr{X}_a \times \boldsymbol{T}_a^{\mathcal{X}} = \boldsymbol{0}. \tag{D.2}$$

where

$$\mathscr{X}_a = \begin{cases} \boldsymbol{x}_a^n, & \text{if } \mathcal{X} = n, \\ \boldsymbol{x}_a^n + \frac{\Delta t}{2\rho_R}\left(\boldsymbol{p}_a^n + \boldsymbol{p}_a^\star\right), & \text{if } \mathcal{X} = \star. \end{cases} \tag{D.3}$$

A least-square minimisation procedure is used to obtain a modified set of internal nodal forces $\hat{\boldsymbol{T}}_a$ that satisfy the conditions introduced in Eq. (D.2). This can be achieved by computing the

minimum of the following functional [6, 118] (ignoring time arguments for brevity)

$$\mathit{\Pi}\left(\hat{\boldsymbol{T}}_a, \boldsymbol{\lambda}_{\text{ang}}, \boldsymbol{\lambda}_{\text{lin}}\right) = \frac{1}{2}\sum_a \Omega_R^a \left(\hat{\boldsymbol{T}}_a - \boldsymbol{T}_a\right) \cdot \left(\hat{\boldsymbol{T}}_a - \boldsymbol{T}_a\right) \tag{D.4}$$

$$- \boldsymbol{\lambda}_{\text{ang}} \cdot \left(\sum_a \Omega_R^a \mathscr{X}_a \times \hat{\boldsymbol{T}}_a\right) - \boldsymbol{\lambda}_{\text{lin}} \cdot \left(\sum_a \Omega_R^a \hat{\boldsymbol{T}}_a\right). \tag{D.5}$$

After some simple algebra, a modified set of internal nodal forces $\hat{\boldsymbol{T}}_a$ arise

$$\hat{\boldsymbol{T}}_a = \boldsymbol{T}_a + \boldsymbol{\lambda}_{\text{ang}} \times \mathscr{X}_a + \boldsymbol{\lambda}_{\text{lin}}. \tag{D.6}$$

The Lagrange multipliers $\{\boldsymbol{\lambda}_{\text{ang}}, \boldsymbol{\lambda}_{\text{lin}}\}$ are the solutions of the following system of equations

$$\begin{bmatrix} \boldsymbol{\lambda}_{\text{ang}} \\ \boldsymbol{\lambda}_{\text{lin}} \end{bmatrix} = \begin{bmatrix} \sum_a \Omega_R^a \left[(\mathscr{X}_a \cdot \mathscr{X}_a)\boldsymbol{I} - \mathscr{X}_a \otimes \mathscr{X}_a\right] & \sum_a \Omega_R^a \hat{\mathscr{X}}_a \\ \sum_a \Omega_R^a \hat{\mathscr{X}}_a & -\sum_a \Omega_R^a \end{bmatrix}^{-1} \begin{bmatrix} -\sum_a \Omega_R^a \mathscr{X}_a \times \boldsymbol{T}_a \\ \sum_a \Omega_R^a \boldsymbol{T}_a \end{bmatrix}, \tag{D.7}$$

with the indicial notation $\left[\hat{\mathscr{X}}_a\right]_{ik} = \mathcal{E}_{ijk}\left[\mathscr{X}_a\right]_j$. In addition, an extra condition must be added for the satisfaction of the global angular momentum preservation, namely,

$$\sum_a \Omega_R^a \boldsymbol{\mathcal{D}}(\boldsymbol{p}_a) = \boldsymbol{0}; \qquad \sum_a \Omega_R^a \mathscr{X}_a \times \boldsymbol{\mathcal{D}}(\boldsymbol{p}_a) = \boldsymbol{0}. \tag{D.8}$$

Similarly to the least-square minimisation procedure described above, a set of modified upwinding dissipation terms can now be obtained by replacing $\{\hat{\boldsymbol{T}}_a, \boldsymbol{T}_a, \boldsymbol{\lambda}_{\text{ang}}, \boldsymbol{\lambda}_{\text{lin}}\}$ in Eq. (D.6) and Eq. (D.7) with $\{\hat{\boldsymbol{\mathcal{D}}}(\boldsymbol{p}_a), \boldsymbol{\mathcal{D}}(\boldsymbol{p}_a), \boldsymbol{\mu}_{\boldsymbol{\mathcal{D}}_{\boldsymbol{p}}}, \boldsymbol{\lambda}_{\boldsymbol{\mathcal{D}}_{\boldsymbol{p}}}\}$.

Appendix E

# Alternative descriptions of the formulations

The main objective of this section is to alternatively describe the mixed-based system of conservation laws, expressed in Chapter 2, Eq. (2.58), in two other descriptions, namely, Updated Lagrangian and Eulerian formalisms. It is first useful to recall the Total Lagrangian form of conservation law

$$\frac{d}{dt}\int_{\Omega_R} \boldsymbol{\mathcal{U}}\, d\Omega_R + \int_{\partial\Omega_R} \boldsymbol{\mathcal{F}}_{\boldsymbol{N}}\, dA = \int_{\Omega_R} \boldsymbol{\mathcal{S}}\, d\Omega_R. \tag{E.1}$$

where $\boldsymbol{\mathcal{U}}$ stands for a set of conservation variables, $\boldsymbol{\mathcal{F}}_{\boldsymbol{N}}$ represents their corresponding flux vectors and $\boldsymbol{\mathcal{S}}$ is the set of possible source terms [3].

## E.1 Updated Lagrangian

In order to obtain the Updated Lagrangian description of the formulations, it is possible to push forward the integral form of the conservation law formulation presented in Eq. (E.1). To achieve this, the application of Nanson's rule and volume mapping transformation are required

$$\boldsymbol{N}dA = \boldsymbol{H}^{-1}\boldsymbol{n}da \tag{E.2a}$$

$$d\Omega_R = J^{-1}d\Omega(t). \tag{E.2b}$$

Application of Eq. (E.2) into Eq. (E.1) leads to the integral form of the Updated Lagrangian formalism as

$$\frac{d}{dt}\int_{\Omega(t)} \mathbf{U}\, d\Omega = \int_{\partial\Omega(t)} \mathbf{F}_{\boldsymbol{n}}\, da + \int_{\Omega(t)} \mathbf{S}\, d\Omega, \tag{E.3}$$

with

$$\mathbf{U} := J^{-1}\boldsymbol{\mathcal{U}}; \qquad \mathbf{F}_{\boldsymbol{n}} := \sum_{i=1}^{3} \left(\boldsymbol{H}^{-T}\boldsymbol{\mathcal{F}}\right)_i n_i; \qquad \mathbf{S} := J^{-1}\boldsymbol{\mathcal{S}}, \tag{E.4}$$

and where $\boldsymbol{n}$ represents the spatial outward unit normal vector on a moving boundary surface $\partial\Omega(t)$. Subsequently, a representation of the strong form of the formulations are expressed here

in an Updated Lagrangian description as follows

$$\rho \frac{\partial \boldsymbol{v}}{\partial t} = \operatorname{div}(\boldsymbol{\sigma}) + \boldsymbol{f}; \tag{E.5a}$$

$$\frac{\partial \boldsymbol{F}}{\partial t} = J \operatorname{div}\left(\boldsymbol{v} \otimes \boldsymbol{H}^{-1}\right); \tag{E.5b}$$

$$\frac{\partial J}{\partial t} = J \operatorname{div}(\boldsymbol{v}); \tag{E.5c}$$

$$\frac{\partial \boldsymbol{H}}{\partial t} = J \operatorname{div}\left(\boldsymbol{F} \times \left(\boldsymbol{v} \otimes \boldsymbol{H}^{-1}\right)\right); \tag{E.5d}$$

$$\frac{\partial E}{\partial t} = J \operatorname{div}(\boldsymbol{\sigma}\boldsymbol{v} - \boldsymbol{q}) + \boldsymbol{f} \cdot \boldsymbol{v} + s. \tag{E.5e}$$

Here $\rho = J^{-1}\rho_R$ denotes the spatial density, $\boldsymbol{q} = \boldsymbol{H}^{-T}\boldsymbol{Q}$ stands for spatial heat flux vector, $\boldsymbol{f} = J^{-1}\boldsymbol{f}_R$ and $s = J^{-1}s_R$ are the body force and the heat source term per unit of deformed volume.

## E.2 Eulerian

The Eulerian description of the mixed-based system of equations can be expressed by the aid of Reynolds transport theorem. This theorem helps to represents the formulations with respect to a fixed domain (e.g. control volume) instead of a moving domain and that yields the introduction of convective fluxes along the boundaries of the fixed domain. The principal difference between a Lagrangian and Eulerian description is already explored in Section 2.2.2.

Applying the Reynolds transport theorem on the left hand side of Eq. (E.3) reads

$$\frac{d}{dt}\int_{\Omega(t)} \mathbf{U}\, d\Omega = \int_{\Omega_f} \frac{\partial \mathbf{U}}{\partial t}\, d\Omega_f + \int_{\partial\Omega_f} (\mathbf{U} \otimes \boldsymbol{v})\, \boldsymbol{n}\, da, \tag{E.6}$$

with $\Omega_f$ representing a fixed domain coincident at the current time $t$. By substituting Eq. (E.6) in Eq. (E.3), the integral form of the conservation law formulation in Eulerian description renders

$$\int_{\Omega_f} \frac{\partial \mathbf{U}}{\partial t}\, d\Omega_f + \int_{\partial\Omega_f} (\mathbf{U} \otimes \boldsymbol{v})\, \boldsymbol{n}\, da = \int_{\partial\Omega_f} \mathbf{F}_{\boldsymbol{n}}\, da + \int_{\Omega_f} \mathbf{S}\, d\Omega_f. \tag{E.7}$$

To this end, the strong form of the mixed-based set of conservation laws is expressed in Eulerian description as

$$\frac{\partial \rho}{\partial t} + \operatorname{div}(\rho \boldsymbol{v}) = 0; \tag{E.8a}$$

$$\frac{\partial (\rho \boldsymbol{v})}{\partial t} + \operatorname{div}(\rho \boldsymbol{v} \otimes \boldsymbol{v} - \boldsymbol{\sigma}) = \boldsymbol{f}; \tag{E.8b}$$

$$\frac{\partial \left(J^{-1}\boldsymbol{F}\right)}{\partial t} + \operatorname{div}\left(J^{-1}\boldsymbol{F} \otimes \boldsymbol{v} - \boldsymbol{v} \otimes \boldsymbol{H}^{-1}\right) = \mathbf{0}; \tag{E.8c}$$

$$\frac{\partial \left(J^{-1}\boldsymbol{H}\right)}{\partial t} + \operatorname{div}\left(J^{-1}\boldsymbol{H} \otimes \boldsymbol{v} - \boldsymbol{F} \times \left(\boldsymbol{v} \otimes \boldsymbol{H}^{-1}\right)\right) = \mathbf{0}; \tag{E.8d}$$

$$\frac{\partial J^{-1}E}{\partial t} + \operatorname{div}\left(J^{-1}E\boldsymbol{v} + \boldsymbol{\sigma}\boldsymbol{v} - \boldsymbol{q}\right) + \boldsymbol{f} \cdot \boldsymbol{v} + s = 0. \tag{E.8e}$$

Notice that in the Eulerian description, the conservation of mass is not automatically satisfied anymore and, therefore, Eq. (E.8a) represents the mass continuity equation which is a replacement for the conservation of volume map in Total/Updated Lagrangian formulation.

# Bibliography


[1] T. J. Baker. Three dimensional mesh generation by triangulation of arbitrary point sets. In *AIAA 8th Computational Fluid Dynamics Conference 87-1124-CP*, 1987.

[2] R. Lohner and P. Parikh. Generation of three-dimensional unstructured grids by the advancing-front method. *International Journal of Numerical Methods in Fluids*, 8:1135–1149, 1988.

[3] J. Bonet, A. J. Gil, C. H. Lee, M. Aguirre, and R. Ortigosa. A first order hyperbolic framework for large strain computational solid dynamics. part i: Total lagrangian isothermal elasticity. *Computer Methods in Applied Mechanics and Engineering*, 283:689–732, 2015.

[4] C. H. Lee, A. J. Gil, G. Greto, S. Kulasegaram, and J. Bonet. A new Jameson-Schmidt-Turkel Smooth Particle Hdrodynamics algorithm for large strain explicit fast dynamics. *Computer Methods in Applied Mechanics and Engineering*, 311:71–111, 2016.

[5] C. H. Lee, A. J. Gil, O. I. Hassan, S. Kulasegaram, and J. Bonet. A variationally consistent Streamline Upwind Petrov Galerkin Smooth Particle Hydrodynamics algorithm for large strain solid dynamics. *Computer Methods in Applied Mechanics and Engineering*, 318:514–536, 2017.

[6] J. Haider, C. H. Lee, A. J. Gil, and J. Bonet. A first order hyperbolic framework for large strain computational solid dynamics: An upwind cell centred total lagrangian scheme. *International Journal for Numerical Methods in Engineering*, 109:407–456, 2017.

[7] M. Aguirre, A. J. Gil, J. Bonet, and C. H. Lee. An upwind vertex centred Finite Volume solver for Lagrangian solid dynamics. *Journal of Computational Physics*, 300:387–422, 2015.

[8] R. J. Leveque. *Finite Difference Methods for Ordinary and Partial Differential Equations*. SIAM, 2007.

[9] G. D. Smith. *Numerical solution of partial differential equations: finite difference methods*. Oxford University Press, third ed, 1985.

[10] R. Taylor O. Zienkiewicz. *The finite element method: fluid dynamics*. Volume 3, Butterworth-Heinemann, fifth ed, 2000.

[11] R. J. Leveque. *Finite-Volume Methods for Hyperbolic Problems*. Cambridge University Press, 2004.

[12] G. R. Gerard, R. Papirno, and H. Becker. On experimental solid dynamics. *TP336-EB Symposium on Dynamic Behavior of Materials*, 10:82–103, 1963.

[13] B. Moran K. Elkhodary T. Belytschko, W. W. Liu. *Nonlinear Finite Elements for Continua and Structures*. Wiley, 2014.

[14] J. Bonet and R. D. Wood. *Nonlinear Continuum Mechanics for Finite Element Analysis*. Cambridge University Press, 2nd edition, 2008.

[15] J. Haider. *An upwind cell centred Finite Volume Method for large strain explicit solid dynamics in OpenFOAM*. Phd thesis, Swansea University, 2018.

[16] O. I. Hassan, A. Ghavamian, C. H. Lee, A. J. Gil, J. Bonet, and F. Auricchio. An upwind vertex centred finite volume algorithm for nearly and truly incompressible explicit fast solid dynamic applications: Total and Updated Lagrangian formulations. *Journal of Computational Physics: X*, 3:100025, 2019.

[17] C. H. Lee, A. J. Gil, and J. Bonet. Development of a stabilised Petrov-Galerkin formulation for conservation laws in lagrangian fast solid dynamics. *Computer Methods in Applied Mechanics and Engineering*, 268:40–64, 2014.

[18] C. H. Lee, A. J. Gil, and J. Bonet. Development of a cell centred upwind finite volume algorithm for a new conservation law formulation in structural dynamics. *Computers and Structures*, 118: 13–38, 2013.

[19] D. P. Flanagan and T. Belytschko. A uniform strain hexahedron and quadrilateral with orthogonal hourglass control. *International Journal for Numerical Methods in Engineering*, 17:679–706, 1981.

[20] T. J. R. Hughes. *The finite element method: Linear static and dynamic finite element analysis*. Dover Publications, 2000.

[21] T. Belytschko, J. S. Ong, W. K. Liu, and J. M. Kennedy. Hourglass control in linear and nonlinear problems. *Computer Methods in Applied Mechanics and Engineering*, 43:251–276, 1984.

[22] C. H. Lee, A. J. Gil, A. Ghavamian, and J. Bonet. A Total Lagrangian upwind Smooth Particle Hydrodynamics algorithm for large strain explicit solid dynamics. *Computer Methods in Applied Mechanics and Engineering*, 344:209–250, 2019.

[23] A. J. Gil, C. H. Lee, J. Bonet, and M. Aguirre. A stabilised Petrov-Galerkin formulation for linear tetrahedral elements in compressible, nearly incompressible and truly incompressible fast dynamics. *Computer Methods in Applied Mechanics and Engineering*, 276:659–690, 2014.

[24] A. J. Gil and P. D. Ledger. A coupled *hp*-finite element scheme for the solution of two-dimensional electrostrictive materials. *International Journal for Numerical Methods in Engineering*, 91:1158–1183, 2012.

[25] X. Zeng, G. Scovazzi, N. Abboud, O. Colomés, and S. Rossi. A dynamic variational multiscale method for viscoelasticity using linear tetrahedral elements. *International Journal for Numerical Methods in Engineering*, 112:1951–2003, 2018.

[26] A. Bayliss, T. Belytschko, M. Kulkarni, and D. A. Lott-Crumpler. On the dynamics and the role of imperfections for localization in thermo-viscoplastic materials. *Modelling and Simulation in Materials Science and Engineering*, 2:941–964, 1994.

[27] W. K. Liu S. Li. *Meshfree Particle Methods*. Springer, 2007.

[28] R. Taylor O. Zienkiewicz. *The finite element method*. Volume 2, Butterworth-Heinemann, fifth ed, 2000.

[29] C. W. Shu B. Cockburn, G. E. Karniadakis. *Discontinuous Galerkin methods. Theory, computation and applications*. Springer-Verlag, 2000.

[30] M. Dumbser, D. Balsara, E. Toro, and C. Munz. A unified framework for the construction of one-step finite–volume and discontinuous galerkin schemes. *Journal of Computational Physics*, 227:8209–8253, 2008.

[31] M. Dumbser, O. Zanotti, R. Loubère, and S. Diot. A posteriori subcell limiting of the discontinuous galerkin finite element method for hyperbolic conservation laws. *Journal of Computational Physics*, 278:47–75, 2014.

[32] J. Haider, C. H. Lee, A. J. Gil, A. Huerta, and J. Bonet. A an upwind cell centred Total lagrangian finite volume algorithm for nearly incompressible explicit solid dynamic applications. *Computer Methods in Applied Mechanics and Engineering*, 340:684–727, 2018.

[33] F. M. Andrade Pires, E. A. de Souza Neto, and J. L. de la Cuesta Padilla. An assessment of the average nodal volume formulation for the analysis of nearly incompressible solids under finite strains. *Communications in Numerical Methods in Engineering*, 20:569–583, 2004.

[34] J. Bonet, H. Marriott, and O. Hassan. An averaged nodal deformation gradient linear tetrahedral element for large strain explicit dynamic applications. *Communications in Numerical Methods in Engineering*, 17:551–561, 2001.

[35] Y. Onishi and K. Amaya. A locking-free selective smoothed finite element method using tetrahedral and triangular elements with adaptive mesh rezoning for large deformation problems. *International Journal for Numerical Methods in Engineering*, 99:354–371, 2014.

[36] H. M. Hilber, T. J. R. Hughes, and R. L. Taylor. Improved numerical dissipation for time integration algorithms in structural dynamics. *Earthquake Engineering and Structural Dynamics*, 5: 283–292, 1977.

[37] W. L. Wood, M. Bossak, and O. C. Zienkiewicz. An alpha modification of Newmark's method. *International Journal for Numerical Methods in Engineering*, 15:1562–1566, 1980.

[38] K. Washizu. *Variational Methods in Elasticity and Plasticity*. Elsevier Science & Technology, 1974.

[39] M. A. Yerry and M. S. Shepard. Automatic three-dimensional mesh generation by the modified-octree technique. *International Journal for Numerical Methods in Engineering*, 20:1965–1990, 1984.

[40] M. S. Shepard and M. K. Georges. Automatic three-dimensional mesh generation by the finite octree technique. *International Journal for Numerical Methods in Engineering*, 32:709–749, 1991.

[41] G. Scovazzi. Lagrangian shock hydrodynamics on tetrahedral meshes: A stable and accurate variational multiscale approach. *Journal of Computational Physics*, 231:8029–8069, 2012.

[42] J. Bonet and A. J. Burton. A simple average nodal pressure tetrahedral element for incompressible and nearly incompressible dynamic explicit applications. *Communications in Numerical Methods in Engineering*, 14:437–449, 1998.

[43] S. K. Lahiri, J. Bonet, and J. Peraire. A variationally consistent mesh adaptation method for triangular elements in explicit Lagrangian dynamics. *International Journal for Numerical Methods in Engineering*, 82:1073–1113, 2010.

[44] M. W. Gee, C. R. Dohrmann, S. W. Key, and W. A. Wall. A uniform nodal strain tetrahedron with isochoric stabilization. *International Journal for Numerical Methods in Engineering*, 78: 429–443, 2009.

[45] M. A. Puso and J. Solberg. A stabilized nodally integrated tetrahedral. *International Journal for Numerical Methods in Engineering*, 67:841–867, 2006.

[46] C. R. Dohrmann, M. W. Heinstein, J. Jung, S. W. Key, and W. R. Witkowski. Node-based uniform strain elements for three-node triangular and four-node tetrahedral meshes. *International Journal for Numerical Methods in Engineering*, 47:1549–1568, 2000.

[47] E. A. de Souza Neto, D. Peric, M. Dutko, and D. R. J. Owen. Design of simple low order finite elements for large strain analysis of nearly incompressible solids. *International Journal of Solids and Structures*, 33:3277–3296, 1996.

[48] Y. Guo, M. Ortiz, T. Belytschko, and E. A. Repetto. Triangular composite finite elements. *International Journal for Numerical Methods in Engineering*, 10:287–316, 2000.

[49] Y. Onishi and K. Amaya. F-Bar aided edge-based smoothed finite element method with 4-node tetrahedral elements for static large deformation elastoplastic problems. *International Journal of Computational Method*, 18400108, 2017.

[50] A. K. Slone, C. Bailey, and M. Cross. Dynamic solid mechanics using finite volume methods. *Applied Mathematical Modelling*, 27:69–87, 2003.

[51] G. A. Taylor and C. Baileyand M. Cross. A vertex-based finite volume method applied to non-linear material problems in computational solid mechanics. *International Journal for Numerical Methods in Engineering*, 56:507–529, 2003.

[52] H. Jasak and H. G. Weller. Application of the finite volume method and unstructured meshes to linear elasticity. *International Journal for Numerical Methods in Engineering*, 48:267–287, 2000.

[53] I. Bijelonja, I. Demirdžić, and S. Muzaferija. A finite volume method for incompressible linear elasticity. *Computer Methods in Applied Mechanics and Engineering*, 195:6378–6390, 2006.

[54] P. Cardiff, A. Karač, and A. Ivanković. Development of a finite volume contact solver based on the penalty method. *Computational Materials Science*, 64:283–284, 2012.

[55] P. Cardiff, A. Karač, and A. Ivanković. A large strain finite volume method for orthotropic bodies with general material orientations. *Computer Methods in Applied Mechanics and Engineering*, 268:318–335, 2014.

[56] I. Peshkov, W. Boscheri, R. Loubere, E. Romenski, and M. Dumbser. Theoretical and numerical comparison of hyperelastic and hypoelastic formulations for eulerian non-linear elastoplasticity. *Journal of Computational Physics*, 387:481–521, 2019.

[57] P. Cardiff, Ž. Tuković, P. D. Jaeger, M. Clancy, and A. Ivanković. A Lagrangian cell-centred finite volume method for metal forming simulation. *International Journal for Numerical Methods in Engineering*, 109:1777–1803, 2017.

[58] Y. D. Fryer, C. Bailey, M. Cross, and C. H. Lai. A control volume procedure for solving the elastic stress-strain equations on an unstructured mesh. *Applied Mathematical Modelling*, 15: 639–645, 1991.

[59] Y. D. Fryer, C. Bailey, M. Cross, and P. Chow. Predicting micro-porosity in shape casting using an integrated control volume unstructured mesh framework. *Modelling of Casting, Welding and Advanced Solidification Processes VI*, pages 143–152, 1993.

[60] C. Bailey, M. Cross, Y. D. Fryer, and K. Pericleous. Multiphysics modelling of metals casting process. *Proceedings of the Royal Society of London: A Mathematical, Physical and Engineering Sciences*, pages 459–486, 1996.

[61] S. R. Idelsohn and E. Onate. Finite volumes and finite elements: Two 'good friends'. *International Journal for Numerical Methods in Engineering*, 37:3323–3341, 1994.

[62] C. Bailey and M. Cross. A finite volume procedure to solve elastic solid mechanics problems in three dimensions on an unstructured mesh. *International Journal for Numerical Methods in Engineering*, 38:1757–1776, 1995.

[63] B. R. Baliga and Patankar. S. V. A new finite-element formulation for convection-diffusion problems. *Numerical Heat Transfer, Part B: Fundamentals*, 3:393–409, 1980.

[64] N. Fallah, C. Bailey, M. Cross, and G. A. Taylor. Comparison of finite element and finite volume methods application in geometrically nonlinear stress analysis. *Applied Mathematical Modelling*, 24:439–455, 2000.

[65] G. A. Taylor, C. Bailey, and M. Cross. Solution of the elastic/visco-plastic constitutive equations: A finite volume approach. *Applied Mathematical Modelling*, 19:746–760, 1995.

[66] C. Bailey, G. A. Taylor, M. Cross, and P. Chow. Discretisation procedures for multiphysics phenomena. *Journal of Computational and Applied Mathematics*, 103:3–17, 1999.

[67] A. K. Slone, K. Pericleous, C. Bailey, and M. Cross. Dynamic fluid-structure interaction using finite volume unstructured mesh procedures. *Computers & Structures*, 80:371–390, 2002.

[68] G. A. Taylor, Hughes. M., N. Strusevich, and K. Pericleous. The application of threedimensinal finite volume methods to the modelling of welding phenomena. *Applied Mathematical Modelling*, 26:309–320, 2002.

[69] T. Liu, Liu. K., and J. Zhang. Unstructured grid method for stress wave propagation in elastic media. *Computer Methods in Applied Mechanics and Engineering*, 193:2427–2452, 2004.

[70] A. J. Williams, Slone. A. K., T. N. Croft, and M. Cross. A mixed eulerian-lagrangian method for modelling metal extrusion processes. *Computer Methods in Applied Mechanics and Engineering*, 199:2123–2134, 2010.

[71] I. Demirdžić P. Cardiff. Thirty years of the finite volume method for solid mechanics. *arXiv:1810.02105 [math.NA]*, 2018.

[72] M. A. Biot. Variational principles in irreversible thermodynamics with application to viscoelasticity. *PHYSICAL REVIEW*, 97:1463–1469, 1954.

[73] M. A. Biot. Thermoelasticity and irreversible thermodynamics. *Journal of Applied Physics*, 27: 240–253, 1956.

[74] H. W. Lord and Y. Shulman. A generalized dynamical theory of thermoelasticity. *Journal of the Mechanics and Physics of Solids*, 15:299–309, 1967.

[75] F. Armero and J. C. Simo. An unconditionally stable fractional step method for non-linear coupled thermomechanical problems. *International Journal for Numerical Methods in Engineering*, 35: 737–766, 1992.

[76] A. Entezaria, M. Filippia, E. Carreraa, and M. A. Kouchakzadeh. 3D-wave propagation in generalized thermoelastic functionally graded disks. *Composite Structures*, 206:941–951, 2018.

[77] Y. Hayati and M. Eskandari-Ghadi. Three-dimensional coupled thermoelastodynamic stress and flux induced wave propagation for isotropic half-space with scalar potential functions. *Journal of Applied Mathematics and Physics*, 69:18, 2018.

[78] J. C. Simo and C. Miehe. Associative coupled thermoplasticity at finite strains: Formulation, numerical analysis and implementation. *Computer Methods in Applied Mechanics and Engineering*, 98:41–104, 1992.

[79] P. Chadwick and C. F. M. Creasy. Modified entropic elasticity of rubberlike materials. *Journal of the Mechanics and Physics of Solids*, 32:337–357, 1984.

[80] C. Miehe. Entropic thermoelasticity at finite strains. Aspects of the formulation and numerical implementation. *Computer Methods in Applied Mechanics and Engineering*, 120:243–269, 1995.

[81] G. A. Holzapfel and J. C. Simo. Entropy elasticity of isotropic rubber-like solids at finite strains. *Computer Methods in Applied Mechanics and Engineering*, 132:17–44, 1996.

[82] I. Demirdžić and D. Martinović. Finite volume method for thermo-elasto-plastic stress analysis. *Computer Methods in Applied Mechanics and Engineering*, 109:331–349, 1993.

[83] I. Demirdžić and S. Muzaferija. Finite volume method for stress analysis in complex domain. *International Journal for Numerical Methods in Engineering*, 37:3751–3766, 1994.

[84] I. Demirdžić, I. Horman, and D. Martinović. Finite volume analysis of stress and deformation in hygro-thermo-elastic orthotropic body. *Computer Methods in Applied Mechanics and Engineering*, 190:1221–1232, 2000.

[85] I. Demirdžić and E. Džaferović. Finite-volume approach to thermoviscoelasticity. *Numerical Heat Transfer, Part B*, 47:213–237, 2007.

[86] J. Aboudi. Micromechanical analysis of fully coupled electro-magneto-thermo-elastic multiphase composites. *Smart Materials and Structures*, 10:867–877, 2001.

[87] J. Aboudi. Micromechanical analysis of the fully coupled finite thermoelastic response of rubberlike matrix composites. *International Journal of Solids and Structures*, 39:2587–2612, 2002.

[88] J. Aboudi. Finite strain micromechanical modeling of multiphase composites. *International Journal for Multiscale Computational Engineering*, 6:411–434, 2008.

[89] A. Berezovski and G. A. Maugin. Simulation of thermoelastic wave propagation by means of a composite wave-propagation algorithm. *Journal of Computational Physics*, 168:249–264, 2001.

[90] L. X. Wang and Roderick V. N. Melnik. Finite volume analysis of nonlinear thermo-mechanical dynamics of shape memory alloys. *Heat and Mass Transfer*, 43:535–546, 2007.

[91] A. Osman, S. Ahmad, and K. A. Arshad. A one-dimensional simulation of an electrofusion welding process. In *International Conference on Modeling, Simulation and Applied Optimization (ICMSAO)*, 2011.

[92] K. S. Bibin and A. Ramarajan. Unstructured finite volume approach for 3-d unsteady thermo-structural analysis using bi-conjugate gradient stabilized method. *International Journal of Innovative Research in Science, Engineering and Technology*, 2:1389–1400, 2013.

[93] J.-F. Gong, L.-K. Xuan, P.-J. Ming, , and W.-P. Zhang. Thermoelastic analysis of functionally graded solids using a staggered finite volume method. *Composite Structures*, 104:134–143, 2013.

[94] J.-F. Gong, P.-J. Ming, L.-K. Xuan, and W.-P. Zhang. Thermoelastic analysis of three dimensional functionally graded rotating disks based on finite volume method. *Journal of Mechanical Engineering Science*, 228:583–598, 2014.

[95] T. Heuzé. Lax–wendroff and tvd finite volume methods for unidimensional thermomechanical numerical simulations of impacts on elastic–plastic solids. *Journal of Computational Physics*, 346: 369–388, 2017.

[96] S.R. Sabbagh-Yazdi, A. Farhoud, and S.A. Gharebaghi. Simulation of 2d linear crack growth under constant load using gfvm and two-point displacement extrapolation method. *Applied Mathematical Modelling*, 61:650–667, 2018.

[97] P. Cardiff, P. De Jaeger A. Karač, H. Jasak, J. Nagy, A. Ivanković, and Ž. Tuković. An open-source finite volume toolbox for solid mechanics and fluid-solid interaction simulations. *arXiv:1808.10736v2 [math.NA]*, 2018.

[98] I. González, A. Naseri, J. Chiva, J. Rigola, , and C. D. Pérez-Segarra. An enhanced finite volume based solver for thermoelastic materials in fluid-structure coupled problems. In *6$^t$h European Conference on Computational Mechanics (ECCM 6), 7$^t$h European Conference on Computational Fluid Dynamics (ECFD 7)*, 2018.

[99] J. A. Trangenstein and P. Colella. A higher-order Godunov method for modeling finite deformation in elastic-plastic solids. *Communications on Pure and Applied Mathematics*, 44(1):41–100, 1991.

[100] J. A. Trangenstein. A second-order Godunov algorithm for two-dimensional solid mechanics. *Computational mechanics*, 13(5):343–359, 1994.

[101] B. J. Plohr and D. H. Sharp. A conservative eulerian formulation of the equations for elastic flow. *Advances in Applied Mathematics*, 9(4):481–499, 1988.

[102] B. Després and C. Mazeran. Lagrangian Gas Dynamics in Two Dimensions and Lagrangian systems. *Archive for Rational Mechanics and Analysis*, 178(3):327–372, 2005. ISSN 0003-9527.

[103] Pierre-Henri Maire, Rémi Abgrall, Jérôme Breil, and Jean Ovadia. A Cell-Centered Lagrangian Scheme for Two-Dimensional Compressible Flow Problems. *SIAM Journal on Scientific Computing*, 29(4):1781–1824, 2007.

[104] Pierre-Henri Maire. A high order cell-centered Lagrangian scheme for two-dimensional cylindrical geometry. *Journal of Computational Physics*, 228:6882–6915, 2009.

[105] P.-H. Maire, R. Abgrall, J. Breil, R. Loubère, and B. Rebourcet. A nominally second-order cell-centered Lagrangian scheme for simulating elastic-plastic flows on two-dimensional unstructured grids. *Journal of Computational Physics*, 235:626–665, 2013.

[106] G. Kluth and B. Després. Discretization of hyperelasticity on unstructured mesh with a cell-centered Lagrangian scheme. *Journal of Computational Physics*, 229:9092–9118, 2010.

[107] G. Georges, J. Breil, and P.-H. Maire. A 3D finite volume scheme for solving the Updated Lagrangian form of hyperelasticity. *International Journal for Numerical Methods in Fluids*, 84(1): 41–54, 2017.

[108] P. Wenke and M. A. Wheel. A finite volume method for solid mechanics incorporating rotational degrees of freedom. *Computers & Structures*, 81:321–329, 2003.

[109] W. Pan, M. Wheel, and Y. Qin. Six-node triangle finite volume method for solids with a rotational degree of freedom for incompressible material. *Computers & Structures*, 88:1506–1511, 2010.

[110] W. Pan and M. Wheel. A finite-volume method for solids with a rotational degrees of freedom based on the 6-node triangle. *International Journal of Numerical Methods in Biomedical Engineering*, 27:1411–1426, 2011.

[111] I. Bijelonja, I. Demirdžić, and S. Muzaferija. A finite volume method for large strain analysis of incompressible hyperelastic materials. *International Journal for Numerical Methods in Engineering*, 64:1594–1609, 2008.

[112] S. Rossi, N. Abboud, and G. Scovazzi. Implicit finite incompressible elastodynamics with linear finite elements: A stabilized method in rate form. *Computer Methods in Applied Mechanics and Engineering*, 311:208–249, 2016.

[113] G. Scovazzi, B. Carnes, X. Zeng, and S. Rossi. A simple, stable, and accurate tetrahedral finite element for transient, nearly and fully incompressible solid dynamics: A dynamic variational multiscale approach. *International Journal for Numerical Methods in Engineering*, 106:799–839, 2015.

[114] G. Scovazzi, T. Song, and X. Zeng. A velocity/stress mixed stabilized nodal finite element for elastodynamics: Analysis and computations with strongly and weakly enforced boundary conditions. *Computer Methods in Applied Mechanics and Engineering*, 325:532–576, 2017.

[115] N. Abboud and G. Scovazzi. Elastoplasticity with linear tetrahedral elements: A variational multiscale method. *International Journal for Numerical Methods in Engineering*, 115:913–955, 2018.

[116] N. A. Fallah, C. Bailey, and M. Cross. CFD approach for solid mechanics analysis. In *European Congress on Computational Methods in Applied Sciences and Engineering (ECCOMAS)*, 2000.

[117] I. Bijelonja, I. Demirdžić, and S. Muzaferija. Mixed finite volume method for linear thermoelasticity at all poisson's ratios. *Numerical Heat and Mass transfer, Part A*, 72:215–235, 2017.

[118] M. Aguirre, A. J. Gil, J. Bonet, and A. A. Carreño. A vertex centred finite volume Jameson–Schmidt–Turkel (JST) algorithm for a mixed conservation formulation in solid dynamics. *Journal of Computational Physics*, 259:672–699, 2014.

[119] I. A. Karim, C. H. Lee, A. J. Gil, and J. Bonet. A two-step Taylor Galerkin formulation for fast dynamics. *Engineering Computations*, 31:366–387, 2014.

[120] A. J. Gil, C. H. Lee, J. Bonet, and R. Ortigosa. A first order hyperbolic framework for large strain computational solid dynamics. part ii: Total Lagrangian compressible, nearly incompressible and truly incompressible elasticity. *Computer Methods in Applied Mechanics and Engineering*, 300: 146–181, 2016.

[121] T. Belytschko and M. Tabbara. Dynamic fracture using element-free galerkin methods. *International Journal for Numerical Methods in Engineering*, 39:923–938, 1996.

[122] Sonia Fernandez Mendez. *Mesh-free methods and finite element: friend or foe?* Phd thesis, Universitat Politéchnica de Catalunya, 2001.

[123] S. Li and W. K. Lui. Numerical simulations of strain localization in inelastic solids using mesh-free methods. *International Journal for Numerical Methods in Engineering*, 48:1285–1309, 1996.

[124] M. B. Liu and G. R. Liu. Smooth Particle Hydrodynamics: an Overview and Recent Development. *Archives of Computational Methods in Engineering*, 17:25–76, 2010.

[125] Y. Vidal, J. Bonet, and A Huerta. A locking-free selective smoothed finite element method using tetrahedral and triangular elements with adaptive mesh rezoning for large deformation problems. *International Journal for Numerical Methods in Engineering*, 69:2687–2710, 2007.

[126] L. D. Libersky, P. W. Randless, T. C. Carney, and D. L. Dickinson. Recent improvements in sph modeling of hypervelocity impact. *International Journal of Impact Engineering*, 20:525–532, 1997.

[127] S. Li and W. K. Lui. Meshfree and particle methods and their applications. *Applied Mechanics Review*, 55:1–34, 2002.

[128] J. J. Monaghan. Smoothed particle hydrodynamics and its diverse applications. *Annual Review of Fluid Mechanics*, 44:323–346, 2012.

[129] S. Li and W. K. Lui. A numerical approach to the testing of the fission hypothesis. *Astronomical Journal*, 82:1013–1024, 1977.

[130] R. A. Gingold and J. J. Monaghan. Smooth Particle Hydrodynamics: theory and application to non-physical stars. *Monthly Notices of the Royal Astronomical Society*, 181:375–389, 1977.

[131] J. Bonet and S. Kulasegram. A simplified approach to enhance the performance of smooth particle hydrodynamics methods. *Applied Mathematics and Computation*, 126:133–155, 2002.

[132] T. Belytschko, Y. Y. Lu, and L. Gu. Element-free Galerkin Methods. *International Journal for Numerical Methods in Engineering*, 37:229–256, 1994.

[133] W. K. Liu, S. Jun, and F. Zhang. Reproducing Kernel Particle Methods. *Computational Mechanics*, 20:1081–1106, 1995.

[134] G. R. Liu and Y. T. Gu. Meshless local petrov-galerkin (mlpg) method in combination with finite element and boundary element approaches. *Computational Mechanics*, 26:536–546, 2000.

[135] D. Sulsky, Z. Chen, and H. L. Schreyer. A particle method for history-dependent materials. *Computer Methods in Applied Mechanics and Engineering.*, 118:179–196, 1994.

[136] A. Renaud, T. Heuze, and L. Stainier. A discontinuous galerkin material point method for the solution of impact problems in solid dynamics. *Journal of Computational Physics*, 369:80–102, 2018.

[137] G. B. Jacobs and J. S. Hesthaven. High-order nodal discontinuous galerkin particle-in-cell method on unstructured grids. *Journal of Computational Physics*, 214:96–121, 2006.

[138] T. Belytschko, Y. Kronguaz, D. Organ, M. Fleming, and P. Krysl. Meshless methods: an overview and recent developments. *Computer Methods in Applied Mechanics and Engineering*, 139:3–47, 1996.

[139] SR. Idelsohn and E. Onate. To mesh or not to mesh. That is the question. . . *Computer Methods in Applied Mechanics and Engineering*, 195:4681–4696, 2006.

[140] V. P. Nguyen, T. Rabczuk, S. Bordas, and M. Duflot. Meshless methods: a review and computer implementation aspects. *Computer Methods in Applied Mechanics and Engineering*, 79:763–813, 2008.

[141] J. J. Monaghan. Why particle methods work. *SIAM Journal on Scientific and Statistical Computing*, 3:422–433, 1982.

[142] J. J. Monaghan. An introduction to sph. *Computer Physics Communications*, 48:89–96, 1988.

[143] B. Berczik. Modeling the star formation in galazies using the chemodynamical sph code. *Astronomy and Astrophysics*, 360:76–84, 2000.

[144] J. B. Katjar and J. J. Monaghan. On the swimming of fish like bodies near free and fixed boundaries. *European Journal of Mechanics*, 33:1–13, 2012.

[145] A. M. Tartakovsky, N. Trask, K. Pan, B. Jones, and J. R. Williams. Smoothed particle hydrodynamics and its applications for multiphase flow and reactive transport in porous media. *Computational Geosciences*, 20:807–834, 2016.

[146] A. Colle, J. Limido, and J. P. Vila. An accurate sph scheme for dynamic fragmentation modelling. In *The European Physical Journal Conferences*, 2018.

[147] L. D. Libersky, Petschek A., T. Carney, J. Hipp, and F. Allahdadi. High strain Lagrangian hydrodynamics: A Three-Dimensional SPH Code for Dynamic Material Response. *Journal of Computational Physics*, 109:67–75, 1993.

[148] J. Limido, Espinosa C., M. Salaun, and J. L. Lacome. SPH method applied to high speed cutting modeling. *International Journal of Mechanical Sciences*, 49:898–908, 2007.

[149] H. Bui, Fukagawa R., K. Sako, and S. Ohno. Lagrangian meshfree particles method (SPH) for large deformation and failure flows of geomaterial using elastic-plastic soil constitutive model. *International Journal for Numerical and Analytical Methods*, 32:1537–1570, 2008.

[150] V. Lemiale, Karangtis L., and P Broadbridge. Smoothed particle hydrodynamics applied to the modelling of landslides. *Applied Mechanics and Materials*, 553:519–524, 2008.

[151] B. Maurel and A. Combescure. An sph shell formulation for plasticity and fracture analysis in explicit dynamic. *International Journal for Numerical Methods in Engineering*, 76(7):949–971, 2008.

[152] J. W. Swegle, D. L. Hicks, and S. W. Attaway. Smoothed Particle Hydrodynamics stability analysis. *Journal of Computational Physics*, 116:123–134, 1995.

[153] T. Belytschko, Y. Guo, W. K. Liu, and S. P. Xiao. A unified stability analysis of meshless particle methods. *International Journal for Numerical Methods in Engineering*, 48:1359–1400, 2000.

[154] J. J. Monaghan. SPH without a tensile instability. *Journal of Computational Physics*, 159:290–311, 2000.

[155] M. A. Puso, J. S. Chen, and W. Zywicz, E. Elmer. Meshfree and finite element nodal integration methods. *International Journal for Numerical Methods in Engineering*, 74:416–446, 2008.

[156] J. K. Chen, J. E. Beraun, and T. C. Carney. A corrective smoothed particle method for boundary value problems in heat conduction. *International Journal for Numerical Methods in Engineering*, 46:231–252, 1999.

[157] J. K. Chen and J. E. Beraun. A generalized smoothed particle hydrodynamics method for nonlinear dynamic problems. *Computer Methods in Applied Mechanics and Engineering*, 190:225–239, 2000.

[158] J. S. Chen, C. Pan, C. T. Wu, and W. K. Liu. Reproducing Kernel Particle Methods for large deformation analysis of non-linear structures. *Computer Methods in Applied Mechanics and Engineering*, 139:195–227, 1996.

[159] T. Rabczuk, T. Belytschko, and S. P. Xiao. Stable particle methods based on lagrangian kernels. *Computer Methods in Applied Mechanics and Engineering*, 193:1035–1063, 2004.

[160] M. B. Liu and G. R. Liu. Restoring particle consistency in smoothed particle hydrodynamics. *Applied Numerical Mathematics*, 56:19–36, 2006.

[161] J. Bonet and S. Kulasegram. Correction and stabilization of smooth particle hydrodynamics methods with applications in metal forming simulations. *International Journal for Numerical Methods in Engineering*, 47:1189–1214, 2000.

[162] C. T. Dyka and R. P. Ingel. An approach for tension instability in smoothed particle hydrodynamics (SPH). *Computers and Structures*, 57:573–580, 1995.

[163] C. T. Dyka, P. W. Randles, and R. P. Ingel. Stress points for tension instability in SPH. *International Journal for Numerical Methods in Engineering*, 40:2325–2341, 1997.

[164] P. W. Randles and L. D. Libersky. Normalized SPH with stress points. *International Journal for Numerical Methods in Engineering*, 48:1445–1462, 2000.

[165] R. Vignjevic, J. Campbell, and L. Libersky. A treatment of zero-energy modes in the smoothed particle hydrodynamics method. *Computer Methods in Applied Mechanics and Engineering*, 184: 67–85, 2000.

[166] G. C. Ganzenmuller, M. Sauer, M. May, and S. Hiermaier. Hourglass control for Smooth Particle Hydrodynamics removes tensile and rank-deficiency instabilities. *The European Physical Journal Special Topics*, 225:385–395, 2016.

[167] R. C. Barta and G. M. Zhang. Analysis of adiabatic shear bands in elasto-thermo-viscoplastic materials by modified smoothed-particlen hydrodynamics (MSPH) method. *Journal of Computational Physics*, 201:172–190, 2004.

[168] M. M. Rahaman, A. Pathak, and D. Roy. A thermo-visco-plastic damage model and sph simulations of plugging failure. *MECHANICS OF ADVANCED MATERIALS AND STRUCTURES*, 25:1374–1382, 2017.

[169] Z. Zhang, H. Qiang, and W. Gao. Coupling of smoothed particle hydrodynamics and finite element method for impact dynamics simulation. *Engineering Structures*, 2011:255–264, 2011.

[170] K. A. Fraser, L. St Georges, L. I. Kiss, and Y. Chiricota. Hybrid Thermo-Mechanical Contact Algorithm for 3D SPH-FEM MultiPhysics Simulations. In *IV International Conference on Particle-Based Methods*, 2015.

[171] K. A. Fraser, L. I. Kiss, L. St Georges, and D. Drolet. Optimization of friction stir weld joint quality using a meshfree fully-coupled thermo-mechanics approach. *Metals*, 8:101–125, 2018.

[172] H. Hu, F. Fetzer, P. Berger, and P. Eberhard. Simulation of laser welding using advanced particle methods. *GAMM-Mitt*, 39:149–169, 2016.

[173] H. Hu and P. Eberhard. Thermomechanically coupled conduction mode laser welding simulations using smoothed particle hydrodynamics. *Computational Particle Mechanics*, 4:473–486, 2017.

[174] K. Ba and A. Gakwaya. Thermomechanical total lagrangian sph formulation for solid mechanics in large deformation problems. *Computer Methods in Applied Mechanics and Engineering*, 342: 458–473, 2018.

[175] K. Damaziak and J. Malachowski. Comparison of SPH and FEM in thermomechanical coupled problems. In *AIP Conference Proceedings 2078*, 2019.

[176] G. C. Ganzenmuller. An hourglass control algorithm for lagrangian smooth particle hydrodynamics. *Computer Methods in Applied Mechanics and Engineering*, 286:87–106, 2015.

[177] J. J. Monaghan. Smooth Particle Hyydrodynamics. *Annual Review of Astronomy and Astrophysics*, 30:543–574, 1992.

[178] P. W. Randles and L. D. Libersky. Smoothed Particle Hydrodynamics: Some recent improvements and applications. *Computer Methods in Applied Mechanics and Engineering*, 139:375–408, 1996.

[179] J. S. Chen, C. T. Wu, S. Yoon, and Y. You. A stabilized conforming nodal integration for Galerkin mesh-free methods. *International Journal for Numerical Methods in Engineering*, 50: 435–466, 2001.

[180] A. J. Chorin. The numerical solution of the Navier-Stokes equations for an incompressible fluid. *Bulletin of the American Mathematical Society*, 73:928–931, 1967.

[181] A. J. Chorin. Numerical solution of the Navier-Stokes equations. *Mathematics of Computation*, 22:745–762, 1968.

[182] A. J. Chorin. On the convergence of discrete approximations to the Navier-Stokes equations. *Mathematics of Computation*, 23:341–353, 1969.

[183] C. Hirsch. *Numerical Computation of Internal and External Flows. Volume 1: Fundamentals of Computational Fluid Dynamics*. Elsevier, 2007.

[184] C. M. Dafermos. *Hyperbolic Conservation Laws in Continuum Physics*. Springer, Forth Edition, 2009.

[185] J. Bonet, A. J. Gil, and R. Ortigosa. A computational framework for polyconvex large strain elasticity. *Computer Methods in Applied Mechanics and Engineering*, 283:1061–1094, 2015.

[186] L. Anand M. E. Gurtin, E. Fried. *The mechanics and thermodynamics of continua*. Cambridge University Press, 2010.

[187] G. H. Miller. An iterative Riemann solver for systems of hyperbolic conservation laws, with application to hyperelastic solid mechanics. *Journal of Computational Physics*, 193:198–225, 2003.

[188] B. D. Coleman and W. Noll. The thermodynamics of elastic materials with heat conduction and viscosity. *Archive for Rational Mechanics and Analysis*, 13:167–178, 1963.

[189] Rogelio Ortigosa Martinez. *On a new variational and computational framework for polyconvex nonlinear continuum mechanics and convex multi-variable nonlinear electro-elasticity.* Phd thesis, Swansea University, 2016.

[190] J. C. Simo. Algorithms for static and dynamic multiplicative plasticity that preserve the classical return mapping schemes of the infinitesimal theory. *Computer Methods in Applied Mechanics and Engineering*, 99:61–112, 1992.

[191] J. Bonet, C. H. Lee, A. J. Gil, and A. Ghavamian. A first order hyperbolic framework for large strain computational solid dynamics. part iii: Thermo-elasticity and thermo-plasticity. *Computer Methods in Applied Mechanics and Engineering*, 2019. Under review.

[192] A. Ghavamian, C. H. Lee, A. J. Gil, J. Bonet, and L. Stainier. Thermodynamically consistent smooth particle hydrodynamics algorithm for large strain thermo-elasticity. *Computer Methods in Applied Mechanics and Engineering*, 2019. Under review.

[193] John M. Ball. Convexity conditions and existence theorems in nonlinear elasticity. *Archive for rational mechanics and Analysis*, 63(4):337–403, 1976.

[194] S. K. Godunov. A difference method for numerical calculation of discontinuous solutions of the equations of hydrodynamics. *Mat. Sb. (N.S.)*, 47:271–306, 1959.

[195] A. Preissmann. Propagation des intumescences dans les canaux et les rivieres. In *Premier congres de l'Association Francaise de Calcul*, 1961.

[196] P. W. McDonald. The computation of transonic flow through two-dimensional gas turbine cascades. In *International Gas Turbine Conference and Products Show (ASME)*, 1971.

[197] R. W. MacCormack and A. J. Paullay. Computational efficiency achieved by time splitting of finite difference operators. In *10th Aerospace Sciences Meeting (AIAA)*, 1972.

[198] A. W. Rizzi and M. Inouye. Time-split finite-volume method for three-dimensional blunt-body flow. *AIAA*, 11:1478–1485, 1973.

[199] J. Blazek. *Computational Fluid Dynamics: Principles and Applications.* Elsevier, Edition third, 2015.

[200] E. F. Toro. *Riemann solvers and numerical methods for fluid dynamics, A Practical Introduction.* Springer, Edition third, 2009.

[201] K. A. Sorensen, O. Hassan, K. Morgan, and N. P. Weatherill. A multigrid accelerated hybrid unstructured mesh method for 3d compressible turbulent flow. *Computational Mechanics*, 31: 101–114, 2003.

[202] H Luo, J. D Baum, and R. Lohner. An improved finite volume scheme for compressible flows on unstructured grids. *AIAA paper*, pages 95–0348, 1995.

[203] G. J. Charney, R. FjOrtoft, and J. V. Neumann. Numerical integration of the barotropic vorticity equation. *Tellus*, 2:237–254, 1950.

[204] R. Loubére, P.-H. Maire, and P. Vachal. Staggered lagrangian discretization based on cell-centered riemann solver and associated hydro-dynamics scheme. *Communication in Computational Physics*, 10:940–978, 2011.

[205] M. E. Hubbard. Multidimensional slope limiters for MUSCL-type finite volume schemes on unstructured grids. *Journal of Computational Physics*, 155:54–74, 1999.

[206] W. Boscheri, Loubére, and P.-H. Maire. A second-order cell-centered Lagrangian ADER-MOOD finite volume scheme on multidimensional unstructured meshes for hydrodynamics. *Journal of Computational Physics*, 358:103–129, 2018.

[207] G. Luttwak and J. Falcovitz. Slope limiting for vectors: A novel vector limiting algorithm. *International Journal for Numerical Methods in Fluids*, 65(11-12):1365–1375, 2011.

[208] P. Hoch and E. Labourasse. A frame invariant and maximum principle enforcing second-order extension for cell-centered ALE schemes based on local convex hull preservation. *International Journal for Numerical Methods in Fluids*, 76(12):1043–1063, 2014.

[209] T. J. Barth and D. C. Jespersen. The design and application of upwind schemes on unstructured meshes. *AIAA*, 89-0366, 1989.

[210] G. Liu and M. B. Liu. *Smooth Particle Hydrodynamics-A mesh-free particle method.* World Scientific Publishing Co. Pte. Ltd., 2003.

[211] J. Bonet and T. Lok. Variational and momentum preservation aspects of smooth particle hydrodynamic formulations. *Computer Methods in Applied Mechanics and Engineering*, 180:97–115, 1999.

[212] P. Hoch and E. Labourasse. An analysis of 1-D smoothed particle hydrodynamics kernels. *Journal of Computational Physics*, 126:165–180, 1996.

[213] J. P. Morries. A study of the stability properties of smooth particle hydrodynamics. *Publications of the Astronomical Society of Australia*, 13:97–102, 1996.

[214] G. R. Johnson, R. A. Stryk, and S. R. Beissel. SPH for high velocity impact computations. *Computer Methods in Applied Mechanics and Engineering*, 139:347–373, 1996.

[215] H. B. Jin and X. Ding. A study of the stability properties of smooth particle hydrodynamics. *Journal of Computational Physics*, 202:699–709, 2005.

[216] M. Omang, S. Brove, and J. Trulsen. Alternative kernel functions for smoothed particle hydrodynamics in cylindrical symmetry. *Shock Waves*, 14:293–298, 2005.

[217] J. J. Monaghan and J. C. Lattanzio. A refined particle method for astrophysical problems. *Astronaut Astrophysics*, 149:135–143, 1985.

[218] D. J. Price. Smoothed Particle Hydrodynamics and Magnetohydrodynamics. *Journal of Computational Physics*, 231:759–794, 2012.

[219] P. Lancaster and K. Salkauskas. Surfaces generated by moving least square methods. *Mathematics and Computation*, 37:141–158, 1981.

[220] A. Huerta and S. Fernandez-Mendez. Locking in the incompressible limit for the element-free galerkin method. *International Journal for Numerical Methods in Engineering*, 51:1361–1383, 2001.

[221] S. Fernandez-Mendez and A. Huerta. Continuous blending of sph with fnite elements. *Computers & Structures*, 83:1448–1458, 2005.

[222] R. Courant, K. Friedrichs, and H. Lewy. On the partial difference equations of mathematical physics. *Mathematische Annalen*, 83:32–74, 1928.

[223] J. P. Morris, P. J. Fox, and Y. Zhu. Modeling low Reynolds number incompressible flows using SPH. *Journal of Computational Physics*, 136:214–226, 1997.

[224] C. Mingham and D. Causon. High resolution finite volume method for shallow water flows. *Journal of Hydraulic Engineering*, 124:605–614, 1998.

[225] L. Felgueroso, I. Colominas, J. Fe, F. Navarrina, and M. Casteleiro. High order finite volume schemes on unstructured grids using moving least squares reconstruction. application to shallow water dynamics. *International Journal for Numerical Methods in Engineering*, 65:295–331, 2006.

[226] A. Harten, P. D. Lax, and B. van Leer. On upstream differencing and godunov-type schemes for hyperbolic conservation laws. *SIAM Review*, 25:35–61, 1983.

[227] J. Blazek. *Finite Element Methods for Flow Problems.* Elsevier, 2001.

[228] A. Huerta J. Donea. *Computational fluid dynamics: principles and applications.* John Wiley & Sons, Ltd, 2003.

[229] R. F. Warming and B. J. Hyett. The modified equation approach to the stability and accuracy analysis of finite-difference methods. *Journal of Computational Physics*, 14:159–179, 1974.

[230] M Dehghan. On the numerical solution of the one-dimensional convection-diffusion equation. *Mathematical Problems in Engineering*, 2005:61–74, 2005.

[231] R. D. Ritchmyer and K. W. Morton. *Difference Methods for Initial-Value Problems.* Interscience Publishers, a division of John Wiley & Sons, 1967.

[232] B. Wendroff. A two-dimensional hlle riemann solver and associated godunov-type difference scheme for gas dynamics. *Computers and Mathematics with Applications*, 38:175–185, 1999.

[233] D. S. Balsara. Multidimensional hlle riemann solver: Application to euler and magnetohydrodynamic flows. *Journal of Computational Physics*, 229:1970–1993, 2010.

[234] J. Vides, B. Nkonga, and E. Audit. A simple two-dimensional extension of the hlle riemann solver for gas dynamics. *Journal of Computational Physics*, 280:643–675, 2015.

[235] S. F. Davis. Simplified second–order godunov–type methods. *SIAM Journal on Scientific Computing*, 9:445–473, 1988.

[236] V. V. Rusanov. Calculation of interaction of non–steady shock waves with obstacles. *Journal of Computational Mathematics and Mathematical Physics USSR*, 1:267–279, 1961.

[237] G. A. Sod. A survey of several finite difference methods for systems of nonlinear hyperbolic conservation laws. *Journal of Computational Physics*, 27:1–31, 1978.

[238] P. Woodward and P. Colella. The numerical simulation of two-dimensional fluid flow with strong shocks. *Journal of Computational Physics*, 54:115–173, 1984.

[239] X. N. Meng and T. A. Laursen. Energy consistent algorithms for dynamic finite deformation plasticity. *Computer Methods in Applied Mechanics and Engineering*, 191:1639–1675, 2002.

[240] S. Dong. BDF-like methods for nonlinear dynamic analysis. *Journal of Computational Physics*, 229:3019–3045, 2010.

[241] G. Taylor. The use of flat-ended projectiles for determining dynamic yield stress. i. theoretical considerations. *Proceedings of the Royal Society of London A: Mathematical, Physical and Engineering Sciences*, 194:289–299, 1948.

[242] E. Boatti, G. Scalet, and F. Auricchio. A three-dimensional finite-strain phenomenological model for shape-memory polymers: formulation, numerical simulations, and comparison with experimental data. *International Journal of Plasticity*, 83:153–177, 2013.

[243] A. Huerta and F. Casadei. New ALE applications in non-linear fast-transient solid dynamics. *Engineering Computations*, 11(4):317–345, 1994.

[244] A. Rodríguez Ferran, A. Pérez Foguet, and A. Huerta. Arbitrary Lagrangian Eulerian (ALE) formulation for hyperelastoplasticity. *International Journal for Numerical Methods in Engineering*, 53(8):1831–1851, 2002.

[245] J. D. Humphery. Continuum biomechanics of soft biological tissues. *The Royal Society*, 459:3–46, 2003.